Modeling and Simulation of Electrochemical Metallization Memory Cells for Neuromorphic Passive Crossbar Architecture

Von der Fakultät für Elektrotechnik und Informationstechnik
der Rheinisch-Westfälischen Technischen Hochschule Aachen
zur Erlangung des akademischen Grades eines Doktors
der Ingenieurwissenschaften genehmigte Dissertation

vorgelegt von

Rana Walied Ahmad, M.Sc.

aus Düsseldorf

Berichtende: Seniorprofessor Dr.-Ing. Rainer Waser
Universitätsprofessor Dr.-Ing. Max Christian Lemme

Tag der mündlichen Prüfung: 28.01.2026

Diese Dissertation ist auf den Internetseiten der Universitätsbibliothek online verfügbar.

Curriculum Vitae

28.01.2026	Doctoral Examination for *Doktor der Ingenieurwissenschaften* (Dr.-Ing.)
2020 – 2026	Enrolled Ph.D. Student Electrical Engineering RWTH Aachen University, Germany
2020 – 2024	Research Assistant and Doctoral Candidate Peter Grünberg Institut (PGI-7) Forschungszentrum Jülich GmbH, Germany
2014 – 2020	Studies of Physics Heinrich-Heine-Universität Düsseldorf, Germany
May 2020	Master of Science
March 2018	Bachelor of Science
2006 – 2014	General Higher Education Entrance Qualification (Abitur) Gymnasium St. Wolfhelm, Schwalmtal, Germany
1996	born in Düsseldorf, Germany

Abstract

Future computing applications such as artificial intelligence require the processing of unprecedented volumes of data. This exposes the energy inefficiency and bandwidth limitations of conventional von Neumann computer architectures, where memory and processing units are physically separated and data must be constantly moved between them. In contrast, resistive random access memory (ReRAM) devices based on nanoionic redox phenomena enable in-memory data processing and thus offer a route to mitigate the von Neumann bottleneck. In such devices, information is encoded in different resistance states of a nanoscale cell. ReRAM is therefore considered a promising candidate for the basic building blocks of novel hardware accelerators for Artificial/Spiking Neural Networks (ANN/SNN) and logic-in-memory applications. In many of these concepts, analog or multilevel ReRAM cells arranged in crossbar arrays perform Vector–Matrix Multiplication (VMM) or Multiply–Accumulate (MAC) operations in hardware, with each cross-point occupied by a nanoscale ReRAM device. Two important device classes are Electrochemical Metallization Memory (ECM) cells and Valence-Change Mechanism (VCM) cells. Nonvolatile ReRAM devices can mimic weighted synapses through multiple stable resistance states, while volatile ReRAM devices, often referred to as threshold switches, can be used to realize artificial neuron circuits. In addition, volatile devices can act as selector elements at the crossbar junctions to suppress leakage currents. Due to their inherent variability, they are also attractive for emulating the stochastic behavior of biological neurons and for the realization of True Random Number Generators (TRNGs).

In this thesis, different physics-based compact models for ECM-type ReRAM devices are developed, with a particular focus on device variability and volatile threshold switching. Both aspects have not been addressed in a consistent compact-model framework for ECM devices so far. Compared with the widely used three-terminal, transistor-based one-transistor-one-resistor (1T1R) crossbar arrays, which suffer from increased design complexity, reduced integration density and limited vertical stacking capability, two-terminal selector-based passive one-selector-one-resistor (1S1R) crossbar arrays avoid these drawbacks and are therefore highly attractive. However, due to their purely passive nature, ensuring reliable operation of 1S1R arrays is challenging, and only few works propose comprehensive solutions. In this context, this thesis advances the understanding and design of such passive arrays by means of physics-based compact-model circuit simulations. The strength of physics-based compact models lies in their ability to capture the internal dynamics and kinetics of a device based on its geometry and material stack. Once such a model is established, a broad range of operating conditions and application scenarios can be explored by adjusting geometry- or material-related parameters, while the underlying physical mechanisms remain consistently described during simulation.

Building on the previously developed JART ECM v1 model, two extensions are introduced in this thesis. First, to account for the naturally occurring device-to-device and cycle-to-cycle variability in ECM cells, a variability-aware and stochastic, physics-based compact model termed JART ECM v1 var is developed. Second, by incorporating the electromotive force (emf) arising from the nanobattery effect into a newly developed model called JART v-ECM v1, a physics-based compact model for volatile threshold-switching ECM (v-ECM) devices is established. In an application study, this v-ECM model is employed as a selector element in 1S1R crossbar arrays. Its behavior during read and VMM operations is investigated, compared to another threshold-switch compact model, and critically discussed. The simulations indicate that, due to its large achievable resistance window and highly nonlinear switching kinetics, the v-ECM device offers high potential as a selector in the desired 1S1R crossbar architecture. By performing and analyzing these compact-model-based simulations, this thesis contributes an additional step towards the reliable realization of neuromorphic and logic-in-memory applications on passive 1S1R ReRAM crossbar arrays.

Kurzfassung

Zukünftige Rechenanwendungen wie die Künstliche Intelligenz erfordern die Verarbeitung bislang unerreichter Datenmengen. Dies offenbart die Energieineffizienz und Bandbreitenbeschränkungen konventioneller von-Neumann-Architekturen, bei denen Speicher- und Verarbeitungseinheiten physisch getrennt sind und Daten ständig zwischen ihnen übertragen werden müssen. Im Gegensatz dazu ermöglichen Resistive-RAM-(ReRAM)-Bauelemente, die auf nanoionischen Redoxphänomenen basieren, eine Datenverarbeitung direkt im Speicher („in-memory computing“) und bieten damit einen Ansatz zur Abmilderung des von-Neumann-Flaschenhalses. In solchen Bauelementen wird Information in unterschiedlichen Widerstandszuständen einer nanoskaligen Zelle codiert. ReRAM gilt daher als vielversprechender Kandidat für grundlegende Bausteine neuartiger Hardwarebeschleuniger für Artificial/Spiking Neural Networks (ANN/SNN) sowie für „logic-in-memory“-Anwendungen. In vielen dieser Konzepte führen analoge oder multilevelfähige ReRAM-Zellen, die in Crossbar-Arrays angeordnet sind, Vector–Matrix-Multiplikationen (VMM) oder Multiply–Accumulate-(MAC)-Operationen direkt in Hardware aus, wobei jeder Kreuzungspunkt von einem nanoskaligen ReRAM-Bauelement besetzt ist. Zwei wichtige Gerätekategorien sind Electrochemical Metallization Memory (ECM)-Zellen und Valence-Change Mechanism (VCM)-Zellen. Nichtflüchtige ReRAM-Bauelemente können gewichtete Synapsen durch mehrere stabile Widerstandszustände nachbilden, während flüchtige ReRAM-Bauelemente, oft als Threshold-Switches bezeichnet, zur Realisierung künstlicher Neuronenschaltungen eingesetzt werden können. Darüber hinaus können flüchtige Bauelemente in Crossbar-Knoten als Selektorelemente dienen, um Leckströme zu unterdrücken. Aufgrund ihrer inhärenten Variabilität sind sie außerdem attraktiv für die Emulation des stochastischen Verhaltens biologischer Neuronen und für die Realisierung von True Random Number Generators (TRNGs).

In dieser Dissertation werden verschiedene physikbasierte Kompaktmodelle für ReRAM-Bauelemente des Typs ECM entwickelt, mit besonderem Fokus auf Zellenvariabilität und flüchtiges Threshold-Switching. Beide Aspekte wurden bisher noch nicht in einem konsistenten Kompaktmodellrahmen für ECM- Zellen adressiert. Im Vergleich zu den weit verbreiteten dreipoligen, transistorbasierten Ein-Transistor-Ein-Resistor (1T1R)-Crossbar-Arrays, die unter erhöhter Designkomplexität, verringerter Integrationsdichte und eingeschränkter vertikaler Stapelbarkeit leiden, vermeiden zweipolige, selektorbasierte passive Ein-Selektor-Ein-Resistor (1S1R)-Crossbar-Arrays diese Nachteile und sind daher besonders attraktiv. Aufgrund ihrer rein passiven Natur ist die Gewährleistung eines zuverlässigen Betriebs von 1S1R-Arrays jedoch herausfordernd, und nur wenige Arbeiten schlagen umfassende Lösungen vor. In diesem Zusammenhang leistet die vorliegende Dissertation einen Beitrag zum Verständnis und zur Auslegung solcher passiven Arrays mittels physikbasierter Kompaktmodell-Schaltungssimulationen. Die Stärke physikba-

sierter Kompaktmodelle liegt darin, die internen Dynamiken und Kinetiken eines Geräts auf Grundlage seiner Geometrie und Materialzusammensetzung präzise abzubilden. Ist ein solches Modell einmal etabliert, kann ein breites Spektrum an Betriebsbedingungen und Anwendungsszenarien durch Anpassung geometrie- oder materialbezogener Parameter untersucht werden, während die zugrunde liegenden physikalischen Mechanismen während der Simulation konsistent beschrieben bleiben.

Aufbauend auf dem zuvor entwickelten JART ECM v1-Modell werden in dieser Dissertation zwei Erweiterungen vorgestellt. Erstens wird, um der natürlich auftretenden Variabilität zwischen verschiedenen Zellen und zwischen verschiedenen Schaltzyklen in ECM-Zellen Rechnung zu tragen, ein variabilitätsbewusstes und stochastisches physikbasiertes Kompaktmodell namens JART ECM v1 var entwickelt. Zweitens wird durch die Einbindung der elektromotorischen Kraft (emf), die aus dem Nanobatterie-Effekt entsteht, in ein neu entwickeltes Modell namens JART v-ECM v1 ein physikbasiertes Kompaktmodell für flüchtig schaltende ECM-Schwellenbauelemente (v-ECM) bereitgestellt. In einer Anwendungsstudie wird dieses v-ECM-Modell als Selektorelement in 1S1R-Crossbar-Arrays eingesetzt. Sein Verhalten während Lese- und VMM-Operationen wird untersucht, mit einem anderen Threshold-Switch-Kompaktmodell verglichen und kritisch diskutiert. Die Simulationen zeigen, dass das v-ECM-Bauelement aufgrund seines großen erreichbaren Widerstandsfensters und seiner stark nichtlinearen Schaltkinetik ein hohes Potenzial als Selektor in der angestrebten 1S1R-Crossbar-Architektur bietet. Durch die Durchführung und Analyse dieser kompaktmodellbasierten Simulationen leistet diese Dissertation einen weiteren Schritt in Richtung einer zuverlässigen Realisierung neuromorpher und „logic-in-memory“-Anwendungen auf passiven 1S1R-ReRAM-Crossbar-Arrays.

Acknowledgements

This dissertation was prepared at the Peter–Grünberg Institute (PGI-7), Forschungszentrum Jülich, in collaboration with the Institut für Werkstoffe der Elektrotechnik II (IWE2) at RWTH Aachen University. I sincerely thank the many people whose support and contributions were instrumental to this work.

I wish to thank Prof. Rainer Waser and Prof. Max C. Lemme for serving as the first and second reviewers. I also thank Prof. Alexander Raake and Prof. Peter Knott for joining my Doctoral Commission. They all generously made time for my thesis and exam despite their demanding schedules. I am especially indebted to Prof. Waser for the opportunity to conduct my research in his institute and the excellent academic environment he provided.

My deepest appreciation goes to my supervisor, Dr. Stephan Menzel. His guidance, insightful suggestions, and steady encouragement shaped every stage of this dissertation. I learned countless lessons from him that will influence my future work, and I feel fortunate to have had him as a mentor.

At the beginning, Dr. Christopher Bengel and Dr. Nils Sommer offered invaluable technical and organizational support, helping me navigate the early research phases with confidence.

I am highly grateful to our collaborators and project partners. Many provided essential tools or experimental data, investing significant effort in clean rooms and labs. In particular, I thank Prof. Regina Dittmann, Dr. Dirk Wouters, Dr. Florian Maudet, Dr. Onur Toprak, Prof. Catherine Dubourdieu, Dr. Solomon A. Chekol, Julius Rasbach, and Dr. Susanne Hoffmann-Eifert for their indispensable cooperation. Further support came from Jimin Lee, Lukas Völkel, Yuan Fa, and Prof. Max C. Lemme. For fruitful discussions on ECM chemistry and physics, I thank Milan Buttberg and Dr. Ilia Valov. I also thank our MEMMEA project partners: Tom Stumpp, Dr. Peter Jones, Alex Wiemhoefer, Prof. Roland Thewes, and Christian Bruchatz.

I thank my office colleagues for the motivating atmosphere: Dr. Carsten Funck, Feng Liu, Xin Zheng, and Yaohui Liu. I am grateful to my former student Yaohui - now a fellow doctoral student - for his work during his project thesis, and to Alana Bestaeva for her dedicated assistance.

Furthermore, I acknowledge those who enriched the daily life at the institute: Seokki Son, Byoung Gun Han, Dr. Nils Kopperberg, Dr. Johannes Mohr, Kristof Lange, Denise Köhn, Anja Krieger, Petra Grewe, Daliborka Erdoglija, Dr. Jan Lübben, Dr. Pascal Stasner, Faisal Munir, Siyuan Jia, Dr. Stefan Wiefels, Dr. Moritz von Witzleben, Daniel Schön, and Dr. Leon Brackmann. I especially thank Daniel and Leon for their ongoing advice and interesting conversations. I also thank Ankit Bende, Iliyas Dossayev, Dr. Gwangmin Kim, Dr. Xiaohua Liu, Godwin Paul, Dr. Kristoffer Schnieders, Dr. Yongmin Wang, Dr. Fabiana Taglietti, Clemens Wittberg, Johannes Hellwig, Jinhao Zhang, and Xinyi Zhao. Being part of the PGI-7 team together made the time especially lively and enjoyable.

I am thankful for the administrative and technical assistance of Maria Garcia, Martina Heins, Udo Evertz, Marcel Gerst, Malte Deckers, Thomas Pössinger - whose graphics improved several parts of this thesis - Dr. Ulrich Böttger, and Dr. Theodor Schneller.

Among my friends, family, and close acquaintances, many of whom I have known for years, I express my gratitude to Nawied, Ijaz, Misbah, Nida, Danial, Frasat, Danish, and their sisters, Kashif, Sameem, Sajiel, and his sisters, Nayla, Patrick, Sebastian, Alex, Alex, Max, Abbas, Hannah, Lakshmi, Marten, and Pilut for their companionship, affection and encouragement. I am equally grateful to members of my community who supported me in numerous situations and were always ready to lend a hand: Ali, Tahir, Aman, Tanzeel, Rehan, Basharat, Zaheer, Ata, Umar, Ghalib, Saqib, Amir, Ali, Ehsan, Ahmad, Rehmat and many others. Furthermore, my cousin Adeel, Hasanat Ahmad and Prof. Nabeel Aslam have been a huge inspiration and valuable guides.

I extend my deep appreciation to my two sisters and my wife for their patience, help and understanding throughout this journey. Above all, my son's cute smiles were priceless. The same applies to my niece. I also thank my grandparents for their prayers and unwavering confidence in my path, as well as my aunts, uncles and cousins. Above all, I owe an immeasurable debt of gratitude to my parents. Their encouragement towards any kind of education, dedication, sacrifices, and steadfast support since the very beginning of my life made this milestone achievable.

Finally, I express my deepest thanks to the Almighty and Gracious God, whose guidance, protection, and blessings have accompanied me at every step. Alhamdulillah.

Linguistic Note: Large language models (ChatGPT) were used for linguistic optimization and paraphrasing of author-owned drafts to improve clarity. All scientific content remains the sole work of the author.

Contents

1 Introduction **1**

2 Fundamentals **5**
2.1 General Characteristics and Classification of ReRAM 5
2.1.1 Measurements characterizing a ReRAM Cell 7
2.2 Resistive Switching in ECM Cells 10
2.2.1 Variability Effects within ECM Devices 14
2.3 Charge Transport/Transfer Mechanisms in ECM Cells 16
2.3.1 Ionic Transport in ECM Insulators 16
2.3.2 Electron Transfer Processes within ECM Cells 17
2.3.3 Electrocrystallization as a special Reduction Process 20
2.3.4 Electronic Transport across MIM Structures 21
2.4 The Nanobattery Effect within ECM Cells 23
2.4.1 The Origin of the Nanobattery Effect 23
2.5 Two-Dimensional Materials for use in ECM Cells 27
2.6 Memristive Crossbar Arrays for Computation-In-Memory 29
2.6.1 Selector Devices in Crossbar Arrays 31
2.6.2 Read/Write Schemes in a Passive Crossbar Array 33
2.6.3 Vector-Matrix Multiplication on Crossbar Arrays 34

3 Used Models from the Literature **37**
3.1 Classification and Utilization of Compact Models 37
3.2 Selected ReRAM Device and TS Models from Literature 39
3.2.1 The Nonvolatile JART ECM v1 Model 39
3.2.2 The Nonvolatile JART VCM v1 Model 42
3.2.3 The NbO_2-based Threshold Switch Model 44

4 Newly Developed Models and Simulation Methodology **47**
4.1 Newly Developed Models for ECM Cells 47
4.1.1 The Variability-Aware Nonvolatile JART ECM v1 var Model . . . 48
4.1.2 The Volatile JART v-ECM v1 Model 51
4.1.3 The Variability-Aware Volatile JART v-ECM v1 var Model 56
4.2 Simulation Framework 56
4.2.1 Cadence Spectre 57
4.2.2 Simulation Framework for Variability Modeling 58

5 Variability-Aware Simulations of ECM Devices: Results and Discussion **61**
5.1 Fit to a Cu/SiO_2/W ECM Device 62

5.2 Fit to Two-Dimensional Material ECM Devices . . . 70
5.2.1 Modeling of reduced Variability in a $Ag/SiO_x/VAMoS_2/Au$ Device 70
5.2.2 Modeling the Influence of Moisture in a Ni/h-BN/Pd Device . . . 76
5.3 Comprehensive Simulation Study regarding Model Parameters . . . 77
5.3.1 SET Kinetics Parameter Study . . . 78
5.3.2 *I-V* Characteristics Parameter Study . . . 91
5.3.3 Influence of Sweep Rate Variation on *I–V* Characteristics . . . 102
5.4 Fitting Procedure Guide . . . 106
5.5 Summary . . . 111

6 Simulations of v-ECM Devices: Results and Discussions 113
6.1 Fit to a $Ag/HfO_2/Pt$ v-ECM Device . . . 115
6.2 Simulation Studies on Read Process, Kinetics, emf Strength, and Sweep Rate . . . 122
6.3 Comparison with other Volatile ECM Models in Literature . . . 127
6.3.1 Comparison with v-ECM Compact Models . . . 127
6.4 Summary . . . 131

7 Passive Crossbar Array Simulations of Read and VMM Operations 133
7.1 Simulated Characteristics of a Single 1S1R Crossbar Device . . . 134
7.1.1 The 1S1R Device consisting of a Threshold Switch . . . 135
7.1.2 The 1S1R Device consisting of a Volatile ECM Cell . . . 138
7.2 Read Scheme for 1S1R Crossbar Devices . . . 141
7.2.1 Read Scheme in a Threshold Switch-based 1S1R Crossbar Array . 143
7.2.2 Read Scheme in a Volatile ECM-based 1S1R Crossbar Array . . . 144
7.3 Vector-Matrix Multiplication on 1S1R Crossbar Arrays . . . 146
7.3.1 Vector-Matrix Multiplication on a Threshold Switch-based 1S1R Crossbar Array . . . 149
7.3.2 Vector-Matrix Multiplication on a Volatile ECM-based 1S1R Crossbar Array . . . 153
7.4 Summary . . . 155

8 Conclusions and Outlook 157
8.1 Summary and Conclusions . . . 157
8.2 Outlook . . . 159

Bibliography 163

List of Figures 183

List of Tables 185

List of Abbreviations 187

Supervised Students 189

List of Publications 191

1 Introduction

In conventional von-Neumann-based memory and computation concepts, both the memory unit and the Central Processing Unit (CPU) are located separately. Data needs to be transferred between both units, which results in the energy-costly rate-limiting von-Neumann bottleneck of data transfer [1–3]. As new applications, such as Artificial Intelligence (AI), are emerging and require a huge amount of data and data processing, the hardware-based conventional concepts will soon reach their limits and become highly inefficient in terms of energy consumption. In the coming years, the energy demand of such applications is expected to rise substantially, accounting for a significant share of global energy consumption [4]. New computation paradigms, such as hardware-based Computation-In-Memory (CIM), are seen to offer a solution for this arising deficiency [5]. CIM operations are enabled by utilizing resistive switching devices as future building blocks within redox-based resistive random access memory (ReRAM) architecture [6–12]. The two-terminal ReRAM devices built of a simple metal/insulator/metal (MIM) structure offer huge benefits: Besides their stacking capability and high density [13], they offer good endurance [14], power-efficiency [5], a nano-scale size [15, 16], and an ultrafast switching speed [17–19] resulting from a development over the last years. Among ReRAM devices, there are different types. The most known and studied are electrochemical metallization memory- (ECM-)type and valence-change mechanism (VCM)-type cells [6, 11]. Nanoionic processes, especially redox phenomena, within the insulating layer dominate the reversible switching between at least two resistance states. These resistance states in nonvolatile ReRAM devices are exploited for memory and computation processes. Even brain-inspired processing as in synapses can be emulated [20, 21]. However, volatile ReRAM cells and threshold switches offer the possibility to play a key role within artificial neuron circuits [22, 23]. They are also seen as two-terminal select devices for the crossbar junctions within passive crossbar array structures of ReRAM [24]. In the CIM paradigm, these crossbar arrays make up a huge part of Artificial Neural Networks (ANN) required for AI [25–27]. In this regard, the ReRAM devices on their crossbar junctions are utilized for Vector-Matrix Multiplication (VMM) operations for ANNs [24, 28]. As leakage current through low-resistive paths occurs in such arrays,

a select device for each crossbar node is essential [29–31]. However, the utilization of three-terminal transistors as select devices at each node in the active one-transistor-one-resistor (1T1R) crossbar array architecture avoids a highly dense, and simple crossbar array design [29]. These missing benefits and stackability are gained by utilizing two-terminal select devices as part of a one-selector-one-resistor (1S1R) design within each crossbar junction enabling highly dense passive crossbar arrays. When ECM devices are switched with a relatively small electric bias, they exhibit volatile threshold switching features [32] that can be exploited for a two-terminal select device within 1S1R crossbar arrays. The voltage-time dilemma states that a ReRAM device should remain in the same resistance state for days or even months when a small read voltage is applied, but should switch within nanoseconds when a higher write voltage is used. This challenge is effectively mitigated by the strongly nonlinear SET kinetics. [11, 33].

A key disadvantage for nonvolatile ECM devices in terms of reliability is their naturally inherent variability that arises from device to device and cycle to cycle [34–38]. Accompanied by a highly nonlinear SET kinetics, this variability can prove itself as an undesired feature for memory operations. For volatile ECM (v-ECM) cells, the variability contributes to a decreased reliability. However, for special applications, such as emulating the inherent stochastic behavior of natural neurons [39–41] or True Random Number Generator (TRNG) [42] applications, the variability becomes beneficial and desired.

Owing to their huge potential and to their reliability issues, physics-based models contribute to understanding the physical and dynamical mechanisms within the ReRAM devices that e. g. lead to the beneficial highly nonlinear SET kinetics. Also the occurrence of preserving or loosing its resistance state over time can be accessed by a physics-based modeling. Reliability issues such as variability can be incorporated and considered via variability-aware models. Compact models are based on some equations that describe the electronic device's behavior. Their simple design allows for implementing them into circuit simulators to test, simulate and design larger higher-level circuits for several applications.

As consistent works on physics-based variability-aware compact models and on physics-based v-ECM models are missing, this thesis targets these gaps. Furthermore, it presents the newly developed v-ECM model in the framework of a 1S1R crossbar array as an application case that targets the need of highly scalable ReRAMs and ANNs. While different types of variabilities are induced to model parameters to enable variability in electrical and dynamical results, the v-ECM model is realized by introducing the

electromotive force (emf) as nanobattery effect within the nanoionic processes [43]. Its incorporation effectively shifts the ionic dynamic equilibrium to a non-zero electrical bias. Both the variability simulations and simulations of v-ECM cells are verified with several experimental measurements supporting the models' theories and their validity. Regarding the 1S1R crossbar array simulations, the v-ECM model as select device is compared with a threshold switch model from literature. Furthermore, the feasibility of read and VMM operations is investigated with respect to crossbar array size and wire resistance values. Also, the interplay of the involved ReRAM device's and select device's SET/switching kinetics, their resistance windows and their impact on the crossbar array operations is assessed.

Chapter 2 presents the fundamentals that build a basis of all approaches and studies. Chapter 3 introduces any model that is used during the simulation studies but is taken from literature, whereas Chapter 4 provides an overview of the newly developed models in the framework of this thesis. It also presents the simulation methodology utilized within the generation of this thesis. Chapter 5 deals with the model development of variability-aware ECM devices. This model is verified by several experimental considerations, among them are two-dimensional material-based ECM devices that are attracting great attention. Model parameter studies contribute to a better understanding of the device's physics and its impact on the model. Chapter 6 presents the volatile ECM model based on the electromotive force. It is also validated by measurements. A simulation study shows the novelty and the effect of this new approach's theory. The v-ECM model is compared to more than a dozen models presented in the literature. Its consistency compared to other models is discussed and ascertained. Chapter 7 addresses the simulation of passive 1S1R crossbar array operations. Utilizing the newly developed v-ECM as select device and comparing it to another threshold switch device model enables to evaluate the feasibility of 1S1R crossbar array operations, such as read schemes and VMM operations. An interplay of the requirements of a 1S1R cell, the crossbar array size, and the wire resistances contribute to the gained insights. Finally, this thesis' outcomes and conclusions are summarized in Chapter 8, and an outlook is presented.

2 Fundamentals

2.1 General Characteristics and Classification of ReRAM

Due to their huge potential of revolutionizing parts of computerized electric processing, *redox-based resistive switching random access memory* (**ReRAM**) devices belonging to the class of resistive RAM (RRAM) make up a novel research area [6, 7, 11]. The term RRAM refers to memories whose physical storage principle is based on the change of the electric resistive state. Alongside ReRAM, there are further types of RRAM, such as magnetoresistive random access memory (MRAM) [44] or phase change memory (PCM) [45]. ReRAM devices feature a resistance change through chemical redox reaction processes. They consist in the simplest form of an MIM design structure, where an insulating layer (I) is sandwiched between two metal electrodes (M). The redox processes inducing ions into the system are often accompanied by ion migration processes throughout the insulating layer. Initiating both of these ionic processes requires an electric field applied across the device structure. The insulating layer might be either an insulating ion conductor or a mixed ionic electronic conductor [6, 11].

ReRAM cells can be further classified into *nonvolatile* and *volatile* devices. Distinguishing between these two types depends on the retention of the device after programming: If the device is able to keep its resistance state over a long time period like months or years when no or little voltage bias is applied, it is classified as nonvolatile, whereas it is seen as a volatile device, if it looses its information packed in its resistance state relatively fast, like in milliseconds. There are no hard definition boundaries between these two types, as they rather depend on the application use of the device and the corresponding required time of holding the resistive state. Volatile ones that switch abruptly between two states are also known as threshold switching (TS) devices.

Both types, volatile and nonvolatile, can be switched between at least two resistance state levels, respectively. The low-ohmic/*high-resistive state* (**HRS/OFF**) is switched to the high-ohmic/*low-resistive state* (**LRS/ON**) upon applying a certain polarized *SET voltage* V_{SET} in the shape of an abrupt pulse or a slower sweep. This is valid for bilevel

devices. There are as well multilevel devices which feature various accessible resistance state levels. Some specific nonvolatile devices that are discussed in this thesis behave in a *bipolar* fashion, which means that they switch back from the LRS to the HRS upon applying the opposite voltage bias across the device, the *RESET voltage* V_{RESET} [11]. Nevertheless, there are nonvolatile devices that are *unipolar*: Upon applying the same polarity but a different voltage amplitude the device switches back to the HRS [11]. In volatile devices, a single voltage polarity is typically sufficient for the device's operations as the transition back to the HRS occurs spontaneously through relaxation rather than requiring an actively driven RESET pulse: The device switches to the LRS upon applying a relative high *threshold voltage* V_{th} and relaxes back to the HRS by decreasing the applied voltage below V_{hold} [23]. The time both a nonvolatile and a volatile device take to switch from the HRS/OFF to the LRS/ON after applying the voltage bias is called *SET time* t_{SET} or *switching time* t_{sw}. The time a nonvolatile device takes to switch off after applying V_{RESET} is called *RESET time* t_{RESET}, whereas the time to relax back after applying a certain voltage below V_{hold} is called relaxation time t_{r} (volatile device). These times highly depend on the strength of the applied signal and the strength of the corresponding prior resistive state. Thus, their dynamics depends on their corresponding highly nonlinear *SET/switching kinetics* or *RESET/relaxation kinetics*.

Among ReRAM devices based on ions inducing redox effects three types can be distinguished: firstly *electrochemical metallization memory* (**ECM**), also known as *conductive-bridge random access memory* (**CBRAM**) [11], secondly valence change memory (VCM), also known as oxide-based random access memory (Ox-RAM) [11] and thirdly thermochemical memory (TCM) [6, 11]. VCM devices consist of two electrodes of typically different material and a mixed ionic electronic conducting (MIEC) layer in between. The switching of this device occurs through the migration of ionic defects and a simultaneous valence change of the cation sublattice [11]. In TCM devices, the switching to a lower resistive state occurs through thermochemical reactions, which subsequently induce stoichometric changes within the material. These thermochemical reactions are triggered by thermal gradients and, hence, solely depend on the current amplitude and not on the applied voltage polarity. Therefore, TCM devices show a unipolar switching behavior [11]. In ECM devices, bipolar switching to a lower resistive state occurs as a consequence of an electrochemically triggered metallic filament formation bridging the insulating layer after applying an electrical stimuli, i.e., a voltage bias. Besides the electrochemical activity, this stimuli activates further ionic processes that lead to fil-

ament growth/dissolution processes. The RESET/relaxation process occurs, when the filament is dissolved. ECM device stacks consist of a chemically active metal electrode, an ion-conducting insulating host layer in between and a chemically inert electrode. Many works have shown that ECM devices exist both as volatile and nonvolatile devices and have described, investigated, modeled or reported on at least one of the two device types [23, 32]. Often, a nonvolatile behavior is achieved, when a strong electrical stimulus is applied; correspondingly, the ECM device exhibits volatile behavior, when it experiences a weak electrical stimulus. In the context of their application, this beneficial property of them is employed and they are used either as the one or the other type. This thesis mainly focuses on the modeling of ECM devices, whereas in a small part of the thesis a well-established VCM device model is employed for an application case.

2.1.1 Measurements characterizing a ReRAM Cell

Characterizing a ReRAM cell before exploiting its static and dynamic features in higher-level hardware architectures is essential to understand both its potential benefits and its inherent limitations.

To test their basic functionalities regarding switching between resistive states, their switching polarities, and their type/possible long-time retention, triangular current-voltage (I-V) sweep measurements have been established. Figures 2.1 (a) and (b) present typical nonvolatile and volatile I-V sweep characteristic for ECM devices, respectively: Starting in the HRS, the voltage is swept and increased continuously with a specific sweep rate β until a highest allowed voltage value is reached. During this part of the sweep, the current through the device might increase slowly first, but once a conductive filament has built, the cell switches to the LRS in a very abrupt fashion at a specific SET/threshold voltage $V_{\mathrm{SET,th}}$ in the case of an ECM cell. To prevent the cell's permanent electric breakdown, i. e., to prevent that the cell's switching becomes irreversible as a permanent filament has built upon applying a too strong bias, a certain circuitry sets the compliance current I_{cc} as the highest possible current that passes through the cell. If the applied voltage increases further while the current is restricted by the current compliance, the voltage across the ReRAM device drops from the V_{th} value due to the snapback and is then determined by the compliance current. While the volatge is swept back to 0 V, a linear LRS current is perceived, once it falls below I_{cc}. In the case of volatile devices, the cell additionally switches back to the HRS/OFF before reaching 0 V (cf. Figure 2.1 (b)). Otherwise, the current linearly decreases with decreasing voltage (cf. Figure 2.1 (a)). For both device types, volatile and nonvolatile, the current is zero or

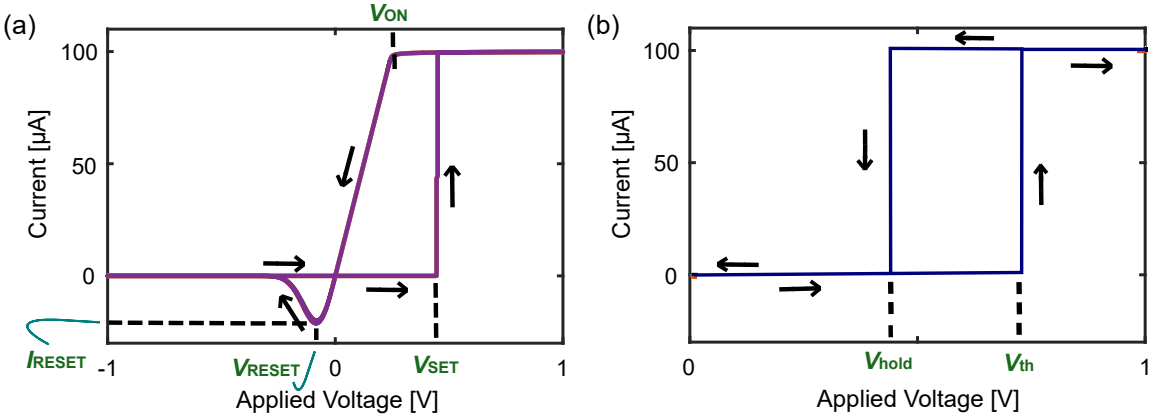

Figure 2.1: Conceptual illustration of a (a) nonvolatile ECM cell's I-V sweep highlighting the SET voltage, ON voltage, RESET voltage, and RESET current as characteristic values, and of a (b) volatile ECM cell's I-V sweep highlighting the threshold voltage and hold voltage as characteristic values. Adapted under the terms of CC-BY 4.0 license [34, 46].

very small while crossing 0 V. Sweeping further into the direction of increasing negative polarity makes the absolute negative current rise again linearly with increasing absolute voltage for nonvolatile devices. Then, at V_{RESET} they experience a big enough driving force to let them switch back to the HRS. After reaching a preset highest negative voltage, the nonvolatile devices are swept back to 0 V to complete a full I-V sweep cycle. This characterization process ensures a check of the ReRAM cell's static functionalities, and it helps determining resistance states, $V_{\mathrm{SET,th}}$ and $V_{\mathrm{hold}}/V_{\mathrm{RESET}}$ for a specific sweep rate.

An insight to the dynamic features of a ReRAM device enables a further crucial characterization: Applying a relatively small read voltage V_{read} to the ReRAM device should not change the resistive state, i. e., the applied bias should trigger a change in resistance after a long time period that is much longer than the read process (e. g., years vs. microseconds). However, a higher programming/write voltage V_{p}/ V_{write} should immediately change the resistive state within microseconds or less time. Thus, a check of the device's dynamic features is inevitable and is performed by designing a measurement scheme that accesses dynamical parameters, such as t_{SET}, t_{RESET} or t_{r}, while ensuring that according to their inherent nonlinear switching kinetics nature, these dynamical parameters vary by orders of magnitude in time depending on the strength of the applied bias. Such a measurement scheme is designed for accessing the SET time in the following way: Rectangular voltage pulses of different amplitudes V_{p} are applied to the cell in its HRS. Depending on the amplitude, the time between the start of the pulse

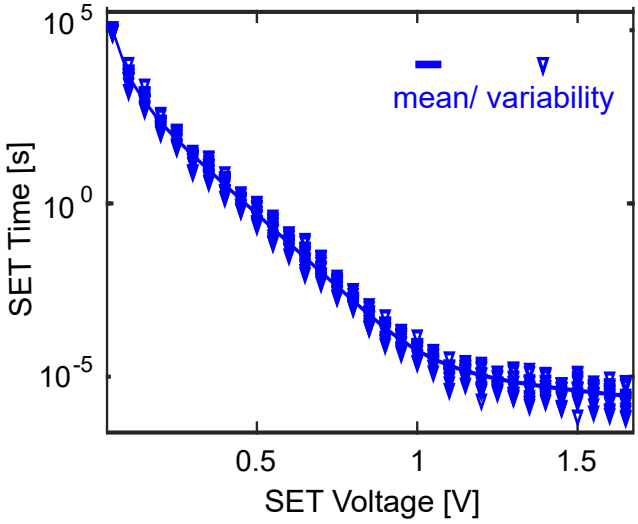

Figure 2.2: Exemplary SET kinetics of an ECM cell plotted over many orders of magnitude in SET time: A mean curve and several data points show the nonlinear decrease in SET time with increasing applied voltage. Different slopes can be observed.

and the switching, i. e., the switching delay, varies by orders of magnitude. It shall be noticed that this switching time t_{SET} decreases nonlinearly while the voltage amplitude is increased in a linear manner. Upon transferring the data points into a $\log t_{\mathrm{SET}}$ - V_{p} plane, the full switching kinetics can be accessed in an illustrative way, as exemplarily a SET kinetics mean curve and individual data points are shown in Figure 2.2. Usually different slopes of the switching kinetics curve within the $\log t_{\mathrm{SET}}$ - V_{p} plane are observed [47]. Low voltages represent the range for reading the device, whereas high voltages are attributed to programming or writing the device. The switching kinetics is an example of a simple and established characterization that checks the dynamical features of a ReRAM device. A similar approach is followed to access the nonlinear RESET kinetics, while negative rectangular voltage pulses are applied. The higher the absolute applied voltage the faster the device's RESET occurs. Also, this relation is a highly nonlinear relation. The relaxation kinetics is accessed in a very related manner. The only difference is that pulse amplitudes smaller than V_{hold} are applied to the device, positively biased as well as negatively biased.

A further advanced measurement checking the device's dynamic functionality for volatile devices consists of programming the device followed by measuring the relaxation of it while applying a read voltage that is smaller than the hold voltage. The relaxation time is then defined as the time from the start of the read voltage to the relaxation back to the HRS. This measurement should be repeated for different programming amplitudes.

Emulating spike time-dependent plasticity benefits from the insights of volatile device's relaxation kinetics.

2.2 Resistive Switching in ECM Cells

The chemically active electrode material in an ECM cell is typically a pure metal, such as Cu, Ag, Ni and Te or alloys containing Cu or Ag, such as CuTe, AgCu and AgTe [22, 34, 48, 49]. The chemically inert electrode material is usually chosen to be W, Au, Ir, Pt or TiN [34, 50–52]. The insulating layer is chosen from a vast variety of materials, as its main role is to enable electron and ion conduction as well as filament formation from one electrode to the other electrode. Different type of materials that are used as insulating materials for the host layer have been investigated, including oxide insulators such as SiO_2 [34], HfO_2 [23, 48], and Ta_2O_5 [51]; pure electrolytes such as AgI [47]; mixed ion–electron conductors such as Ge_xSe_{1-x} [53]; as well as van der Waals-type two-dimensional materials, including hexagonal boron nitride (h-BN) [49] and molybdenum disulfide (MoS_2) [50, 54, 55]. An ECM cell in its HRS state is characterized by a resistive state in GΩ or TΩ range. The exact resistance value depends on the insulating material that is used for the insulating layer or on a possible remnant filament size and its distance from the active electrode. Different ionic processes that are exemplarily shown in the context of an *I-V* sweep in Figure 2.3 trigger the switching mechanism from the HRS to the LRS in ECM cells. When exemplarily a positive voltage is applied to the active electrode, whilst the inert electrode is grounded, the following ionic processes occur within a nonvolatile ECM cell:

1. A crucial ionic process is the physiochemical process of electron transfer. It describes the formation of ions from metal atoms and vice versa by redox processes [47]. In an ECM cell, these redox processes occur
   - at the active electrode/insulating layer interface: a part of the applied voltage drops as overpotential across this interface enabling the oxidation process of active metal atoms to ions according to
     $$\mathrm{M} \longrightarrow \mathrm{M}^{z+} + z\mathrm{e}^{-},$$
   - at the insulating layer/inert electrode interface: a part of the applied voltage drops as overpotential across this interface enabling the electrodeposition as reduction process of ions to metal atoms according to
     $$\mathrm{M}^{z+} + z\mathrm{e}^{-} \longrightarrow \mathrm{M}.$$

Here, M is the metal atom, M^{z+} the z-valent ion and z is the number of transferred electrons. These two redox processes enable that the charge which is carried by ions and triggers the resistive switching and relaxation process can be transferred through the interfaces. Both redox processes are assumed to occur simultaneously in the memristive cell, as charge neutrality needs to be ensured if these processes within the cell are continuing over time [56]. In most cases, in which metal ions originating from the active electrode material are not part of a pristine device's insulating layer, the water splitting reduction process at the inert electrode

$$2H_2O + 2e^- \rightleftharpoons 2OH^- + H_2$$

is the counterpart process of the very first metal ion forming oxidation processes at the active electrode [57]. As no active metal ions are present in such a pristine device before its first switching, this step is the necessary initiator for enabling resistive switching within the device. For some other rare cases in which chalcogenides containing active metal electrode material are used as insulating layer, there may be no need for a counter reaction including water. Then, the reduction process involving the active metal ions available in the insulator is responsible for the initial charge neutrality within the memristive cell. This reduction process including active metal ions is the same reduction process that occurs in a non-pristine cell on a later stage. In another work, the water splitting reduction process is presented by the expression [58]

$$\tfrac{1}{2}O_2 + H_2O + 2e^- \longrightarrow 2OH^-.$$

The water splitting reduction process turns out to be essential for the resistive switching mechanism in devices in which chalcogenides containing the active electrode material are not involved: As humidity/water is requisite for the onset of resistive switching in a pristine device, the switching mechanism is not possible in vacuum conditions [49]. Water usually originates from the moisture of the ambient air or from components of fabrication steps, e. g. from atomic layer deposition (ALD) precursors.

2. The ion migration/hopping process is the charge transport process triggered by the applied electric field. The charge which is carried by the ions needs to move through the insulating layer from one electrode to the other electrode so that the switching process and the relaxation process can be realized by successive filament formation and preceding filament dissolution [47].

3. When there is no remnant filament in the insulating layer, a new nucleus has to be built. The nucleation process is a special type of electrodeposition, as it

descibes the very first reduction processes of several metal ions at the insulating layer/inert electrode interface before the onset of filament formation. A critical number of metal atoms has to be achieved in order to enable a successive filament growth on top of them. These few metal atoms form the nucleus. This nucleus might be rebuilt after a strong relaxation or RESET process, when no remnant filament is left. Also, in pristine devices, a very first nucleus formation occurs necessarily [47].

In the following, the introduced ionic mechanisms are presented in the right order and context-based sufficiently detailed as integrated mechanisms within first switching, consecutive switching and relaxation/RESET events:

Besides the water splitting reduction process at the insulator/inert electrode material within a pristine device, most of the devices in a pristine state go through an electroforming process. This process is applicable to ECM cells that do not have an insulating material containing any type of active metals/ions, for example solid-state oxide materials. The electroforming process is the incorporation of mobile M ions from the active electrode into the insulating layer [59]. In a simple picture, Figure 2.3, reproduced from [60], illustrates the HRS before electroforming/switching in the inset A. Usually, the very first switching, also typically called electroforming, occurs at a higher voltage V_{form} than consecutive switching events. They take place at a lower $V_{\mathrm{th}}/V_{\mathrm{SET}}$. Hence, the incorporation of M mobile ions leads to a growth channel that enables easier and reversible resistive switching for consecutive cycles.

The following order of ionic processes, exemplarily explained for one active metal atom/ion is applicable to both the switching in the first electroforming cycle and switching in consecutive cycles:

Upon applying an electrical stimulus, such as a positively biased rectangular voltage pulse or a corresponding voltage sweep to the active electrode, a metal atom M in the active electrode is oxidized to a metal ion M^{z+} (inset B of Figure 2.3). Under the influence of the applied electric field, it migrates towards the inert electrode. If it is one of the first ions to arrive at the inert electrode and becomes part of a filament growth, by a reduction process it becomes a metal atom M again and is part of a nucleus consisting of a critical number of metal atoms that is crucial to allow for further filament growth. If it arrives at a filament's tip that has already gone through a nucleation process, it becomes part of the filament as metal atom M after a reduction process and contributes to the filament growth towards the active electrode (inset C of Figure 2.3). After further and further ions arrive and contribute to the filament growth as metal atoms, the gap

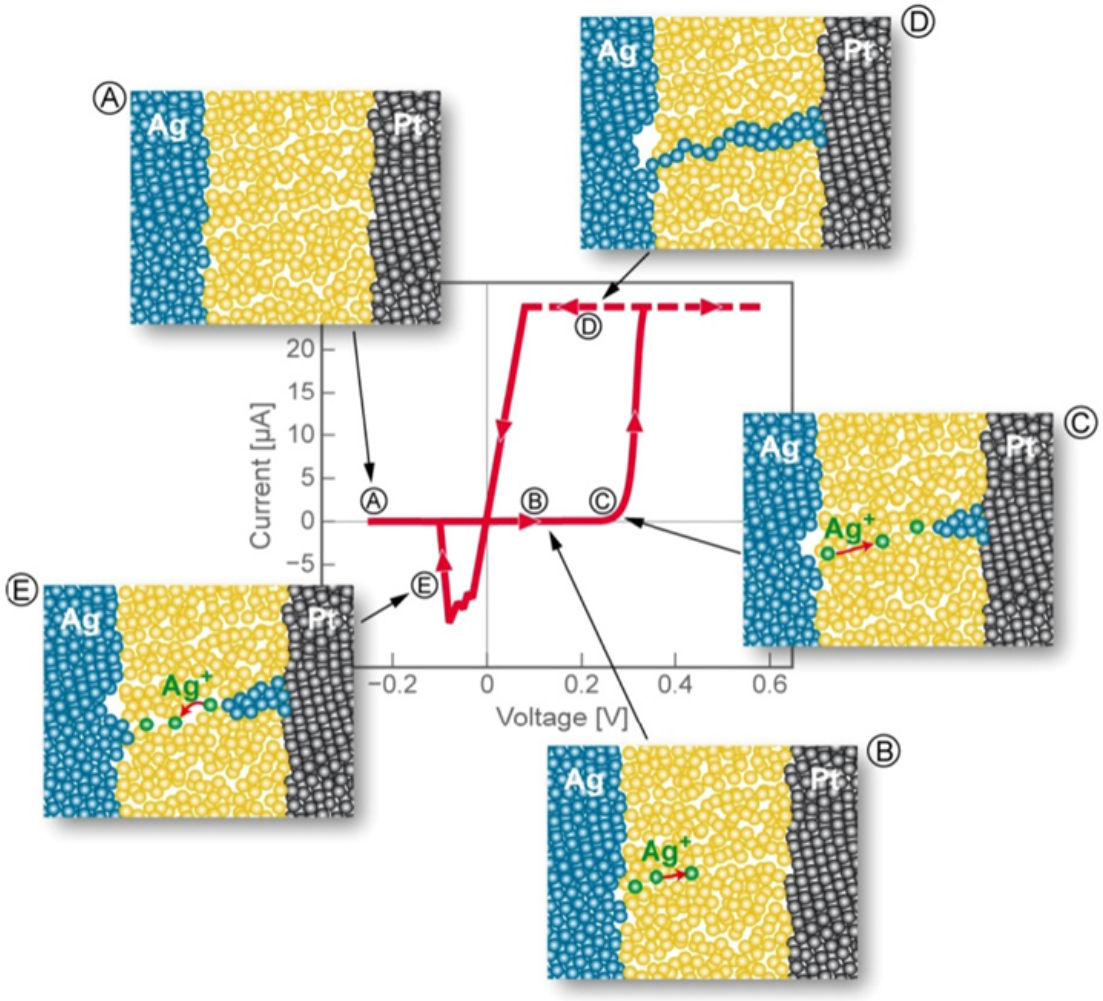

Figure 2.3: Illustrated ionic processes within a nonvolatile ECM cell, exemplarily shown for the *I-V* sweep in a Ag/Insulator/Pt stack: A - The ECM cell is in its HRS before a positive electrical stimulus is applied. The two electrodes are not electrically bridged. B - Upon applying positive bias, individual Ag atoms are oxidized to Ag cations at the active electrode; they migrate to the inert Pt electrode under the influence of an applied electric field. Only a relatively small ionic current is measured. C - At higher applied voltages, shortly before switching to the LRS is proceeded, a conductive Ag metal has formed between the two electrodes. It establishes itself upon nucleation and subsequent reduction of the arriving Ag cations. D - After switching, a high pronounced electronic current is measured, and the filament can bridge the whole insulator: The cell is in its LRS. A current compliance stabilizes the LRS current level. E - Upon applying a sufficiently large negative voltage, the filament undergoes a dissolution process that is initiated by the reduction of the filament's Ag atoms. As the filament dissolves, the cell switches back to its HRS. Again, only a small ionic current is dominating. Reproduced with permission from [60], © 2011 IOP Publishing Ltd.

between active electrode and filament tip shrinks. A tunneling electronic current from the filament tip to the active electrode gets stronger with decreasing gap size. As soon as a pronounced tunneling current is measured due to a small enough gap size, the switching/SET event has finally concluded; often this small gap is referred to a tunneling current value of between several nanoamperes to microamperes, as the ionic current contributions dominating the HRS and triggering the switching event are by orders of magnitude smaller. The device has switched to the LRS (inset D of Figure 2.3).

In a RESET/relaxation process, the filament is removed in a dissolution process upon applying an effective negative voltage bias to the active electrode as pulse or sweep: Mainly, the relaxation/RESET event is driven by an oxidation process that gradually converts filament metal atoms M into ions M^{z+}, thereby removing them from the filament. These ions migrate back to the active electrode, where they are reduced and reincorporated as metal atoms. As the filament gets smaller and smaller by this process, the previously pronounced electronic tunneling current through the gap between filament tip and active electrode gets very weak. A switching back to the HRS occurs (inset E of Figure 2.3). If this event occurs at a negative applied voltage, the correspondig voltage is known as RESET voltage V_{RESET}, otherwise if the device spontaneously switches back to the HRS at a positive (effectively negative) applied voltage bias, it is known as hold voltage V_{hold}. $V_{\mathrm{hold}} < V_{\mathrm{th}}$ is always valid. The nucleation process is the only ionic process among the processes introduced before that does not contribute to the RESET/ relaxation event.

2.2.1 Variability Effects within ECM Devices

As ReRAM devices are tuned to specific characteristic values, such as $V_{\mathrm{SET,th}}$, V_{RESET}, V_{hold}, t_{SET}, t_{r} for use in application, variabilities in these characteristics might lead to serious errors [38]. However, for some application types, such as TRNG, variabilities can turn out to be beneficial and can be exploited for various tasks within the application. Therefore, quantizing the variability and estimating its range that is intrinsically inherent within a device remains crucial. After accessing the variability extent, a circuit- or system-level application might be designed. Accurate modeling of device variability via a variability-aware compact model embedded in a circuit simulator is essential for ensuring reliable circuit design. It allows for estimating the acceptable extent of variability in the scope of the application.

Due to their intrinsic filamentary nature, ECM devices suffer from non-idealities, especially various kinds of variabilities during operation. These variabilities are ascribed to

different geometries or slightly varying dynamics/physics regarding filaments' strength or ionic processes' speed, or to stochasticity arising from the stochastic movement of individual atoms/ions.

There are different types of variabilities that differ in their extent:

1. device-to-device (d2d) variability

2. cycle-to-cycle (c2c) variability

3. variability induced by stochasticity

d2d variability arises between different devices, while they are operating in the same mode. Variabilities that differ from device to device originate from slight differences in the fabrication process or in the material composition. Different thicknesses of insulator layers, structural inhomogeneities or interfacial differences are known to be inducing variabilities [38]. This type of variability usually has the highest extent, whereas the variabilities experienced by the other two are often smaller. It shall be noted that d2d variability also naturally covers c2c variability and stochasticity. Therefore, it might be challenging to distinguish between these.

c2c variabilities are referred to the differences that occur from cycle to cycle within one device. A cycle is attributed to the full operation of a SET process followed by a RESET or relaxation process in any manner. In this dissertation, a focus lies upon c2c variabilities of I-V sweeps. As the full filament or parts of it are built and dissolved repeatedly from cycle to cycle, the occurring variability is ascribed to a slightly distinguishable filament growth and dissolution from cycle to cycle: The filament radius, the ion concentration within the insulator or the reaction rate of individual ionic processes might differ. Also, a different nucleation site, and thus, a different filament growth site during a certain cycle operation might lead to c2c variability [38].

Variability that is induced by stochasticity arises from randomly occurring (partly thermally-assisted) jumps of metal ions or atoms away from or to the filament tip, respectively. Also, such variability on the smallest scale can have a huge impact, as only one additional atom is sufficient to decisively increase the filament length so that the remaining tunneling gap is small enough for allowing an abrupt pronounced current increase. The opposite process has a similar probability [38].

2.3 Charge Transport/Transfer Mechanisms in ECM Cells

In the following, the fundamental theory of

- ionic transport in solids,
- electron transfer, and
- electronic transport across metal-insulator-metal structures

is presented. These three processes are crucial for enabling resistive switching in ECM cells.

2.3.1 Ionic Transport in ECM Insulators

One possible mechanism of ion migration due to an electric field in a solid material is described in an atomistic consideration as hopping of the ion from vacant site to vacant site into a preferred direction. The distance of vacant sites corresponds to the mean ion hopping distance a, which is on the scale of interatomic distances related to the intrinsic energy landscape of ionic crystals, as illustrated in Figure 2.4 [61]. The hopping direction is specified by the direction of the electric field, whereas the hopping occurs randomly into vacant sites of all directions with net flux of zero, when no electric field is applied. Then, a hopping activation barrier of ΔG_{hop} must be overcome through an activation energy of the ion induced by thermal fluctuations. According to an energy diagram the movement from vacant site to vacant site corresponds to hopping from one energy minimum to another energy minimum with a potential barrier ΔG_{hop} in between (upper illustration of Figure 2.4). However, when an electric field E is applied, the barrier into one direction of the electric field is lowered by $zeaE/2$ and increased by $zeaE/2$ into the other direction of the electric field. The hopping into the direction of the barrier lowering becomes more probable and thus, a ionic net flux arises (lower illustration of Figure 2.4). Here, z is the number of electric charges that is carried by one ion, and e is the fundamental electric charge. The ion migration process takes place in ECM cells whenever an ion migrates within the insulator between the two electrodes. Its corresponding ionic current density J_{hop} is mathematically described by the Mott-Gurney law of ion hopping [62]:

$$J_{\mathrm{hop}} = 2zecaf \exp\Big(-\frac{\Delta G_{\mathrm{hop}}}{k_{\mathrm{B}}T}\Big)\sinh\Big(\frac{zea}{2k_{\mathrm{B}}T}E\Big). \tag{2.1}$$

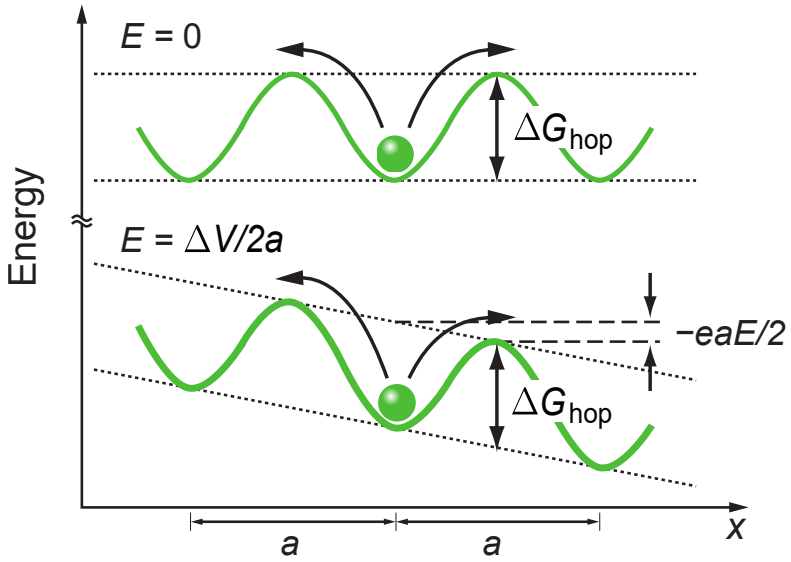

Figure 2.4: The upper illustration shows that ionic hopping from one energy minimum to another over the distance a remains equally probable into all directions when no voltage is applied, thus, no electric field exists. An energy barrier of ΔG_{hop} separates the energy minima. No ionic net flux is perceived, as the hopping in all directions is equally probable. The lower illustration depicts the case of an applied voltage and an existing electric field $E = \Delta V/(2a)$. In the direction of the electric field the energy barrier is lowered by $-eaE/2$, whereas it is increased by $+eaE/2$ in the other direction. An ionic net flux arises. Reproduced with permission from [63], © 2012 Wiley-VCH.

Here, c is the ion concentration, f is the ion hopping attempt frequency, k_{B} is the Boltzmann constant and T is the temperature. Due to the sinh() function, the ionic hopping current density becomes exponentially dependent on the electric field E, if $E \gg 2k_{\text{B}}T/(aez)$ and linearly dependent on E, if $E \ll 2k_{\text{B}}T/(aez)$.

2.3.2 Electron Transfer Processes within ECM Cells

Ions carry their charge throughout the insulator of an ECM cell, as they migrate due to an applied electric field. Once they arrive at the electrodes, their further migration is blocked and so is the charge transportation, as the metal electrodes are ion blocking. Thus, the ions can only contribute to the overall current and charge transportation, when they transfer their charge to the electrodes through redox reactions [47]. Also when metal atoms become ions, they experience such charge transferring redox reactions. One, two or several electrons are transferred during one redox reaction depending on the ion's valence number. Figure 2.5 shows two cases with two potential wells [61]: The left potential well shows an atom of the active metal electrode surface in its energy minimum, whereas the right potential well is occupied by a metal ion in the insulator near the interface

in its own energy minimum. Both potential wells are separated by a potential barrier. In the first case for no applied voltage (grey energy profile), both potential wells have the same depth, and for both redox processes to happen, namely oxidation (the metal atom on the left side loses an electron, leaves the metal surface and becomes a charged ion in the insulator on the right side) and reduction (the positively charged ion on the right side receives an electron, deposits at the metal surface and becomes an uncharged atom on the metal electrode surface on the left), the same amount of electron transfer activation energy $\Delta G_{\mathrm{et}} = \Delta G^0_{\mathrm{ox}} = \Delta G^0_{\mathrm{red}}$ is required. Thermal fluctuations might drive these processes, however, none of them is pronounced, leading to an effective dynamic equilibrium of both. If a positive voltage is applied to the active electrode (second case, red energy profile), the potential well of the ion in the insulator gets deeper by $ze\eta$, whilst the highest barrier value between both potential wells decreases by $\alpha_{\mathrm{et}} ze\eta$. z is the number of transferred electrons during one redox process, e is the electronic charge, η is the overpotential that drives the redox process at this interface and α_{et} is the electron transfer coefficient that generally describes the portion of the total available redox overpotential which is used for lowering the activation energy for the particular process. For $0 < \alpha_{\mathrm{et}} < 0.5$ the oxidation is favored compared to the reduction, while for $0.5 < \alpha_{\mathrm{et}} < 1$ the reduction process is more probable for any metal/insulator interface, independent of the overpotential's polarity. However, as a positive voltage is applied to the active electrode and the inert electrode is grounded in this case, the oxidation process at the active metal electrode/insulator interface is dominant (shown in Figure 2.5), whereas the reduction is dominant at the insulator/inert electrode interface (not shown). This effect is controlled by the overpotential's polarity η as well as by both exponential dependencies on it within the Butler-Volmer ionic current density. This current density describes the electron transfer process mathematically as follows [64, 65]

$$J_{\mathrm{et}} = zeck_{0,\mathrm{et}} \exp\Big(-\frac{\Delta G_{\mathrm{et}}}{k_{\mathrm{B}}T}\Big) \cdot \Big[\exp\Big(\frac{(1-\alpha_{\mathrm{et}})ze}{k_{\mathrm{B}}T}\eta\Big) - \exp\Big(-\frac{\alpha_{\mathrm{et}}ze}{k_{\mathrm{B}}T}\eta\Big)\Big]. \tag{2.2}$$

Here, $k_{0,\mathrm{et}}$ is the electron transfer reaction rate. The left term in the square bracket describes the oxidation process, while the right term is associated to the reduction process at the same interface. Due to the equation's composition the following is valid: When the overpotential across the interface is low, i. e. $\eta << \frac{k_B T}{ze}$, the current rises linearly with η, and it rises exponentially with η, when the overpotential across the interface is relatively high, i.e. $\eta >> \frac{k_B T}{ze}$.

However, if a negative voltage is applied to the active electrode (third case, not shown in Figure), the potential well where the ion sits in the insulator gets shallower by $ze\eta$,

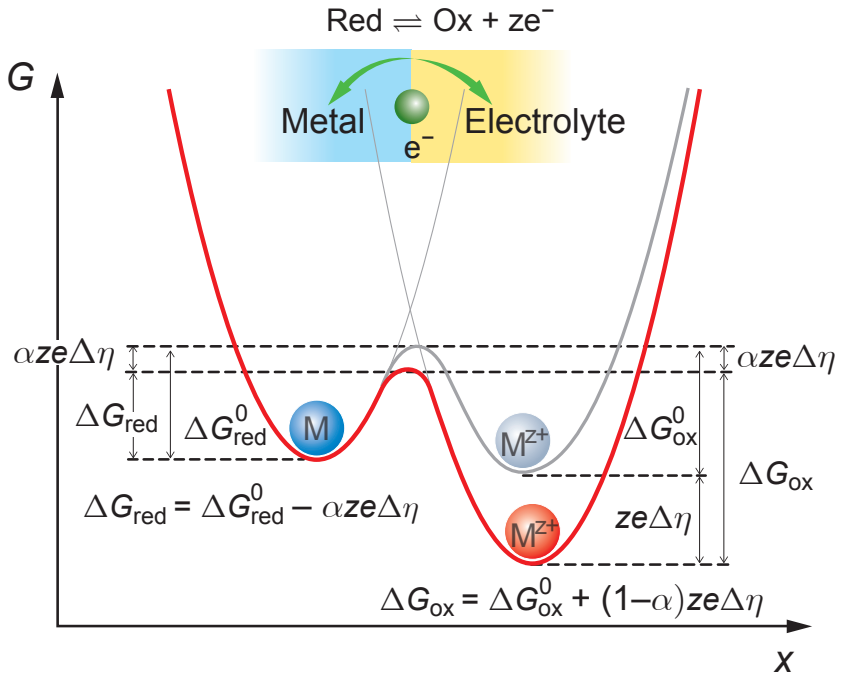

Figure 2.5: The grey energy profile describes the charge transferring redox process for a missing electric field. As no voltage is applied, the probability for both the left atom oxidizing to an ion and the right ion for reducing to a metal atom by overcoming the barrier $\Delta G_{\mathrm{et}} = \Delta G^0_{\mathrm{ox}} = \Delta G^0_{\mathrm{red}}$ by thermal fluctuations is the same. When an electric field is applied (energy profile in red), a favored direction for charge transfer is created depending on the polarity of the applied voltage. Due to a lowering of the electron transferring barrier as seen from the left metal atom, oxidation becomes more probable than a reduction of the left ion, as a higher barrier than before is seen by it. Reproduced with permission from [63], © 2012 Wiley-VCH.

while the barrier between the two potential wells is increased by $\alpha_{\mathrm{et}} ze\eta$ compared with the case of equilibrium. At the active electrode/insulator interface, reduction processes are dominant, whereas the oxidation is favored at the insulator/inert electrode interface - again due to the polarity of the overpotentials within the exponential functions.

It should be noted that a positive applied bias at the active electrode combined with $\alpha_{\mathrm{et}} < 0.5$ strengthens the oxidation process at the active electrode/insulator interface, as both the voltage bias and the α_{et}-value (the majority of the overpotential drives the oxidation process across this interface) lead to an effective oxidation barrier decrease of the reduced metal from $\Delta G^0_{\mathrm{red}}$ to ΔG_{red}; whereas only the bias - but not the value of $\alpha_{\mathrm{et}} < 0.5$ - efficiently decreases the effective reduction barrier of the oxidized metal from

$\Delta G_{\mathrm{ox}}^{0}$ to ΔG_{ox} at the insulator/inert electrode interface. This is valid as only less than the majority of the overpotential across this interface drives the reduction process.

The effect is altered for a negative applied bias at the active electrode and for $\alpha_{\mathrm{et}} > 0.5$: Given the negative polarity of the corresponding overpotential, the reduction process dominating at the active electrode/insulator interface is additionally promoted by the choice of α_{et}. Through this choice more portion of the overall electron transfer overpotential at this interface drives the reduction process.

Due to the cell's charge neutrality, every redox process at one electrode interface is accompanied by the opposite redox process at the opposite electrode interface.

2.3.3 Electrocrystallization as a special Reduction Process

A filament can only grow at the insulator/inert electrode interface, when a stable nucleus by electrocrystallization is built there. This process is also a reduction process as metal ions originating from the active electrode reduce to atoms upon applying a positive bias. However, the nucleus which consist of a number of N atoms is only stable if a critical size of this metal cluster consisting of N_{c} metal atoms is achieved [47]. This is only achieved, if a sufficiently big overpotential drives this nucleus formation. Otherwise, its formation is blocked. However, the nucleation rate exponentially increases upon applying at least the required overpotential. These considerations are incorporated into the nucleation rate which is expressed as

$$J_{\mathrm{nuc}} = K(k_{0,\mathrm{nuc}}) \exp\Big(- \frac{\Delta G_{\mathrm{nuc}}}{k_{\mathrm{B}} T} \Big) \exp\Big(\frac{(N_{\mathrm{c}} + \alpha_{\mathrm{nuc}}) z e}{k_{\mathrm{B}} T} \eta_{\mathrm{nuc}} \Big). \tag{2.3}$$

$K(k_{0,\mathrm{nuc}})$ is a prefactor which depends on the nucleation reaction rate $k_{0,\mathrm{nuc}}$ [61]. ΔG_{nuc} is the nucleation activation energy. These both parameters evolve from the number of available nucleation sites as well as from the minimum number of metal atoms N_{c} to enable nucleation. α_{nuc} is the nucleation-specific charge transfer coefficient, whereas η_{nuc} is the overpotential that drives the nucleation process. It should be noted that the nucleation process only occurs when a filament is fully dissolved after a RESET process, or if the nucleus needs to be formed before the very first switching event. Otherwise, it is not considered to be speed-limiting under any circumstances.

2.3.4 Electronic Transport across MIM Structures

Quantum mechanical tunneling enables electronic transport across insulating nanostructures in cases where classical conduction is suppressed due to high energy barriers. In ECM cells, such tunneling effects become increasingly prominent as the filament grows close to the active electrode, reducing the gap between filament tip and electrode to a range between a single metal atom radius and a few nanometers. Also, when the thickness of an insulating layer between two electrodes is in this thin range, direct tunneling from one electrode to the other becomes feasible. Simmons has mathematically expressed the tunneling current density in terms of the applied voltage to such a MIM structure for similar [66] as well as dissimilar electrodes [67]. As the filament's atoms originate from the active electrode, the equation for similar electrodes in the context of an ECM cell in LRS becomes relevant. Though, for very thin insulating films the direct tunneling from electrode to (a dissimilar) electrode should not be disregarded. However, as the last case is rather rare, the tunneling equation by Simmons for similar electrodes is introduced in the following. It should be noted that there are three cases that are identified as such: low, intermediate and high voltage regime. For small applied voltages fulfilling $eV \approx 0$, the approximated shape of the tunneling barrier is rectangular, as shown in Figure 2.6 (a), and the tunneling current density equation as introduced by Simmons [66] reads

$$J = \frac{3\sqrt{2m_{\text{eff}}\Delta W_0}}{2x}\left(\frac{e}{h}\right)^2 \exp\left(-\frac{4\pi x}{h}\sqrt{2m_{\text{eff}}\Delta W_0}\right) V. \tag{2.4}$$

Here, $m_{\text{eff}} = m_{\text{r}}m_0$ denotes the effective electron mass, whereas m_{r} is the relative effective mass and m_0 is the electron mass itself. ΔW_0 is the tunneling barrier height, x is the tunneling gap distance, and h is Planck's constant. A clear linear relationship between current density and applied voltage is prominent. If the applied voltage V is larger but still smaller than $\frac{\Delta W_0}{e}$, the case is referred as the intermediate voltage regime. Here, the formerly rectangular barrier gets tilted and becomes trapezoidal; the mean tunneling barrier height shrinks by $\frac{eV}{2}$ (cf. Figure 2.6 (b)). Simmons derived the following equation as tunneling current density for intermediate applied voltages [66]:

$$\begin{aligned} J &= \frac{e}{2\pi h x^2}\left(\Delta W_0 - \frac{eV}{2}\right)\exp\left(-\frac{4\pi x}{h}\sqrt{2m_{\text{eff}}\left(\Delta W_0 - \frac{eV}{2}\right)}\right) \\ &- \frac{e}{2\pi h x^2}\left(\Delta W_0 + \frac{eV}{2}\right)\exp\left(-\frac{4\pi x}{h}\sqrt{2m_{\text{eff}}\left(\Delta W_0 + \frac{eV}{2}\right)}\right). \end{aligned} \tag{2.5}$$

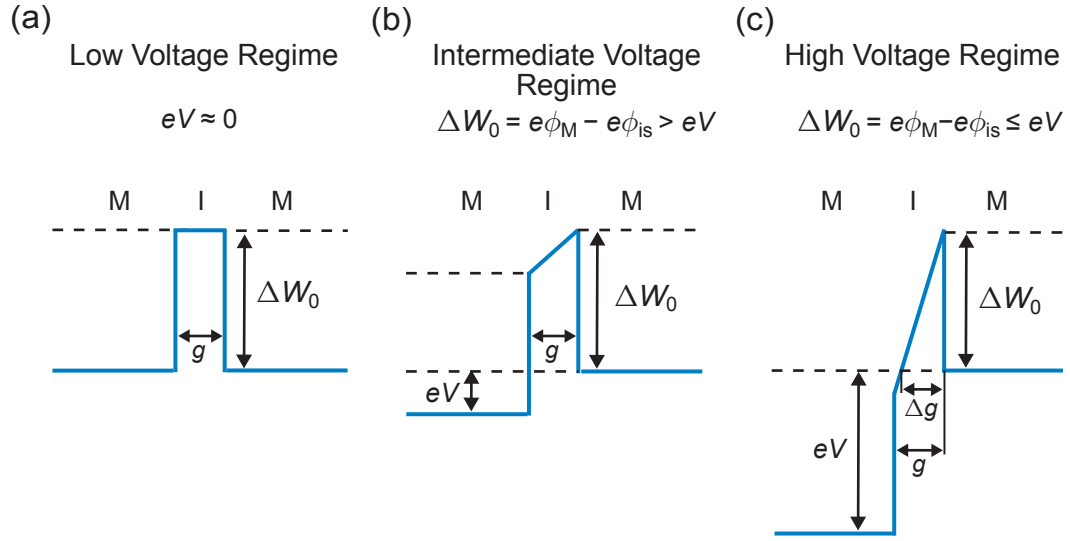

Figure 2.6: The energetic profile for electronic transport across metal-insulator-metal differs depending on the applied voltage: (a) For very small applied voltages an approximated rectangular tunneling barrier is assumed. (b) For intermediate voltages, the barrier lowers on one side by eV, leading to a trapezoidal barrier shape. (c) High applied voltages lead to a very pronounced lowering of the barrier by eV on one side. Due to it an effective triangular barrier is present, and the effective barrier distance shrinks as well. Adapted from [61].

For very small applied voltages $V \ll \frac{\Delta W_0}{e}$, this equation transitions as an approximation into equation 2.4. For very large applied voltages $V > \frac{\Delta W_0}{e}$, the trapezoidal barrier takes the shape of a triangular barrier, as its tilting becomes very pronounced. Figure 2.6 (c) illustrates that the mean barrier height is $\frac{\Delta W_0}{2}$. Also, the effective tunneling gap distance is reduced by the relation between the tunneling barrier height ΔW_0 and the applied voltage V. Therefore, the effective tunneling distance reads $x_{\text{eff}} = x \cdot \frac{\Delta W_0}{eV}$. The electron tunneling current density according to Simmons for high applied voltages is expressed as:

$$\begin{aligned} J &= \frac{2.2e^3V^2}{8\pi h\Delta W_0 x^2} \exp\left(-\frac{8\pi x}{2.96heV}\sqrt{2m_{\text{eff}}}\,\Delta W_0^{3/2}\right) \\ &- \frac{2.2e^3V^2}{8\pi h\Delta W_0 x^2}\left(1+\frac{2eV}{\Delta W_0}\right)\exp\left(-\frac{8\pi x}{2.96heV}\sqrt{2m_{\text{eff}}}\,\Delta W_0^{3/2}\left(1+\frac{2eV}{\Delta W_0}\right)^{1/2}\right) \end{aligned} \quad (2.6)$$

Contrary to the applied voltage V, a decrease in tunneling distance x exponentially increases the current density for all three regimes. Hence, a small decrease in the tunneling distance x might contribute to a huge current density J increase. This scenario occurs whenever the device switches from HRS to LRS, as there will be always a point at which the current jumps abruptly due to the filament growth towards the active electrode.

It should be noted that while introducing the current density equations (2.4) - (2.6) an ideal barrier shape has been considered. However, an image force acts upon the barrier leading to a smaller barrier width and height. This would lead to a more parabolic shape of the tunneling barrier and to an increase of the current density compared to an ideal barrier consideration. However, the shape of the current density-voltage (J-V) relation does not change. Also, a dependence on the insulating layer's dielectric constant contributes to a real barrier consideration. It leads to a higher tunneling current for smaller permittivities.

2.4 The Nanobattery Effect within ECM Cells

An intrinsic built-in electromotive force (emf) within ECM cells leads to the occurrence of the so-called nanobattery effect [43]: Without any applied external voltage, the emf leads to ionic processes promoting either filament growth or filament dissolution - depending on the respective cell and respective origin. This effect occurs for the ionic current and without any external force. These ionic processes involve redox processes and ion migration, whereas the electronic current, i. e., the quantum mechanical tunneling of electrons, is not affected. As no applied voltage causes the occurrence of an ionic process, another certain applied voltage enables the state of dynamic equilibrium. At this emf voltage V_{emf} all ionic processes in both directions are equally strong and therefore, cancel out. Hence, when V_{emf} is applied, effectively there is no applied voltage or no driving force. When V_{emf} is a positive value, the dynamic equilibrium is shifted to postive applied voltages so that any voltage below V_{emf} contributes to ionic processes leading to a filament dissolution. Hence, such a consideration demonstrates that the nanobattery effect provides a basis for understanding volatile ECM cells. It should be noted that if an ECM cell experiences a strong SET event leading to a full bridging of the insulator by the filament, the device becomes nonvolatile and the emf effect fully vanishes. As no tunneling gap remains and the electrons directly flow through the short-circuited device to the active electrode, a loss of the LRS for stable filaments becomes unlikely [43].

2.4.1 The Origin of the Nanobattery Effect

Many ECM cells show a volatile behavior when they undergo a weak SET process [23, 32, 68]. It means that after the SET event, they can only hold their LRS for a certain time. Depending on the experimental conditions, this relaxation time t_{r} differs. ECM

devices, programmed in a fashion that they are volatile, relax back to the HRS after t_r losing their digital state or memory.
Cyclic voltammetry (CV) measurements play a key role in investigating the existence and the origin of the nanobattery effect. CV measurements' operation is similar to the *I-V* sweep measurement but differs in one aspect: While sweeping from 0 V to positive voltages, the forward sweep stops before an abrupt switching can occur and consecutively, a sweep back to 0 V is followed. After that, the sweep continues towards negative voltages, and then, at a certain negative voltage value, the sweep again changes direction and finishes when reaching 0 V again. Thus, the full CV measurement is performed in the HRS. The aim of such a CV measurement is to access insights of ionic processes through the access of the ionic current. Increased peak current values at a specific voltage value may hint towards an enhanced ionic activity rate, e. g. towards a higher redox activity. Such CV measurements for ECM cells have shown that the ionic dynamic equilibrium can be shifted towards one of both polarities [56, 58, 69]. The ionic current is zero for a non-zero applied voltage of one specific polarity. The direction of the polarity depends on the specific material and the equilibrium shift's underlying cause. Whenever the dynamic equilibrium is shifted towards the positive direction and establishes itself at a specific positive voltage value, all voltages smaller than this value, either positive or negative, promote ionic processes that are related to a RESET event. Thus, this phenomenon explains how relaxation might occur for small applied positive voltages.

The reasons for such an effect can be found in the theory of the emf providing a nanobattery within the ECM cell. This "nanobattery" and spontaneous filament dissolution effect usually manifests as an emf counteracting to the driving force effect of switching and filament growth [43]. In most stacks the emf's origin lies in the requirement of a cathodic reduction reaction at the inert electrode that balances the anodic oxidation at the active electrode, thereby preserving charge neutrality at the interfaces. Cyclic voltammetry has shown that atmospheric moisture participates at the inert electrode: water reduces to hydroxide ions OH^- in a water splitting reaction [56]. With increasing ambient water partial pressure, the concentrations of hydroxide anions as well as metal cations rise. The latter rises as charge neutrality provider whenever the anion concentration rises. Consequently, the emf is attributed to a diffusion potential established by the electrochemical half-cell reactions at both electrode/insulator interfaces [43, 56]. The Nernst potential associated with those half-cells also contributes to the emf [43, 56]. A further contribution is the Gibbs–Thomson potential that results from differences in

surface free energy between macroscopic surfaces (the active electrode) and nanoscale objects (the filament tip) [43]. The emf exists only while a filament terminates at a finite gap in front of the active electrode; once the filament fully bridges the dielectric and short-circuits the electrodes, the emf vanishes [43] and the device behaves nonvolatile. Thus, modeling strongly nonvolatile behavior is incompatible with a pronounced emf. As a counteracting force, the emf shifts the dynamical equilibrium to a nonzero device voltage. However, it should be noted that the V_{emf}-concept proposed to explain the v-ECM phenomena currently remains an exploratory approach. Experimentally determined values for V_{emf} can be lower than the voltages that would theoretically be required to account for the observed switching events solely through this effect. Thus, the origin of volatile switching in ECM cells can be clarified through further investigations.

There are three prominent origins of the emf give, and they give rise to an additional internal voltage V_{emf}:

1. the Nernst potential V_{N}
2. the diffusion potential V_{D}
3. the Gibbs-Thomson potential V_{GT}

Further detailed information regarding the three emf's origins and for the case of a highly conducting short circuit ECM cell is given in [43]. In the following, a short introduction of these different effects is presented.

The Nernst potential V_{N}

At each electrode/insulator interface one half-cell redox reaction takes place, whereas the counterpart half-cell reaction takes place at the other opposing electrode/insulator interface. Both reactions take place with different chemical potentials μ'_{M} and μ''_{M}. Thus, their chemical potential difference $\Delta\mu_{\mathrm{M,N}}$ is defined as $\Delta\mu_{\mathrm{M,N}} = \mu'_{\mathrm{M}} - \mu''_{\mathrm{M}}$. The Nernst potential - as one possible origin of the emf - is the force that counteracts against the chemical potential difference: $V_{\mathrm{emf}} = V_{\mathrm{N}} = -\frac{\Delta\mu_{\mathrm{M,N}}}{ze}$. Thus, in ECM cells, the Nernst potential V_{N} describes the equilibrium voltage V_{emf} that develops between the two electrodes due to the difference in chemical potentials of metal ions, as depicted in Figure 2.7 (a).

The Diffusion Potential V_{D}

Metal ions from the active electrode often accumulate differently at different regions of the insulator, depending on the geometry, electric field and ion concentration regarding

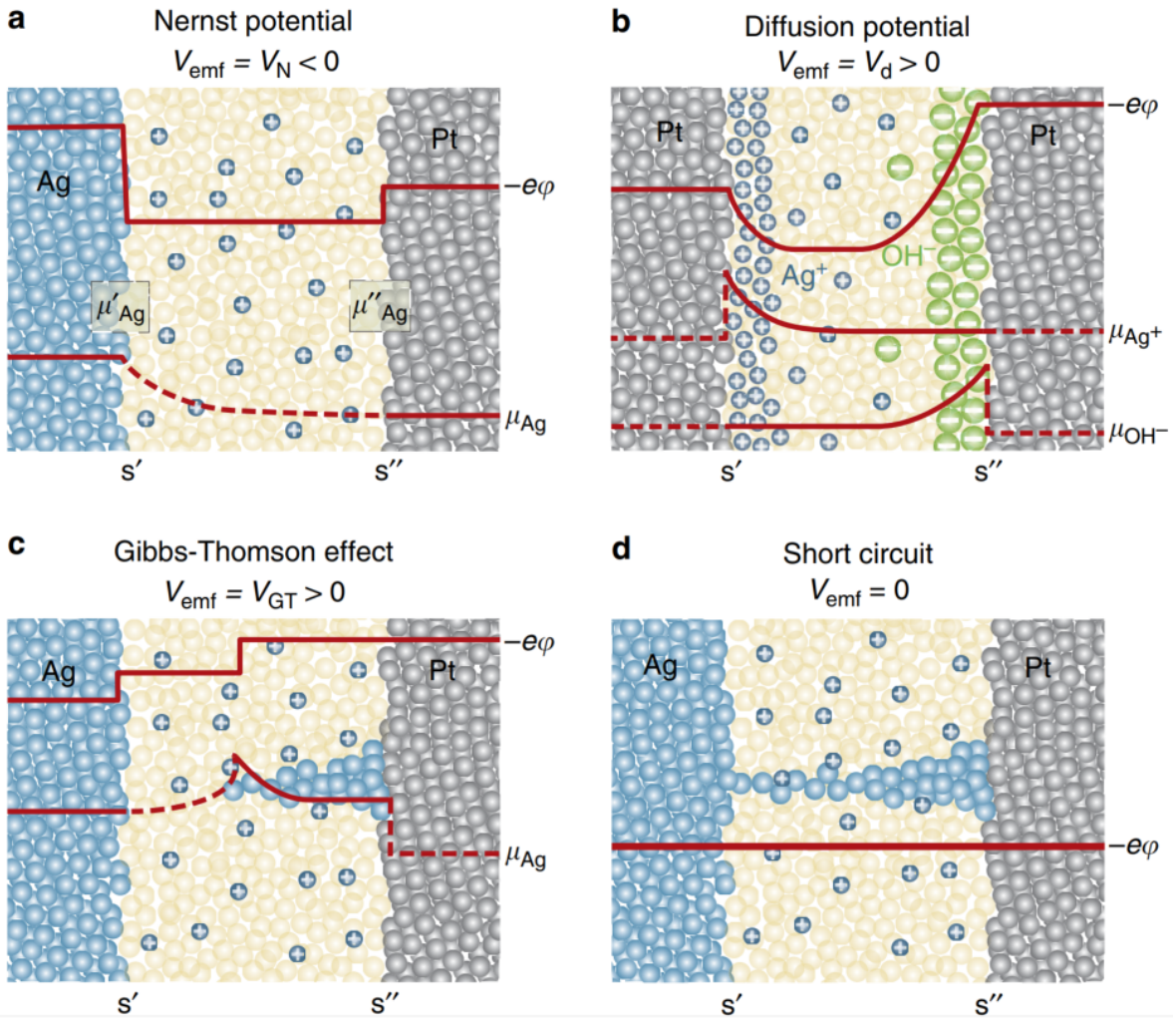

Figure 2.7: Different physical and chemical processes can lead to the occurrence of the electromotive force: (a) The Nernst potential as origin of the emf is attributed to both half-cell redox reactions takin place at the corresponding electrode/insulator interfaces. (b) Diffusion potential as origin of the emf occurs whenever ionic species are unequally distributed among the insulating layer. (c) The Gibbs-Thomson potential as origin of the emf occurs due to differences in surface energies between the micro-sized electrode/insulator interface and nano-sized filament tip/insulator interface. (d) A short circuit through a fully bridging filament between both electrodes contributes to a vanishing emf. Adapted under the terms of CC BY-NC-ND 3.0 license [43].

the insulator. The same is true for OH^- ions. Near the electrodes, an excessive accumulation of the corresponding ion species is found, e. g., an accumulation of active metal ions near the active electrode/insulator interface and an accumulation of hydroxide OH^- ions near the insulator/inert electrode. Thus, different ion concentrations at different regions generate a force, the diffusion potential. Its value V_D describes the voltage value at which the diffusion effects cancel out and a dynamic equilibrium is realized. The chemical potential gradients of both ion species between both interfaces - the chemical potential gradient of the metal ion $\Delta\mu_{\mathrm{M}^+,\mathrm{D}} = \mu'_{\mathrm{M}^+} - \mu''_{\mathrm{M}^+}$ and of the hydroxide ion $\Delta\mu_{\mathrm{OH}^-,\mathrm{D}} = \mu'_{\mathrm{OH}^-} - \mu''_{\mathrm{OH}^-}$, respectively - partly contribute to the full diffuison potential V_D. Thus, the diffusion potential V_D being the dynamic equilibrium V_emf originates from the different ion concentrations within the ECM cell, as illustrated in Figure 2.7 (b).

The Gibbs-Thomson potential V_GT

Owing to a difference of the surface energies between the micro-sized active electrode/insulator interface and the nano-sized interface at the filament tip, a chemical potential gradient $\Delta\mu_\mathrm{M,GT} = \mu_\mathrm{M-micro} - \mu_\mathrm{M-nano}$ arises. Hence, the dynamic equilibrium is defined at the Gibb-Thomson potential V_GT as $V_\mathrm{emf} = V_\mathrm{GT} = -\frac{\Delta\mu_\mathrm{M,GT}}{ze}$. It emerges due to the surface energy differences between the differently sized interfaces at the active electrode and filament tip areas, respectively, as shown in Figure 2.7 (c).

Galvanic contact as short circuit

Whenever the filament fully bridges the insulator and directly connects both electrodes, a galvanic contact is achieved. As an electric connection is built, the ECM cell becomes a short circuit, as illustrated in Figure 2.7 (d). A spontaneous relaxation is not possible anymore, as the emf vanishes for such a galvanic bridge. A RESET process with a negative applied voltage as external force becomes necessary in order to reverse the ECM cell's resistance state to HRS. Thus, a full-bridging galvanic contact cannot be described by the emf. This also applies to a highly conducting tunneling gap.

2.5 Two-Dimensional Materials for use in ECM Cells

Two-dimensional (2D) materials have attracted extensive interest in recent years due to their atomically thin structure, unique physical properties, and the possibility of integrating them into a broad range of electronic devices [70, 71]. A 2D material is typically defined as a crystalline solid consisting of a single or only a few layers of

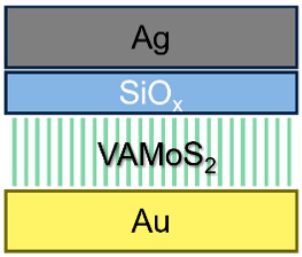

Figure 2.8: The $Ag/SiO_x/VAMoS_2/Au$ ECM stack provides an example for 2D materials as part of the insulating layer. The vertically aligned MoS_2 ($VAMoS_2$) serves as a variability-reducing element. Adapted under the terms of CC-BY 4.0 license [78].

atoms, which are strongly bonded within the plane by covalent or ionic interactions but held together between planes only by weak van der Waals forces. This characteristic allows for mechanical exfoliation into thin sheets, as well as scalable growth methods such as chemical vapor deposition (CVD) [72].

The family of 2D materials is diverse, comprising semimetals (e.g., graphene [70]), semiconductors (e.g., transition-metal dichalcogenides such as MoS_2, WS_2, or WSe_2 [73]), insulators (e.g., hexagonal boron nitride, h-BN [74]), and a variety of emerging systems such as layered oxides and halides. Among these, insulating 2D materials have gained particular attention in the context of nanoelectronic devices because their atomically precise thickness can serve as a well-defined tunneling or switching medium [75].

Replacing or complementing conventional ECM devices' insulating layer materials with 2D insulators provides several potential advantages. First, their ultimate thickness control - down to a single monolayer - opens the possibility of achieving ultralow switching voltages and highly confined conductive paths. Second, their intrinsic mechanical stability and chemical inertness may enhance device endurance under repeated switching cycles [76]. Figure 2.8 represents an illustration of a MoS_2-based ECM stack [50, 77, 78]. The vertically aligned MoS_2 ($VAMoS_2$) serves as second insulating layer beside SiO_x and provides a path for the filament growth direction as a 2D material enabling less variability from cycle to cycle.

The most prominent candidate among insulating 2D materials is h-BN. It exhibits a wide band gap of approximately 5–6 eV, excellent thermal stability, and compatibility with graphene and other 2D systems in van der Waals heterostructures [74, 79]. In ECM cells, h-BN has been reported to act as a robust insulating barrier enabling ionic transport and redox processes within h-BN and at its interfaces with the electrodes, respectively [49].

In addition to h-BN, other layered materials are being explored. Transition-metal dichalcogenides, although semiconducting in nature, can exhibit high resistance in few-layer form and may therefore function as quasi-insulating barriers under appropriate conditions [73].

For the purposes of this thesis, the discussion of 2D materials will remain limited to a concise modeling perspective. Only selected aspects relevant for ECM memory operation - specifically their role as insulating layers and their influence on switching variability - will be considered. Although 2D materials exhibit promising properties, the exact switching mechanism in these layered structures has not yet been fully clarified. Since intrinsic ion migration perpendicular to the 2D layers is energetically highly unfavorable, it is assumed that transport occurs primarily laterally between the layers or vertically along grain boundaries.

2.6 Memristive Crossbar Arrays for Computation-In-Memory

ReRAM device's features are usually fed in into hardware computation-in-memory (CIM) schemes. Unlike to classical computation in which the working memory and processing (CPU) unit are located in separate regions, ReRAM devices contribute to the CIM architecture for which the memory and processing units are parts of only one structural design. Mainly the same unit is responsible for both crucial components of computation: processing and memory. Examples for such a hardware computation-in-memory architecture are ANNs, spiking neural networks (SNNs), or logic-in-memory concepts.

All these examples are realized on the so-called crossbar array architecture. In this architecture, word lines and bit lines intersect at crosspoint junctions, each integrating a ReRAM device. The word lines access all bit lines of the crossbar array in a specific row for reading and writing information on the ReRAM device. Writing or programming is achieved by changing the corresponding ReRAM device's resistance state level. Hence, a full word can be computed in parallel. For such reading or writing processes, both lines that connect the selected junction are used to generate a certain voltage drop across the corresponding junction device by biasing the lines accordingly. Also, the output information of an operation can be carried by the bit lines and it can be read by measuring the current on the corresponding (selected) bit lines by connecting them to a sense amplifier. The ReRAM devices at the crosspoint junction sites are individually programmed to different resistance states during training [80]. Certain resistance state

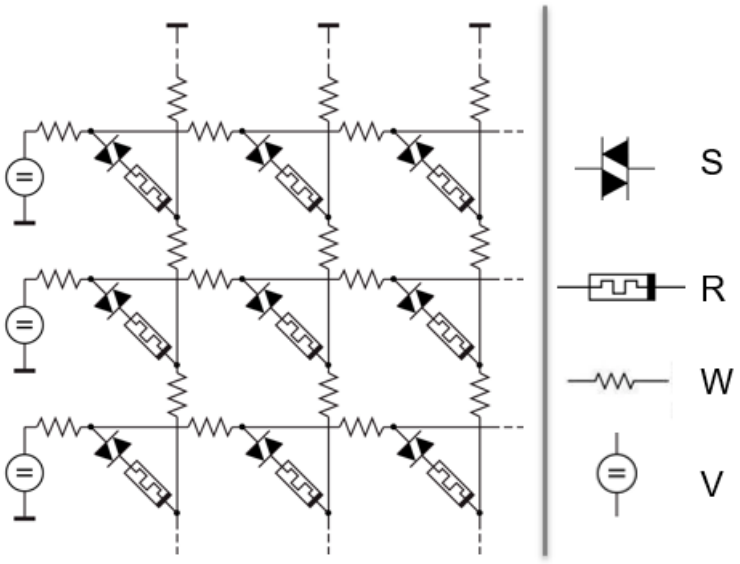

Figure 2.9: A 3×3 - crossbar array is exemplarily shown: Each word line is biased by a voltage source (V). Each connecting line between any junction hosts a wire resistance (W). In this example, the crossbar array junctions are occupied by a select device (S) and the ReRAM device (R). All bit lines are grounded. Reproduced with permission from [24], © 2022 IEEE.

ranges refer to certain resistive binary or multistate levels. Thus, multiplying an input from the line with a ReRAM device's level at the junction during the read process gives a certain output that is also classified into levels. This is known as VMM operation on crossbar arrays. AI schemes heavily rely on such VMM operations. Analog outputs can be transformed into digital outputs by Analog-Digital Converters (ADCs) in the peripherical circuitry. Several layers of such crossbar arrays might contribute to an ANN design for AI schemes. Neural networks in humans' brains work with a comparable design. In a simple picture, the programming state of synapses with different and tunable strengths compares to the resistance state of the ReRAM devices in the crossbar array junctions, whereas neurons compare to the processing on input and output lines and further circuitry connecting the crossbar array layers - as synapses connect neurons to each other. An example of one 3x3 passive crossbar array together with wire resistances and a select device for each crossbar junction is given in Figure 2.9: Each word line is driven by an input voltage source ('V') located at its left end. At every crosspoint junction, the select device ('S') determines whether the associated ReRAM cell ('R') is activated for a read or write operation. All bit lines are grounded, as illustrated at the top. The interconnection, either between crosspoint nodes or between voltage sources/grounds and the remaining circuitry, are depicted using wire resistances ('W').

2.6.1 Selector Devices in Crossbar Arrays

Owing to leakage currents throughout the array structure that may cause crosstalk between neighboring or nearby devices in the crosspoint junctions, there are two types of crossbar arrays: passive and active. In the case of active crossbar arrays, a third so-called source line allows for a usage of a controlling transistor at each crosspoint junction [81]. The gate is connected to a word line near the corresponding junction. It enables operating the junction's ReRAM device only upon selecting it through the transistor, i. e., through sufficiently biasing the transistor's gate upon applying a voltage between its source and drain. Rather large transistors and the additional design effort for source lines make an active crossbar array architecture highly inefficient in terms of design complexity and area size. A clear benefit is a good and reliable selecting principle. This combination of one transistor and one resistive switching device at each junction crosspoint of an active crossbar array is known as 1T1R. However, passive crossbar arrays describe arrays with two-terminal device junctions that are not controlled by any additional third external line, i. e., either only the ReRAM device makes up the junction point or a two-terminal selector device is placed additionally in series to the ReRAM device into the junction point [29–31, 81–86]. No further active controlling is necessary. Leakage currents/sneak paths are prevented either by an ideal selection behavior of only ReRAM devices in the junctions or by the selector devices that allow access to the corresponding ReRAM device only when it has been selected by the external input. Benefits arising from such a passive crossbar array structure are its simple and compact design and the possibility of several arrays' stacking on top of each other. Thus, only a relatively small area is occupied by the crossbar array with a high number of operating ReRAM devices. However, a successful selecting operation depends on further circumstances, such as select devices' successful suppression of sneak paths originating from certain high-conductive junctions within the array, the number and value of wire resistances, the crossbar array size, as well as the dynamics of the selector and ReRAM device, as investigated later in this work. The crosspoint junction on passive crossbar arrays consisting of one resistive switching device and one selector device is also known as 1S1R device. The array in Figure 2.9 is such a 1S1R crossbar array.

In the case of a 1S1R device, selector devices are chosen from a variety of devices that show threshold switching, i. e., their switching process is a volatile operation with a threshold voltage V_{th} and hold voltage V_{hold}. Examples are volatile ECM devices and NbO_2-based threshold switches. The ReRAM device, however, should be able to save its

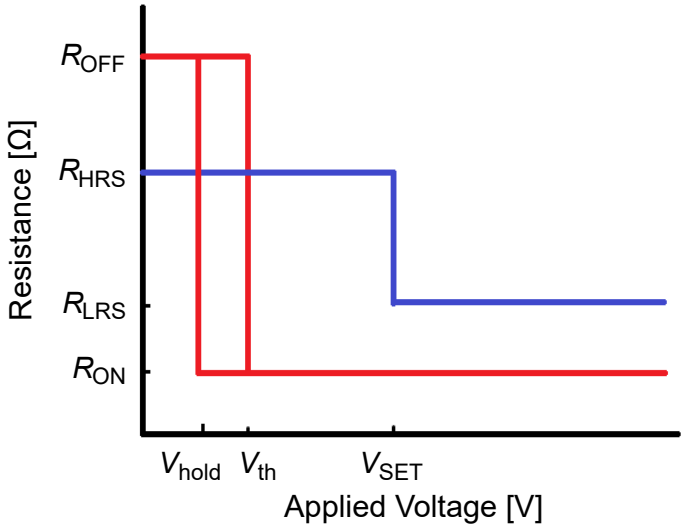

Figure 2.10: Simplified diagram of requirements for a 1S1R device design: Both resistance states of both devices (selector device and ReRAM device) are shown together with characteristic switching and hold voltage values of them. R_{OFF}, R_{ON}, V_{hold}, V_{th} belong to the selector device, and R_{HRS}, R_{LRS}, V_{SET} belong to the ReRAM device. Reproduced with permission from [24], © 2022 IEEE.

state regardless of state-maintaining applied electrical stimuli. Examples are nonvolatile ECM and VCM devices.

Figure 2.10 shows the requirements to such a passive two-terminal selector device in a simplified picture: As the same signal affects the selector device as well as the ReRAM device, the selector device - on the one hand - needs to be higher conducting in its ON state than the LRS and HRS of the ReRAM device. This needs to be ensured, as the selector device should allow access to the ReRAM device by unblocking the junction point through its high conduction. Furthermore, no significant voltage drop across the selector device is desired once this junction crosspoint is selected. Only the ReRAM device should dominate the operations once the corresponding crosspoint has been selected. On the other hand, the select device's OFF state should be less conducting than the HRS of the ReRAM device, as only then is blocking of the corresponding junction crosspoint ensured. Otherwise, an access to the ReRAM device through leakage current is possible.

Furthermore, owing to the operation's nature, the SET voltage V_{SET} of the nonvolatile ReRAM device should be larger than the threshold voltage V_{th} and the hold voltage V_{hold}. Both characteristic voltages of the volatile selector device within a 1S1R design are smaller, as the applied voltages need to be higher or lower than these values to permit or deny access to the corresponding junctions/ReRAM devices, respectively. If

an access is permitted, a further read or write process can be initiated. A voltage V with $V_{\mathrm{th}} < V < V_{\mathrm{SET}}$ allows for a selection of the 1S1R device for reading but not writing it. V_{th} of the volatile device is larger than V_{hold} and larger than the comparably low voltage that drops across the select device once it has switched. It ensures that the selector does not switch off immediately after it has jumped in its ON state, and switch off again - due to the voltage divider effect - creating resistance state oscillations. It implicates that the read operation would become inaccessible. The write regime is entered once a voltage V higher than V_{SET} drops across the ReRAM device.

2.6.2 Read/Write Schemes in a Passive Crossbar Array

As passive crossbar arrays, such as 1S1R array structures, suffer from leakage current, special schemes for reading and writing ReRAM devices within these arrays have been developed and designed [87, 88]. They contribute to avoiding accidental write processes of other devices than the selected one (based on a write scheme) and to avoiding reading out the wrong state of the selected device (based on a read scheme). By implementing such schemes only the selected crossbar junction is affected by an input voltage, otherwise an uncontrolled array biasing can overwrite an arbitrary number of crosspoint devices or falsely read a selected device's state. One such read/write scheme is the $V/2$-scheme. Its characteristic is that the one selected crosspoint junction is biased such that the full voltage V drops across this selected 1S1R device. The ReRAM device only experiences a SET process, once a voltage V with $V/2 < V_{\mathrm{SET}} < V$ has dropped across the selected ReRAM device. It is read out if V_{read} drops across the select device with $V_{\mathrm{read}}/2 < V_{\mathrm{th}} \approx V_{\mathrm{read}}$. An example for a selected 1S1R device according to the $V/2$-scheme is the following: Its corresponding word line is biased with V_{read} and its bit line with 0 V. Due to one shared line (the same word line or the same bit line) with the selected cell, other half-selected 1S1R cells are treated in a special way: The value $V_{\mathrm{read}}/2$ drops across half-selected cells. This is accomplished by biasing the corresponding shared word line with V_{read} and the corresponding bit line with $V_{\mathrm{read}}/2$ or by biasing the corresponding word line with $V_{\mathrm{read}}/2$ and the corresponding shared bit line with 0 V. For a read process with $V_{\mathrm{read}}/2 < V_{\mathrm{th}}$, the biasing of a 1S1R cell with $V_{\mathrm{read}}/2$ should block the selection of this half-selected cell and give no false information when reading the full-selected 1S1R cell on the same word or bit line with V_{read}. The half-selected cells' resistance state should not be changed at all. The selected cell's resistance state during the read process should also not change, however, slight drifts caused by repeated read operations stay possible. All 1S1R devices that do not share any word or bit line with

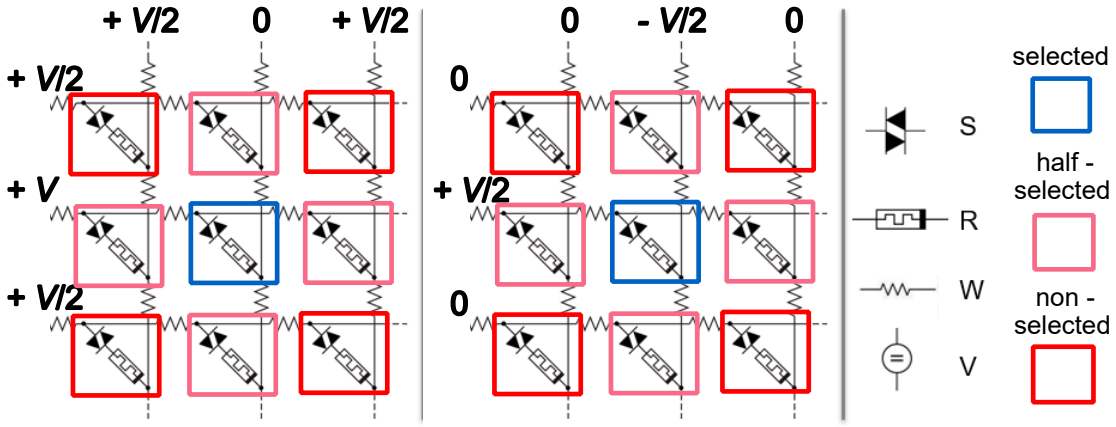

Figure 2.11: Two versions of the $V/2$ - scheme are schematically illustrated for a 3×3 1S1R crossbar array: The blue cell is selected for read or write by the applied voltage V. The light pink half-selected cells experience a voltage drop of $V/2$ across them; typically, this voltage is sufficient to avoid reading or writing them. As the red unselected cells see no voltage, they are not affected at all, if no leakage current flows through them.

the selected device are biased by both related lines with 0 V so that no voltage drops across all these devices. More schemes, such as the $V/3$-scheme, are known. They can have several advantages or disadvantages compared to the $V/2$-scheme. Two examples for a $V/2$-scheme on a 3x3-crossbar array are shown in Figure 2.11.

2.6.3 Vector-Matrix Multiplication on Crossbar Arrays

VMM operations are the most fundamental operations in ANN systems for new emerging AI architectures [24, 28]. A simple illustration is shown in Figure 2.12 for a 3x3 binary crossbar array: The left binary input vector related to the word lines represents the applied voltages to the crosspoint junction devices connected to the corresponding word lines. Either the voltage is $V < V_{\mathrm{SET}}$ or 0 V, corresponding to the input '1' or '0', respectively. The matrix related to the ReRAM devices in the crossbar array represents the devices' states, either in the LRS ('1') or HRS ('0'). The VMM operation describes the multiplication of the input vector with the matrix. The measured current on the bit lines represents the output vector, i. e., the result of the VMM calculation. If the added-up output current on one bit line is higher than a threshold/limit value I_{limit}, it correponds to the output '1', whereas it corresponds to the output '0' for added-up currents smaller than I_{limit}. This interpretation is achieved by peripheral circuitry connected to the bit lines, including sense amplifiers and ADCs. The peripheral architecture might also allow for multistate outputs resulting from the VMM operation.

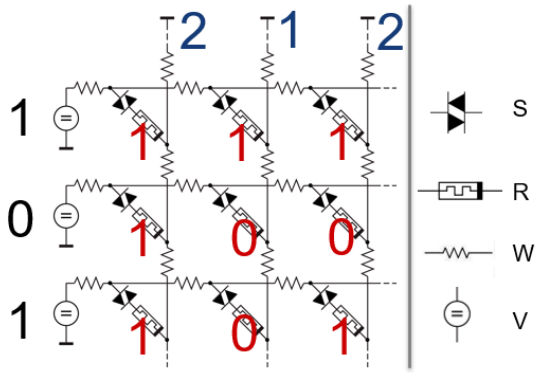

Figure 2.12: The VMM is presented exemplarily on a 3×3 1S1R crossbar array: The binary voltage vector input in black is multiplied by the binary resistance state matrix of the 1S1R crossbar array in red, resulting in the current output vector in blue. Reproduced with permission from [24], © 2022 IEEE.

In the case of a passive crossbar array with junctions only occupied by ReRAM devices without any selector, usually leakage currents emerge that highly disturb the VMM operation and give false results. Introducing 1S1R devices at each crosspoint junction aims to effectively mitigate this problem. However, successful mitigation depends on the desired number of (input-, matrix- and) output states, the selector device's efficiency and interplay with the ReRAM device, the crossbar array size, and the wire resistances. These aspects will be examined in detail throughout this thesis.

3 Used Models from the Literature

In this thesis, ReRAM device models and one threshold switch device model from literature are used either as input for simulations or as a basis for new models and model extensions, whose features are demonstrated through model fits and simulation studies throughout this thesis. This chapter explicitly introduces the models used from the literature.

3.1 Classification and Utilization of Compact Models

Compact models are used as description of an electric device as a block within circuit simulator applications to provide a fast mathematical model that is efficient in terms of computational cost. These models can be motivated by their intrinsic physics so that they capture dynamical features correctly. As the implementation of detailed physics can lead to more complex models, physics-based models can be slower and the computational cost might be relatively high. However, their unique feature of capturing the correct dynamics has proven to be beneficial, especially for ReRAM devices. They also contribute to the fact that mostly any application case is covered by well-developed physics-based compact models. It should capture electrical and dynamic features of the corresponding device. To make physics-based compact models faster, the geometrical dimension of physical processes can be reduced, e. g., to a one-dimensional filament evolution within ReRAM devices, mostly still providing an accurate result.

A comparison between three types, namely physics-based, mathematical and empirical compact models is provided in Table 3.1, highlighting different advantages and disadvatanges. Certain models can also combine features of two types of them or even of all three. The comparison helps in understanding their individual strengths and weaknesses, underscoring the strength of physics-based compact models that are the scope of this thesis. Although a physics-based compact model's implementation effort is high compared to mathematical or empirical models, however, such a physical approach provides outstanding benefits: Its accuracy, its scalability, its extrapolation capability and

accurate dynamics and its interpretability is very high compared to the other mentioned approaches. An evaluation regarding the simulation cost and the number of parameters of a model type is not given, as they depend on the introduced amount of equations. Further details are presented in Table 3.1.

Criterion	**Physics-based**	**Mathematical**	**Empirical**
Underlying principle	Physical laws	Analytical formulas	Curve fitting to measurement data
Relation to physics	High	Low to medium	Low to medium
Accuracy	High (even for extrapolation)	Medium (in fitted range)	High (within data range)
Scalability	High	Low to medium	Low to medium
Extrapolation capability and accurate dynamics	High	Low	Low
Implementation effort	High	Low	Medium
Model development approach	Theoretical modeling + calibration	Equation design	Data fitting
Interpretability	High (physical meaning)	Medium (mathematical meaning)	Low
Typical example	JART models	$I = aV^2 + bV + c$	Fitted I-V curve from measurements

Table 3.1: Comparison of physics-based, mathematical, empirical, and behavioral compact models

As compact models are meant to be used for higher-level circuit design within circuit simulators, there are model approaches targeting purposes on lower scale: Atomistic and Molecular Dynamics simulations comprise modeling on the smallest scale, as single atoms' and molecules' behavior within a small-scale environment is physically captured. These simulations are the largest regarding computational costs. Kinetic Monte Carlo models usually capture a small scale on a statistical basis as well. Especially when all three dimensions are captured simultaneously, the computational cost is relatively high. However, they provide the best approach to explain and model physics-based statistical phenomena, especially relevant for modeling retention and endurance within ReRAM devices [89–92]. Finite-element method approaches cover the medium scale.

The computational cost can increase with increasing device size, as the number of finite elements might increase. This three-dimensional approach can capture different physics-based phenomena within electronic devices providing an accurate dynamic investigation and model. However, their computational cost is so large that they are not meant to be used within circuit simulators, as compact models are.

3.2 Selected ReRAM Device and TS Models from Literature

3.2.1 The Nonvolatile JART ECM v1 Model

In [47], a nonvolatile ECM device compact model, known as the "Jülich Aachen Resistive Switching Tool (JART) ECM v1" model, has been introduced. The JART ECM v1 model is based on the electrochemical-physical principles introduced in section 2.3 and is presented in the following. It is publicly available implemented as verilog-A code [93].

Figure 3.1 shows this model's equivalent circuit diagram (ECD): The circuit that connects the filament with the active electrode is divided into two parallel branches. The left branch represents the ionic current I_{ion}, whereas the right branch shows the electronic tunneling current I_{Tu}. The driving force of resistive switching, i. e. of the filament growth, in ECM cells are ionic processes triggered by an applied voltage across the device, thus, the driving force are the processes of the ECD's left branch. The resistive switching process itself is divided into two parts: (i) nucleation, (ii) filament growth. The filament growth starts once the nucleation is completed after the time t_{nuc}.

The time the nucleus takes to built at the insulator/inert electrode interface is calculated as

$$t_{\mathrm{nuc}} = t_{0,\mathrm{nuc}} \exp\left(\frac{\Delta G_{\mathrm{nuc}}}{k_{\mathrm{B}}T}\right) \exp\left(-\frac{(N_{\mathrm{c}} + \alpha_{\mathrm{nuc}})ze}{k_{\mathrm{B}}T}\eta_{\mathrm{nuc}}\right). \tag{3.1}$$

Here, $t_{0,\mathrm{nuc}}$ describes the nucleation time prefactor. It should be noted that the full voltage that drops across the cell V_{app} is driving the nucleation process, i. e. $\eta_{\mathrm{nuc}} = V_{\mathrm{app}}$. It should be emphasized that nucleation is the only process that does not contribute to a RESET and becomes unnecessary if a remnant filament remains after a weak RESET. The Butler-Volmer equation for electron transfer processes introduced in section 2.3.2 is simplified to the Tafel equation in the JART ECM v1 model. This simplification is valid for an overpotential driving the corresponding redox process that fulfils $\eta \gg$

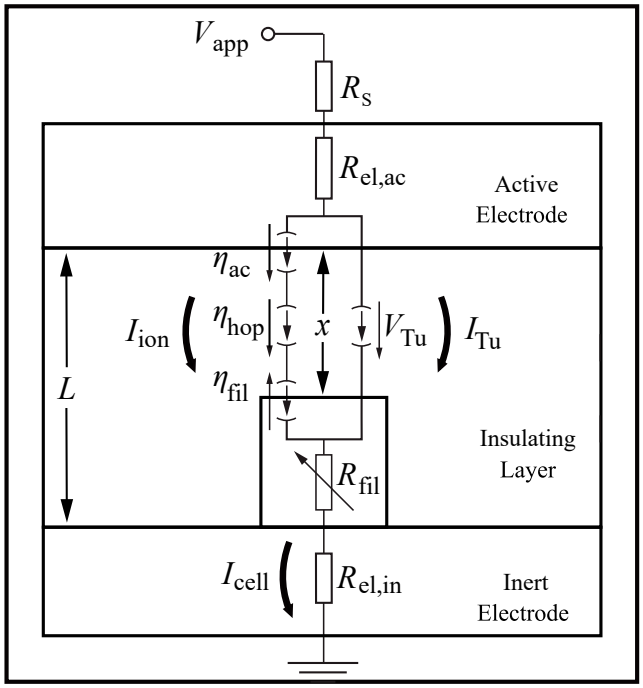

Figure 3.1: The illustration depicts the equivalent circuit diagram of the nonvolatile ECM model. Within this abstraction, two distinct current paths can be identified. The first is the ionic current path, which comprises the overpotentials associated with ionic redox reactions and ion migration. The second current path corresponds to electronic tunneling, which becomes the dominant conduction mechanism once the filament gap has narrowed sufficiently - typically after the SET event. In combination, these two contributions capture the coupled ionic–electronic nature of transport in ECM devices and form the basis of the model's predictive capability. Adapted under the terms of CC-BY 4.0 license [34].

$\frac{k_B T}{ze}$ and allows for numerical simplicity. The electron transfer current at the active electrode/insulator interface for the SET process according to the Tafel equation reads

$$I_{ac,SET} = j_{0,et} A_{ac} \Big(\exp\Big(\frac{(1-\alpha_{et})ze}{k_B T} \eta_{ac,SET} \Big) - 1 \Big). \tag{3.2}$$

Here, $j_{0,et}$ is defined as $j_{0,et} = zeck_{0,et} \exp\Big(-\frac{\Delta G_{et}}{k_B T} \Big)$, whereas the active electrode cross section A_{ac} is $A_{ac} = \pi r_{ac}^2$ with r_{ac} being the active elecrode cross section radius. The electron transfer current at the insulator/inert electrode (filament tip) for the SET process interface is according to the Tafel equation given as

$$I_{fil,SET} = j_{0,et} A_{fil} \Big(\exp\Big(-\frac{\alpha_{et} ze}{k_B T} \eta_{fil,SET} \Big) - 1 \Big). \tag{3.3}$$

Here, A_{fil} is the filament cross section defined as $A_{\mathrm{fil}} = \pi r_{\mathrm{fil}}^2$ with r_{fil} as the filament radius. The ion hopping/migration current is displayed in the model according to the Mott-Gurney law as [62]

$$I_{\mathrm{hop}} = j_{0,\mathrm{hop}} A_{\mathrm{is}} \sinh\left(\frac{zea}{2k_{\mathrm{B}}T}\frac{\eta_{\mathrm{hop}}}{x}\right). \tag{3.4}$$

Here, $j_{0,\mathrm{hop}}$ is defined as $j_{0,\mathrm{hop}} = 2zecaf \exp\left(-\frac{\Delta G_{\mathrm{hop}}}{k_{\mathrm{B}}T}\right)$, $A_{\mathrm{is}} = \pi r_{\mathrm{is}}^2$ is the cross section of ion migration with r_{is} as the ion migration cross section radius, and $\eta_{\mathrm{hop}} = E \cdot x$ is the ion hopping overpotential. The increase and decrease of the gap x between active electrode and filament tip is controlled by the strength of the ionic currents. For the ionic currents I_{ion} the following is valid: $I_{\mathrm{ion}} = I_{\mathrm{ac}} = I_{\mathrm{hop}} = I_{\mathrm{fil}}$. Hence, one of the ionic currents from equations (3.2) - (3.4) is fed in as ionic current density j_{ion} into the ordinary differential equation (ODE) of the gap's transient evolution in order to access this model's state variable x. The ODE reads

$$\frac{\mathrm{d}x}{\mathrm{d}t} = -\frac{M_{\mathrm{Me}}}{ze\rho_{\mathrm{m,Me}}} j_{\mathrm{ion}}. \tag{3.5}$$

Here M_{Me} is the atomic mass of the deposited active metal, and $\rho_{\mathrm{m,Me}}$ is its mass density. The gap x determines and exponentially contributes to the electronic tunneling current according to equation 2.4 [66]

$$I_{\mathrm{Tu}} = C\frac{3\sqrt{2m_{\mathrm{eff}}\Delta W_0}}{2x}\left(\frac{e}{h}\right)^2 \exp\left(-\frac{4\pi x}{h}\sqrt{2m_{\mathrm{eff}}\Delta W_0}\right) V_{\mathrm{Tu}}. \tag{3.6}$$

C is introduced to match the linear tunneling equation to the medium voltage regime, e. g. $C = 2.7$ [47]. The tunneling voltage V_{Tu} drives the tunneling current, which becomes pronounced in the LRS, once the gap x has become small enough. When x increases, the ECM cell undergoes a RESET process. Due to Kirchhoff's law the following relation is valid during filament growth or dissolution: $V_{\mathrm{Tu}} = \eta_{\mathrm{ac}} + \eta_{\mathrm{hop}} + \eta_{\mathrm{fil}}$. The total current through the ECM cell I_{cell} is given by

$$I_{\mathrm{cell}} = I_{\mathrm{ion}} + I_{\mathrm{Tu}} \tag{3.7}$$

In the LRS, the electronic tunneling current I_{Tu} exceeds the ionic current I_{ion} by orders of magnitude. The cell voltage V_{cell} according to Kirchhoff's law is

$$V_{\mathrm{cell}} = I_{\mathrm{cell}}\left(R_{\mathrm{series}} + \frac{\rho_{\mathrm{fil}}(L-x)}{A_{\mathrm{fil}}}\right) + V_{\mathrm{Tu}}. \tag{3.8}$$

$R_{\text{series}}$is an optional series resistance, whereas the filament resistance R_{fil} is given by $R_{\text{fil}} = \frac{\rho_{\text{fil}}(L-x)}{A_{\text{fil}}}$. Here ρ_{fil} is the active metal's specific resistance, and L is the length of the insulator. The newly developed models presented in section 4.1 are based on this JART ECM v1 model.

3.2.2 The Nonvolatile JART VCM v1 Model

Apart from ECM-type ReRAM devices, VCM-type ReRAM devices are also promising candidates for building blocks in CIM architectures. VCM devices typically rely on transition metal oxides such as HfO_x or TiO_x as insulating material [94, 95]. One electrode forms an ohmic contact while the other, due to a higher work function, forms a Schottky barrier - this asymmetry defines the latter as "active" electrode at which switching occurs [94, 95].

Initially, the oxide is in a highly resistive state, requiring a forming process in which a high voltage locally modifies the material structure, forming oxygen vacancies through reduction processes that serve as mobile ionic charge carriers. A resulting oxygen-deficient volume forms a nanoscale conductive filament that spans the oxide layer between the electrodes.

To simplify the physical modeling of this filamentary switching behavior, the filament is conceptually divided into two regions: a *disc* region near the active electrode where resistive switching occurs, and a *plug* region that remains highly conductive and connects the disc to the ohmic electrode. The disc corresponds to the Schottky depletion region and is where the concentration of oxygen vacancies is dynamically modulated during switching.

When a negative voltage is applied to the active electrode (SET operation), positively charged oxygen vacancies are attracted from the plug into the disc region, increasing its conductivity and reducing its resistance. Since the plug contains a comparatively large reservoir of vacancies, its resistance remains approximately constant. After SET, both disc and plug are low-resistance, placing the cell in the LRS.

Conversely, during a RESET operation, a positive voltage repels vacancies back into the plug, decreasing their concentration in the disc and raising its resistance. The plug's role remains largely passive, acting as a transport medium for vacancies. The resistance of the cell in this HRS is therefore primarily determined by the state of the disc region, as the plug remains nearly invariant in its conductive properties.

This abstraction of the switching region into two serial resistive elements, disc and plug, provides a tractable basis for compact modeling of the device, capturing the es-

sential physics of vacancy migration and its impact on the resistance modulation during SET and RESET cycles. In the following, a nonvolatile VCM compact model, called "JART VCM v1" [94] is presented.

The switching behavior of VCM cells is governed by the drift of oxygen vacancies to and away from the metal/insulating oxide interface, such as the interface Pt/HfO_2. In this compact model, the oxygen vacancy concentration in the interface region (referred to as the disc) is defined as the state variable N_{disc}, whose transient evolution is expressed by

$$\frac{\mathrm{d}N_{\mathrm{disc}}}{\mathrm{d}t} = -\frac{I_{\mathrm{ion}}}{z_{\mathrm{Vo}} e A l_{\mathrm{disc}}}. \tag{3.9}$$

Here, I_{ion} denotes the ionic current, z_{Vo} is the charge number of oxygen vacancies, $A = \pi r_{\mathrm{fil}}^2$ is the active cross-sectional area of the filament, and l_{disc} is the disc length.

The ionic current is described by

$$I_{\mathrm{ion}} = 2 z_{\mathrm{Vo}} e A c_{\mathrm{Vo}} \nu_0 a \cdot \exp\left(-\frac{\Delta W_{\mathrm{A}}}{k_B T}\right) \cdot \sinh\left(\frac{a z_{\mathrm{Vo}} e E_{\mathrm{SET,RESET}}}{2 k_B T}\right), \tag{3.10}$$

with ν_0 representing the attempt frequency, a the ion hopping distance, ΔW_{A} the ion hopping potential barrier and $E_{\mathrm{SET,RESET}}$ the electric field,

$$E_{\mathrm{SET}} = \frac{V_{\mathrm{disc}}}{l_{\mathrm{disc}}}, \tag{3.11}$$

$$E_{\mathrm{RESET}} = \frac{V_{\mathrm{cell}}}{l_{\mathrm{cell}}}, \tag{3.12}$$

where $V_{\mathrm{cell}} = V_{\mathrm{disc}} + V_{\mathrm{plug}} + V_{\mathrm{Schottky}}$ is the voltage across the cell, and l_{cell} is defined as $l_{\mathrm{cell}} = l_{\mathrm{plug}} + l_{\mathrm{disc}}$. Moreover, c_{Vo} is the average oxygen vacancy concentration throughout the full plug and disc region:

$$c_{\mathrm{Vo}} = \frac{N_{\mathrm{plug}} + N_{\mathrm{disc}}}{2}. \tag{3.13}$$

The local temperature T of the device is modeled as:

$$T = I \cdot V_{\mathrm{cell}} \cdot R_{\mathrm{th,eff}} + T_0. \tag{3.14}$$

Here, T_0 is the ambient temperature, I is the electric current, and $R_{\mathrm{th,eff}}$ is the effective equivalent thermal resistance.

Further modeling details, such as the resistive elements R_{disc} and R_{plug}, the nonlinear Schottky interface, the corresponding state(N_{disc})-dependent Schottky current, and series resistance contributions, are incorporated to ensure an accurate representation of

the SET and RESET dynamics. The total resistance and switching behavior result from the coupled evolution of temperature, electric field, and ionic distributions, driven by the applied bias conditions. The LRS is dominated by the polarity-dependent Schotky current.

3.2.3 The NbO_2-based Threshold Switch Model

The threshold switching (TS) model from [96] accounts for the abrupt, volatile transition of NbO_2 filamentary devices from a high-resistive OFF-state to a low-resistive ON-state and the emergence of a negative differential resistance (NDR) region under bias. It explains the full, quasi-static I–V characteristic without invoking a metal–insulator transition; instead, transport is described by field-enhanced Poole-Frenkel (PF) emission combined with moderate Joule self-heating (temperature rise on the order of 150 K). This purely electro-thermal framework captures the temperature dependence below threshold and the curvature of the NDR region in a unified way.

Below threshold, conduction is dominated by PF emission from traps, which yields a temperature- and field-dependent device resistance with

$$R_{\mathrm{m}} \;=\; R_0 \,\exp\!\left(\frac{E_{\mathrm{a}} - \beta\sqrt{E}}{k_{\mathrm{B}} T_{\mathrm{m}}}\right), \qquad \beta \;=\; \sqrt{\frac{e^3}{\pi \varepsilon_0 \varepsilon_{\mathrm{r}}}}, \tag{3.15}$$

where R_0 is a constant prefactor, E_{a} the activation energy of the traps, E the electric field across the oxide, T_{m} the filament (internal) temperature, ε_0 the vacuum permittivity, and ε_{r} the relative permittivity. The field is set by the device voltage drop across the oxide thickness l_{ox},

$$E \;=\; \frac{V_{\mathrm{m}}}{l_{\mathrm{ox}}}. \tag{3.16}$$

The thermal dynamics of the filament follow an energy balance between Joule heating and heat outflow to the surroundings:

$$C_{\mathrm{th}} \,\frac{dT_{\mathrm{m}}}{dt} \;=\; R_{\mathrm{m}}\, I_{\mathrm{m}}^2 \;-\; G_{\mathrm{th}} \left(T_{\mathrm{m}} - T_{\mathrm{amb}}\right). \tag{3.17}$$

Here, C_{th} is the thermal capacitance, G_{th} the thermal conductance, the ambient temperature is T_{amb}, the device current is I_{m}, and the temperature difference is $\Delta T = T_{\mathrm{m}} - T_{\mathrm{amb}}$. Electrical coupling to the measurement circuit by a series resistance R_{series} is expressed by Ohm's law:

$$V \;=\; (R_{\mathrm{m}} + R_{\mathrm{series}})\, I_{\mathrm{m}} \;=\; V_{\mathrm{m}} + R_{\mathrm{series}}\, I_{\mathrm{m}}. \tag{3.18}$$

Here, V is the applied terminal voltage and V_{m} the voltage across the threshold switching memristive device.

Under quasi-static conditions (slow sweeps), the thermal transient vanishes and (3.17) reduces to

$$R_{\mathrm{m}}\, I_{\mathrm{m}}^2 \;=\; G_{\mathrm{th}}\, \Delta T, \qquad \Rightarrow \qquad T_{\mathrm{m}} \;=\; T_{\mathrm{amb}} \;+\; \frac{R_{\mathrm{m}}\, I_{\mathrm{m}}^2}{G_{\mathrm{th}}}. \tag{3.19}$$

Equations (3.15)–(3.18), together with (3.19) in steady state, form a closed, self-consistent system that reproduces (i) the increase of current below threshold via PF conduction, and (ii) the onset of TS and the NDR branch due to positive electrothermal feedback once a critical field is reached.

The model attributes TS entirely to electronic transport with moderate self-heating: as I_{m} grows, Joule power raises T_{m}, which lowers the effective barrier (via the exponential in (3.15)) and further increases I_{m}. This feedback explains the sharp transition and the temperature dependence of the NDR curvature.

4 Newly Developed Models and Simulation Methodology

Three new compact models have been developed: A variability-aware ECM model, a volatile ECM model and a variability-aware volatile ECM model. In this chapter, all three newly developed ECM models are introduced. Simulations based on them are performed as fits to experimental data or as simulation studies and are presented in subsequent chapters of this thesis. Any model fit or simulation study has followed a simulation framework that is introduced in the last section of this chapter. The newly developed models have been published in [34, 46].

4.1 Newly Developed Models for ECM Cells

Naturally inherent to ECM devices is their variability from cycle to cycle and from device to device. This variability can be beneficial for nonvolatile ECM devices when used for Physical Unclonable Function (PUF) applications [97] or TRNG applications [42]. However, a memory application as well as artifical nonvolatile neuromophic synapses do not allow for variabilities. The latter do not forget their state due to missing relaxation. Volatile ECM devices can be used in artificial neuron circuits, being a crucial building block for neuromorphic computing [22, 23]. In this sense, variability can be a beneficial feature, when the focus is on realising a short-term plasticity as experienced in biological neurons [39–41]. Furthermore, variability in volatile ECM devices is beneficial for TRNG applications [42] as well as for probabilistic bits [98, 99], as the inherent stocasticity can be perfectly exploited. Therefore, depending on the application purpose variability is seen either as a disruptive feature or as a beneficial and crucial part of the application. Considering this naturally inherent variability in nonvolatile as well as volatile ECM devices for any type of application, and providing this device-related feature in a compact model to be used in circuit simulators contributes to understanding the variability's

impact on potential applications on the level of circuit design.

In the following, several new developed ECM models are presented that are all based on physics-based framework of the nonvolatile JART ECM v1 model, presented in section 3.2.1. The new models comprise a variability-aware nonvolatile ECM model, a volatile ECM model that describes relaxation of ECM devices over time, and a model adding variability to this new developed volatile ECM model.

4.1.1 The Variability-Aware Nonvolatile JART ECM v1 var Model

In [34], a nonvolatile ECM model is developed that especially comprises variability experienced in measurements with such devices. Thus, it is crucial to consider this variability while performing circuit design for applications based on these devices with their corresponding stochastic nature. A variability-aware compact model, such as the "JART ECM v1 var" presented in the following, allows for such a consideration. It is publicly available implemented as verilog-A code [100].

The variability is imposed on some of the physical, dynamic and geometrical parameters of the nonvolatile JART ECM v1 model from the section 3.2.1, similar to the variability-aware VCM model presented in [95]. Hence, the equations (3.1) - (3.8) from there are also valid for this model.

To reproduce the experimentally observed variability of resistance states, SET/RESET voltages, as well as SET delay times in ECM cells, the deterministic description is extended by introducing a variability-aware model. This extension captures two distinct sources of variability frequently encountered in experiments: *device-to-device variability* and *cycle-to-cycle variability*. The first originates from inherent differences in device geometry and material properties, caused by inevitable fluctuations during fabrication. The latter occurs within the same device over repeated switching cycles, reflecting stochastic fluctuations in filament evolution despite an identical initial geometry and material composition. However, cycle-to-cycle variability inherently accompanies any device-to-device variability.

The following eight model parameters are subject to variability in the proposed framework:

- r_{ac}, r_{is}, r_{fil}: radius of the active electrode, cross section radius of ionic drift, and filament radius,
- c: concentration of active metal ions in the insulating layer,

- α_{et} and $k_{0,\mathrm{et}}$: electron transfer coefficient and electron transfer rate constant,
- $t_{0,\mathrm{nuc}}$: nucleation prefactor,
- L: thickness of the isulating layer (considered only for device-to-device variability).

(1) Device-to-device variability. Prior to variability simulations, each parameter ξ is assigned a truncated Gaussian distribution centered around its nominal mean. In contrast to a standard Gaussian distribution, truncation ensures that unphysical values are avoided by imposing strict lower and upper bounds $\xi_{\mathrm{d2d,low}}$ and $\xi_{\mathrm{d2d,up}}$. For each simulated device, a parameter set is generated by randomly sampling values for all eight parameters from their respective distributions. These parameter sets are prepared in MATLAB and written into text files, which are subsequently imported into the circuit simulator (Spectre). During simulation, each of the n devices is thus represented by one such set of parameter values, as outlined in [95].

(2) Cycle-to-cycle variability. Fluctuations between switching cycles of the same device are introduced by modifying parameter values after every SET or RESET operation, extending the strategy used previously for VCM models [95]. For each parameter ξ, overall lower and upper limits for cycle-to-cycle variability are defined as

$$\xi_{\mathrm{c2c,low}} = \xi_{\mathrm{init}} \cdot (1 - \Delta\xi_{\mathrm{max,all}}), \tag{4.1}$$

$$\xi_{\mathrm{c2c,up}} = \xi_{\mathrm{init}} \cdot (1 + \Delta\xi_{\mathrm{max,all}}), \tag{4.2}$$

where ξ_{init} is the initial parameter value (drawn from the truncated Gaussian distribution) and $\Delta\xi_{\mathrm{max,all}}$ denotes the maximum allowed fractional change during the entire simulation. These bounds ensure that parameter variations remain physically meaningful. In practice, the cycle-to-cycle range is narrower or equal to the device-to-device Gaussian range. If the calculated range extends beyond the truncated Gaussian limits, it is clipped accordingly.

At each subsequent SET/RESET cycle, the parameter is updated following a random walk process in one dimension, implemented as a discrete Bernoulli sequence [95, 101]. The random walk is a mathematical theory that aims to describe random discrete stepwise changes in a stochastic manner. In this theory, every step is connected to but independent from its previous step. The update step is described by

$$\xi_k = \xi_{k-1} \cdot \Big(1 \pm \Delta\xi_{\mathrm{max}} \cdot P\Big), \tag{4.3}$$

where k is the update index, $\Delta\xi_{\max}$ is the maximum fractional change per step, and $P \in [0, 1]$ is a uniformly distributed random number determining the step size. The sign $\pm$ is chosen implying equal probability, so that each step may either increase or decrease the parameter value. As for device-to-device variability, all update values are precomputed in MATLAB and provided to the circuit simulator through parameter tables. For some parameters (r_{ac}, r_{is}, r_{fil}, c), variations are coupled to the tunneling gap x, implying that these quantities are updated only when x changes.

For instance, the variability parameter $r_{\mathrm{ac,var}}$ is inserted into the model in the following manner for positive voltages (SET direction):

$$r_{\mathrm{ac,var}} = r_{\mathrm{ac,old}} + (r_{\mathrm{ac,new}} - r_{\mathrm{ac,old}}) \left(\frac{x_{\mathrm{old}} - x}{x_{\mathrm{old}} - 0} \right) \tag{4.4}$$

Likewise, the following definition holds for negative voltages (RESET direction):

$$r_{\mathrm{ac,var}} = r_{\mathrm{ac,old}} + (r_{\mathrm{ac,new}} - r_{\mathrm{ac,old}}) \left(\frac{x - x_{\mathrm{old}}}{0 - x_{\mathrm{old}}} \right) \tag{4.5}$$

The variability parameters $r_{\mathrm{is,var}}$, $r_{\mathrm{iu,var}}$, and c_{var} are determined in the same manner. The denotation “var” is introduced, as only this parameter out of the three (“var”, “new”, “old”) is inserted into the model instead of the original parameter and connects to the physical equations in this specific time step. For instance, the parameter with the new denotation, i. e. $r_{\mathrm{ac,var}}$, is inserted into the model instead of r_{ac}. “old” denotes the parameter in the previous time step, whereby “new” denotes the parameter determined through random walk in the current time step. Therefore, both only interact with the physical model via the connection to “var”, which is introduced in equations (4.4) and (4.5). Owing to this connection, only intermediate values are attained by the “var” parameters, when the switching is not complete, i.e., when the gap does not attain the limit values “L” or zero.

Refined treatment of cycle-to-cycle variability. In contrast to earlier approaches [95], we extend the implementation of cycle-to-cycle variability through two modifications:

(a) **Random walk linked to staircase sweep steps.** Instead of applying random updates only once before each SET/RESET transition, as in [95], here the random walk can be applied after every voltage step of the staircase sweep. This results in cycle-to-cycle fluctuations within, e. g., a single sweep, capturing stochastic current variations during the I-V characteristics.

(b) **Stochasticity in the differential equation.** To reflect the inherently random character of filament evolution, the deterministic gap evolution (equation (3.5)) is augmented with an additional noise term:

$$x_{k+1} = x_k - \frac{M_{\mathrm{Me}}}{ze\rho_{m,\mathrm{Me}}} j_{\mathrm{ion}}\, \Delta t_{\mathrm{sim,step}} \pm \delta \cdot p_{\mathrm{jump}}. \tag{4.6}$$

Here, $\Delta t_{\mathrm{sim,step}}$ is the simulation time step, $\delta \ll 1\,\mathrm{nm}$ defines the noise amplitude (e.g., $\delta = 0.005\,\mathrm{nm}$), and p_{jump} is a random number between zero and one. The noise update occurs at an after each simulation step randomly chosen time step. The choice of δ can be physically motivated: if e. g. a single metal atom M (e. g. diameter $d_{\mathrm{M}} = 0.26\,\mathrm{nm}$) is added to or removed from the filament, the stochastic gap change δ scales as

$$\delta = d_{\mathrm{M}} \cdot \frac{r_{\mathrm{M}}^2}{r_{\mathrm{fil}}^2} \tag{4.7}$$

with the metal radius $r_{\mathrm{M}} = 0.13\,\mathrm{nm}$. For r_{fil} between 0.8 - 2 nm, this yields δ values in the range of 0.007 - 0.001 nm.

Summary. The variability model thus incorporates both device-to-device and cycle-to-cycle fluctuations in a physics-based and stochastic framework. This extended model enables a more accurate reproduction of experimental *I-V* sweeps and switching kinetics, as it considers the stochastic variability inherent to ECM devices, and can therefore serve as a compact model for variability-aware circuit design.

4.1.2 The Volatile JART v-ECM v1 Model

Based on the nonvolatile JART ECM v1 model from section 3.2.1, the newly developed volatile JART v-ECM v1 model is presented in the following. It is publicly available implemented as verilog-A code [102]. Mainly, the equations describing ionic processes as driving force for the switching/filament growth and relaxation/filament dissolution experience a modification as the emf is introduced into the model.

Introduction

The SET process in a v-ECM device, also referred to as a diffusive memristor [23, 68], induces a rapid and abrupt transition from the HRS to the LRS once an external positive voltage bias is applied. When the electrical bias is removed or sufficiently reduced, the

device spontaneously relaxes back to the HRS. The corresponding certain time interval, after which the device switches off again, is defined as the relaxation time t_r [23]. Both the SET time and the relaxation time typically vary significantly from device to device, from cycle to cycle, and also with respect to the materials employed for fabrication. The stability of the metallic filament plays a decisive role in determining the operational characteristics and application types of ECM devices. The robustness of the filament is directly linked to the strength of the electrical stimulus applied across the device [32]. When a high voltage bias is applied, the device exhibits nonvolatile behavior, implying that dissolution of the filament, i.e., execution of the RESET process, requires an additional voltage of opposite polarity. In contrast, under specific programming conditions, ECM cells can also demonstrate volatile characteristics: if only a small voltage is applied, or if a low current compliance restricts filament growth, the subsequent dissolution of the filament occurs spontaneously once the applied bias is sufficiently reduced or removed. In this case, the device relaxes back to its HRS without the need for an oppositely polarized voltage. Hence, reducing the applied voltage below the hold voltage V_{hold} is sufficient to trigger the relaxation process [23].

A positive device bias V_{dm} across a v-ECM cell therefore yields distinct filament-evolution scenarios, as sketched in Figure 4.1. The emf imposes a dynamic equilibrium at $V_{\mathrm{dm}} = V_{\mathrm{emf}}$ (rather than $V_{\mathrm{dm}} = 0$). At this point no net ionic current flows through the device (although an electronic current is still present). As a consequence, filament dissolution sets in whenever the applied voltage falls below the emf, $V_{\mathrm{dm}} < V_{\mathrm{emf}}$. According to the relaxation kinetics, a value $V_{\mathrm{dm}} \ll V_{\mathrm{emf}}$ accelerates dissolution compared with a value closer to equilibrium, $V_{\mathrm{dm}} \lesssim V_{\mathrm{emf}}$ [59, 103]. Conversely, for $V_{\mathrm{dm}} > V_{\mathrm{emf}}$ the filament grows and the switching kinetics speed up nonlinearly with increasing V_{dm}.

The novelty of the robust and coherent model for v-ECM devices presented here originates from incorporating the theory of the nanobattery effect, which is driven by the emf, into the nonvolatile model. This concept has already been introduced and discussed in relation to experimentally observed non-ideal nonvolatile behavior of ECM devices [43, 104], but has so far not been utilized to establish models for v-ECM devices. Earlier cyclic voltammetry measurements [56, 58, 69] strongly suggest a naturally intrinsic presence of the emf within ECM-based systems, which may account for the volatile behavior of these devices. The theoretical framework of this model is supported by this clear understanding that ionic processes trigger switching events in such devices, and also lead to the emf and resulting non-zero crossing I–V characteristics. Specifically, the ionic current remains zero when the applied voltage is shifted to a certain non-zero

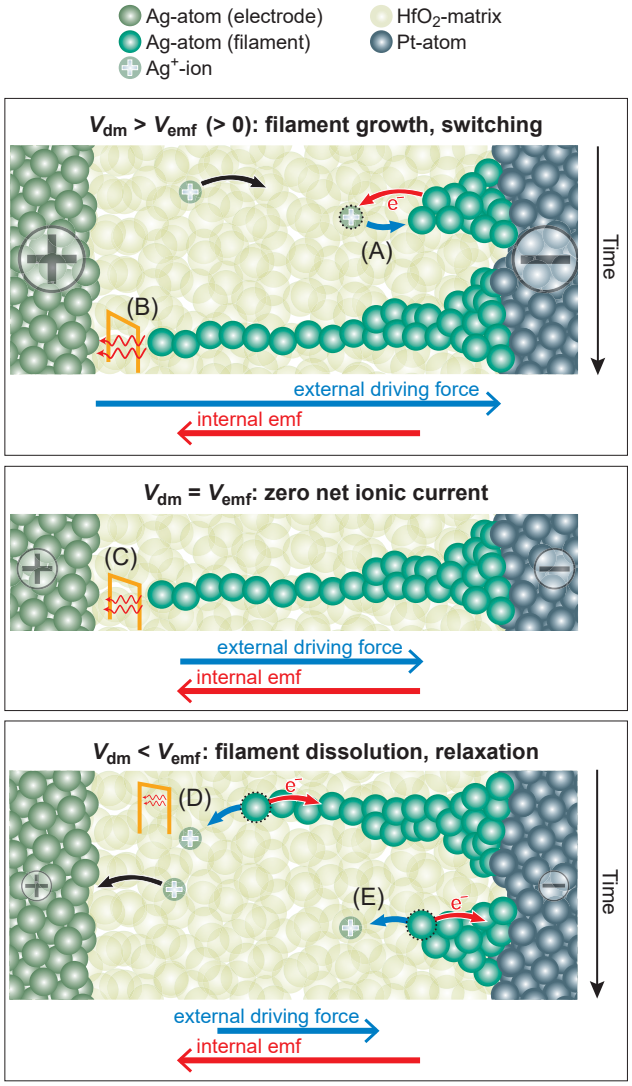

Figure 4.1: The figure schematically illustrates the different dynamical regimes of a v-ECM device as a function of the voltage drop across the device, V_{dm}, in relation to the electromotive force, V_{emf}. When $V_{\mathrm{dm}} > V_{\mathrm{emf}}$, a switching event is initiated, which consists of the electrochemical growth of the metallic filament driven by ionic redox reactions and ion migration (A), followed by the establishment of a tunneling current through the formed filament (B). The time required for this transition is defined as the switching time t_{SET}. In the case of $V_{\mathrm{dm}} = V_{\mathrm{emf}}$, the driving forces for filament growth and for filament dissolution exactly counterbalance one another, such that a dynamic equilibrium is established. In this state, no net ionic current can be detected because the effective ionic driving force is zero. Nevertheless, an electronic tunneling current persists under the applied bias (C). When the condition $V_{\mathrm{dm}} < V_{\mathrm{emf}}$ is met, the processes that promote filament dissolution, also induced by ionic redox reactions and ion migration (D, E), dominate over the competing filament growth processes. This imbalance leads to a gradual removal of the metallic filament and thus to the relaxation of the ECM device into its HRS after a finite relaxation time t_{r}, the duration of which depends on the magnitude of V_{dm}. Adapted under the terms of CC-BY 4.0 license [46].

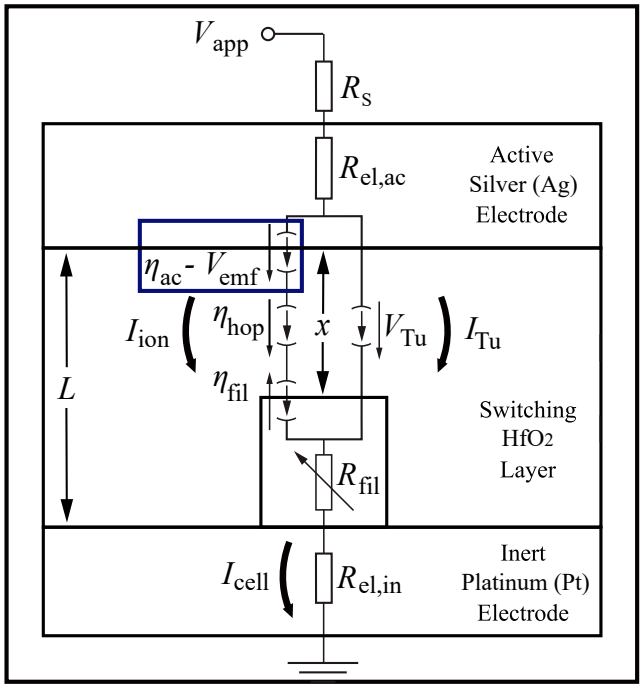

Figure 4.2: The illustration depicts the equivalent circuit diagram of the v-ECM model, exemplarily shown for a $Ag/HfO_2/Pt$ device stack. Within this abstraction, two distinct current paths can be identified. The first is the ionic current path, which comprises the overpotentials associated with ionic redox reactions and ion migration. This path provides the fundamental driving force for both the switching process into the LRS and the subsequent spontaneous relaxation back to the HRS: the electromotive force. The second current path corresponds to electronic tunneling, which becomes the dominant conduction mechanism once the filament gap has narrowed sufficiently - typically after the switching event and before the onset of relaxation. In combination, these two contributions capture the coupled ionic–electronic nature of transport in v-ECM devices and form the basis of the model's predictive capability. Adapted under the terms of CC-BY 4.0 license [46].

value, while it does not apply for 0 V. This phenomenon's theoretical framework is given in section 2.4. As demonstrated in the upcoming fits and studies, including the emf in the model provides a solid foundation for reproducing the dynamic behavior of volatile devices, such as accurately predicting switching and relaxation times under various bias conditions. This model extension ensures that the model becomes more reliable and consistent with a wide range of experimental observations.

The Model

The ECD of the v-ECM's model is shown in Figure 4.2.

The equation describing the nucleation time in equation 3.1 is modified as follows:

$$t_{\mathrm{nuc}} = t_{0,\mathrm{nuc}} \exp\left(\frac{\Delta G_{\mathrm{nuc}}}{k_{\mathrm{B}}T}\right) \exp\left(-\frac{(N_{\mathrm{c}} + \alpha_{\mathrm{nuc}})ze}{k_{\mathrm{B}}T}(\eta_{\mathrm{nuc}} - V_{\mathrm{emf}})\right). \tag{4.8}$$

In comparison to the nonvolatile model, the emf is substracted from the voltage that drives the nucleation, which is the full voltage that drops across the v-ECM device in a simplified picture, i. e. $V_{\mathrm{app}} = \eta_{\mathrm{nuc}}$. As no other ionic process simultaneously assists the nucleation process, this modified nucleation description shifts the ionic processes' dynamic equilibrium from 0 to the value V_{emf} during nucleation. It should be noted that nucleation is the only process that does not contribute to relaxation and is not required when a remnant filament exists after a weak relaxation. Therefore, for voltages $V_{\mathrm{dm}} < V_{\mathrm{emf}}$, relaxation is governed solely by the two ionic processes - electron transfer redox reactions and ion migration. Once nucleation is completed during the switching event at $V_{\mathrm{dm}} > V_{\mathrm{emf}}$, also these two processes take over: Ionic electron transfer reactions occur as metal atom oxidation at the active electrode and reduction at the inert electrode, accompanied by ion migration from the active electrode to the inert electrode. In contrast, during the relaxation process, i.e., for $V_{\mathrm{dm}} < V_{\mathrm{emf}}$, metal ion reduction occurs at the active electrode, while oxidation first takes place at the filament tip and subsequently at the inert electrode, also accompanied by ion migration to the active electrode. To avoid that the simplified Tafel formalism from the equations (3.2) and (3.3) produce distorted results due to the shift of the definiton of dynamic equlibrium, the generalised Butler-Volmer equations - in parts additionally modified by the emf - are implemented for the electron transfer reactions. Independently from the applied polarity, The electron transfer current for the redox reactions at the active electrode/insulating layer interface I_{ac} reads

$$\begin{aligned} I_{\mathrm{ac}} &= j_{0,\mathrm{et}}\, A_{\mathrm{ac}} \left[\exp\left(\frac{(1-\alpha_{\mathrm{et}})ez}{k_{\mathrm{B}}T}(\eta_{\mathrm{ac}} - V_{\mathrm{emf}})\right) \right. \\ &\quad \left. - \exp\left(-\frac{\alpha_{\mathrm{et}}ez}{k_{\mathrm{B}}T}(\eta_{\mathrm{ac}} - V_{\mathrm{emf}})\right)\right]. \end{aligned} \tag{4.9}$$

Similarily, the electron transfer current at the insulating layer/filament tip interface I_{fil} is given as

$$I_{\mathrm{fil}} = j_{0,\mathrm{et}}\, A_{\mathrm{fil}} \left[\exp\left(-\frac{\alpha_{\mathrm{et}}ez}{k_{\mathrm{B}}T}\eta_{\mathrm{fil}}\right) - \exp\left(\frac{(1-\alpha_{\mathrm{et}})ez}{k_{\mathrm{B}}T}\eta_{\mathrm{fil}}\right)\right]. \tag{4.10}$$

As shown in Figure 4.2, η_{fil} is defined in the direction opposite to both the applied voltage and η_{ac}. Subtracting $1 \cdot V_{\text{emf}}$ from η_{ac} in equation (4.9) is equivalent to adding $0.5 \cdot V_{\text{emf}}$ to η_{fil} in equation (4.10) while simultaneously subtracting $0.5 \cdot V_{\text{emf}}$ from η_{ac} in equation (4.9). Thus, it is sufficient to include the emf modification in only one of the equations. By incorporating the emf into equations (4.8) and (4.9), the modified dynamic equilibrium is established at $V_{\text{dm}} = V_{\text{emf}}$, which represents the voltage at which filament growth and filament dissolution processes are balanced. The ion migration I_{hop} is still governed by equation (3.4). Since the hopping overpotential is connected in series with both electron transfer overpotentials, referencing the emf solely to η_{ac} provides a reasonable and general formulation without loss of generality.
Further equations, including the ODE that describes the transient evolution of the state variable gap x between active electrode and filament tip (equation (3.5)), the electronic tunneling current I_{Tu} (equation (3.6)), the total cell current I_{cell} (equation (3.7)) and the cell voltage V_{cell} (equation (3.8)), complete the v-ECM model, are given unchanged as for the nonvolatile ECM model in section 3.2.1.

4.1.3 The Variability-Aware Volatile JART v-ECM v1 var Model

The variability-aware volatile ECM model is constructed by extending the volatile JART v-ECM v1 model (section 4.1.2) with variability in the same manner as previously applied to the nonvolatile JART ECM v1 model, described in detail in section 4.1.1. Variability is incorporated into all parameters listed in section 4.1.1 - namely r_{ac}, r_{is}, r_{fil}, c, α_{et}, k_{et}, $t_{0,\text{nuc}}$, and L - although in practice it can be restricted to a subset of them. A key distinction from the variability-aware nonvolatile ECM model is the additional inclusion of variability in the parameter V_{emf}. This is implemented analogously to the treatment of the other variability parameters in section 4.1.1, and is essential, as the shifted dynamic equilibrium can vary both from cycle to cycle and across different devices. This model is publicly available implemented as verilog-A code [105].

4.2 Simulation Framework

This thesis, its results, and conclusions are heavily simulation based. In the following, the usual simulation framework that has led to the results is introduced. It comprises the role of the circuit simulator Cadence Spectre, the MATLAB interface that controls the simulation and the framework for variability modeling.

4.2.1 Cadence Spectre

The circuit simulating programm “Cadence Spectre” enables simulations and testing of vast circuits. Therefore, it heavily contributes to circuit design for complex circuits. Either electronic devices with simple behavior like resistors can be chosen from the available database, or models of devices with a more complex electric and dynamic behavior can be constructed, e. g., as a verilog-A model, and fed in into the circuit simulator. Placing electronic devices into its position within the circuit can be relaised either by the Electronic Design Automation (EDA) software “Cadence Virtuoso” as Graphical User Interface (GUI) or Interactive Design Environment (IDE), where a circuit environment is visible and devices and wires can be connected to a circuit manually or in an automated fashion, or netlists can be written as a text document, which contain all information related to the aimed circuit design. Also, this can be achieved manually or by programming the netlist, e. g., in MATLAB. In the first case, also a netlist is generated; however, it is not created actively by the user, rather it is created by the EDA software itself after the circuit design has been completed by the user. In both cases, the netlist is forwarded to the circuit simulator.

Cadence Virtuoso

The IDE “Cadence Virtuoso” enables the design of electric circuits without actively writing codes as netlists. Instead, a GUI interface is provided and can be used to design and see the layout simultaneously. After designing the circuit and before the start of the simulation, several inputs are necessary:

- assignment of model parameter values,
- assignment of potential resistance, capacitance, inductance values,
- specification of voltage/current source parameters,
- type of simulation: Direct current (DC), transient, etc.,
- specification of desired output/simulation results.

After the simulation the outputs/simulation results can be seen in a window that opens. Also, further treatment of the outputs can be done within the software or this window.

MATLAB interface

The design of circuits via netlists, the specification of simulation setup, and the running of the simulation can be also controlled via MATLAB, and its corresponding interface to Cadence Spectre. As each step leading to the final simulation is documented, a better control and an efficient way of automatization is given, the use of such an interface can be beneficial depending on its usage purpose. One coding command that connects to Cadence Spectre is sufficient in this term. A main file within MATLAB can be constructed that runs the simulation and contains several functions that contribute to the simulation setup. These functions are also organized in separate files. Among the functions that are called by the main are functions that

1. generate the netlist,
2. specify model and device parameter values,
3. specify the dynamic electric stimulus input,
4. get results from Spectre after the simulation to be accessed in MATLAB,
5. visualize the results after simulation.

Upon calling up these functions within the main file before/while running the simulation, all simulation setup aspects introduced in the section 4.2.1 are addressed. The generated netlist created by the corresponding function together with the other functions is fed in into the circuit simulator. The interaction with it allows direct simulation setup input and access to the results afterwards.

4.2.2 Simulation Framework for Variability Modeling

The implementation of the variability simulation approach, as discussed in section 4.1.1 and 4.1.3, and its simulation framework are introduced in the following. For this implementation, the MATLAB interface is exploited to control the simulation in an efficient way. Additionally to the functions mentioned for a simulation control via a MATLAB interface in section 4.2.1, a function is constructed that programs the workaround for variability realization. A similar approach is presented in [95].

Implementation of d2d variability. This additional function instructs to create truncated Gaussian distributions for each parameter that should experience variability, and

to take a random value out of the truncated Gaussian distribution each. This procedure is repeated for n number of devices. The generated parameter values are saved in the first row of a variability matrix. This matrix's column size is $m \cdot n + 1$, where m is the number of parameters that experience variability. The very fist column is the time column. Hence, for d2d variability, $t = 0$ s is assigned to the first column in the the first row. All other $m \cdot n$ columns contain the parameter values. This function also creates parameters that represent any boundaries required for the variability simulations.

Implemetation of c2c variability. The additional function enabling variability calls up a further function that implements the random walk process from equations (4.1) - (4.3). For each time step that is specified in the main file, a new row in the variability matrix is generated containing all parameter values for the corresponding random walk time step. Also, these added rows assign m parameter values to n devices for the corresponding random walk step. If the radom walk update step is after each SET and RESET event, or after each staircase sweep step, or at any time else, can be specified in the main file. Stochasticity of the state variable gap x, as indicated by equations (4.6) and (4.7), and the coupling to this state variable for some chosen parameters, as indicated by equations (4.4) and (4.5), are included into the corresponding verilog-A model.

Variability simulation. Variability parameter names, their mean values, the standard deviation values for the truncated Gaussian distribution, its truncation values, all random walk process related parameter values are set in one of the previosuly mentioned functions from section 4.2.1. The variability matrix, which includes all update time values as well as the variability of all parameters and devices, is converted into a table in a text file. The names are fed in into the netlist generating function. Thus, the netlist accesses the table in the text file and provides the corresponding variability parameter values at specific time steps to the circuit simulator. Hence, d2d variability (only first row of the variability matrix/table) or c2c variability (consecutive rows each representing one update random walk time step) is realized by the simulation.

5 Variability-Aware Simulations of ECM Devices: Results and Discussion

Multiple reliability facets of memristive devices and systems have been addressed and, in many cases, improved [106–114]. These advances have been achieved through several routes, including tailoring the size of ECM cells and engineering either the thickness of individual layers or the overall device stack [107, 115–120]. The choice of materials and their combinations has likewise been shown to influence performance and reliability in ECM devices [107, 121–124]. In particular, retention can be enhanced by structural refinements such as introducing interfacial or bi-layer designs [120, 125], as well as by incorporating suitable dopants [109, 126]. Moreover, both multilevel states [127, 128] and quantized conduction states [128–130] have been demonstrated and analyzed in ECM technology. Interest has also grown in leveraging 2D materials within ECM architectures [115, 131, 132].

Despite these efforts, variability remains an inherent and dominant feature of ECM devices, underscoring the need for models that explicitly account for it. Experimentally observed dispersion in dynamic behavior and in electrical characterization persists as an unwelcome challenge. One approach is to model variability by systematically perturbing relevant geometrical and physical parameters.

To date, deterministic continuum descriptions for ECM cells [133] and compact modeling frameworks [47, 134, 135] have been proposed. Complementary simulation methodologies include Kinetic Monte Carlo (KMC) [136] and Atomic Monte Carlo studies [137], alongside Molecular Dynamics models [135], *ab initio* simulations [138], and retention-oriented formulations [139, 140]. A simplified analytical treatment has also been introduced [141, 142]. With respect to variability, non-physical behavioral models [143] and other stochastic mathematical formulations have been explored [37, 143]. There exist variability-aware KMC approaches [143], and additional physical models that incorpo-

rate variability sufficiently to fit a device's I-V characteristics while omitting the full ECM cell dynamics - most notably, an accurate representation of SET kinetics [143]. A concise overview of variability-aware strategies is provided in [143]. Building on the Stanford VCM framework in [134], a physics-based extension introduces variability through fluctuations in the gap distance [143]. Another variability-aware VCM model considers spatial variations in oxygen ion concentration within a defined region of the switching layer [95]. Nevertheless, a physics-grounded, dynamical compact model for ECM cells that captures the full device physics while concurrently representing variability arising from distributions of geometrical and material parameters is still missing.

As presented in section 4.1, variability is a key feature of ECM devices. It can be exploited for certain application realization but can also show itself to be a disturbing and weak point for other applications that make use of highly reliable repeatable operations. Thus, the need to consider the intrinsic device variability within simulations via compact models is highly significant. Based on the variability model for ECM devices "JART ECM v1 var" from section 4.1.1 and on its implementation within the simulation framework, presented in section 4.2.2, the fits to measurement data, corresponding simulations and simulation studies are performed. This chapter first shows several measurement-based case studies for which a variability-aware fit to measurement data has been achieved succesfully and which have been published in different articles, among them are articles with F. Maudet, O. Toprak, C. Dubourdieu, J. Lee, L. Völkel and M. C. Lemme and others [34, 49, 50, 78]. An additional emphasis besides the method of variability-aware fitting is given to the modeling of 2D material-based ECM devices [49, 50, 78]. Then, simulation studies regarding the model parameters' effect on characteristic static and dynamic characteristics, as introduced in section 2.1.1, are performed and their result is presented. Based on these insights, also a fitting procedure guide to experimental data is given. These simulation studies and the fitting procedure guide have been published as well [34].

5.1 Fit to a Cu/SiO_2/W ECM Device

One of the devices investigated is a SiO_2 dielectric sandwiched between an active Cu top electrode and an inert W bottom electrode. A schematic of the stack and a cross-sectional transmission electron micrograph of the ECM device are shown in Figure 5.1. The fit has been achieved by simulations performed using the JART ECM v1 var model.

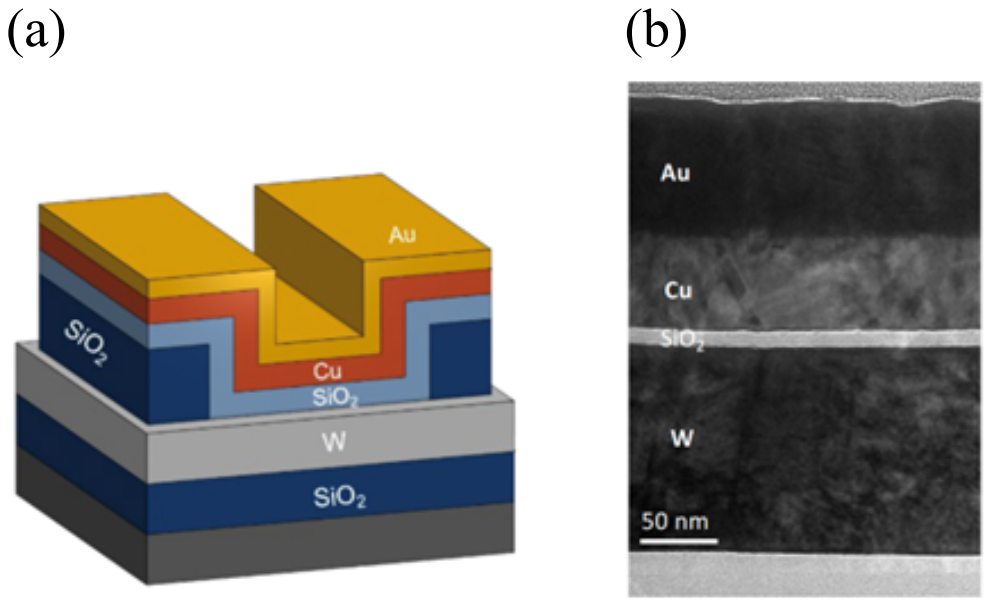

Figure 5.1: (a) presents a schematic representation of the device stack structure. The functional stack comprises 65 nm Cu / 10 nm SiO_2 / 135 nm W. For electrical characterization, the voltage is applied to the top electrode. (b) shows the cross-sectional transmission electron microscopy image of the complete stack. Adapted under the terms of CC-BY 4.0 license [34].

The values of the deterministic and variability-aware model parameters are given in Table 5.1 and in Table 5.2, respectively.

Measurement overview Electrical characterization has been carried out on a probe station using a semiconductor parameter analyzer and a fast waveform/measurement unit. This characterization has been performed by F. Maudet, O. Toprak and C. Dubourdieu [34]. For quasi-static I–V sweeps, a staircase ramp has been applied with the step pair $(\Delta V_{\text{step}}, \Delta t_{\text{step}}) = (5\ \text{mV},\ 0.2\ \text{s})$, sweep rate $0.025\ \text{V}\,\text{s}^{-1}$, and a current compliance of 100 µA. To obtain SET kinetics, the current transient under constant-voltage pulses has been recorded over a wide time window ($\sim 10^{-5}$–10^{2} s); the SET time t_{SET} is defined as the difference between the moment when the current reaches 99% of its final (highest) value and the moment when the applied pulse starts. This value needs to be hold for at least four recorded data points to count as successful switching event. Pulses with amplitude $V_p \in [0.3, 4.8]$ V have been tested, and measurements have been repeated over multiple cycles and devices to capture device-to-device and cycle-to-cycle variability.

Table 5.1: Deterministic mean model parameters for measurement fit.

Symbol	Value	Symbol	Value
M_{me}	$1.06 \cdot 10^{-22}$ g	r_{ac}	3.5 nm
z	2	r_{fil}	1 nm
$\rho_{\mathrm{m,me}}$	8.96 g cm^{-3}	r_{is}	2 nm
m_{r}	0.86	L	10 nm
ΔW_0	3.6 eV	ρ_{fil}	$1.68 \cdot 10^{-8}$ Ωm
α_{et}	0.95	R_{el}	> 1 Ω
$k_{0,\mathrm{et}}$	$1 \cdot 10^{4}$ m s^{-1}	R_{S}	1 mΩ
c	$3 \cdot 10^{24}$ m^{-3}	T	298 K
ΔG_{et}	0.6 eV	$t_{0,\mathrm{nuc}}$	$1 \cdot 10^{-6}$ s
a	0.2 nm	ΔG_{nuc}	0.8 eV
f	$1 \cdot 10^{12}$ Hz	N_{c}	3
ΔG_{hop}	0.1 eV	α_{nuc}	0.3
$\beta = V_{\mathrm{max}}/t_{\mathrm{rise}}$	0.025 V s^{-1}	ΔV_{step}	5 mV
		Δt_{step}	0.2 s
		δ	0.005 nm

Experimental trends in t_{SET} The scatter of t_{SET} against V_{p} spans several orders of magnitude (cf. Fig. 5.2), in line with earlier reports on ECM/VCM-type cells [23, 47, 68, 95]. In individual traces, the SET event appears as an abrupt jump in current (e. g. up to 100 µA) following a plateau due to the current compliance; example data for four devices at $V_{\mathrm{p}} = 0.9$ V illustrate the spread. The data is collected using both slow and fast setups (up to $V_{\mathrm{p}} = 2$ V for the slow mode; $\approx$ 0.9–4.8 V for the fast mode). Fewer data points are recorded by the fast measurement setup. No SET event is observed for $V_{\mathrm{p}} < 0.3$ V, and thus no points exist in that range.

Variability-aware fitting of SET kinetics For model calibration in the $\log t_{\mathrm{SET}}$–V_{p} plane, truncated Gaussian distributions with parameter-specific widths/standard deviations are adopted; the corresponding variability-aware simulations employ the parameter ranges summarized in Table 5.2. Hence, $n = 12$ devices for $V_{\mathrm{p}} = 0.3$ - 2.0 V and $n = 2$ devices for $V_{\mathrm{p}} = 2.1$ - 4.8 V in 0.1 V increments are simulated. For each device and voltage, t_{SET} is extracted and plotted versus V_{p}. With mean parameter values (black reference line), the simulated SET kinetics follows the experimental result (cf. Figure 5.3).

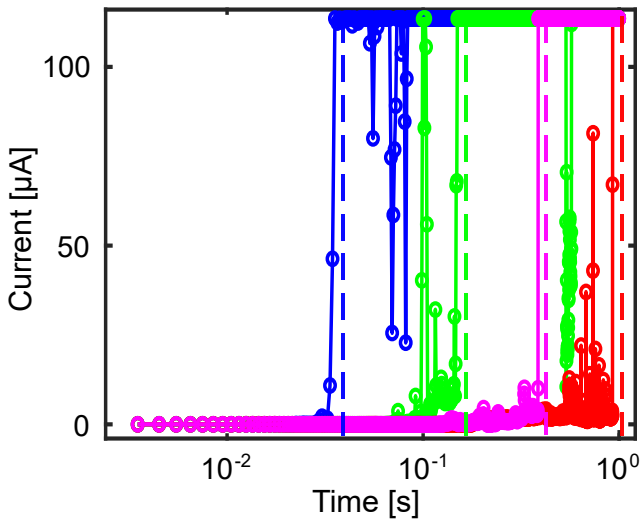

Figure 5.2: Transient current responses highlighting the SET delay times of four representative devices subjected to a constant voltage pulse of 0.9 V. The dashed vertical lines indicate the extracted SET times for each device, revealing substantial variability that spans nearly two orders of magnitude, thereby underscoring the pronounced stochastic nature of the switching process. Adapted under the terms of CC-BY 4.0 license [34].

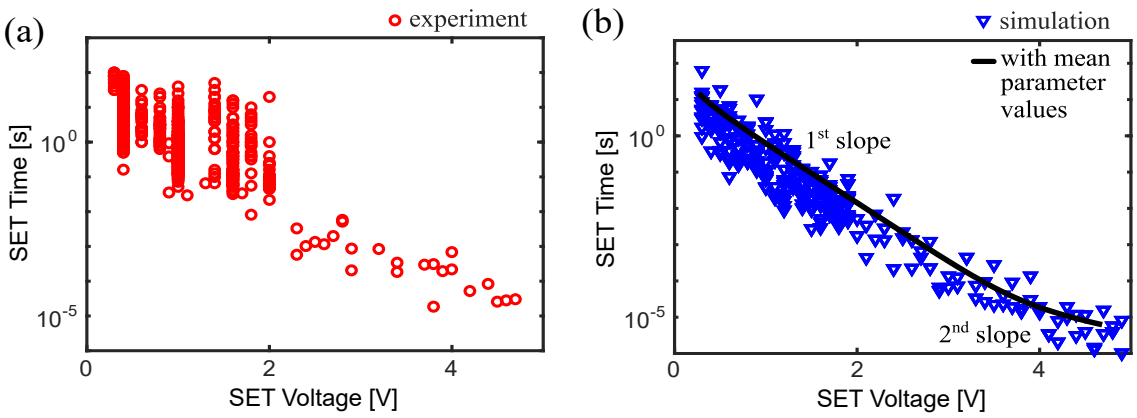

Figure 5.3: (a) Experimentally obtained and (b) simulation-verified device-to-device variability in the analysis of SET kinetics. The simulations further include the averaged SET kinetics curve, derived from mean parameter values (shown in black). This curve exhibits two distinct regimes: an initial, steeper slope extending from approximately 0.3 to 3.5 V, which is attributed to electron transfer-limited switching, followed by a more gradual slope in the range of 3.5 to 4.8 V, corresponding to a mixed control regime. Adapted under the terms of CC-BY 4.0 license [34].

Table 5.2: Variability model parameters for measurement fit (Gaussian distribution relevant for device-to-device variability + random walk relevant for cycle-to-cycle variability + truncation of Gaussian distribution relevant for both).

Symbol	σ Std. dev. of Gaussian distr.	Truncation of Gaussian distr. ($\xi_{\mathrm{d2d,low}}$ | $\xi_{\mathrm{d2d,up}}$)	$\Delta\xi_{\mathrm{max,all}}$ eqs. (4.1) - (4.2)	$\Delta\xi_{\mathrm{max}}$ eq. (4.3)
r_{ac}	3.5 nm	(2.5 | 5) nm	0.4	0.9
r_{is}	1 nm	(1.5 | 2.5) nm	0.25	0.9
r_{fil}	0.5 nm	(0.5 | 1.5) nm	0.1	0.2
c	$3 \cdot 10^{24}$ m^{-3}	$(2 \mid 6) \cdot 10^{24}$ m^{-3}	0.5	0.9
α_{et}	0	0.92 | 0.98	0.0316	0.1
$k_{0,\mathrm{et}}$	$1 \cdot 10^{4}$ m s^{-1}	$(0.4 \mid 3) \cdot 10^{4}$ m s^{-1}	0.3	0.9
$t_{0,\mathrm{nuc}}$	$1 \cdot 10^{-6}$ s	$(0.5 \mid 1.5) \cdot 10^{-6}$ s	0.05	0.1
L	5 nm	(9.95 | 10.05) nm	0	0

Interpretation of SET kinetics regimes Following prior analyses related to ECM devices' SET kinetics [23, 47, 68], two voltage ranges can be distinguished by their slopes in the $\log t_{\mathrm{SET}}$ - V_{p} map (cf. Figure 5.3(b)). At low voltages, a nucleation-limited regime would produce an even steeper slope; this regime does not manifest here, indicating that the observed t_{SET} and the resulting fit is largely insensitive to nucleation-related parameters, presented in equation (3.1). In contrast, the behavior in the intermediate- and high-voltage regime is governed by electron transfer and ion migration processes. Hence, parameters entering the electron transfer current (equations (3.2) and (3.3)) and the ion migration current (equation (3.4)) are fitted to the SET kinetics data, while device-to-device spread is introduced as described in section 4.1.1. The variability settings resulting from the truncated Gaussian distributions (Table 5.2; σ, $\xi_{\mathrm{d2d,up}}$, $\xi_{\mathrm{d2d,low}}$) are used in the simulations.

Emulation of Measurement Conditions Two special simulation modifications have been applied to get a better emulation of measurement conditions: As in measurements, the voltage input, especially in the case of raising or falling I-V sweeps, is given by discrete voltage steps, the emulation of it enables a more realistic result. This can also be applied to fits to other measurements apart from I-V sweeps. The same is valid for emulating the measurement restriction of current averaging, also enabling to reproduce

a more accurate version of a measurement outcome. Both adjustment are presented in the following:

(a) Staircase sweep The first modification prescribes an exact reproduction of the voltage stimulus. To achieve this, both the temporal length of each step and the corresponding voltage increment are encoded in the simulation so that the discrete step size of the experimental setup is faithfully mirrored. During each step, the applied voltage is held at a plateau - rather than ramped - for the full step duration. It then undergoes a short, discrete transition to the next voltage level at the step boundary. The staircase sweep is thus parameterized by the pair (ΔV_{step}, Δt_{step}), e. g., as given in Table 5.1.

(b) Current averaging A further refinement incorporates the current-averaging practice used in experiments. For every interval in which the voltage remains constant, the current is integrated over that period and subsequently normalized by the step duration Δt_{step}. Consequently, each plateau of the staircase sweep yields exactly one averaged data pair (V, I).

Variability-aware I-V fitting The I-V fit starts by embedding the experimental sweep conditions: the sweep rate β and the staircase pair $(\Delta V_{\text{step}}, \Delta t_{\text{step}})$ (Table 5.1) are included to remain consistent with the deterministic SET kinetics fit. Parameter values from Table 5.1 fixed by the identification of the two limiting regimes in the $\log t_{\text{SET}}$ - V_{p} plane are retained and used as well for the I-V sweep simulations. A cycle-to-cycle variability description for I-V sweeps is incorporated using a random walk for selected variability parameter values; the random walk parameter values $\Delta\xi_{\text{max,all}}$ and $\Delta\xi_{\text{max}}$ are given in Table 5.2. With all four modifications activated (staircase sweep, current averaging, per-step variability parameter variation, and ODE's stochasticity), the simulated I-V curves reproduce the experimental traces, including cycle-to-cycle variability (cf. Figures 5.4 (a),(b)), and overall agreement between experiment and simulation is achieved. To highlight the role of variability, the ion concentration mean value and variability bounds given in Tables 5.1 and 5.2 are adopted. A slightly wider truncation is chosen: $c = 4 \cdot 10^{24}$ m^{-3} with distinct lower/upper cutoffs ($c_{\text{d2d,low}} = 0.1 \cdot 10^{24}$ m^{-3}, $c_{\text{d2d,up}} = 100 \cdot 10^{24}$ m^{-3}). Since the overall random walk spread is still controlled by $\Delta c_{\text{max,all}} = 0.5$ (as in Table 5.2), values between $c = 2 \cdot 10^{24}$ m^{-3} and $c = 6 \cdot 10^{24}$ m^{-3} can be governed. This setting is used to get the combined effect of the four modifications on the I-V variability, as shown in Figure 5.4 (b).

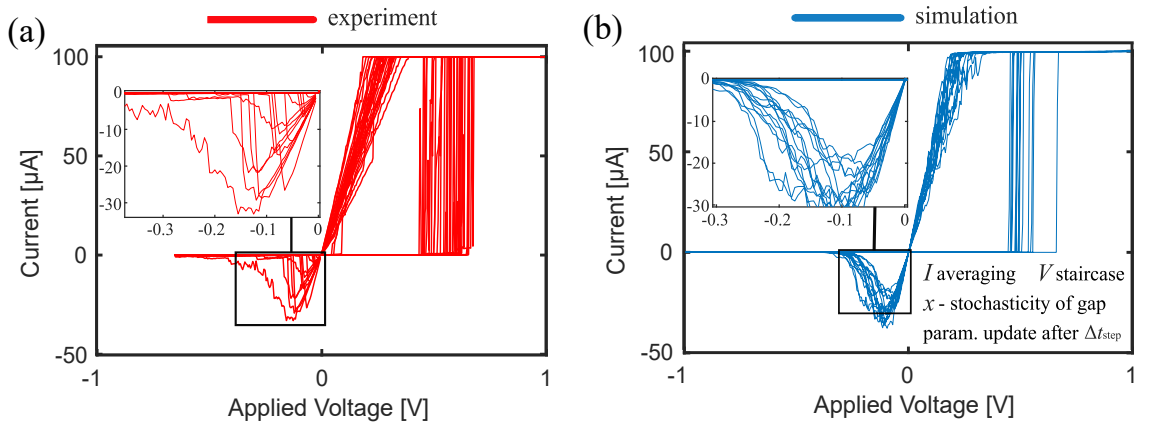

Figure 5.4: Experimentally measured current–voltage (I–V) sweeps, depicted in red, are compared with the corresponding simulated sweeps, shown in blue, both displaying c2c variability. (a) presents representative experimentally recorded I–V characteristics, while (b) displays the simulated I–V responses incorporating all four model modifications. Adapted under the terms of CC-BY 4.0 license [34].

Isolated effects of the four modifications

1. **Staircase voltage stimulus.** Feeding the deterministic fit with a staircase rather than a continuous ramp captures the stepwise nature of the applied signal and yields a more faithful current response. Small abrupt changes at the step edges are reproduced, and parameters are only updated after each SET/RESET to enable variability while remaining deterministic within each half cycle; Figure 5.5 (a) illustrates this case.

2. **Current averaging.** Mimicking the experimental averaging (integration over each step and division by Δt_{step}) reproduces the sharp current jumps observed in practice, which originate from the discrete step timing. Allowing parameter updates after each measurement step broadens the non-deterministic description of cycle-to-cycle scatter across time and voltage; the combined impact of staircase input, current averaging, and per-step variation is shown in Figure 5.5 (b).

3. **Per-step parameter variation.** Tying parameter changes to the voltage staircase step significantly improves the fit within a single sweep. The effect becomes stronger for smaller β or longer Δt_{step}, as more variation can arise during slow sweeps. It can also produce more rising or falling current sections in the simulated current -especially during RESET - in line with experiment; an example isolating only this modification (triangular analogue sweep, no current averaging) is given in Figure 5.5 (c).

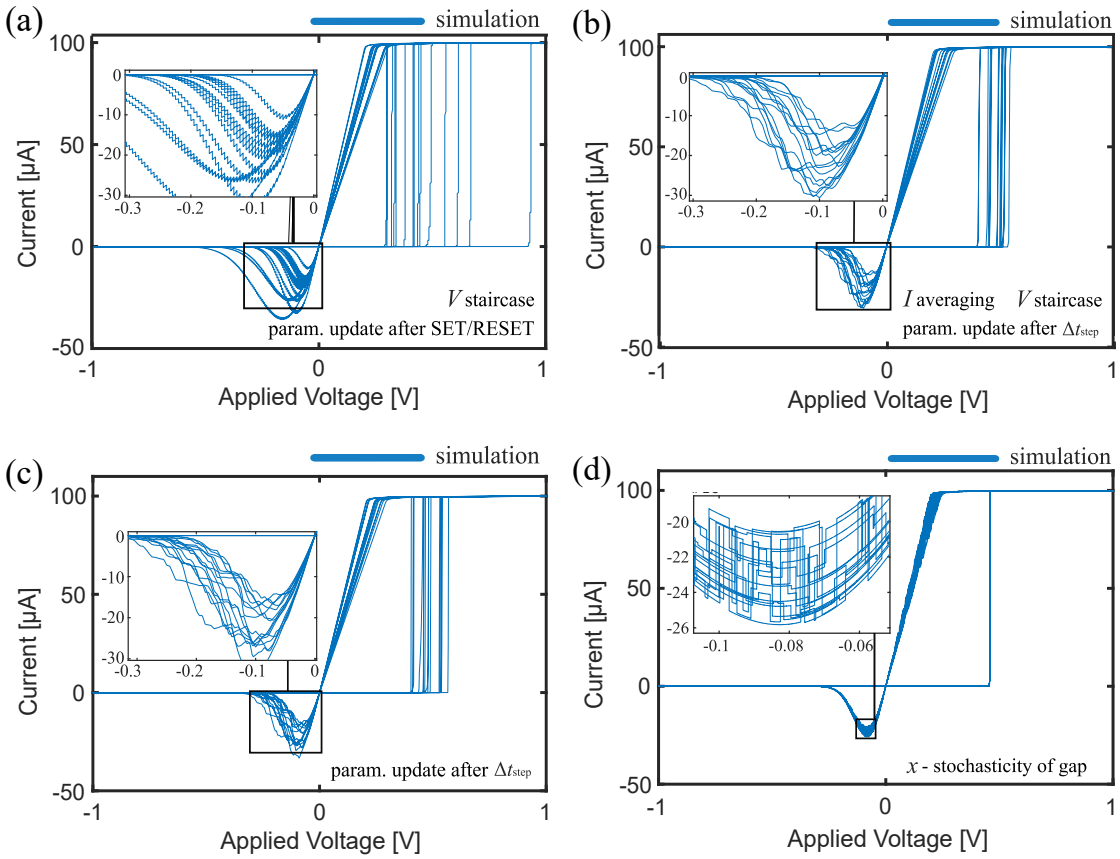

Figure 5.5: Simulated current–voltage (I–V) sweeps illustrating the impact of the four individual model modifications. (a) depicts the case where only a staircase I–V sweep is applied, combined with parameter variation after each SET and RESET event. (b) shows the scenario with a staircase I–V sweep in which current values are averaged over each step, and parameter variations are introduced after every voltage staircase increment. (c) presents the condition where parameter variations occur exclusively after each staircase step, while both the voltage sweep and the current remain continuous. Finally, (d) highlights the effect of incorporating stochastic fluctuations in the gap evolution within the ordinary differential equation (ODE) framework. Together, these results disentangle the contribution of each modification to the overall I–V characteristics. Adapted under the terms of CC-BY 4.0 license [34].

4. **Stochastic ODE term.** Introducing stochasticity in the dynamics of the state variable gap x can trigger abrupt transitions between noisy resistance states. This adds randomness to the switching process by making the instantaneous gap value more stochastic; Figure 5.5 (d) shows the effect when applied alone.

Summary With the above extensions, both device-to-device and cycle-to-cycle variability are embedded in the prior deterministic ECM model framework. Using a single parameter set with variability bounds, the simulations reproduce the measured SET kinetics and the *I-V* characteristics, including the experimentally observed variability spread.

5.2 Fit to Two-Dimensional Material ECM Devices

2D materials for employment as insulator within ECM devices show benefits regarding reduction of variability [144–146] and control of the filament grwoth site [50] through the exploitation of confined filament growth via the van-der-Waals (vdW) gaps. Two cases are presented in this regard, and the variability-aware model is used to investigate their intrinsic properties. Both cases have been presented in corresponding works [49, 77]. The fits presented here assume an effective ionic mobility; however, it remains unclear whether ion migration perpendicular to the 2D layers can occur and, if so, whether it is facilitated by structural defects or interfacial effects.

5.2.1 Modeling of reduced Variability in a Ag/SiO_x/$VAMoS_2$/Au Device

The focus of this study lies in investigating the differences regarding variability between a 2D material Ag/SiO_x/$VAMoS_2$/Au device and a 2D material-free Ag/SiO_x/Au device [77]. Furthermore, beneficial features of the 2D material implementation are derived and by utilizing the model the distinct behavior is explained.

Experimental Study

Pulsed voltage experiments have been employed by J. Lee, M. C. Lemme and others to study the transient switching dynamics. The insights and results of this part have been published in [50, 77, 78]. In each experiment, the time-dependent current response is measured under applied voltage pulses. As illustrated in Figure 5.6, the switching time

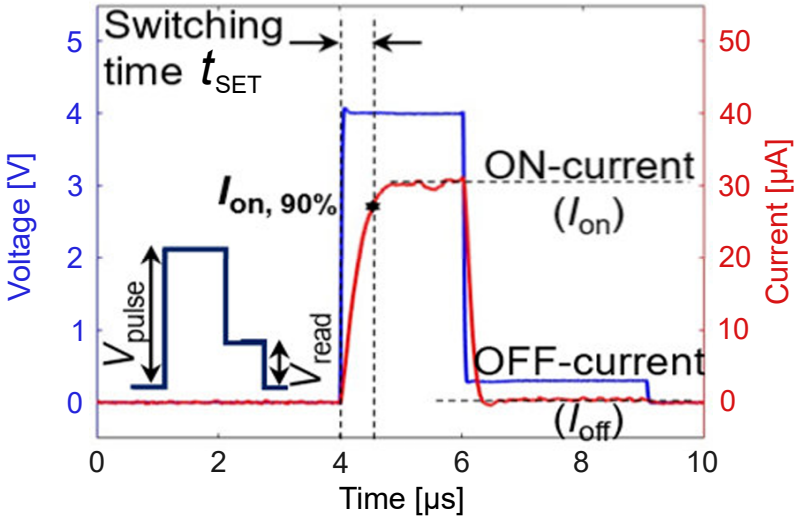

Figure 5.6: The black curve presents the applied rectangular voltage pulse to the $SiO_x/VAMoS_2$ and SiO_x-only devices, whereas the red curve is the resulting current response. The SET/switching time is determined, when 90% of the maximum current has reached. Reproduced with permission from [77], © 2025 IEEE.

t_{SET} is defined as the duration required for the current to reach 90% of the maximum SET current I_{on} [77]. For every measurement, a voltage pulse is applied that switches the device from the HRS to the LRS within the respective t_{SET}. The SET current I_{on} is evaluated over thirty consecutive cycles using a pulse of $V_{pulse} = 4\,V$ with a duration of $2\,\mu s$ for both device types, $SiO_x/VAMoS_2$ and SiO_x-only (Figures 5.7 (a) and 5.7 (b)). The heterostructure device reveals a distinctly lower c2c variation in I_{on} (3.0%) compared to the SiO_x-only device (46.5%). The t_{SET} values have been analyzed with Gaussian distributions, resulting in mean values (μ) and standard deviations (σ) of 620 ns and 160 ns for the $SiO_x/VAMoS_2$ device, and 940 ns and 450 ns for the SiO_x-only device, respectively. The broader distribution in the SiO_x-only device thus indicates a significantly higher variability.

This finding suggests that the vertically aligned vdW gaps in the $VAMoS_2$ layers act to confine filament growth, thereby enabling controlled filament formation and rupture, improved switching speed, and reduced variability. Subsequently, the analysis of switching variability and filament formation mechanisms is extended by correlating the experimental observations with the physics-based JART ECM variability model [34, 100], comparing devices with and without the $VAMoS_2$ layer.

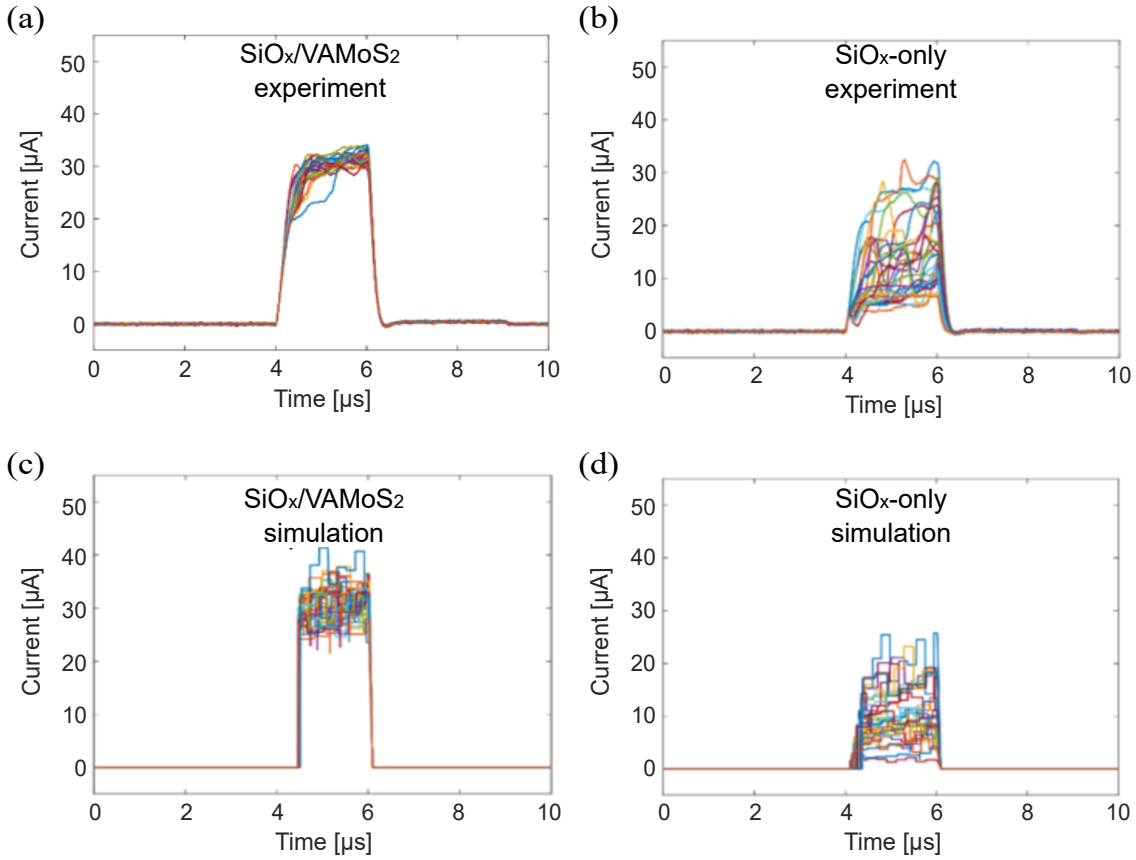

Figure 5.7: Measured and simulated current reponses: (a) and (b) present the measured current response for the SiO_x/$VAMoS_2$ and SiO_x-only devices for 30 cycles, respectively. These measurements are reproduced by simulations in (c) and (d), resepctively. Adapted under the terms of CC-BY 4.0 license [78].

Variability-Aware Filament Growth Modeling

Figure 5.8 depicts the filament growth in SiO_x/$VAMoS_2$ and SiO_x-only devices, leading to the LRS. In both cases, applying a positive bias to the Ag top electrode triggers Ag oxidation, producing ions that drift toward the Au bottom electrode. At the bottom electrode, these ions are reduced, generating a metallic nucleation seed at the interface between switching medium and bottom electrode [22, 34]. This seed initiates filament growth upward from the bottom electrode toward the top electrode, thereby switching the device from HRS to LRS [34].

In the SiO_x/$VAMoS_2$ device, the vdW gaps within the $VAMoS_2$ layers serve as ion-conducting channels that confine Ag filament grwoth after ions have migrated through them [147, 148]. This confinement starts with nucleation of ultra-thin seeds at the bottom electrode, which then extend as filaments along the vdW gaps. Thus, the $VAMoS_2$

layer directs and constrains filament growth. At the $SiO_x/VAMoS_2$ interface, these pre-confined filaments provide favorable initiation sites for further growth into the overlying SiO_x layer, enabling the formation of thicker filaments. By contrast, in the SiO_x-only device, such guided pathways are absent. Here, thin filaments nucleate randomly at the Au bottom electrode without confinement. In both device types, however, the filaments remain sufficiently thin to rupture spontaneously, enabling TS.

Figures 5.7 (a) and 5.7 (b) present the transient current responses of the $SiO_x/VAMoS_2$ and SiO_x-only devices, respectively, under $V_{\text{pulse}} = 4\,\text{V}$ with a duration of 2 µs, repeated for 30 cycles. The experimental results confirm that the $SiO_x/VAMoS_2$ heterostructure switches faster and with better repeatability than the SiO_x-only device. The variability-aware ECM model from Chapter 4 [34] is used to fit the experimental data for both device types, incorporating the c2c variability description, as illustrated in Figures 5.7 (c) and 5.7 (d).

For modeling the device's c2c variability, two distinct approaches from section 4.1.1 are incorporated into the simulation framework [34, 100], each outlined separately below: (i) a simplified version of the c2c variability model, and (ii) the stochastic simulation scheme of the state variable gap, according to equations (4.6) and (4.7).

The c2c variability is mapped onto the filament radius parameter r_{fil}, which varies from cycle to cycle. In the simplified model [34], this parameter is described by a truncated Gaussian distribution with standard deviation $r_{\text{fil},\sigma}$ centered around a predefined mean r_{fil}. Unlike a conventional Gaussian that allows extreme values, the truncated version imposes physical boundaries $r_{\text{fil,trunc,up}}$ and $r_{\text{fil,trunc,low}}$ to ensure realistic ranges. For each switching cycle, a value $r_{\text{fil},i}$ is drawn from this distribution. In SPICE-level simulations, 30 such values are pre-generated in MATLAB and stored in a text file, which is subsequently imported into the Verilog-A compact model via Spectre. Each simulation cycle thus uses a unique, predefined r_{fil} value.

Noise is directly incorporated at each simulation step to reflect stochastic contributions in the gap x as state variable [34]. While the deterministic update follows Faraday's law (Chapter 3, equation (3.5)), an additional stochastic term is introduced immediately after each time-step solution. The update interval is randomly selected at each step, which modifies the tunneling distance length, following equation (4.6). According to equation (4.7), the process of stochastically adding or removing a single Ag atom ($d_{\text{Ag}} = 0.344$ nm, $r_{\text{Ag}} = 0.172$ nm) yields with $r_{\text{fil}} = 1.22$ nm for the $VAMoS_2/SiO_x$ device and $r_{\text{fil}} = 0.8$ nm for the SiO_x-only device a δ-value of $\delta = 0.0068$ nm or 0.0159 nm, respectively.

The corresponding fitting parameters are listed in Table 5.3. The model reproduces the experimental data with high fidelity, successfully capturing the shorter switching time and narrower t_{SET} distribution observed in the $SiO_x/VAMoS_2$ device.

Symbol	Value	Symbol	$SiO_x/VAMoS_2$	SiO_x-only
M_{me}	$1.7912 \cdot 10^{-25}$ kg	r_{ac}	10 nm	10 nm
z	1	r_{fil}	1.22 nm	0.8 nm
$\rho_{m,\mathrm{me}}$	$10.49 \cdot 10^{3}$ kg m^{-3}	r_{is}	2.4 nm	2.0 nm
m_{r}	0.86	L	30 nm/10 nm	10 nm/10 nm
ΔW_0	3.6 eV	ρ_{fil}	$1.59 \cdot 10^{-8}$ Ω m	$1.59 \cdot 10^{-8}$ Ω m
α_{et}	0.1	R_{el}	40 Ω	40 Ω
$k_{0,\mathrm{et}}$	$3 \cdot 10^{5}$ m s^{-1}	R_{S}	40 Ω	40 Ω
c	$2 \cdot 10^{26}$ m^{-3}	T	298 K	298 K
ΔG_{et}	0.55 eV	$t_{0,\mathrm{nuc}}$	$2 \cdot 10^{-10}$ s	$2 \cdot 10^{-10}$ s
a	0.2 nm	ΔG_{nuc}	0.8 eV	0.8 eV
f	$1 \cdot 10^{13}$ Hz	N_{c}	3	3
ΔG_{hop}	0.2 eV	α_{nuc}	0.5	0.5
p_{jump}	$0 < p_{\mathrm{jump}} < 1$	Δt_{step}	24.44 ps	24.44 ps
r_{Ag}	0.172 nm	δ	0.0068 nm	0.0159 nm
d_{Ag}	0.344 nm	$r_{\mathrm{fil},\sigma}$	0.24 nm	0.24 nm
		$r_{\mathrm{fil,trunc,low}}$	1.17 nm	0.172 nm
		$r_{\mathrm{fil,trunc,up}}$	1.27 nm	0.85 nm

Table 5.3: Model parameters and values.

The simulations demonstrate that the variability originates from both the filament radius (r_{fil}) and the stochastic gap distance (x) between the filament tip and the top electrode. In the heterostructure device, the interlayer spacing of the $VAMoS_2$ layers leads to the formation of ultra-thin filaments that are estimated to extend over only one to two vdW gaps within this specific layer. The gap spacing of approximately 6.5 Å [147, 149] is larger than the atomic diameter of Ag (3.44 Å) [150], enabling confined growth. As the filament within the $VAMoS_2$ region is constrained, it primarily grows vertically along the vdW channels [147, 148]. Following nucleation, lateral expansion is suppressed, and the filament diameter remains confined to the nucleus size at the $VAMoS_2$/Au interface. These ultra-thin nuclei ($r_{\mathrm{fil},1,\mathrm{VAMoS_2}}$) subsequently extend into the SiO_x layer, where they seed the development of thicker filaments $(r_{\mathrm{fil},1,\mathrm{SiO_x}}) > (r_{\mathrm{fil},1,\mathrm{VAMoS_2}})$. In contrast, in SiO_x-only devices, filaments nucleate randomly at the Au/SiO_x interface with radii that are

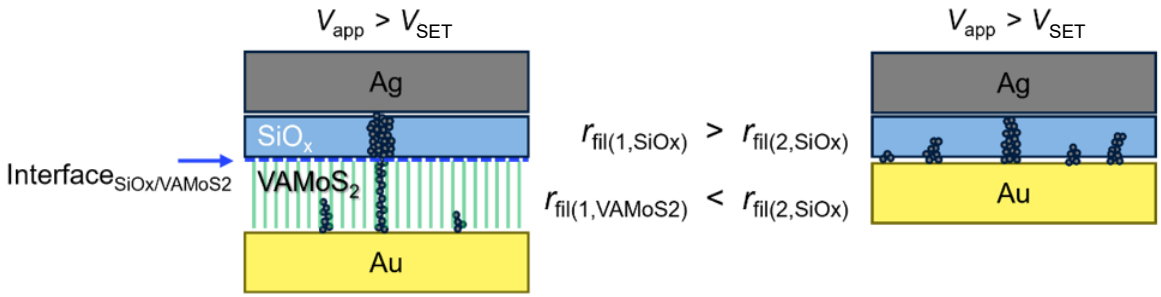

Figure 5.8: Proposed filament growth within the SiO_x/$VAMoS_2$ and SiO_x-only device. The $VAMoS_2$ layer promotes very thin filaments with a radius $r_{\mathrm{fil,1,VAMoS2}}$. As soon as it reaches the SiO_x layer, the filament radius increases to $r_{\mathrm{fil,1,SiOx}}$. The filaments in the SiO_x-only device have a radius of $r_{\mathrm{fil,2,SiOx}}$. The following relation is valid: $r_{\mathrm{fil,1,SiO_x}} > r_{\mathrm{fil,2,SiO_x}} > r_{\mathrm{fil,1,VAMoS_2}}$. Adapted under the terms of CC-BY 4.0 license [78].

larger than those formed in the $VAMoS_2$ region but smaller than those within the SiO_x part of the heterostructure device $(r_{\mathrm{fil,1,SiO_x}}) > (r_{\mathrm{fil,2,SiO_x}}) > (r_{\mathrm{fil,1,VAMoS_2}})$, see Figure 5.8. Hence, in SiO_x-only devices the subsequent filament diameter is not constrained by the nucleus size at the Au/SiO_x interface and instead adopts larger values.

The pre-defined nuclei at the SiO_x/$VAMoS_2$ interface therefore play a decisive role in initiating thicker and more reproducible filament growth within the SiO_x layer of the heterostructure compared to the SiO_x-only device. The c2c variability model further indicates that the filament radius is strongly correlated with the stochastic parameter δ, which describes random variations in the distance x between the filament tip and the top electrode. Larger filaments correspond to lower variability and smaller δ, since the addition or removal of individual atoms does not significantly affect filament geometry or the resulting current. By contrast, narrow filaments display higher variability and larger δ, because single-atom modifications strongly impact geometry and current conduction. This stochasticity gives rise to discrete current jumps: when only a few atoms are added or removed at the filament tip, the tunneling distance x changes abruptly, producing sharp variations in current response.

The switching performance is therefore attributed to the $VAMoS_2$ layer, which guides the growth of thin filaments and localizes their rupture at the structurally weakest point of the filament, namely the SiO_x/$VAMoS_2$ interface. At this location the filament can be broken easily, enabling repeatable switching. These findings are consistent with earlier studies demonstrating that restricted Ag ion transport through defects in graphene reduces switching time variability [146]. As a result, the SiO_x/$VAMoS_2$ heterostructure device exhibits substantially more stable and faster switching behavior than the SiO_x-only device.

5.2.2 Modeling the Influence of Moisture in a Ni/h-BN/Pd Device

The measurement data in this section originates from experiments conducted by L. Völkel, M. C. Lemme and others. The insights and results of this part have been published in [49]. The variability-aware ECM model and its implications, also presented later in section 5.3, can be exploited in order to model and explain various electrical and dynamical phenomena within ECM devices. For this sake, model parameter values can be varied, and their outcome can be studied in terms of physical explanation. This is in alignment with simulation studies of the variability-aware model. For instance, first the impact of the ion concentration within the insulator on the overall dynamical behavior needs to be evaluated in order to consider it as variability parameter. This evaluation is utilized in the following to model the influence of moisture on the switching behavior of a 2D material ECM device based on a Ni/h-BN/Pd stack. In [56, 57], it has been shown that the amount of moisture influences the ion concentration within the insulator siginificantly. The ion concentration itself determines the dynamic switching behavior. In the following, this phenomenon is explained in detail.

Electron transferring redox processes are a fundamental foundation contributing to resistive switching in ECM cells. Light has been shed on this crucial process in section 2.2. It has been explained that every anodic oxidation at the active electrode/insulator interface demands a counteracting cathodic reduction process at the insulator/inert electrode interface. However, when no metal ions are present in the insulator - as is the case for a pristine device or in a device after a strong RESET [57] - charge neutrality is preserved through water splitting reduction reactions at the insulator/inert electrode interface while metal atoms are oxidizing to ions at the active electrode/insulator interface. Two water splitting reactions have been introduced: While water participates in both, oxygen is only needed for one of them [43, 56]. Thus, the dominating reaction depends on both individual reaction rates. Hence, given appropriate reaction rate constants, moisture is sufficient to initiate resistive switching, whereas additional oxygen can further enhance this effect.

Whenever the moisture concentration/humidity is high, the active metal ion's concentration is accordingly high, as both species are required for the redox reactions at the corresponding electrodes ensuring charge neutrality. In vacuum, however, moisture is less present, thus, the active metal ion's concentration is also low, here the Ni ion concentration. From the upcoming model parameter study in section 5.3 it is concluded that a lower ion concentration c leads to significantly larger switching times in the second (electron transfer-limited) and third (mixed control-limited) regime of the SET

kinetics. The measured SET kinetics data is fitted utilizing the JART ECM model with parameters presented in Table 5.4, i. e., $c = 1 \cdot 10^{24}\mathrm{m}^{-3}$. This fit is illustrated in Figure 5.9 by the orange line. The green line with $c = 1 \cdot 10^{-21}\mathrm{m}^{-3}$ is exemplarily added to demonstrate a SET kinetics that has a lower ion concentration due to a vacuum condition. It qualitatively shows that a decreased ion concentration leads to distinctly slower switching times, eventually to no switching at all. Thus, a suppression of forming in vacuum conditions as shown for experimental data in Figure 5.9 in comparison with ambient conditions is explained by the evaluation of this variability-aware ECM model. In ambient conditions, the relatively high moisture and metal ion concentration c contributes to successful filament formation and switching, whereas in vacuum conditions both concentrations are low.

Symbol	**Value**	**Symbol**	**Value**
M_{me}	$9.75 \cdot 10^{-26}$ kg	r_{ac}	10 nm
z	2	r_{fil}	1 nm
$\rho_{m,\mathrm{me}}$	$8.91 \cdot 10^{3}$ kg m^{-3}	r_{is}	10 nm
m_{r}	2.21	L	3 nm
ΔW_0	3.71eV	ρ_{fil}	$6.85 \cdot 10^{-8}$ Ω m
α_{et}	0.07	R_{el}	40 Ω
$k_{0,\mathrm{et}}$	$1 \cdot 10^{3}$ m s^{-1}	R_{S}	120 Ω
c	$1 \cdot 10^{24}$ m^{-3}	T	298 K
ΔG_{et}	0.65 eV	$t_{0,\mathrm{nuc}}$	$6 \cdot 10^{-10}$ s
a	0.17 nm	ΔG_{nuc}	0.8 eV
f	$1 \cdot 10^{13}$ Hz	N_{c}	3
ΔG_{hop}	0.22 eV	α_{nuc}	0.3

Table 5.4: Model parameters and values for the h-BN device model.

This consideration is crucial, as ECM devices are often encapsulated and protected from ambient/atmospheric conditions. Thus, the effects of such encapsulations should not be disregarded.

5.3 Comprehensive Simulation Study regarding Model Parameters

When employing a model, it is crucial to possess a thorough grasp of its physical and dynamical characteristics to achieve a suitable deterministic and/or variability-aware fit.

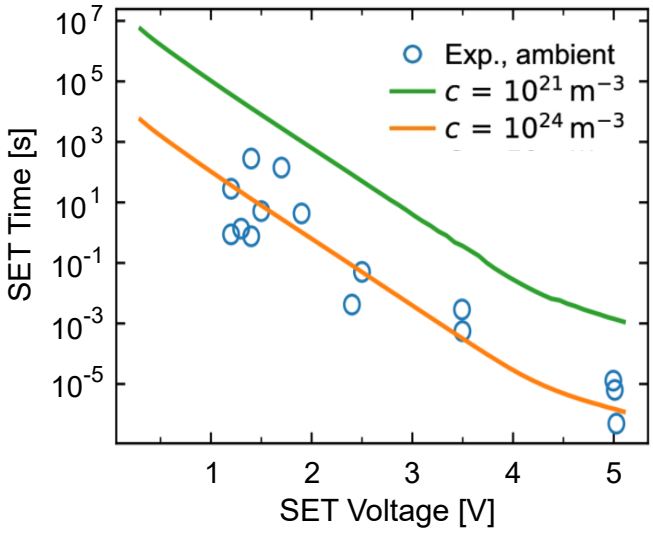

Figure 5.9: The experimental SET kinetics data for ambient conditions (blue circles) is fitted with an ion concentration of $c = 1 \cdot 10^{24}$ m^{-3}. A qualitative analysis of vacuum conditions is given by the choice $c = 1 \cdot 10^{21}$ m^{-3}: As due to missing moisture the ion concentration decreases, the SET process becomes very slow. Adapted under the terms of CC-BY 4.0 license [49].

Understanding how the individual model parameters influence the simulation outcomes, as well as identifying the parameter ranges required to ensure physical validity represent essential insights. Having access to this information facilitates and promotes the fitting process. Moreover, it is demonstrated that a fit lacking physical validity or failing to reproduce the actual physical and dynamical behavior can result in poor predictive power and limited emulation capability. In this context, a parameter study of the JART ECM v1 (var) model focusing on the SET kinetics and the corresponding I-V characteristics is presented. It should be noted that only limited experimental data on RESET kinetics is available in the literature [151, 152], and that this aspect has generally received little attention. A model investigation related to RESET kinetics can be carried out in an analogous manner to the approach taken for the SET kinetics.

5.3.1 SET Kinetics Parameter Study

Consistent with earlier studies [23, 47, 133], it is found that ECM memory cells exhibit three distinct regimes in their SET kinetics, governed by the voltage drop across the device. The model permits three different slopes in the log t_{SET} - V_{p} plane, each corresponding to a separate rate-limiting ionic mechanism. Any of these processes may determine the switching speed depending on the voltage V_{p}: nucleation at small V_{p},

electron transfer at intermediate V_p, and, at large V_p, electron transfer as well as ion hopping. In these mentioned voltage ranges the corresponding mentioned ionic processes are rate-limiting, i. e. they are the slowest one. Hence, the slowest process fixes the SET delay time t_SET through the filament-evolution dynamics described by equation (3.5). This SET event is reached once a conductive filament has formed and a sufficient tunneling current can pass.

Using equations (3.1) - (3.4), the slopes and vertical intercepts of the three regimes in the log t_SET - V_p representation can be written compactly as

$$\log\, t_\mathrm{SET} \;=\; -\, m_\mathrm{ion} \cdot V_\mathrm{p} \;+\; \log\, b_\mathrm{ion}, \tag{5.1}$$

where m_ion denotes the slope and b_ion sets the vertical offset for the corresponding limiting mechanism. In the following, it is examined how the parameters in each of the three regimes shape the SET kinetics. Throughout, the total applied voltage is assumed to drive the active process(es). Currents prior to the abrupt SET transition are too small to produce significant Joule heating; therefore, the temperature T is treated as constant.

The objective of the SET kinetics parameter study is to specify, for each rate-limiting regime, the fastest- and slowest-switching boundary curves in the log t_SET - V_p plane, and to demonstrate that all simulated d2d variability realizations fall between these two extremes. To achieve this, regime-specific parameters are varied within the bounds prescribed by the variability model of the respective regime. Consequently, the influence of the ionic rate-limiting parameters on the SET kinetics is the central feature under investigation.

All simulations regarding the SET kinetics reported here employ the mean and variability parameter values summarized in Tables 5.5 and 5.6. The plots in Figure 5.10 (nucleation parameter study), Figures 5.11 and 5.12 (electron transfer parameter study), and Figure 5.14 (mixed-regime parameter study) display five curves. The central blue trace represents the deterministic mean fit of the SET kinetics. The two adjacent traces indicate the outer limits set by the standard deviations of the variability parameters listed in Table 5.6 - the slower-switching standard-deviation bound is shown in cyan and the faster-switching bound in red. The two outermost traces on each side correspond to the Gaussian truncation limits of the variability parameters, $\xi_\mathrm{d2d,up}$ and $\xi_\mathrm{d2d,low}$, depicting the extreme edge cases: the slowest attainable switching in green and the fastest in magenta. Figure 5.12 additionally contains a sixth (black) curve, whose role is clarified

later. Blue triangles mark individual d2d variability samples obtained by simulation; they lie within these bounds in the log t_{SET} - V_{p} plane.

Table 5.5: Deterministic mean model parameters for SET kinetics parameter and variability study.

Symbol	Value	Symbol	Value
M_{me}	$1.06 \cdot 10^{-22}\,\mathrm{g}$	r_{ac}	$100\,\mathrm{nm}$
z	2	r_{fil}	$4\,\mathrm{nm}$
$\rho_{\mathrm{m,me}}$	$8.59\,\mathrm{g\,cm^{-3}}$	r_{is}	$4\,\mathrm{nm}$
m_r	0.86	L	$10\,\mathrm{nm}$
ΔW_0	$3.05\,\mathrm{eV}$	ρ_{fil}	$1.7 \cdot 10^{-8}\,\Omega\mathrm{m}$
α_{et}	0.46	R_{el}	$> 1\,\Omega$
$k_{0,\mathrm{et}}$	$1.93 \cdot 10^{5}\,\mathrm{m\,s^{-1}}$	R_{S}	$100\,\mathrm{k}\Omega$
c	$1 \cdot 10^{23}\,\mathrm{m^{-3}}$	T	$298\,\mathrm{K}$
ΔG_{et}	$0.75\,\mathrm{eV}$	$t_{0,\mathrm{nuc}}$	$2 \cdot 10^{-5}\,\mathrm{s}$
a	$0.25\,\mathrm{nm}$	ΔG_{nuc}	$0.8\,\mathrm{eV}$
f	$1 \cdot 10^{12}\,\mathrm{Hz}$	N_{c}	2
ΔG_{hop}	$0.1\,\mathrm{eV}$	α_{nuc}	0.3
$\beta = V_{\mathrm{max}}/t_{\mathrm{rise}}$	$0.025\,\mathrm{V\,s^{-1}}$	V_{step}	$5\,\mathrm{mV}$
δ	$0.005\,\mathrm{nm}$	t_{step}	$0.2\,\mathrm{s}$

Nucleation limitation (SET kinetics)

At low applied voltages, the nucleation process typically represents the slowest process, as it strongly benefits from higher overpotentials. In other words, the nucleation event, which marks the onset of filament formation, requires comparatively long times to establish a stable nucleus. Within this voltage regime, most of the other processes remain inactive until t_{SET} is reached, since, in this model, they only occur once a nucleus has formed [47]. A suitable approximation can therefore be obtained by setting $t_{\mathrm{nuc}} = t_{\mathrm{SET}}$. As a result, t_{nuc}, as introduced in equation (3.1), is much larger than the subsequent filament growth time. By combining equations (3.1) and (5.1), the following expression can be written:

$$m_{\mathrm{nuc}} = \frac{(N_{\mathrm{c}} + \alpha_{\mathrm{nuc}})ze}{k_{\mathrm{B}}T}, \qquad b_{\mathrm{nuc}} = t_{0,\mathrm{nuc}} \exp\left(\frac{\Delta G_{\mathrm{nuc}}}{k_{\mathrm{B}}T}\right). \tag{5.2}$$

Table 5.6: Variability model parameters (Gaussian distribution) for SET kinetics parameter and variability study.

Symbol	σ (Standard deviation of Gaussian distr.)	Truncation of Gaussian distr. ($\xi_{\mathrm{d2d,low}} \mid \xi_{\mathrm{d2d,up}}$)
r_{ac}	$30\,\mathrm{nm}$	$(60 \mid 140)\,\mathrm{nm}$
r_{is}	$1.2\,\mathrm{nm}$	$(2.4 \mid 5.6)\,\mathrm{nm}$
r_{fil}	$1.2\,\mathrm{nm}$	$(2.4 \mid 5.6)\,\mathrm{nm}$
c	$0.3 \cdot 10^{23}\,\mathrm{m}^{-3}$	$(0.6 \mid 1.4) \cdot 10^{23}\,\mathrm{m}^{-3}$
α_{et}	0.069	$0.276 \mid 0.644$
$k_{0,\mathrm{et}}$	$0.579 \cdot 10^{5}\,\mathrm{m\,s}^{-1}$	$(1.158 \mid 2.702) \cdot 10^{5}\,\mathrm{m\,s}^{-1}$
$t_{0,\mathrm{nuc}}$	$1.98 \cdot 10^{-5}\,\mathrm{s}$	$(0.002 \mid 3.998) \cdot 10^{-5}\,\mathrm{s}$
L	$3\,\mathrm{nm}$	$(6 \mid 14)\,\mathrm{nm}$

It should be emphasized that, for the variability study presented in Figure 5.10, only $t_{0,\mathrm{nuc}}$ is considered from Table 5.6. Although a variation of $t_{0,\mathrm{nuc}}$, as a constituent of $b_{0,\mathrm{nuc}}$, would theoretically yield a parallel shift of the curve, the lack of simulation data points in the transition region towards the electron transfer-limited regime results in an artefactual appearance of a slope change. The nucleation process is accelerated if the nucleus seed comprises a higher number of critical atoms N_{c}, which can range from zero to a small integer value. Furthermore, an increase in the electron transfer coefficient α_{nuc} leads to a larger effective contribution, with possible values between zero and one, thereby enhancing the nucleation process. Since both N_{c} and α_{nuc} appear in the exponential function that also contains the overpotential η_{nuc} in equation (3.1), their increase amplifies the relatively steep negative slope of the SET kinetics in the log t_{SET}-V_{p} plane. For instance, raising z from 1 to 2 would double the slope in the nucleation-limited regime.

All other parameters outside the exponential contribution - namely the nucleation time prefactor $t_{0,\mathrm{nuc}}$ and the nucleation activation energy ΔG_{nuc} - influence the SET kinetics only in a parallel shift. The trends are illustrated in Figure 5.10: an increase in the following parameters produces the listed effects (in **bold** the variability parameters, in regular thin font the remaining fitting parameters are displayed):

1. A parallel shift of the curve in the log t_{SET}-V_{p} plane towards slower switching, caused by an increase in $\boldsymbol{t_{0,\mathrm{nuc}}}$ and/or ΔG_{nuc}.

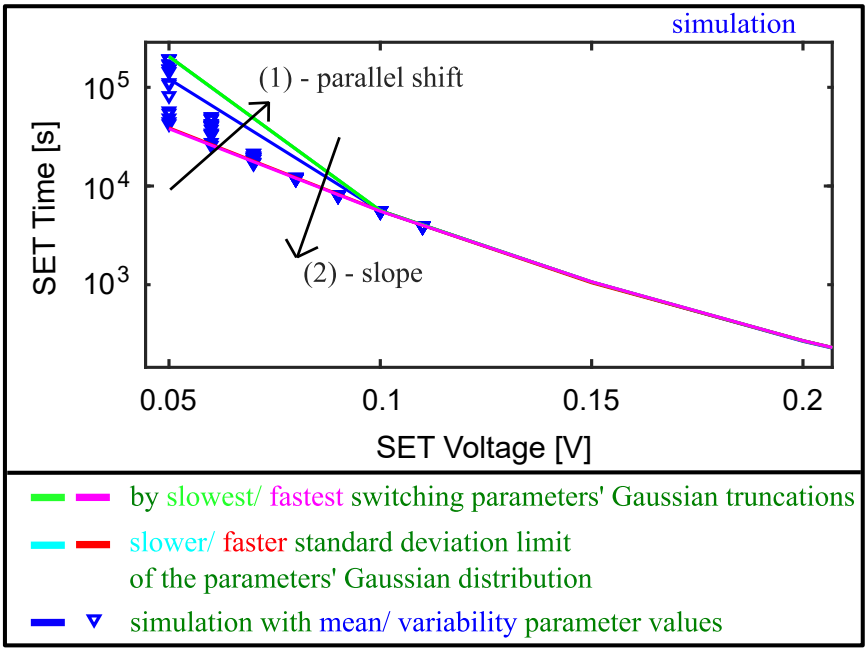

Figure 5.10: Parameter study of the SET kinetics device-to-device variability focusing on the ***nucleation parameters***, carried out by simulations using the parameter sets from Tables 5.5 and 5.6. The figure presents five characteristic curves: the mean deterministic curve at the center (blue), the standard-deviation boundaries on either side of it - a faster switching case (red) and a slower switching case (cyan, barely distinguishable as it coincides with the Gaussian truncation curves) - as well as the Gaussian truncation limits, which define the fastest (magenta) and slowest (green) switching edge cases. In addition, blue triangles depict individual device-to-device variability data points obtained from simulations, thereby illustrating how the stochastic variability is confined within the deterministic bounds. The arrows further indicate the effects of parameter variations, distinguishing between parallel shifts of the curves and changes in slope, both of which are systematically summarized in Table 5.7. Adapted under the terms of CC-BY 4.0 license [34].

2. A change in slope towards steeper switching in the nucleation regime, resulting from an increase in N_c and/or α_{nuc}, as expressed in equation (5.2).

The steepest slopes and the largest parallel shifts of the curves to faster switching define the fastest possible switching edge case.

Electron transfer limitation (SET kinetics)

In the intermediate voltage range, the electron transfer process becomes the dominant rate-limiting step, because the applied voltage is largely partitioned between the overpotentials η_{ac} and η_{fil} until t_{SET} is reached. The transient evolution of these overpotentials prior to the SET event can be visualized as reported in [47]. As the voltage increases, nucleation accelerates to the point that it is much faster than the subsequent filament-

growth stage, and also ion migration proceeds on a timescale shorter than the two electron transfer reactions, namely oxidation at the active electrode/insulator interface and reduction at the insulator/filament interface. For this electron transfer limited regime, two parameter types are identified and investigated: (i) parameters causing a *parallel shift* of the curve in the log t_{SET}-V_{p} plane, and (ii) parameters determining the *slope* in this plane. In addition, we analyze a special case where parameters couple in such a way that both the parallel shift and the slope are set simultaneously, illustrating that the fastest-switching edge case is not always trivial to identify.

Before visualizing electron transfer parameter influences on the SET kinetics, a mathematical expression for the SET time t_{SET} in this regime is derived in the following. The applied voltage is simplified to $V_{\mathrm{cell}} = V_{\mathrm{Tu}} = \eta_{\mathrm{ac}} - \eta_{\mathrm{fil}}$. Considering the current continuity of the two ionic electron transfer currents (cf. equations (3.2) - (3.3)) yields the following simplified analytical expression of equation (3.5) for the SET process [141, 142]

$$\frac{\mathrm{d}x}{\mathrm{d}t} = -\frac{M_{\mathrm{Me}}}{ze\rho_{\mathrm{m,Me}}}\, j_{0,\mathrm{et}} \left(\frac{A_{\mathrm{ac}}}{A_{\mathrm{fil}}}\right)^{\alpha_{\mathrm{et}}} \exp\left[\alpha_{\mathrm{et}}\,(1-\alpha_{\mathrm{et}})\,\frac{ze}{k_{\mathrm{B}}T}\,V_{\mathrm{cell}}(t)\right]. \tag{5.3}$$

Solving this differential equation for t_{SET}, while assuming a constant applied voltage $V_{\mathrm{cell}} = V_{\mathrm{p}}$, leads to the following integral form:

$$\int_{L}^{x_{\mathrm{SET}}} \mathrm{d}x = -\int_{0}^{t_{\mathrm{SET}}} \frac{M_{\mathrm{Me}}}{ze\rho_{\mathrm{m,Me}}}\, j_{0,\mathrm{et}} \left(\frac{A_{\mathrm{ac}}}{A_{\mathrm{fil}}}\right)^{\alpha_{\mathrm{et}}} \exp\left[\alpha_{\mathrm{et}}(1-\alpha_{\mathrm{et}})\frac{ze}{k_{\mathrm{B}}T}\,V_{\mathrm{p}}\right] \mathrm{d}t. \tag{5.4}$$

From this relation, the expression for $\log(t_{\mathrm{SET}})$ is obtained, with the condition $L - x_{\mathrm{SET}} > 0$, where x_{SET} denotes the gap length at which the device undergoes a SET transition:

$$\begin{aligned} \log t_{\mathrm{SET}} &= \log\left(\frac{(L-x_{\mathrm{SET}})\,\rho_{\mathrm{m,Me}}\exp\left(\Delta G_{\mathrm{et}}/\left(k_{\mathrm{B}}T\right)\right)}{M_{\mathrm{Me}}\,c\,k_{0,\mathrm{et}}} \left(\frac{A_{\mathrm{fil}}}{A_{\mathrm{ac}}}\right)^{\alpha_{\mathrm{et}}}\right) \\ &- \alpha_{\mathrm{et}}(1-\alpha_{\mathrm{et}})\frac{ze}{k_{\mathrm{B}}T}\,V_{\mathrm{p}}. \end{aligned} \tag{5.5}$$

Comparing coefficients in equation (5.5) with equation (5.1) yields, for the intermediate (electron transfer limited) regime,

$$m_{\mathrm{et}} = \frac{\alpha_{\mathrm{et}}(1-\alpha_{\mathrm{et}})\,ze}{k_{\mathrm{B}}T}, \tag{5.6}$$

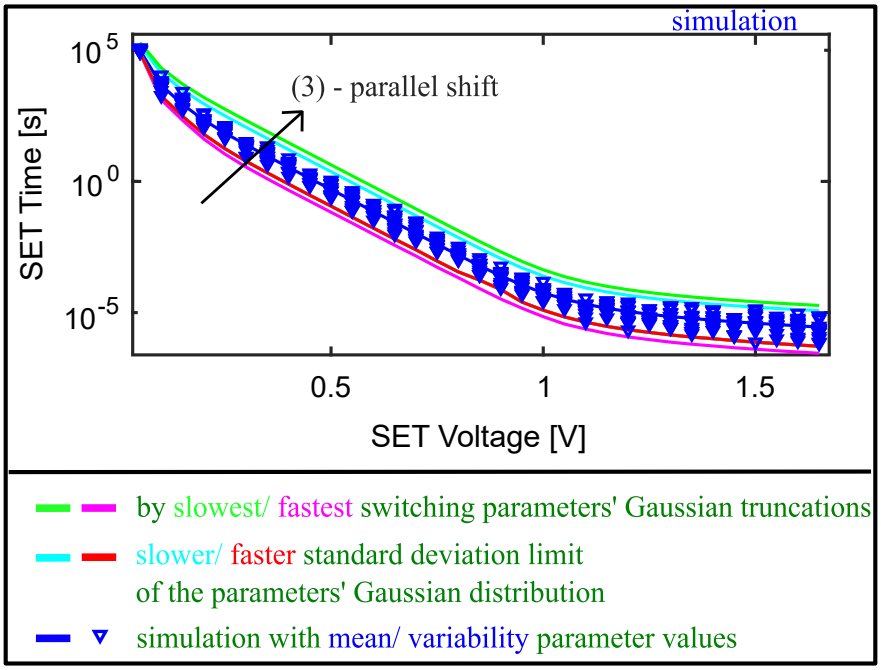

Figure 5.11: Parameter study of the SET kinetics device-to-device variability focusing on the ***parallel-shifting electron transfer parameters***, performed by simulations based on the parameter sets of Tables 5.5 and 5.6. The figure displays five characteristic curves: the mean-value curve in the center (blue), the $\pm 1\sigma$ boundaries on either side (faster switching in red and slower switching in cyan), and the Gaussian truncation limits that define the fastest (magenta) and slowest (green) switching edge cases. The blue triangles represent the results of device-to-device variability simulations, demonstrating the statistical spread of the switching behavior. The arrow highlights the influence of parameter variations on the parallel shift of the SET kinetics, with a summary of this effect provided in Table 5.7. Adapted under the terms of CC-BY 4.0 license [34].

$$b_{\mathrm{et}} \;=\; (L - x_{\mathrm{SET}}) \frac{\rho_{\mathrm{m,Me}} \exp\!\left(\Delta G_{\mathrm{et}} / \left(k_{\mathrm{B}} T\right)\right)}{M_{\mathrm{Me}}\, c\, k_{0,\mathrm{et}}} \left(\frac{A_{\mathrm{fil}}}{A_{\mathrm{ac}}}\right)^{\alpha_{\mathrm{et}}} . \tag{5.7}$$

Analogous to Figure 5.10, Figure 5.11 shows the two extreme (fastest/slowest) switching cases together with the d2d variability simulation data in between. Since the SET kinetics curve is very steep at low voltages in the nucleation-limited regime, the slope visibly flattens in the intermediate voltage range governed by electron transfer.

An increase of the Tafel current density (cf. equations (3.2) - (3.3)) reduces the SET delay time t_{SET} defined by equation (3.5); consequently, the HRS to LRS transition in the electron transfer-limited regime occurs sooner. Consistent with equation (5.7), increasing c or $k_{0,\mathrm{et}}$ shifts the curve *downwards* (towards smaller t_{SET}) in the log t_{SET}-V_{p} plane, whereas increasing ΔG_{et} shifts it *upwards*. If a model enforces $r_{\mathrm{ac}} = r_{\mathrm{fil}}$ and both radii are changed simultaneously to the same value, the curve remains unchanged,

because the ratio $A_{\mathrm{fil}}/A_{\mathrm{ac}}$ stays constant. By contrast, increasing r_{ac} (or A_{ac}) and/or decreasing r_{fil} (or A_{fil}) leads to a parallel shift towards shorter SET delay times. All of these trends directly follow from b_{et} in equation (5.7).

Figure 5.11 summarizes the parameter tendencies via an arrow. Increases of the following parameter-based expressions move the curve *upwards* (slower switching) in the electron transfer regime (in **bold** the variability parameters, in regular thin font the remaining fitting parameters are displayed):

$$\frac{1}{z}, \quad \frac{\mathbf{1}}{\boldsymbol{c}}, \quad \frac{\mathbf{1}}{\boldsymbol{k_{0,\mathrm{et}}}}, \quad \Delta G_{\mathrm{et}}, \quad \boldsymbol{L}, \quad \frac{\mathbf{1}}{\boldsymbol{r_{\mathrm{ac}}}}, \quad \boldsymbol{r_{\mathrm{fil}}}.$$

For this figure, variability from Table 5.6 is included only for the electron transfer variability parameters $r_{\mathrm{ac}}, r_{\mathrm{fil}}, c, k_{0,\mathrm{et}}$ (introduced here as parallel-shifting electron transfer parameters) and L; the remaining three variability entries of that table are not varied.

Equation 5.6 shows that α_{et} governs the slope in the electron transfer-limited regime at intermediate voltages. The slope increases as α_{et} rises from 0 to 0.5 and then decreases as α_{et} approaches 1. Its magnitude is scaled by z through the factor $z\,\alpha_{\mathrm{et}}(1-\alpha_{\mathrm{et}})$, i.e., it is twice as strong for $z = 2$ compared with $z = 1$. In Figure 5.12, a steeper electron transfer slope is thus obtained by increasing z, by increasing $\boldsymbol{\alpha_{\mathrm{et}}}$ when $0 < \alpha_{\mathrm{et}} < 0.5$, and by decreasing α_{et} when $0.5 < \alpha_{\mathrm{et}} < 1$ (α_{et} in **bold** as a variability parameter, z in regular thin font as remaining fitting parameters). Under these conditions, increases in the respective expressions shift the curve in the log t_{SET}-V_{p} plane in the direction indicated by the arrow. For Figure 5.12, variability from Table 5.6 is applied only to α_{et} (here introduced as a slope-changing electron transfer parameter).

A further coupling arises because α_{et} also appears in the prefactor $\left(A_{\mathrm{ac}}/A_{\mathrm{fil}}\right)^{\alpha_{\mathrm{et}}}$ (for $r_{\mathrm{ac}} > r_{\mathrm{fil}}$), thereby affecting *both* the parallel shift and the slope. Figure 5.12 highlights that slope-defining parameters can yield broader variability at the high-voltage end of a regime than at its low-voltage range; this is demonstrated here for the electron transfer-limited regime via variation of α_{et}. Driving the curve to small switching times while simultaneously maximizing the slope within the bounds from Table 5.6 produces the fastest-switching edge case. The insets of Figure 5.12, together with Figure 5.13, reveal that this optimum is not always straightforward. Because $A_{\mathrm{ac}} > A_{\mathrm{fil}}$ and $b_{\mathrm{et}} \propto (A_{\mathrm{fil}}/A_{\mathrm{ac}})^{\alpha_{\mathrm{et}}}$, the largest $\alpha_{\mathrm{et}} > 0.5$ determined by variability bounds yields the fastest edge case at *low* voltages in the log t_{SET}-V_{p} plane (through the prefactor). The steepest slope, however, occurs at $\alpha_{\mathrm{et}} = 0.5$ (black line in Figure 5.12); moving α_{et} away from 0.5 in either direction flattens the slope. Consequently, from some higher voltage value

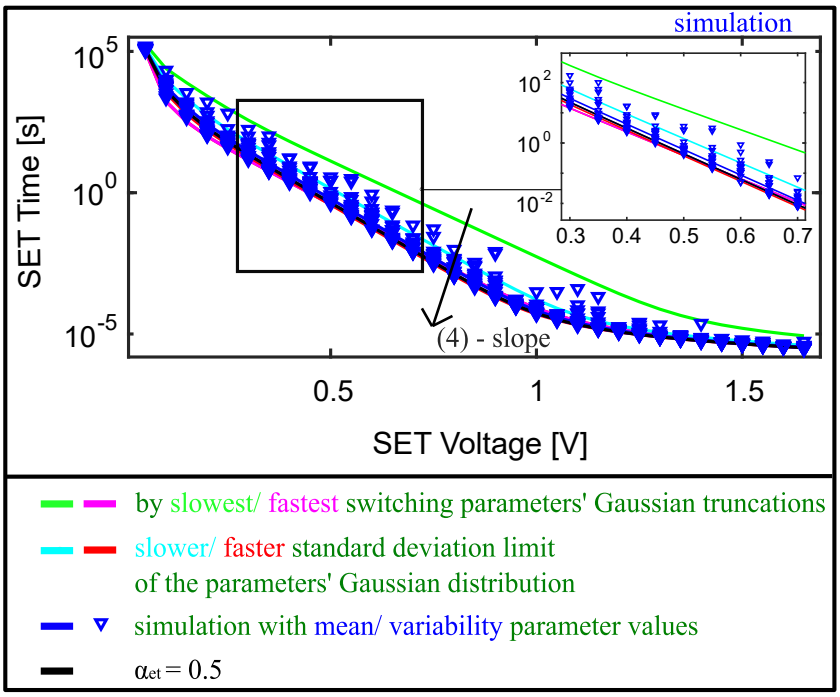

Figure 5.12: Parameter study of the SET kinetics device-to-device variability with respect to the ***slope-changing electron transfer parameters***, carried out through simulations based on the parameter sets of Tables 5.5 and 5.6. The diagram presents six curves: the mean-value curve in the center (blue), the $\pm 1\sigma$ standard-deviation boundaries (faster switching in red and slower switching in cyan), and the Gaussian truncation limits, which define the fastest (magenta) and slowest (green) switching edge cases. In addition, a black curve corresponds to a simulation with $\alpha_{\mathrm{et}} = 0.5$. The blue triangles mark the results of device-to-device variability simulations, illustrating the statistical spread of the switching behavior. The arrow indicates the effect of parameter variations on the slope of the SET kinetics, with a summary provided in Table 5.7. Adapted under the terms of CC-BY 4.0 license [34].

on the fastest switching can be attained by smaller α_{et} but still > 0.5; ultimately, at sufficiently large voltages, $\alpha_{\mathrm{et}} = 0.5$ sets the fastest edge case (in realistic voltage ranges, the corresponding α_{et} is still slightly larger than 0.5). In Figure 5.12, the magenta curve ($\alpha_{\mathrm{et}} = 0.644$) is the fastest at low voltages; over a broad voltage range the red curve ($\alpha_{\mathrm{et}} = 0.529$) becomes fastest; the black curve ($\alpha_{\mathrm{et}} = 0.5$) would prevail only at voltages higher than those displayed.

The α_{et} that optimizes the switching for a given V_{p} follows by minimizing equation (5.5) with respect to α_{et}, i.e., by solving $\mathrm{d}\log(t_{\mathrm{SET}})/\mathrm{d}\alpha_{\mathrm{et}} = 0$. This yields

$$\alpha_{\mathrm{et}} = \frac{1}{2} - \frac{k_{\mathrm{B}}T}{2zeV_{\mathrm{p}}} \log\left(\frac{A_{\mathrm{fil}}}{A_{\mathrm{ac}}}\right). \tag{5.8}$$

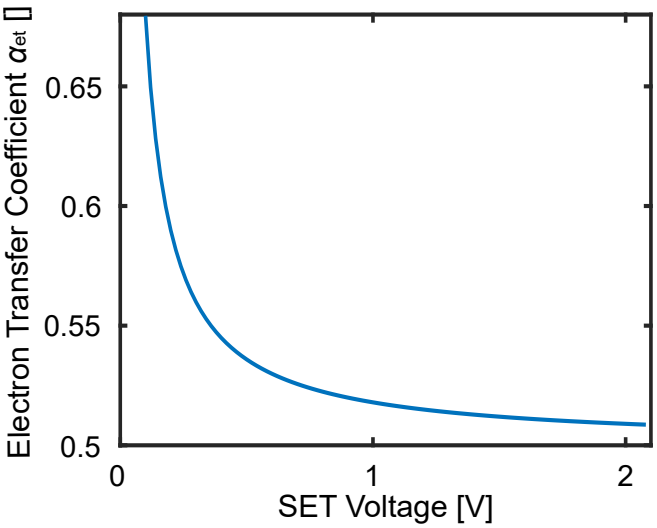

Figure 5.13: Fastest-switching edge case of the slope-changing electron transfer coefficient α_{et} as a function of the applied voltage pulse V_p. In contrast to other investigated model parameters, where the fastest edge case remains constant, the α_{et} value that gives the fastest switching varies with increasing V_p and therefore does not exhibit a fixed value across the entire voltage range. Adapted under the terms of CC-BY 4.0 license [34].

For $k_B T = 25.7\,\text{meV}$, $z = 2$, $r_{fil} = 4\,\text{nm}$ and $r_{ac} = 100\,\text{nm}$, equation (5.8) simplifies to $\alpha_{et} = 0.5 + 0.018\,\text{V}/V_p$, which specifies the optimal α_{et} as a function of V_p; this dependence is shown in Figure 5.13. Unlike the other variability parameters, the α_{et} that yields the fastest switching is therefore *not* a constant.

Electron transfer and ion hopping limitation (SET kinetics)

At high applied voltages, a mixed-control regime emerges in which both the electron transfer process and ion migration are rate-relevant, because all three overpotentials, η_{ac}, η_{fil}, and η_{hop}, attain non-negligible values before t_{SET} is reached [47]. In this high-voltage regime, the electric field is enhanced as the gap narrows, establishing a feedback loop between field amplification and gap reduction that drives a self-accelerating growth. With further voltage increase, ion migration becomes sufficiently rapid that electron transfer again imposes the rate limitation. This regime is therefore referred to as *mixed-control* regime [47]. For practical estimates of the SET delay, the initial slow ion migration is an acceptable approximation; nevertheless, the observations for the purely electron transfer-limited regime at intermediate voltages remain applicable at high voltages and are complemented by the additional constraints introduced by ion migration.

A mathematical expression for t_{SET} in the hypothetical *purely* ion hopping-limited regime follows analogously to the derivation of equation (5.5). Assuming $V_{\mathrm{cell}} = V_{\mathrm{Tu}} = \eta_{\mathrm{hop}}$ and integrating the ion migration current density (cf. equation 3.4) into the ODE defining the gap evolution (cf. equation 3.5) yields the simplified form

$$\frac{\mathrm{d}x}{\mathrm{d}t} \;=\; -\frac{M_{\mathrm{Me}}}{ze\,\rho_{\mathrm{m,Me}}}\, j_{0,\mathrm{hop}}\, \frac{A_{\mathrm{is}}}{A_{\mathrm{fil}}}\, \sinh\!\Big(\frac{aze}{2k_{\mathrm{B}}T\,x}\, V_{\mathrm{cell}}(t)\Big)\,, \tag{5.9}$$

which is introduced to clarify the influence of ion-migration parameters. This relation is not intended for the mixed-control regime; it applies to the hypothetical limiting case dominated by hopping.

For $w \gg 1$, the approximation $\sinh(w) = \frac{1}{2}\big(\mathrm{e}^{w} - \mathrm{e}^{-w}\big) \approx \frac{1}{2}\mathrm{e}^{w}$ is valid in the present context. Adopting a conservative estimate with $x = x_{\max} = L = \text{const.}$ during the pulse gives an upper bound for the SET delay, i. e., the slowest SET delay time. Since x typically decreases as switching proceeds, this assumption would give slower switching times than the actual model. However, the error introduced by this approximation is negligible for the intended purpose, because t_{SET} decreases exponentially with decreasing x. Also, it is naturally governed by the slowest contribution to switching. With $V_{\mathrm{cell}} = V_{\mathrm{p}}$ constant and by following the same integration steps as in equations (5.3) - (5.5), one obtains the relation in the log t_{SET}-V_{p} plane:

$$\log t_{\mathrm{SET}} \;=\; \log\!\left(\frac{(L - x_{\mathrm{SET}})\,\rho_{\mathrm{m,Me}}\,\exp\!\big(\Delta G_{\mathrm{hop}}/\big(k_{\mathrm{B}}T\big)\big)}{M_{\mathrm{Me}}\,c\,a\,f}\,\frac{A_{\mathrm{fil}}}{A_{\mathrm{is}}}\right) \;-\; \frac{aze}{2k_{\mathrm{B}}T\,x}\,V_{\mathrm{p}}. \tag{5.10}$$

Comparison of equation (5.10) with equation (5.1) yields for the hopping-limited contribution in the log t_{SET}-V_{p} representation

$$m_{\mathrm{hop}} \;=\; \frac{aze}{2k_{\mathrm{B}}T\,x}, \tag{5.11}$$

$$b_{\mathrm{hop}} \;=\; (L - x_{\mathrm{SET}})\frac{\rho_{\mathrm{m,Me}}\,\exp\!\big(\Delta G_{\mathrm{hop}}/\big(k_{\mathrm{B}}T\big)\big)}{M_{\mathrm{Me}}\,c\,a\,f}\,\frac{A_{\mathrm{fil}}}{A_{\mathrm{is}}}. \tag{5.12}$$

For the simulation underlying Figure 5.14, variability from Table 5.6 is included for six of the eight entries, namely $r_{\mathrm{ac}}, r_{\mathrm{fil}}, c, k_{0,\mathrm{et}}, \alpha_{\mathrm{et}}$, and L. In the mixed-control regime, the fastest edge case is again obtained by shifting the curve towards the smallest SET delays while realizing the steepest feasible slope. Although the discussion here emphasizes the ion migration impact, the previously established electron transfer trends remain valid and continue to additionally dictate both parallel shifts and slope changes.

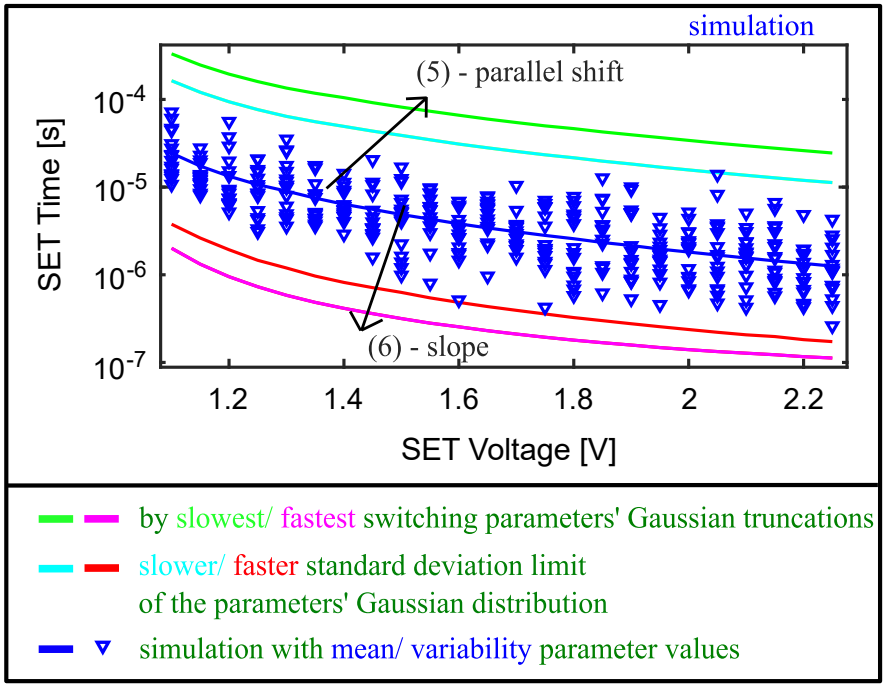

Figure 5.14: Parameter study of the SET kinetics device-to-device variability with respect to the ***parallel-shifting parameters of the mixed-control regime***, carried out through simulations based on the parameter sets listed in Tables 5.5 and 5.6. The plot displays five characteristic curves: the mean-value curve in the center (blue), the $\pm 1\sigma$ boundaries on either side (faster switching in red and slower switching in cyan), and the Gaussian truncation limits representing the fastest (magenta) and slowest (green) switching edge cases. The blue triangles illustrate the outcomes of device-to-device variability simulations, thereby highlighting the stochastic spread of switching times. The arrow denotes the effect of parameter variations in terms of a parallel shift and additionally a slope change of the SET kinetics curve, with a quantitative summary of these trends provided in Table 5.7. Adapted under the terms of CC-BY 4.0 license [34].

Increasing the ion concentration c reduces t_{SET} (smaller delays), an effect that becomes more pronounced in mixed control, as c contributes to the electron transfer as well as ion migration process. A higher hopping attempt frequency f or a lower migration barrier ΔG_{hop} produces a similar (though weaker) reduction, as both parameters enter only via the hopping/migration prefactor b_{hop} in equation 5.12. The hopping distance a appears linearly in the hopping current density (via b_{hop}) and, in addition, controls the slope through m_{hop} in equation (5.11); an increase in a therefore increases the slope as well. Once a filament has formed and the gap x decreases further, field enhancement grows nonlinearly, reinforcing the feedback between field and gap reduction and resulting in self-accelerating growth.

An increase in r_{is} or, equivalently, the ion-migration cross-sectional area A_{is} shifts the mixed-control branch towards shorter SET times, consistent with b_{hop}.

The comprehensive plot in Figure 5.14 indicates the following movements in the log t_{SET}-V_{p} plane (in **bold** the variability parameters, in regular thin font the remaining fitting parameters are displayed):

- Parallel shift toward slower switching (larger t_{SET}): all parallel-shift insights from Figure 5.11 (electron transfer parameters), and in addition increases in $1/a$, $1/f$, ΔG_{hop}, and/or $\mathbf{1/r_{is}}$.
- Slope increase (steeper mixed-control branch): all slope-related insights from Figure 5.12 (electron transfer parameters), and in addition increases in a and/or $\mathbf{1/L}$.

General remarks (SET kinetics)

For clearer comparison and straightforward identification of the rate-limiting process, the voltage increment $\Delta V_{10\times}$ - defined as the additional voltage required to accelerate the switching by a factor of ten in time - has been introduced in Ref. [153]. It is given by

$$\Delta V_{10\times} \;=\; -\frac{1}{m}\,\ln(10). \tag{5.13}$$

The quantity $\Delta V_{10\times}$ can be extracted from experimental data in the log t_{SET}-V_{p} plane. It may also be calculated separately for the different slope regimes by inserting the corresponding parameter values. In this manner, a single limiting process can be isolated and its physical plausibility assessed by restricting the parameters to reasonable ranges. Two criteria are particularly useful [153]: (i) if $\left|m\,k_{\mathrm{B}}T/(ze)\right| > 1$, the regime can be identified as nucleation-limited, since no other regime achieves such a steep slope within physically sensible parameter values; (ii) for ion migration limitation, a physically reasonable ratio a/x should be smaller than 1/5. With a hopping distance a in the range 0.2 - 0.5 nm, this implies a voltage drop over at least $x = 1$ - 2.5 nm. Hence, if $\left|m\,k_{\mathrm{B}}T/(ze)\right|$ or a/x remains larger than 1/10 or 1/5, respectively, ion migration can be excluded as the sole slope-determining process [153].

All fits in this section are performed using the deterministic and variability parameter sets listed in Tables 5.5 and 5.6. The resulting insights are summarized in Figures 5.10 - 5.14 and in Table 5.7. Table 5.7 consolidates the findings from both the SET kinetics fits (discussed above) and the I–V sweep fits (presented below). The influence of the parameters of all three ionic rate-limiting regimes on the shape of the SET kinetics curve (direction of parallel shifts and slope steepness) and on key design quantities - such as

SET and RESET voltages in the I-V characteristics - is presented comprehensively. The collection of tables (e. g. Table 5.1: deterministic fitting parameters; e. g. Table 5.2: variability fitting parameters; Table 5.7: parameter study) provides a practical route for calibrating the variability-aware ECM compact model to experimental data and for interpreting the role and impact of individual parameters in simulation.

An analysis of the device's RESET kinetics indicates that the parameter sensitivities are analogous to those discussed for SET kinetics. The RESET transition occurs under negative applied voltages and is not associated with nucleation, which only takes place during the SET process; during filament dissolution no nucleation is present. Consequently, in the RESET case the relevant ionic process regimes are electron transfer and ion hopping (as mixed control), for which the parameters affect the RESET behavior in the same manner as described for SET [151]. In the log t_{RESET}-V_{p} plane, two slopes can be distinguished. The conclusions regarding parallel shifts and slope changes carry over from the SET study to the RESET case by the corresponding consideration of the electron transfer and ion hopping parameters and apply in an analogous way.

5.3.2 I-V Characteristics Parameter Study

A detailed treatment of I-V modeling has been reported elsewhere [141, 142] for a simplified analytical ECM description that is valid in the electron transfer–limited regime. The relations derived in those works are fully applicable to the I-V measurement data set from the fit in section 5.1, since the measurements indicate that the dynamics are governed by the electron transfer reaction under the chosen sweep conditions with sweep rate $\beta = V_{\mathrm{max}}/t_{\mathrm{rise}}$. On this basis, a concise set of guidelines for fitting and interpreting I-V characteristics is formulated below.

It is important to note that an analysis of the SET current I_{SET} is not included here because a constant current compliance of $I_{\mathrm{cc}} = 100$ µA is enforced throughout. Moreover, unless explicitly stated otherwise, the sweep rate is kept fixed at $\beta = 0.025\ \mathrm{V\,s^{-1}}$ for all ionic rate–limiting scenarios considered (with the sole exception of the nucleation parameter investigation). Unless specified, model parameters are taken from Table 5.1. For each rate–limiting regime, exactly one parameter is varied to reveal that regime's impact on the I-V characteristics; for the nucleation study, however, multiple parameters are adjusted. The concrete parameter value(s) used in a given case are stated at the beginning of that case. In several instances the Gaussian truncation bounds, $\xi_{\mathrm{d2d,low}}$ and $\xi_{\mathrm{d2d,up}}$, are also modified or extended; whenever this is done, the revised limits are indicated at the outset of the corresponding case. As an alternative route, all regimes can

Table 5.7: ECM model parameter study: Influence of the model parameters on characteristic switching properties for pulse and sweep operation for increasing values of the parameters in the leftmost column.

Symbol	Pulse operation (SET kinetics)			Sweep operation (I–V characteristics)					
	Nucl.	Electr.tr.	Mixed	Nucl.		Electron tr.		Mixed	
				V_{SET}	V_{RESET}	V_{SET}	V_{RESET}	V_{SET}	V_{RESET}
r_{ac}		+	+			+	+	+	+
r_{is}			+					+	
r_{fil}		−	− −			−	−	− −	−
ΔG_{et}		−	−			−	−	−	−
c		+	++			+	+	++	+
$k_{0,\mathrm{et}}$		+	+			+	+	+	+
α_{et}		(+ sl)!(− sl)!	(+ sl)!(− sl)!			(+)(-)	(+)(-)	(+)(-)	(+)(-)
ΔG_{hop}			−					−	
a			+ sl!					+	
f			+					+	
L		−	− −			−		− −	
z	+ sl	+ sl	+ + sl	+		(+)(-)	(+)(-)	(+)(-)	(+)(-)
ΔG_{nuc}	−			−					
$t_{0,\mathrm{nuc}}$	−			−					
N_{c}	+ sl			+					
α_{nuc}	+ sl			+					
β				−	−	−	−	−	−

sl: affecting the slope in the log t_{SET}-V_{p} plane; ! : leading to both a change of the slope and a parallel shift; SET kinetics: +/−means faster/slower switching; ++/− −means enhanced effect through contribution from two regimes; (+)(-)means direction of the effect depends on further circumstances; I–V: +/−means switching at smaller/larger absolute voltages; ++/− −means enhanced effect through contribution from two processes; only one of the three rate-limiting ionic regimes is determining the switching voltage depending on the choice of the sweep rate β.

be accessed by varying the sweep rate $\beta = V_{\mathrm{max}}/t_{\mathrm{rise}}$ while holding all model parameters fixed; this complementary approach is discussed as well later.

The present I-V parameter study clarifies how the three ionic rate–limiting regimes and their key parameters shape the significant features of an I-V sweep. In particular, "edge cases" corresponding to the fastest and the slowest attainable switching are identified, whereas measured cycle-to-cycle variability is expected to fall between these limiting situations.

Figures 5.15 - 5.19 summarize the generic outcomes of the I-V investigation across the different rate–limiting regimes. In these plots, the red curves denote switching at the largest voltage and hence represent the slowest switching edge cases under consecutive I-V sweeps that display c2c variability (blue curve). In contrast, the yellow curves correspond to switching at the smallest voltage and therefore mark the fastest switching edge cases. By construction, the variability curves are expected to lie within the envelope spanned by these two Gaussian truncation–defined extremes for the considered variability parameters.

I-V characteristics governed by the nucleation process

In this case study, the nucleation prefactor $t_{0,\mathrm{nuc}}$ is adapted and slowed dwon, as the value $t_{0,\mathrm{nuc}} = 1{\cdot}10^{-6}$ s from Table 5.1 is changed to $9{\cdot}10^{5}$ s. In addition, $z = 1$ and $N_{\mathrm{c}} = 1$ are imposed so that nucleation is intentionally slow in all voltage regimes. Because the filament does not fully dissolve after RESET at the default sweep rate, the voltage ramp is reduced from 0.025 V s^{-1} to 0.0025 V s^{-1} to ensure complete dissolution after RESET. Moreover, the model is adapted to allow removal of the nucleus after RESET so that a fresh nucleation step precedes each new cycle. c2c variability is assigned exclusively to $t_{0,\mathrm{nuc}}$; the corresponding bounds are $t_{0,\mathrm{nuc,d2d,low}} = 1 \cdot 10^{4}$ s, $t_{0,\mathrm{nuc,d2d,up}} = 1.8 \cdot 10^{6}$ s for the Gaussian truncation limits, together with $\Delta t_{0,\mathrm{nuc,max,all}} = 1$ and $\Delta t_{0,\mathrm{nuc,max}} = 0.8$ for the c2c random walk parameters.

Based on these settings, thirteen consecutive I–V sweeps are simulated along with two limiting "edge" cases obtained from the lower and upper truncations of $t_{0,\mathrm{nuc}}$. Figure 5.15 summarizes the results. The red curve corresponds to the slowest switching edge and yields a SET voltage of about 0.9 V, i.e., the largest V_{SET} realised within this set by the upper truncation. Conversely, the yellow curve marks the fastest edge with V_{SET} slightly above 0.8 V. The blue curves show the thirteen variability sweeps. A notable observation is that V_{RESET} remains essentially unchanged across all edges and variability runs. Thus, for sufficiently slow ramps the nucleation–related parameters determine I-V

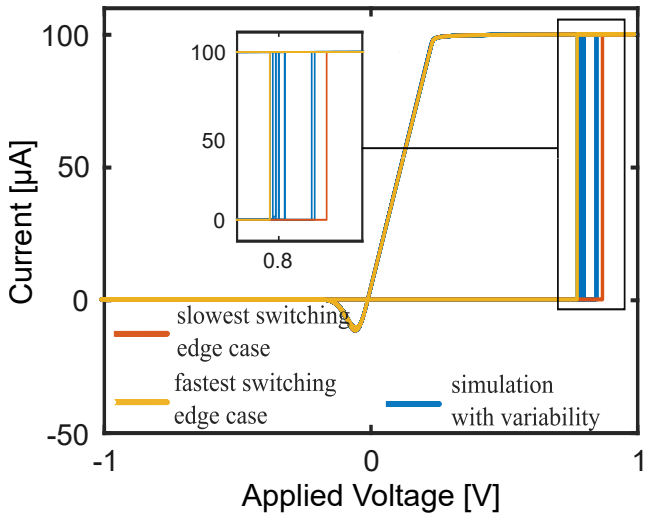

Figure 5.15: Parameter study of the cycle-to-cycle variability in the I–V characteristics, carried out through simulations based on the parameter sets provided in Tables 5.1 and 5.2. In this case, variability is exclusively attributed to the ***nucleation parameters***. The plot contains two characteristic edge-case curves: the yellow line with $t_{0,\mathrm{nuc}} = 1{\cdot}10^4$ s represents the switching at the lowest possible voltage, while the red line with $t_{0,\mathrm{nuc}} = 1.8{\cdot}10^6$ s corresponds to the switching at the highest possible voltage. In addition, the blue curves depict the variability range observed across consecutive cycles, thereby illustrating the extent of cycle-to-cycle fluctuations. Adapted under the terms of CC-BY 4.0 license [34].

characteristics and affect only V_{SET}. Neither the RESET voltage V_{RESET} nor the RESET current I_{RESET} shows any dependence. This is consistent with nucleation being relevant for filament formation and the subsequent SET event, but not for RESET. Also, the voltage V_{ON} until which the current stays in compliance upon the reverse sweep (V_{ON} has been defined in Figure 2.1) is not affected by these parameters. At higher sweep rates the nucleation parameters would not influence the I-V characteristics anymore.

The relation in equation (3.1) rationalises these trends (in bold the variability parameters, in regular thin font the remaining fitting parameters are displayed.): Increasing $\boldsymbol{t_{0,\mathrm{nuc}}}$ raises V_{SET} slightly. An increase in the nucleation activation energy ΔG_{nuc} produces a stronger, yet qualitatively similar, increase because it appears in the exponential factor of equation (3.1). Reductions in N_{c}, α_{nuc}, or z likewise shift V_{SET} upward and can amplify the effect. These dependencies govern the behaviour of the curves in Figure 5.15 and are valid for relatively slow voltage sweeps. For faster sweeps the nucleation process is too fast and no longer limits the switching time; the rate–controlling mechanism then transitions to electron transfer, or a combination of both, electron transfer and ion migration.

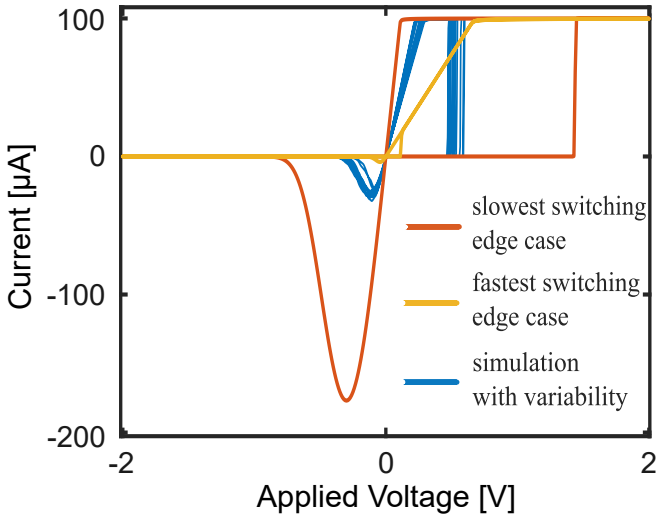

Figure 5.16: Comprehensive parameter study of the cycle-to-cycle variability in the *I-V* characteristics, carried out through simulations based on the parameter sets provided in Tables 5.1 and 5.2. In this analysis, the variability is deliberately restricted to ***parallel-shifting electron transfer-related parameters***, thereby enabling a focused investigation of their contribution to the overall fluctuations in device performance. The plots include two representative traces indicating switching at the extreme voltage conditions, namely the smallest possible SET voltage (shown in yellow) with $r_{\mathrm{ac}} = 4.9$ nm, $r_{\mathrm{fil}} = 0.9$ nm, $c = 4.5 \cdot 10^{24}$ m^{-3}, $k_{0,\mathrm{et}} = 1.3 \cdot 10^{4}$ ms^{-1} and the largest possible SET voltage (shown in red) with $r_{\mathrm{ac}} = 2.5$ nm, $r_{\mathrm{fil}} = 1.1$ nm, $c = 1.5 \cdot 10^{24}$ m^{-3}, $k_{0,\mathrm{et}} = 7 \cdot 10^{3}$ ms^{-1}. In addition, the blue curves depict the simulated variability observed across multiple switching cycles. Adapted under the terms of CC-BY 4.0 license [34].

I-V characteristics determined by the electron transfer process

In the case illustrated in Figure 5.16, the Gaussian truncation limits of both the active electrode cross-section and the ion concentration are modified to $r_{\mathrm{ac,d2d,low}} = 2.5\,\mathrm{nm}$, $r_{\mathrm{ac,d2d,up}} = 8\,\mathrm{nm}$ and $c_{\mathrm{d2d,low}} = 1 \cdot 10^{24}\,\mathrm{m}^{-3}$, $c_{\mathrm{d2d,up}} = 10 \cdot 10^{24}\,\mathrm{m}^{-3}$, respectively, in comparison to the values provided in Table 5.2. The objective of this case and of Figure 5.16 is to assess the influence of the electron transfer parameters that cause a parallel shift of the curve in the SET kinetics $\log t_{\mathrm{SET}} - V_p$ representation on the *I–V* characteristics.

In these simulations, 13 consecutive sweeps are computed for each case, together with the two edge cases defined by the Gaussian truncation boundaries. The red curve again represents the slowest switching edge case, whereas the yellow curve corresponds to the fastest switching edge case. The 13 blue curves depict the simulated cycles with enabled variability. In Figure 5.16, variability is allowed for the parameters $k_{0,\mathrm{et}}$, r_{ac}, r_{fil},

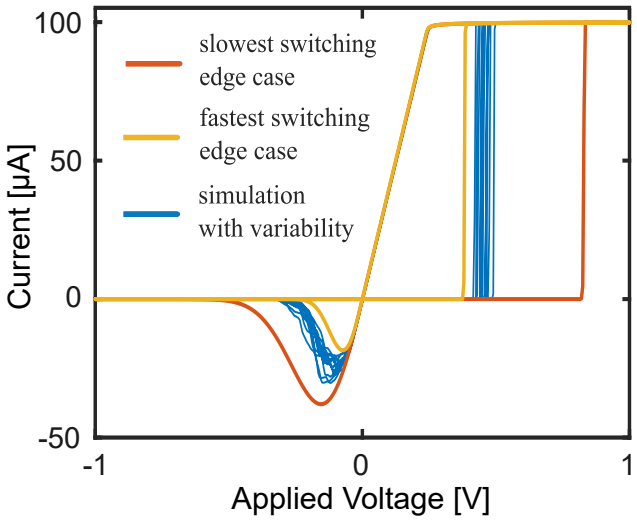

Figure 5.17: Comprehensive parameter study of the cycle-to-cycle variability in the I-V characteristics, performed through simulations based on the parameter sets listed in Tables 5.1 and 5.2. For this analysis, the variability is intentionally constrained to modifications in ***the slope-changing electron transfer-related parameters***, thereby enabling a more targeted examination of how such slope variations govern the overall fluctuations in device performance. The plots include two representative traces illustrating switching at the extreme operating conditions, namely at the lowest accessible SET voltage (yellow) with $\alpha_{\mathrm{et}} = 0.92$ and the highest accessible SET voltage (red) with $\alpha_{\mathrm{et}} = 0.98$. In addition, the blue curves depict the simulated variability observed across successive switching cycles. Adapted under the terms of CC-BY 4.0 license [34].

and c, i.e., the electron transfer parameters identified as inducing parallel shifts in the $\log t_{\mathrm{SET}} - V_p$ plane. The corresponding variability ranges are also listed in Table 5.2.

The variability of the SET voltage shown in Figure 5.16 is placed around the value 0.5 V, with the fastest switching occurring at 0.12 V (yellow curve) and the slowest at 1.5 V (red curve). In contrast, the RESET events of the variability curves occur consistently near −0.1 V. The yellow edge case curve reaches the RESET event at considerably smaller voltages and currents, while the red curve requires much larger absolute values, thus defining the range of observed variability.

From Figure 5.16 and equation (5.3), several insights can be drawn (In **bold** the variability parameters, in regular thin font the remaining fitting parameters are displayed.): An increase in the ion concentration $\boldsymbol{c}$, in the electron transfer prefactor $\boldsymbol{k_{0,\mathrm{et}}}$, or a decrease in ΔG_{et} each cause a reduction in V_{SET}, in the absolute RESET voltage V_{RESET}, and in the absolute RESET current I_{RESET} (yellow curve). A larger oxide thickness L shifts the SET voltage V_{SET} of the electron transfer regime towards higher values. However, the variability of L should not be considered relevant for cycle-to-cycle effects.

In the yellow curve, the SET transition does not abruptly jump into current compliance but instead occurs at a relatively low current with a very small SET voltage of 0.12 V. This implies that filament formation happens quickly, with copper ions supplied efficiently due to the chosen large active electrode radius and high ion concentration to the very thin filament. This results in a large electron transfer rate. Consequently, even a very small voltage is sufficient to reach the minimum gap between filament tip and active electrode, which is comparable in size to, e. g., the copper atom radius (0.13 nm) or the silver atom radius (0.172 nm). Before the external compliance $I_{cc} = 100$ µA is reached, the filament is already formed at significantly lower currents.

For Figure 5.17, which is simulated in a similar manner in order to analyze the effect of slope-determining parameters on the I–V characteristics, all values from Table 5.1 remain unchanged. No further parameter adjustments are required since the original sweep rate $\beta = 0.025\,\mathrm{V\,s^{-1}}$ already permits a description of the I–V characteristics within the electron transfer limited regime. The variability is introduced only for α_{et}, which influences both the slope and the parallel shift in the $\log t_{\mathrm{SET}} - V_p$ plane. The variability range is chosen as in Table 5.2, with the red edge case curve corresponding to $\alpha_{\mathrm{et}} = 0.98$ (yielding higher SET voltages) and the yellow curve to $\alpha_{\mathrm{et}} = 0.92$ (yielding lower SET voltages).

The two edge cases are again considered alongside the variability curves in blue, which fall between them. The trends are similar to those in Figure 5.16, but less pronounced, as only a single parameter is varied. Here, the fastest switching event occurs at 0.38 V (yellow) and the slowest at approximately 0.83 V (red), with the blue variability curves distributed between these bounds. RESET characteristics are likewise affected, with the fastest event occurring at lower voltages and currents, and the slowest event at higher ones.

The strength of the $\boldsymbol{\alpha_{\mathrm{et}}}$ effect strongly depends on the asymmetry ratio $\boldsymbol{A_{\mathrm{fil}}/A_{\mathrm{ac}}}$ [141, 142], analogous to equations (5.7) and (5.8) (all three mentioned parameters are variability parameters, thus, they are given in bold font). The larger the difference between A_{ac} and A_{fil}, the more a value of α_{et} close to 0.5 promotes a SET process with low V_{SET} values. Besides of it, a large α_{et} (e.g., 0.95) for an increasing A_{ac} relative to a constant A_{fil} results in a pronounced shift of V_{SET} towards smaller voltages, alongside a significant reduction in V_{ON}, but at the cost of much higher I_{RESET}. Conversely, for very small α_{et} (e.g., 0.05), and for decreasing A_{ac} relative to a constant A_{fil}, only minor changes are produced in V_{SET} and V_{ON}, as both only slightly decrease, but a substantial

reduction in V_{RESET} and I_{RESET} results. These results are consistent with the analysis in [141, 142].

It is important to note that the edge case simulations (not the variability distributions themselves) are performed for voltage sweeps between $-2\,\mathrm{V}$ and $2\,\mathrm{V}$, in contrast to the $-1\,\mathrm{V}$ to $1\,\mathrm{V}$ range used otherwise. This leads to slightly higher SET voltages, which is explained by a stronger negative voltage drop across the device, causing a more pronounced filament dissolution and consequently a higher HRS after RESET.

Finally, the probability that all four variability parameters simultaneously take extreme near-truncation values is negligible. Since the c2c variability ranges are much smaller than the Gaussian truncation limits, the blue variability curves cluster around the deterministic mean curve, while the red and yellow edge cases define the outer bounds of possible variability.

I-V characteristics governed by the mixed control processes

In the course of examining the influence of mixed control regime parameters, the Gaussian truncation limits of both the active filament radius and the ion concentration (reflecting variability) are adapted to $r_{\mathrm{ac,d2d,low}} = 2.5\,\mathrm{nm}$, $r_{\mathrm{ac,d2d,up}} = 8\,\mathrm{nm}$, as well as $c_{\mathrm{d2d,low}} = 1 \cdot 10^{24}\,\mathrm{m}^{-3}$ and $c_{\mathrm{d2d,up}} = 10 \cdot 10^{24}\,\mathrm{m}^{-3}$. Apart from these changes, all other parameters are kept identical to those values listed in Tables 5.1 and 5.2. For the simulations illustrated in Figure 5.18, variability is enabled for five selected parameters, with their variability intervals maintained as specified in Table 5.2: $k_{0,\mathrm{et}}$, r_{ac}, r_{fil}, r_{is} and c (denoted as the parallel-shifting mixed control regime parameters). In contrast, α_{et} is deliberately excluded from variability within this analysis, since its effect is incorporated in the exponential factor of equation (5.3), where its contribution is too dominant in relation to the others. The corresponding outcomes regarding its effect are already summarized in Figure 5.17, where 13 consecutive sweeps under enabled variability (blue curves) can be recognized in comparison with the limiting cases (red: slowest switching, largest attainable SET voltage; yellow: fastest switching, smallest attainable SET voltage).

Whenever the sweep rate β is chosen relatively high, as presented in a later study, or when the ionic rate-limiting quantities are selected accordingly, the resulting I–V curves are an outcome of both the electron transfer process and the ion hopping process. Especially, when increasing the upper truncation limit of the active electrode radius to larger values (while α_{et} is large, as here), the probability of a faster electron transfer

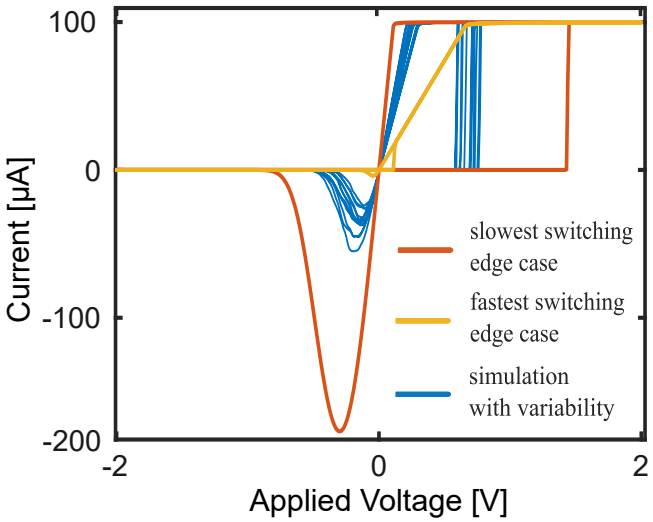

Figure 5.18: Comprehensive parameter study of the cycle-to-cycle variability in the I–V characteristics, carried out through simulations based on the parameter sets provided in Tables 5.1 and 5.2. For this particular investigation, the variability is deliberately restricted to ***parallel-shifting mixed control-regime parameters***, thereby allowing a focused assessment of their influence on the overall fluctuations in device switching performance. The plots display two limiting cases of switching behavior, with the yellow trace corresponding to the lowest achievable SET voltage with $r_{\mathrm{ac}} = 4.9$ nm, $r_{\mathrm{is}} = 2.5$ nm, $r_{\mathrm{fil}} = 0.9$ nm, $c = 4.5 \cdot 10^{24}$ m^{-3}, $k_{0,\mathrm{et}} = 1.3 \cdot 10^{4}$ ms^{-1} and the red trace representing the highest achievable SET voltage with $r_{\mathrm{ac}} = 2.5$ nm, $r_{\mathrm{is}} = 1.5$ nm, $r_{\mathrm{fil}} = 1.1$ nm, $c = 1.5 \cdot 10^{24}$ m^{-3}, $k_{0,\mathrm{et}} = 7 \cdot 10^{3}$ ms^{-1}. In addition, the blue curves illustrate the simulated cycle-to-cycle variability across repeated switching events. Adapted under the terms of CC-BY 4.0 license [34].

rises. Consequently, the effect of ion hopping on the I–V characteristics in the mixed control regime is strengthened, as it becomes more relevant for rate-limitation.

A comparison with the investigation that solely considered the electron transfer process (see Figure 5.16) reveals that the general tendencies of the mixed control regime remain similar, as in this case only r_{is} is introduced as an additional variability parameter. Thus, the overall features of the I–V characteristics, such as SET voltage, RESET voltage and RESET current, assume effects and values close to those obtained earlier (Figure 5.16). The variability of the electron transfer parameters therefore continues to be of significance in the mixed regime.

Referring to Figure 5.18 and based on equation (5.9), which incorporates the ion hopping distance a, further insights can be derived (in bold the variability parameters, in regular thin font the remaining fitting parameters are displayed.): A larger a promotes faster filament growth, which reduces the SET voltage (yellow curve), since the expo-

nential factor in the equation is then dominated by a. On the other hand, the decreasing effect of a higher attempt frequency f or of a higher ion concentration $\boldsymbol{c}$ on V_{SET} is also covered by this equation, although these two parameters enter only linearly via $j_{0,\mathrm{hop}}$. Furthermore, a reduced ΔG_{hop} also decreases the SET voltage. As $\boldsymbol{A_{\mathrm{is}} > A_{\mathrm{fil}}}$ generally holds, an increased asymmetry between these areas under constant A_{fil} results in a lower SET voltage. Altogether, the findings obtained from the electron transfer-controlled I–V curves remain valid when extended to the mixed control regime. Additionally, variations of the oxide thickness L to larger values shift the SET voltage V_{SET} in the mixed control case to higher values, consistent with the effect already discussed for the electron transfer parameters. As mentioned before, L is not considered for c2c variability effects.

It is important to emphasize that as it is improbable that all five parameters ($k_{0,\mathrm{et}}$, r_{ac}, r_{fil}, r_{is}, c) simultaneously lie close to their respective truncation limits, the occurrence of extreme parameter combinations is rare and their joint influence remains small. As a result, nearly all blue curves remain close to the deterministic reference sweep. Moreover, the yellow branch does not reach the compliance limit upon the SET process but instead stabilizes at a modest current level. In this situation, the filament forms extremely rapidly. Since the filament is very thin, copper supply from a relatively large active electrode is sufficient, the cross-sectional ion migration path is wide, and the overall copper ion concentration is high. Accordingly, the electron transfer reaction rate is also high for the yellow extreme case. Thus, switching occurs at low voltages, such that the minimal gap, roughly corresponding to e. g. the copper atomic radius (0.13 nm), is reached before the current compliance of $I_{\mathrm{cc}} = 100$ µA is reached, which would otherwise prevent such a small gap. Thus, here the minimum gap is attained at currents lower than $I_{\mathrm{cc}} = 100$ µA.

I-V characteristics governed by a single, hypothetical ion hopping process

To isolate an ion hopping–dominated switching process, the ion migration process is deliberately slowed by raising the corresponding activation energy from $\Delta G_{\mathrm{hop}} = 0.1$ eV to $\Delta G_{\mathrm{hop}} = 0.5$ eV. With this modification the ion hopping contribution becomes accessible and rate limiting (across all voltage ranges). Alternatively, the ion hopping distance a can be reduced to render the hopping process accessible. It should be noted, however, that a would affect both slope-changing and parallel-shifting parameters if treated as a variability parameter. Consequently, modifying a leads to a slightly more complex overall behavior. All remaining parameters are kept at their values from Table 5.1. To reveal effects attributable solely to the pure ion hopping process, variability is enabled

only for the ion hopping cross section radius r_{is}, using the ranges listed in Table 5.2. Within this setting it is found that increasing r_{is} lowers the SET voltage V_{SET}.

Figure 5.19 summarises the outcome. The red curve marks the slowest switching edge case (largest achievable V_{SET}), whereas the yellow curve indicates the fastest edge case (smallest achievable V_{SET}). Both edge curves bound the set of thirteen variability–aware simulated I–V sweeps shown in blue. This analysis focused on the pure ion hopping limitation shows that only the SET event is affected; equation (5.9) suffices to capture how the ion hopping parameters shape the I–V characteristics. This conclusion is consistent with the physical picture that, at the onset of RESET, the gap is small and the electric field is high, so ion migration proceeds too rapidly to become rate limiting during the RESET half cycle. Consequently, it does not control the dissolution speed of the filament.

Instead, filament dissolution during RESET is governed by electron transfer reactions (oxidation), which set the characteristic I–V features such as the RESET voltage V_{RESET} and the RESET current I_{RESET}. Accordingly, in Figure 5.18 the changes in these RESET characteristics can be attributed primarily to the variability in electron transfer parameters from the mixed control parameter set. However, such effects are not visible in Figure 5.19, as the limiting processes for RESET, namely electron transfer processes, do not experience any variability within this case study. In short, variability originating from the pure ion hopping process manifests itself in V_{SET} only; the remaining parts of the I–V response are essentially unaffected.

General remarks (I-V characteristics)

The I–V characteristics obtained at a fixed sweep rate β are tightly coupled to the corresponding SET kinetics. In practice, the portion of the I–V response - depending on the sweep rate - is governed predominantly by *one* of the three rate-limiting ionic regimes. Moreover, the voltage at which the SET transition occurs within an I–V sweep and the time required to reach this voltage follow, to a good approximation, the SET voltage and SET time inferred from the SET kinetics analysis. Accordingly, the regime identified in the SET kinetics study for a given $(V_{\mathrm{SET}}, t_{\mathrm{SET}})$ combination should be considered as a reference when interpreting the I–V characteristics at that same/similar operating point.

The dominant regime depends on the sweep rate. At *high* sweep rates, parameters associated with the mixed control regime are expected to shape the I–V behaviour most

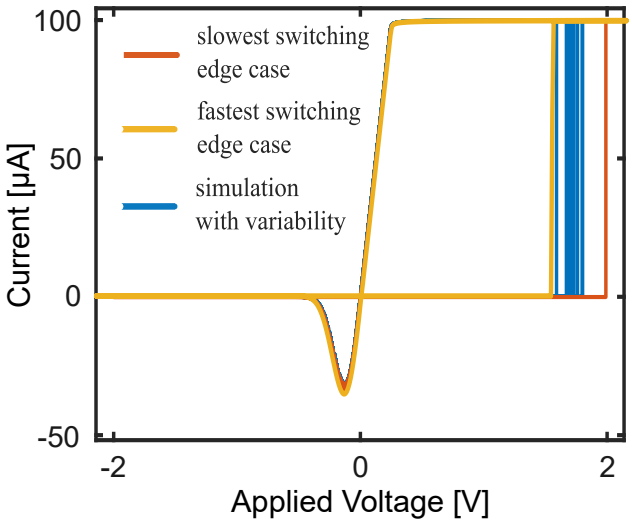

Figure 5.19: Comprehensive parameter study of the variability in the ***purely ion hopping-rate-limited*** I-V characteristics, performed through simulations based on the parameter sets listed in Tables 5.1 and 5.2. In order to ensure observable cycle-to-cycle variability within the simulations, the ion hopping activation energy is set to 0.5 eV. In this study, variability is restricted exclusively to the radius of the ion migration cross-section radius, thereby isolating its specific impact on the device behavior. The diagrams include two limiting cases of switching, with the yellow trace corresponding to the lowest attainable SET voltage ($r_{\mathrm{is}} = 2.5$ nm) and the red trace to the highest attainable SET voltage ($r_{\mathrm{is}} = 1.5$ nm), while the blue curves illustrate the distribution of variability across multiple switching cycles. Adapted under the terms of CC-BY 4.0 license [34].

strongly. For *intermediate* sweep rates, the electron transfer regime becomes decisive, whereas at *low* sweep rates the nucleation regime parameters exert the largest influence.

To probe different rate-limiting regimes within an I–V analysis, the sweep rate β should be varied during the measurements. In simulation studies one can alternatively enforce the desired regime by adjusting parameter values such that the targeted process becomes the slowest one. While feasible in simulation studies or fits, the latter strategy is naturally far less straightforward to realise in experiments. Thus, an investigation regarding adjusting the sweep rate in order to access different rate-limiting processes during I-V sweeps is presented in the following.

5.3.3 Influence of Sweep Rate Variation on I–V Characteristics

A convenient way to determine which ionic mechanism controls the switching at a given operating point is to vary the voltage sweep rate β while keeping all mean model parameters fixed. This is how emulation of measurement investigation regarding rate-limitation is implemented into simulation. In that way, the characteristic time window available

for the elementary ionic processes changes, and the process with the slowest effective kinetics for a specific sweep rate becomes rate limiting. The approach adopted here follows exactly this idea: β is adjusted over several decades, all mean parameters are taken from Table 5.3.3, and for each investigation panel in Figure 5.20 a single variability source is enabled in order to illustrate the spread between cycles together with two "edge cases" (yellow: fastest switching at the smallest V_{SET}; red: slowest switching at the largest V_{SET}). The blue traces show the I–V curves of the simulated cycles with variability.

Table 5.8: Mean model parameters for study of sweep rate β

Symbol	Value	Symbol	Value
M_{me}	$1.06 \cdot 10^{-22}\,\mathrm{g}$	r_{ac}	$3.5\,\mathrm{nm}$
z	1	r_{fil}	$1\,\mathrm{nm}$
$\rho_{\mathrm{m,me}}$	$8.96\,\mathrm{g/cm^3}$	r_{is}	$2\,\mathrm{nm}$
m_{r}	0.86	L	$10\,\mathrm{nm}$
ΔW_0	$3.6\,\mathrm{eV}$	ρ_{fil}	$1.68 \cdot 10^{-8}\,\Omega\,\mathrm{m}$
α_{et}	0.95	R_{el}	$> 1\,\Omega$
$k_{0,\mathrm{et}}$	$1 \cdot 10^{5}\,\mathrm{m/s}$	R_S	$1\,\mathrm{m}\Omega$
c	$3 \cdot 10^{24}\,\mathrm{m^{-3}}$	T	$298\,\mathrm{K}$
ΔG_{et}	$0.6\,\mathrm{eV}$	$t_{0,\mathrm{nuc}}$	$9 \cdot 10^{-6}\,\mathrm{s}$
ρ_{ion}	$1 \cdot 10^{-2}\,\Omega\,\mathrm{m}$	ΔG_{nuc}	$0.95\,\mathrm{eV}$
a	$0.2\,\mathrm{nm}$	N_{c}	1
f	$1 \cdot 10^{12}\,\mathrm{Hz}$	α_{nuc}	0.3
ΔG_{hop}	$0.47\,\mathrm{eV}$		

Variability included for following parameters between corresponding edge cases:

$t_{0,\mathrm{nuc,c2c,low}} = 0.1 \cdot 10^{-6}\,\mathrm{s}$; $t_{0,\mathrm{nuc,c2c,up}} = 18 \cdot 10^{-6}\,\mathrm{s}$
(Figure 5.20 (a))

$r_{\mathrm{fil,c2c,low}} = 0.5\,\mathrm{nm}$; $r_{\mathrm{fil,c2c,up}} = 1.5\,\mathrm{nm}$
(Figure 5.20 (b))

$r_{\mathrm{is,c2c,low}} = 1.5\,\mathrm{nm}$; $r_{\mathrm{is,c2c,up}} = 2.5\,\mathrm{nm}$
(Figure 5.20 (c) + (d))

Very slow sweep — nucleation limited (Figure 5.20 (a)). At a low sweep rate of $\beta = 1.25 \cdot 10^{-4}\,\mathrm{V\,s^{-1}}$, the system operates in the nucleation–limited regime. Variability is assigned to the nucleation pre–exponential factor $t_{0,\mathrm{nuc}}$ to reflect cycle–to–cycle changes of the initial nucleus cluster formation. The resulting c2c curves in blue are bound by

the two edge cases: the yellow curve switches at the lowest voltage, and the red curve at the highest one. The broad horizontal offset between these two traces underlines that the time to form a stable nucleus dictates the onset of switching under such slow ramps. Electron transfer and ion migration proceed comparatively quickly on this time scale and do not control the SET transition.

Intermediate sweep — electron transfer limited (Figure 5.20 (b)). Increasing the sweep rate to $\beta = 1.25 \times 10^{-3}\,\mathrm{V\,s^{-1}}$ shortens the available time for sweep voltage increment, so nucleation ceases to dominate, and the kinetics become governed by the electron transfer process. To demonstrate the sensitivity within this regime, variability is applied to the filament radius r_{fil}. The blue c2c curves cluster between the two edge cases, which exhibit the smaller V_{SET} (yellow) and larger V_{SET} (red) limits. Compared with the nucleation-limitation case, a sweep range is entered where depending on the filament radius value either SET processes occur for very small SET voltages with small electronic tunneling currents (small r_{fil}), or SET processes occur at higher SET voltages. For the latter case (big r_{fil}), the compliance current limit is reached upon switching. It should be noted that a SET process that exihibts tunneling currents smaller than I_{cc} upon switching implies, as mentioned before, that a filament (with a small radius) has grown to the active electrode while the gap has shrinked to its minimum size for a relatively small applied voltage.

Intermediate sweep with ion hopping variability — weak impact under electron transfer control (Figure 5.20 (c)). Keeping β at $1.25 \cdot 10^{-3}\,\mathrm{V\,s^{-1}}$ but assigning variability to the ion hopping cross-section radius r_{is} investigates the influence of ion hopping parameters while the system is still electron transfer limited. The I-V response upon enabled ion hopping variability changes only marginally; the blue traces are tightly grouped, and the red/yellow edge curves move little relative to Figure 5.20 (b). This behaviour highlights that modifications to ion migration parameters have a weak leverage on V_{SET} as long as electron transfer prevails.

Fast sweep — transition to mixed control with pronounced ion hopping influence (Figure 5.20 (d)). At a high sweep rate of $\beta = 2 \cdot 10^{-2}\,\mathrm{V\,s^{-1}}$, the switching shifts toward mixed control in which electron transfer and ion migration interact. Variability in r_{is} now produces a pronounced spread of the switching voltage; the red and yellow edge traces separate clearly, and the blue curves fill the interval between them. The strong sensitivity to r_{is} indicates that migration across the constricted gap bewteen

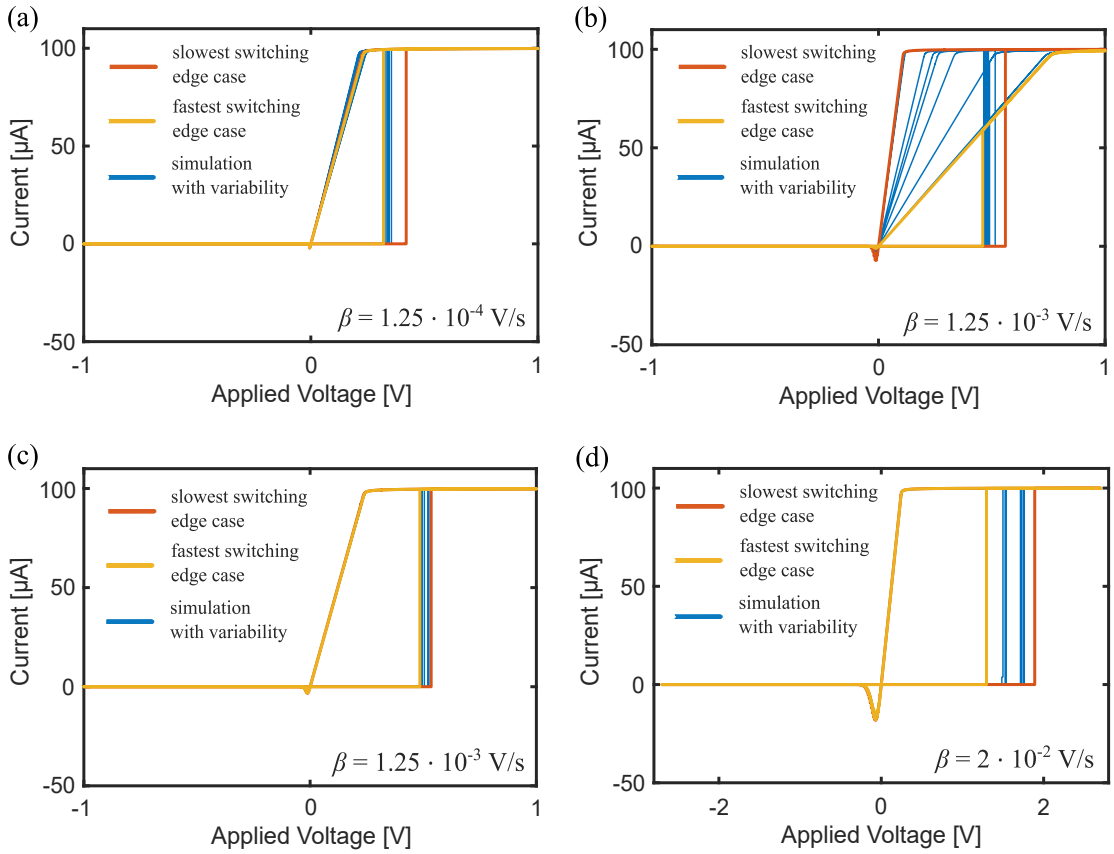

Figure 5.20: Accessing the different ionic rate-limiting regimes achieved by exclusively varying the I–V sweep rate β in the simulations, while keeping all mean model parameter values constant. In addition, variability is introduced for a single model parameter in each case, including the corresponding slowest and fastest switching edge cases. Specifically: (a) nucleation regime with $\beta = 1.25 \cdot 10^{-4}\,\mathrm{V\,s^{-1}}$ and variability applied to $t_{0,\mathrm{nuc}}$, (b) electron transfer regime with $\beta = 1.25 \times 10^{-3}\,\mathrm{V\,s^{-1}}$ and variability applied to r_{fil}, (c) very weak impact of ion hopping parameters within the electron transfer regime at $1.25 \cdot 10^{-3}\,\mathrm{V\,s^{-1}}$ with variability applied to r_{is}, and (d) pronounced impact of ion hopping parameters in the mixed control regime with $\beta = 2 \cdot 10^{-2}\,\mathrm{V\,s^{-1}}$ and variability applied to r_{is}. With increasing β, an increment in V_{SET} is observed. All parameter values are taken from Table 5.3.3. Adapted from the Supporting Information of [34].

active electrode and filament tip plays a central role once the sweep ramp becomes fast enough that transport and field–enhancement enhance each other distinctly.

Systematic trend with β. Across Figure panels 5.20 (a)–(d) the SET voltage increases monotonically with sweep rate, consistent with the reduced time available to reach the critical conditions for filament formation and growth. At very slow sweeps the nucleation time dominates; at intermediate sweeps electron transfer determines V_{SET}; and at fast sweeps the response is shaped by mixed control, so that ion migration parameters exert a strong influence. In each regime, the blue variability curves remain confined by the red/yellow edge cases, which provide a useful, model–based envelope for interpreting experimental cycle–to–cycle scatter.

Summary and practical implications. Varying β alone provides a clean adjustable parameter to activate different rate–limiting regimes without re–tuning the mean model parameters. Very slow ramps reveal nucleation control, intermediate ramps highlight electron transfer control, and fast ramps expose mixed control in which ion migration more significantly affects the outcome. This method offers a straightforward experimental strategy: sweeping β over a few decades and monitoring the evolution of V_{SET} and the spread between cycles can enable regime assignment.

5.4 Fitting Procedure Guide

The guidelines below outline a practical procedure for calibrating the compact model to device measurements. They are intended to make the fitting both efficient and transparent with respect to the roles of the rate–limiting ionic processes and the experimental constraints.

Step 1: Building the $\log t_{\mathrm{SET}}$–V_{p} map from pulse experiments

The starting point is a series of voltage–pulse experiments on pristine devices or devices prepared in the HRS. For each pulse amplitude V_{p}, the time to the SET transition, t_{SET}, is recorded. The measurements begin with the smallest practically useful amplitude and are repeated on multiple devices to capture device–to–device variability. The same sequence is then performed at incrementally larger amplitudes until an upper, still meaningful, V_{p} is reached.

The collected points are plotted in the $\log t_{\mathrm{SET}} - V_{\mathrm{p}}$ plane. When data from adjacent amplitudes are connected, a characteristic SET kinetics curve emerges that typically exhibits three distinct slopes, each associated with one rate–limiting ionic process. In the low–voltage region, the nucleation step is slowest and therefore produces the steepest slope. At intermediate voltages, electron transfer becomes rate limiting and the slope is weaker. At high voltages the response approaches the mixed control regime (electron transfer together with ion migration), where the slope flattens and may tend toward zero.

If the experimental window displays only one or two of these slopes, the accessible voltage range may be too narrow or the missing process(es) may be too fast to be resolved with the measurement setup. In rare cases, one ionic process could be faster than other processes for any voltage range and would not appear as rate-limiting in the $\log t_{\mathrm{SET}} - V_{\mathrm{p}}$ plane. In addition, an apparent flattening at high voltages can indicate a limitation by the pulse generator's rise time t_{rise}: when $t_{\mathrm{SET}} < t_{\mathrm{rise}}$, the true switching time cannot be discriminated. RC delays in the measurement path can likewise erroneously mimic kinetic limitations. Therefore, the setup's RC delay should be quantified independently and included in the analysis; ideally it is small enough in order not to impose an artificial floor on t_{SET} for any applied V_{p}. If restrictions of this kind are present, they must be acknowledged explicitly when interpreting the $\log t_{\mathrm{SET}} - V_{\mathrm{p}}$ curve.

Step 2: Deterministic fit of mean parameters

A deterministic model curve induced by mean parameter values is fitted numerically to the scattered points in the $\log t_{\mathrm{SET}} - V_{\mathrm{p}}$ plane, assuming that all three slopes are in principle observable. Fitting the low–voltage range lead to the nucleation parameters $t_{0,\mathrm{nuc}}$, ΔG_{nuc}, N_{c} and α_{nuc}. Analysis of the intermediate–voltage range provides the electron transfer parameters $k_{0,\mathrm{et}}$, r_{ac} and α_{et}. The high–voltage range, attributed to mixed control, determines a, f, r_{is} and ΔG_{hop}. The ion concentration c, the charge–transfer number z and the filament radius r_{fil} contribute to both latter ranges and are thus obtained consistently across the corresponding regimes.

Step 3: Incorporating device–to–device variability

In a second stage, the variability model is activated. The envelope that captures the fastest switching data points is taken as the *fast* edge case, while the slowest points define the *slow* edge case. For each variability parameter a global lower and upper truncation

is selected, representing the bounds of the truncated Gaussian used in the simulations. These truncations might represent the slowest and fastest switching d2d edge case, respectively, and are chosen within physically meaningful ranges (for several material systems such ranges are documented, e.g., in the JART ECM Verilog–A model [93, 100]). The standard deviation σ of each parameter's Gaussian is set so that they are within the bounds set by the two edge cases. Then, for each device and each voltage, parameter realisations are drawn randomly from the corresponding Gaussian distributions, which generates d2d variability.

If the experiments indicate a broader spread in one regime, a wider Gaussian is assigned to the parameters of that regime only. Conversely, a narrow spread calls for a smaller σ. When a limiting regime occupies a too narrow voltage interval in simulation by mistake, the interval can be broadened by slightly reducing its slope (thus extending to longer t_{SET}) or by shifting the neighbouring regimes to re–balance the voltage coverage. One must keep in mind that modifying one regime may alter a previously fitted boundary. As each of the three regimes is characterized by its own Gaussian distribution with an associated width, the experimentally observed regimes, i. e. the neighboring voltage values at the transition between two regimes, may exhibit strongly differing d2d variability widths of the SET time within the $\log t_{\mathrm{SET}} - V_{\mathrm{p}}$ plane. Furthermore, the model accounts for a possible experimentally observed increase in SET time variability at higher voltages within a given regime. This widening can be attributed to the variability of the parameters that determine the slope, which amplifies the spread of SET times at elevated voltages, whereas at lower voltages within the same regime the variability remains comparatively narrow. For example, within the electron transfer regime of Figure 5.12 the width of the V_{SET} variability envelope tends to be larger at $V_{\mathrm{SET}} = 1\,\mathrm{V}$ than at $V_{\mathrm{SET}} = 0.4\,\mathrm{V}$, a consequence of the local slope.

Step 4: Using I–V sweeps to guide and validate the fit

Independent I–V measurements should accompany the pulse analysis to characterise the device more completely and to stabilise the subsequent modeling. Although the sweep rate $\beta = V_{\mathrm{max}}/t_{\mathrm{rise}}$ is imposed by the experimental protocol rather than chosen in the model fit, it provides critical information. The SET voltage observed in an I–V sweep, $V_{\mathrm{IV,SET}}$, and the time within the sweep at which it occurs, $t_{\mathrm{IV,SET}}$, can be compared to the nearest point of the $\log t_{\mathrm{SET}} - V_{\mathrm{p}}$ map obtained from pulses (with $V_{\mathrm{p,SET}}$ and $t_{\mathrm{p,SET}}$). This comparison gives a first classification of the sweep into one of the three regimes

and thus identifies which parameters are most effective to tune in order to improve the fit beyond the purely pulse–based calibration.

For the device stack and sweep rate considered in section 5.1, the experimental evidence typically points to a limitation governed by electron transfer process, because only its parameters produce significant changes in the I–V modeling. Nevertheless, if parameters belonging to a different regime are varied strongly, the I–V characteristics may respond accordingly. To capture cycle–to–cycle variability in the sweeps, an initial random seed ξ_{init} is drawn from the truncated Gaussian of relevant regime's parameter(s), followed by a determination of the c2c bounds $\xi_{\mathrm{c2c,low}}$ and $\xi_{\mathrm{c2c,up}}$. It leads to the effect that the simulation applies a stochastic random walk within an overall constraint range determined by $\Delta\xi_{\mathrm{max,all}}$. The random walk is applied with a maximum step size ξ_{max} at each sampled voltage of the staircase I–V ramp. The input waveform should be incorporated as an exact reproduction of the experimental ramp, including its direction. Also, an additive stochastic current component reflecting the measured noise is superimposed. This provides a faithful fit of the cycle–to–cycle I–V variability. An overview of the data flow in this fitting workflow is given in Figure 5.21.

Remarks on limitations and practical hints

- If high–voltage data in the $\log t_{\mathrm{SET}} - V_{\mathrm{p}}$ plane flatten anomalously, it should be verified that neither t_{rise} nor RC delays are the cause before attributing the effect to mixed control.

- When only one or two slopes are visible in the measurement data, the voltage range should be extended if possible; otherwise the missing regime(s) should be interpreted as too fast for the present setup; this should be explicitly reported.

- I–V sweeps should not only be used as an independent validation but also as a handle to identify the prevailing regime at the applied sweep rate β. This supports to target parameter adjustments to the most sensitive parameter subset.

By explicitly incorporating the ECM devices' dynamical physical properties into the fitting routine, this approach provides a comprehensive methodology for consistently reproducing both the SET kinetics and the I-V characteristics. In doing so, it considers the inherent c2c and d2d variability of ECM devices across temporal and electrical domains, thereby offering a robust foundation for predictive modeling and fitting of their switching behavior.

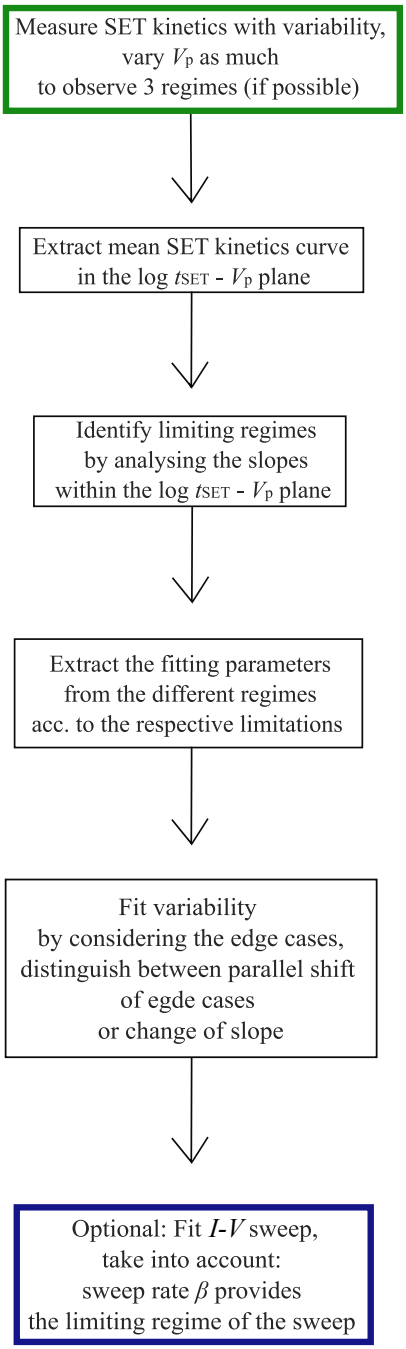

Figure 5.21: Flow chart outlining the variability-aware fitting procedure developed for ECM cells, in which the underlying dynamical physical properties of the devices are systematically considered. This procedure enables a consistent fitting of both the SET kinetics and the I-V characteristics, thereby ensuring that the experimentally observed switching dynamics are faithfully reproduced by the model. Adapted under the terms of CC-BY 4.0 license [34].

5.5 Summary

In this chapter, the JART ECM compact model is extended with several additional features. A central enhancement is the explicit inclusion of device-to-device and cycle-to-cycle variability, which allows the model to reproduce realistic device behavior that deviates from the ideal case, and is therefore highly relevant for circuit design and system-level investigations.

By reproducing and embedding further characteristics of real measurement setups and the inherent stochastic nature of the devices, the variability-aware model achieves a more accurate fit compared to previous fully deterministic approaches for VCM devices reported in [95]. The methodology emulates staircase voltage ramps as inputs, averages the current as the output response, introduces parameter variations after each voltage step, and incorporates stochastic contributions into the state-variable-defining differential equations. In this way, a convincing and realistic reproduction of cycle-to-cycle variability-aware experimental data is obtained. The resulting agreement mirrors what can be achieved under measurement conditions that are limited in resolution and affected by device-intrinsic variability, noise, and stochastic fluctuations during the entire process.

Using one consistent parameter set, the model is able to reproduce the experimental variability observed in SET kinetics and in I-V characteristics while also reflecting the inherent constraints of both the measurement setup and the devices themselves. Furthermore, the model is successfully fitted to two-dimensional material-based ECM devices explaining the confined ultrathin cross-section of the filament growth along vertically aligned van-der-Waals gaps. Also, the crucial role of moisture for enabling switching within ECM devices is confirmed by ion concentration varying simulations within 2D material-based ECM devices.

In addition, a parameter study addressing variability is provided. This study offers deeper insight into the underlying device physics and serves as a comprehensive guideline for the model fitting procedure. Moreover, three different rate-limiting ionic processes are analyzed which, depending on the strength of the applied stimulus, determine the switching speed of an ECM cell. Recognizing and understanding this essential behavior of rate-limitation - a fundamental property of ECM devices - is crucial for enabling accurate model fits to experimental data.

6 Simulations of v-ECM Devices: Results and Discussions

Nonvolatile memristive devices primarily serve as artificial synapses, storing electronic weights directly in hardware implementations of ANNs and SNNs. By contrast, volatile memristive devices are designed to emulate components of hardware neurons, for example in leaky–integrate–and–fire circuits [22, 23]. Beyond neuron emulation, volatile switching elements are attractive for further neuromorphic and adjacent domains: they have been explored as TRNGs for hardware security [154], and as selector devices in memory architectures owing to their intrinsic threshold behavior [18, 19, 155]. Within this landscape, ECM devices exhibit several favorable traits - scalability into the nanometer regime [15], compatibility with three-dimensional stacking [13], fast switching [18, 19], and on/off resistance contrasts spanning multiple orders of magnitude [22, 49].

In volatile-switching ECM devices - often referred to as diffusive memristors (dm) [23] - the switching operation drives an abrupt, stimulus-assisted transition from a high-resistive OFF-state to a low-resistive ON-state under a suitable positive bias. When the electrical excitation is removed or lowered sufficiently, the device then relaxes spontaneously back to the HRS after a characteristic relaxation time t_r [23]. Both the switching time and t_r typically vary across devices, switching cycles, and material stacks.

The stability of the metallic filament formed during switching underpins the observed operating regimes and, consequently, the application space of ECM cells. Filament robustness scales with the strength of the applied electrical stimulus [32]. Under stronger programming conditions (e.g., higher bias), the device becomes nonvolatile; dissolving the filament (RESET) then requires a sufficiently large voltage of opposite polarity. Under gentler programming (e.g., reduced bias or a tight current compliance that limits filament growth), volatility emerges: simply removing or lowering the applied bias triggers filament dissolution, so the return to the OFF-state occurs without an oppositely polarized pulse. In this volatile regime, dropping the bias below the hold voltage V_hold is sufficient [23].

The physics of nonvolatile ECM operation is comparatively well charted, supported by extensive experiments and modeling [47, 156–158]. Understanding of v-ECM behavior, however, has matured more recently as its broad application potential has come into focus. Recent studies report successful device engineering [159–162] and tuning strategies [32, 160, 161, 163]. Further works document an increase of t_r with read voltage [59] and frame applications explicitly around t_r [103], leveraging the interplay between switching time and relaxation time to realize either stochastic or cumulative switching. Overviews of materials, mechanisms, and use-cases for (volatile) ECM devices - together with comparisons to other threshold-switching technologies - are available in [164, 165].

A broad spectrum of modeling approaches has been proposed for volatile ECM behavior. These span mathematical/behavioral formulations [166–168], deterministic but more physics-informed models [169–171], and fully physics-based descriptions that attribute volatility to coupled drift, diffusion, and thermal effects [172–174], or to interfacial/ surface-energy minimization combined with surface diffusion [135, 136, 175–179]. Additional mechanisms have also been incorporated, including direct and Fowler–Nordheim tunneling [180] and the motion of metal atom clusters in tilted potentials [154, 181, 182]. These models operate across multiple scales: atomistic treatments [124, 136, 154, 176–178, 181–183], KMC simulations [136], finite element method (FEM) frameworks [175, 178], and numerical device-level models [177].

This work places particular emphasis on a head-to-head comparison with compact models intended for higher-level circuit simulation [135, 166–174, 176, 179, 180]. Across these prior efforts, several gaps remain. Many models lack sufficient maturity and robustness to consistently reproduce key experimental footprints - e.g., I–V sweeps, switching kinetics, and relaxation kinetics - over varied operating conditions. Consistent dynamic behavior under different programming and subsequent read protocols often relies on additional, external assumptions. Empirical approaches [166–171] typically match I–V characteristics or other static curves, but not inherently dynamical features. Compact models that embed drift, diffusion, and thermophoresis [172–174] may, in principle, capture relaxation behavior, yet demonstrations are limited; also, their reliability for switching dynamics remains unresolved, particularly with respect to the distinct ionic rate-limiting processes determining switching kinetics. Models relying on interfacial-energy minimization and surface diffusion [135, 136, 175–180] likewise tend not to address the switching kinetics explicitly. Frequently, different regimes are postulated for relaxation versus switching, leading to asynchronous descriptions tied to pre-assigned voltage ranges and, ultimately, to internal inconsistencies in the overall model behavior.

For some applications, such as artificial neuron circuits, applications emulating short-term plasticity of biological neurons or for realizing TRNG within hardware security, v-ECM device's variability is exploited and can play a key role. Based on the model for volatile ECM devices "JART v-ECM v1" from section 4.1.2, its variability-aware version "JART v-ECM v1 var" from section 4.1.3 and on its implementation within the simulation framework, presented in section 4.2.1 and 4.2.2, the fits to measurement data, corresponding simulations and simulation studies are performed. This chapter first shows a measurement-based case study for which a variability-aware fit to measurement data of a v-ECM device has been achieved succesfully. Then, simulation studies regarding the model parameters' effect on characteristic static and dynamic characteristics, as introduced in section 2.1.1, are performed and their result is presented. Based on these insights, also a comparison with other volatile ECM models from the literature is given. The insights and results of this chapter have been published in [46].

6.1 Fit to a Ag/HfO_2/Pt v-ECM Device

The experimental verification is based on an Ag/HfO_2/Pt device stack fabricated as described in [23, 68]. The measurements have been performed by S. Chekol, J. Rasbach and S. Hoffmann-Eifert. The silver top electrode has a thickness of 20 nm, the HfO_2 solid electrolyte layer measures 3 nm, and the platinum bottom electrode is 30 nm thick. A 20 nm Pt capping layer is present but does not take part in the switching process; the same applies to the 5 nm Ti layer and the SiO_2 substrate oxide. Alongside characteristic feature values of volatile ECM device's I-V sweeps, such as V_{th} and V_{hold}, the device stack is illustrated in Figure 6.1.

I-V characteristics fit

Quasi-static I–V sweeps are performed with a sweep rate of $\beta = 62.5\ \mathrm{mV\,s^{-1}}$, defined by $V_{\mathrm{max,sweep}} = 1$ V and $t_{\mathrm{rise,sweep}} = 16$ s, using a current compliance of $I_{\mathrm{cc}} = 10$ µA. The experimental curves show good agreement with the fitting obtained by the JART v-ECM model including cycle-to-cycle variability, both shown in Figure 6.2. From these measurements, characteristic voltages of $V_{\mathrm{hold}} = 0.13$ V and $V_{\mathrm{th}} = 0.34$ V can be extracted. The small sweep rate ensures the condition $V_{\mathrm{hold}} = V_{\mathrm{emf}}$ is satisfied (see discussion below). In this context, the given values correspond to the deterministic model, given in Table 6.1.

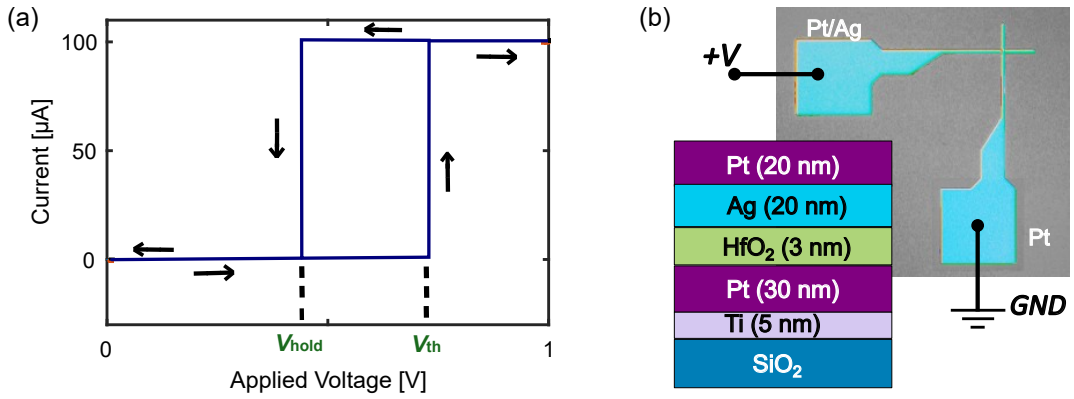

Figure 6.1: (a) Conceptual illustration of the I-V sweep of a v-ECM device, where the characteristic threshold voltage V_{th} and the hold voltage V_{hold} are indicated. (b) Experimental measurements are carried out on a $\mathrm{Ag/HfO_2/Pt}$ ECM device stack, comprising a platinum capping layer on top of the active Ag electrode and a $\mathrm{Ti/SiO_2}$ substrate at the bottom. The micrograph provides a top view of the ECM device integrated in a crossbar array structure, located between the Pt/Ag and Pt electrodes. During the measurements, the voltage is applied to the top Pt/Ag electrode, while the bottom Pt electrode is connected to ground. Adapted under the terms of CC-BY 4.0 license [46].

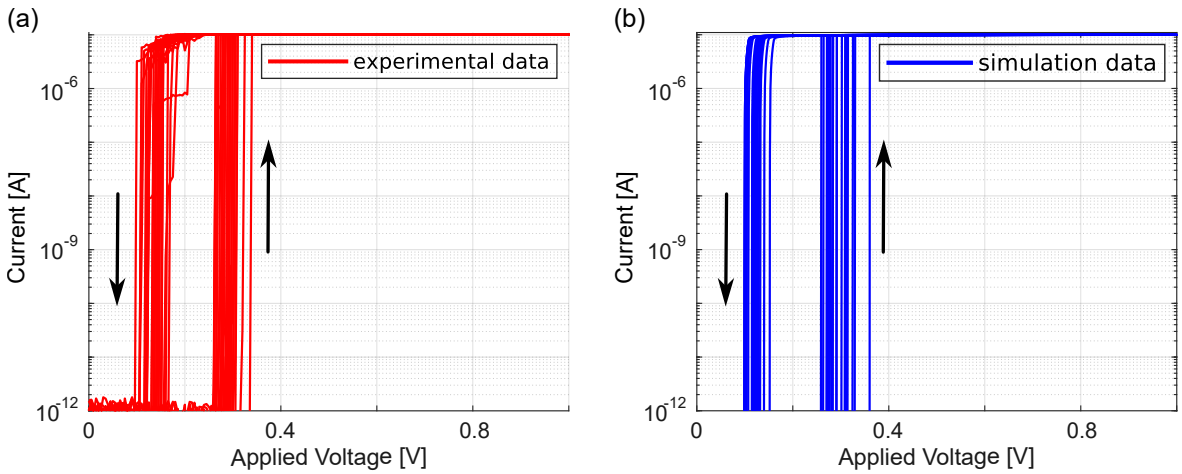

Figure 6.2: (a) Experimentally obtained I-V sweeps of a $\mathrm{Ag/HfO_2/Pt}$ ECM device stack recorded over 30 consecutive switching cycles. The data reveal a pronounced c2c variability, highlighting the stochastic nature of the filament formation and dissolution processes. (b) Simulated I–V sweeps of the same device configuration are presented for 30 consecutive cycles, carried out using the variability-aware v-ECM model. In both the experimental and simulated cases, the device exhibits a threshold switching voltage of $V_{\mathrm{th}} = 0.34$ V and relaxes back to the HRS at the hold voltage $V_{\mathrm{hold}} = 0.13$ V. A sweep rate of about 62.5 mV/s is employed. Adapted under the terms of CC-BY 4.0 license [46].

Table 6.1: Deterministic mean model parameters for measurement fitting

Symbol	Value	Symbol	Value
M_{me}	$1.79 \cdot 10^{-22}\,\mathrm{g}$	r_{ac}	$10\,\mathrm{nm}$
z	1	r_{fil}	$1\,\mathrm{nm}$
$\rho_{\mathrm{m,me}}$	$10.49\,\mathrm{g\,cm^{-3}}$	r_{is}	$1\,\mathrm{nm}$
m_r	0.84	L	$3\,\mathrm{nm}$
ΔW_0	$2.7\,\mathrm{eV}$	ρ_{fil}	$1.59 \cdot 10^{-8}\,\Omega\mathrm{m}$
α_{et}	0.14	R_{series}	$10\,\mathrm{k}\Omega$
$k_{0,\mathrm{et}}$	$1.5 \cdot 10^{4}\,\mathrm{m\,s^{-1}}$	T	$298\,\mathrm{K}$
c	$8 \cdot 10^{26}\,\mathrm{m^{-3}}$	$t_{0,\mathrm{nuc}}$	$6 \cdot 10^{-10}\,\mathrm{s}$
ΔG_{et}	$0.455\,\mathrm{eV}$	ΔG_{nuc}	$0.74\,\mathrm{eV}$
a	$0.15\,\mathrm{nm}$	N_c	1
f	$1 \cdot 10^{14}\,\mathrm{Hz}$	α_{nuc}	0.1
ΔG_{hop}	$0.19\,\mathrm{eV}$	$\beta = \dfrac{V_{\mathrm{max,sweep}}}{t_{\mathrm{rise,sweep}}}$	$0.0625\,\mathrm{V\,s^{-1}}$
V_{emf}	$0.13\,\mathrm{V}$		

For voltages below V_{emf}, the dynamic equilibrium shifts toward filament dissolution, leading the device to relax back into the HRS. Within the quasi-static simulation framework used here, the variability in V_{emf} specified in Table 6.2 is the only factor producing a spread in the observed V_{hold} values. Variations of other model parameters do not translate into a variability of V_{hold} in this operation mode, since the initial tunneling current and the exit from current compliance are not governed by them. The threshold voltage V_{th} is shifted towards higher values by V_{emf} compared to the case of dynamic equilibrium regarding ionic processes at 0 V. The c2c variability associated with the parameter V_{emf}, as well as with all other parameters listed in Table 6.2, has an effect on the V_{th} value. At this low sweep rate, the dominant parameter contributing to cycle-to-cycle variability, alongside V_{emf}, is $t_{0,\mathrm{nuc}}$ [34].

Switching kinetics fit

To record a switching kinetics curve, multiple voltage pulses with varying amplitudes are applied under constant voltage operation. For each pulse, the time t_{SET} required for the device to switch into the LRS is measured starting from the moment the voltage pulse is initially applied. The threshold switching kinetics presented in Figure 6.3 is fitted using the same parameter set as in Table 6.1 and Table 6.2. A close agreement

Table 6.2: Variability model parameters for measurement fit (Gaussian distribution relevant for d2d variability + random walk relevant for c2c variability + truncation of Gaussian distribution relevant for both).

Symbol	σ (Std. deviation of Gaussian distr.)	Trunc. of Gaussian distr. ($\xi_{\mathrm{d2d,low}} \mid \xi_{\mathrm{d2d,up}}$)	$\Delta\xi_{\mathrm{max}}$	$\Delta\xi_{\mathrm{max,all}}$
$k_{0,\mathrm{et}}$	$3 \cdot 10^{4}\,\mathrm{m\,s^{-1}}$	$(0.1 \mid 6) \cdot 10^{4}\,\mathrm{m\,s^{-1}}$	0.9	0.5
c	$8 \cdot 10^{25}\,\mathrm{m^{-3}}$	$(7.7 \mid 8.3) \cdot 10^{26}\,\mathrm{m^{-3}}$	0.2	0.5
$t_{0,\mathrm{nuc}}$	$3 \cdot 10^{-8}\,\mathrm{s}$	$(0.1 \mid 1000) \cdot 10^{-10}\,\mathrm{s}$	0.8	0.5
V_{emf}	$5 \cdot 10^{-4}\,\mathrm{V}$	$(0.1 \mid 0.16)\,\mathrm{V}$	0.3	0.25

between experimental data and simulation is obtained, with the variability being accurately reproduced. The SET time decreases by several orders of magnitude as the pulse amplitude increases. Up to $V_{\mathrm{dm}} = 0.7\,\mathrm{V}$, a pronounced steep slope in the $\log t_{\mathrm{SET}} - V_{\mathrm{dm}}$ plane can be observed. This behavior originates from the nucleation process, which in this voltage range represents the dominant rate-limiting mechanism. For voltages above $V_{\mathrm{dm}} > 0.7\,\mathrm{V}$, a transition into a different regime occurs, in which a combined limitation by electron transfer processes and ion migration takes effect, leading to a flattening of the slope. In this high-voltage regime the SET time t_{SET} decreases to comparatively small values. Within the first regime, the parameter $t_{0,\mathrm{nuc}}$ is decisive for the d2d variability in t_{SET}, whereas in the second regime, the variability is predominantly influenced by the model parameters $k_{0,\mathrm{et}}$ and c.

This updated JART v-ECM model based on the electromotive force V_{emf} indicates that the device theoretically requires infinite time to switch when $V_{\mathrm{dm}} = V_{\mathrm{emf}}$. In contrast, earlier nonvolatile model fits have assumed $V_{\mathrm{dm}} = 0\,\mathrm{V}$ for an infinite time to switch [23, 68], i. e. declaring $V_{\mathrm{dm}} = 0$ V as the dynamic equilibrium. The present adaptation with revised parameter values for the volatile model corrects this discrepancy. Without alignment by a new parameter set, the threshold switching kinetics curve is effectively shifted by 0.13 V to the right due to the inclusion of V_{emf}. This distortion makes the new parameterization of the threshold switching kinetics mandatory, since it restores consistency by shifting the curve back to the left-hand side.

Fit to relaxation behavior

A careful examination of the post-switching relaxation and its dependence on the previously applied pulse amplitude that led to the switching, as well as on the value of a series

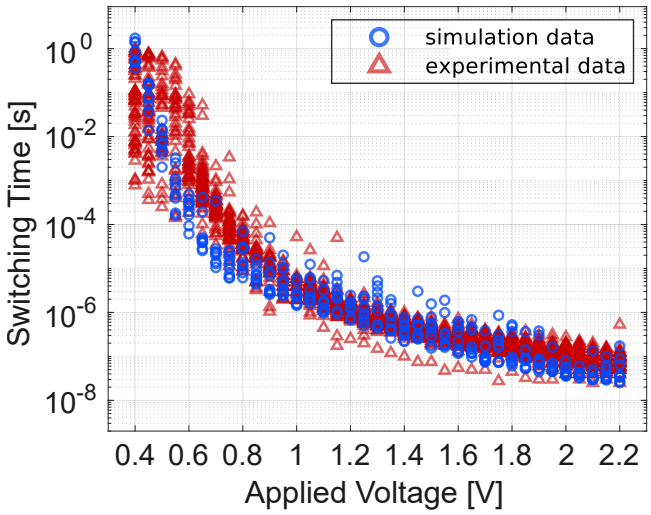

Figure 6.3: The figure presents the experimentally obtained data points of the threshold switching kinetics for an ECM device stack based on $Ag/HfO_2/Pt$. The experimentally measured values, including their d2d variability, are represented in red. In parallel, the results obtained from numerical simulations, which likewise incorporate the corresponding d2d variability, are shown in blue. This direct visual comparison between measurement and simulation highlights the extent to which the model is capable of capturing the experimentally observed distribution of switching kinetics across different devices. Adapted under the terms of CC-BY 4.0 license [46].

resistance, is essential for advancing the understanding of the overall device behaviour and for controlling the relaxation dynamics.

Figure 6.4(a) depicts the transient voltage signal that is applied to the device both in measurement and in simulation. The inset illustrates the electrical circuit, in which the signal is applied to one terminal of the device while the opposite terminal is connected to ground. An additional series resistor R_{series} is inserted into the circuit to limit the current. A programming/write pulse V_{p} of 1 ms duration and selected amplitude is followed by a read pulse with $V_{\text{read}} = 0.1\ \text{V} < V_{\text{emf}} = 0.13\ \text{V}$ (in Fig. 6.4(a) an example with $V_{\text{p}} = 1.2\ \text{V}$ is shown). Multiple measurements are carried out, and corresponding simulations are performed, in which both the programming amplitude V_{p} and the series resistance R_{series} are varied. A representative current response from experiment and simulation, displayed in Fig. 6.4(b), provides insight into the transient current evolution. In line with a previous approach [68], the relaxation time t_{r} is defined as the interval from the start of the 0.1 V read pulse to the instant when the current has decayed to 70 nA. Measurements enabling such an analysis have been already presented in an earlier work [68] and are used here to demonstrate a consistent model fit.

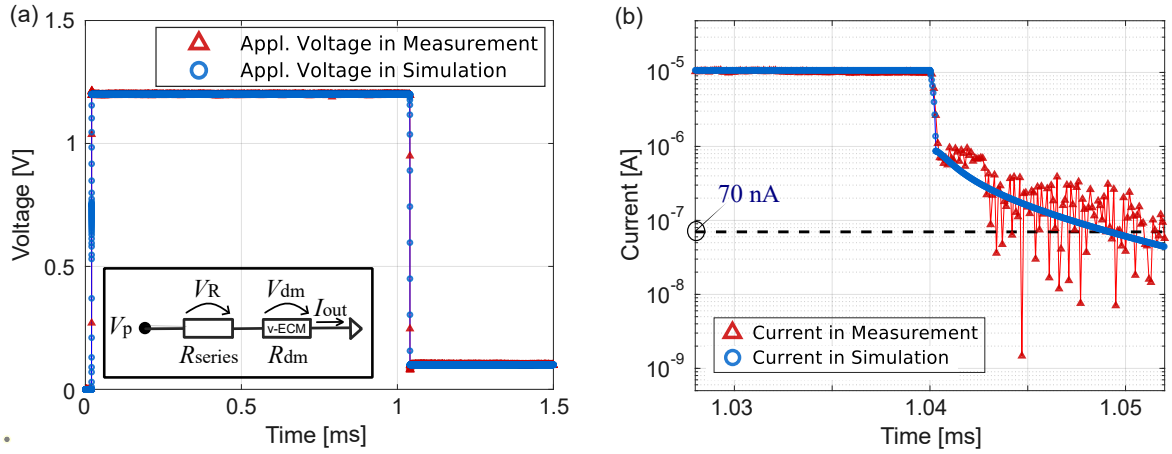

Figure 6.4: (a) The panel illustrates both the applied voltage signals in experiment and simulation for a Ag/HfO_2/Pt ECM device stack, designed to analyze the relaxation dynamics of the system. The measurement protocol consists of a 1 ms programming (write) pulse with amplitude V_p, which is subsequently followed by a read-out voltage of $V_{read} = 0.1$ V. The inset provides a schematic view of the electrical biasing configuration, showing that the programming signal V_p is delivered through a voltage divider circuit: the applied potential is distributed between the external series resistance and the v-ECM device. The resulting electrical current I_{out}, which flows through both components, is also displayed. (b) A transient zoom of I_{out} is presented for both measurement and simulation in the vicinity of $t = 1.04$ ms. At this particular time, the applied voltage abruptly drops to the read level of $V_{read} = 0.1$ V, and the current progressively relaxes toward the HRS. The relaxation time is quantitatively determined as the temporal interval between the onset of the read voltage and the point at which the current decreases below the threshold of 70 nA, thereby marking the complete transition back to the HRS. Adapted under the terms of CC-BY 4.0 license [46].

Figures 6.5(a) and 6.5(b) present two experimental data sets together with their respective simulations, each recorded with a different series resistance ($R_{series} = 560$ kΩ and $R_{series} = 1$ MΩ), plotting the relaxation time t_r versus the applied programming voltage V_p. In each case, d2d variability is evident in the measurements and is reproduced well by the simulations. For both series resistances, a slight increase of t_r with increasing V_p is observed and captured by the model. The simulations indicate that, during programming, the filament grows faster at higher applied V_p, which results in a larger vertical filament length. Consequently, different applied programming voltages V_p produce different LRS with corresponding vertical filament lengths.

During the subsequent read operation, the time required to dissolve the filament from these various LRS levels to the same target HRS is determined: a higher programming voltage V_p (i.e., a lower resulting LRS) leads to a longer dissolution time before the device

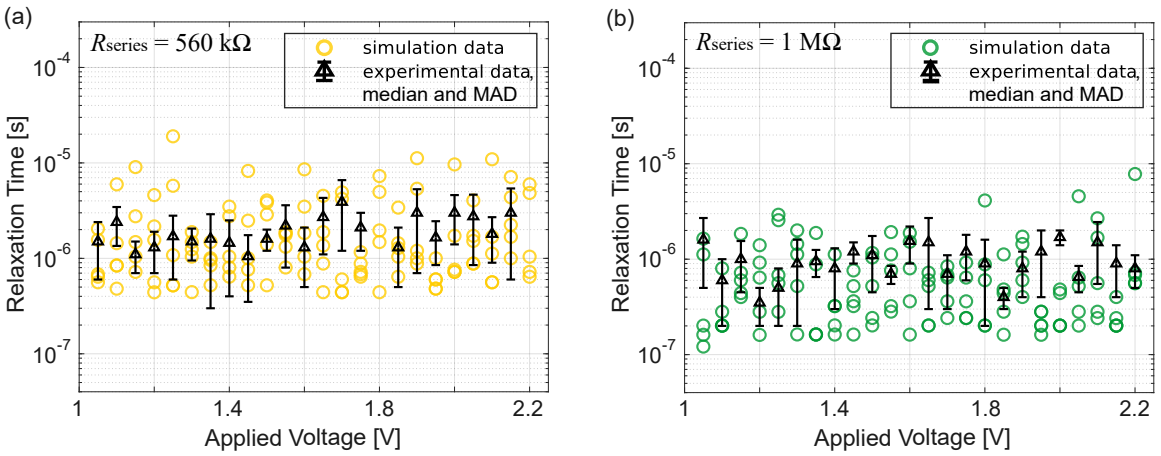

Figure 6.5: (a) Experimental and simulated results for the relaxation time t_r as a function of the applied programming voltage V_p for a configuration with a series resistance of $R_{series} = 560$ kΩ. (b) Corresponding comparison of measurement and simulation for the case of an increased series resistance of $R_{series} = 1$ MΩ. In both scenarios, the d2d variability is explicitly taken into account, enabling a direct assessment of the influence of the series resistance on the statistical distribution of the relaxation dynamics. Adapted under the terms of CC-BY 4.0 license [46].

reaches that HRS. It is also noteworthy that, for the smaller series resistance $R_{series} = 560$ kΩ, the overall relaxation times are longer than for the larger series resistance $R_{series} = 1$ MΩ. According to the simulations, this is because, in the first case, the lower resistance causes a larger fraction V_{dm} of the total applied voltage V_p to drop across the v-ECM device, which yields larger vertical filaments after programming; these filaments require a longer t_r to dissolve during reading. By contrast, with the larger series resistance the filaments do not grow as far during programming and therefore dissolve more easily and more quickly, resulting in shorter t_r. No nucleation step is involved in filament dissolution, as nucleation pertains to filament formation but not to its removal. Hence, at $V_{read} = 0.1$ V $< V_{emf} = 0.13$ V the relaxation is limited by electron transfer processes, consistent with the relaxation kinetics discussed later. It should be emphasized that, as long as the v-ECM device remains in the LRS, only a small portion of the total applied voltage drops across the v-ECM stack, while the larger share appears across the series resistor. Nevertheless, a small device voltage $V_{dm} \approx 0 < V_{emf}$ still corresponds to the same rate-limiting mechanism. Therefore, the measured and simulated relaxation times t_r are governed by charge-transfer redox reactions as the rate-limiting ionic processes. Because variability is introduced in the simulations by applying variability to the corresponding rate-limiting parameters, this finding also implies that the experimentally observed d2d spread is captured by imposing variability

on the electron transfer d2d variability parameters, specifically those associated with $k_{0,\mathrm{et}}$ and c. Owing to the absence of a nucleation step in the relaxation process, neither the deterministic relaxation time nor the variability-aware relaxation time depends on $t_{0,\mathrm{nuc}}$ during reading.

6.2 Simulation Studies on Read Process, Kinetics, emf Strength, and Sweep Rate

Further investigations presenting the predictions of the JART v-ECM model are conducted and discussed in the following. Unless otherwise stated, the same parameter set given in Table 6.1 is applied for these theoretical simulations.

Switching kinetics, read dynamics and relaxation kinetics of v-ECM devices

The read process is typically performed immediately after a programming or write operation of a v-ECM device by selecting $V_{\mathrm{read}} < V_{\mathrm{emf}}$. In this way, access to the relaxation process becomes possible. As already outlined in the introduction of Figure 4.1, the further away V_{dm} is located from the emf value V_{emf}, the faster the relaxation proceeds. The implications of this effect can be illustrated by analyzing the device's relaxation kinetics. In all relaxation simulations, a programmed LRS with a small gap length of 0.172 nm is assumed as the initial state, corresponding to the radius of a silver atom. In contrast, all SET process simulations assume no pre-existing nucleus or filament, both of which must first form prior to switching.

Figure 6.6 presents the switching kinetics together with the relaxation kinetics of the ECM device, displayed in the $\log t_{\mathrm{SET}}/t_{\mathrm{r}}$–$V_{\mathrm{dm}}$ plane. On the right-hand side of V_{emf}, the switching kinetics curve (blue) reveals two distinct slopes, which correspond to three different ionic rate-limiting processes. The first steep slope at low voltages is governed by nucleation-limited dynamics. At higher voltages, the flatter slope is attributed to a mixed rate-limitation arising from two processes: first, electron transfer involving oxidation and reduction of metal atoms or ions, and second, ion hopping or ion migration. In many ECM devices, a medium voltage range can be identified in such plots, usually represented by a moderately steep slope, which is solely associated with electron transfer limitations. This regime emerges because the other two processes proceed on faster timescales at this voltage range [47]. In the present study, electron transfer and ion migration processes

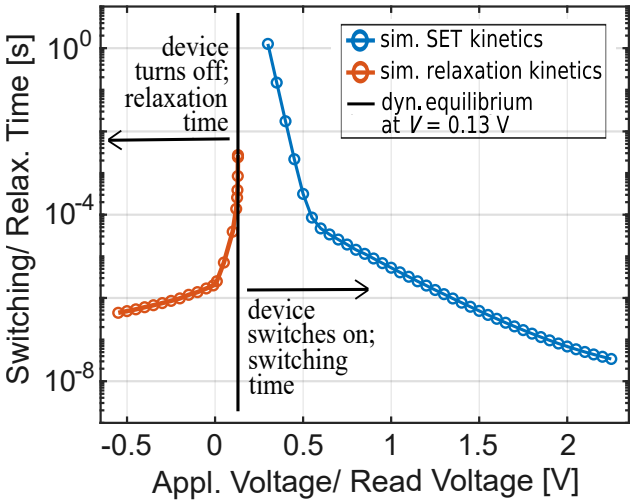

Figure 6.6: Simulated dependencies of v-ECM devices are presented, as the relaxation kinetics in red together with the threshold switching kinetics in blue is displayed. The simulations reveal that the relaxation time decreases in a distinctly nonlinear manner as the applied voltage is reduced. Each relaxation simulation is initialized from a LRS characterized by a filament gap of 0.172 nm, thereby ensuring consistent starting conditions. In contrast, the threshold switching time exhibits a nonlinear decrease with increasing applied voltages, illustrating the strongly voltage-dependent dynamical behavior of the device. Adapted under the terms of CC-BY 4.0 license [46].

operate with comparable rates, leading to the disappearance of the medium voltage regime.

On the left-hand side of V_{emf}, immediately adjacent to the equilibrium value, a steep slope in the relaxation kinetics curve (red) becomes evident. Here, the relaxation is entirely dominated by electron transfer processes, namely redox reactions as expressed in equations (4.9) and (4.10), which drive the dissolution of the filament. For voltages V_{dm} approaching V_{emf}, the relaxation time t_{r} diverges towards infinitely large values. For very small voltages, the exponential behavior described in equations (4.9) and (4.10) transitions into a linear regime. Consequently, the relation $I_{\mathrm{ac}} \sim \eta_{\mathrm{ac}} - V_{\mathrm{emf}}$ holds, which leads to $t_{\mathrm{r}} \sim 1/(\eta_{\mathrm{ac}} - V_{\mathrm{emf}})$. This explains why the relaxation time t_{r} diverges when approaching V_{emf}. A second, less steep slope, located to the left, is attributed to the rate limitation by electron transfer processes, which are responsible for the filament's dissolution.

When a read operation is carried out after programming or writing, a voltage V_{read} larger than 0 V but smaller than V_{emf} is applied. In this context, the choice of V_{read} directly affects the relaxation dynamics, as it determines the relaxation time measured during the read process. The relaxation kinetics curve in the range between 0 V and

0.13 V indicates that the relaxation time increases drastically with higher read voltages, i.e., for $0\,\mathrm{V} < V_{\mathrm{read}} < V_{\mathrm{emf}}$ [59, 103].

Implications about emf strength, sweep rate and ionic current in the I-V characteristics of v-ECM devices

In the subsequent analysis, several I–V sweep simulation results are presented, focusing on the implications of the JART v-ECM model with respect to variations in the electromotive force strength and the sweep rate, as well as the emf's effect on the ionic current. For these I–V sweep simulations, a series resistance of $R_{\mathrm{series}} = 10\,\mathrm{k\Omega}$ is introduced in series with the ECM device.

Figure 6.7 (a) illustrates the influence of selecting different values for V_{emf} in the simulations, shown for the cases $V_{\mathrm{emf}} = 0$ V, 0.07 V, 0.09 V, 0.11 V, 0.15 V, 0.17 V. In comparison to $V_{\mathrm{emf}} = 0\,\mathrm{V}$ with $V_{\mathrm{hold}} = 0\,\mathrm{V}$, the introduction of $V_{\mathrm{emf}} > 0$ causes a rightward shift of V_{th}. Furthermore, V_{hold} increases with higher V_{emf}. For a specific assumed V_{emf}, the maximum achievable V_{hold} equals V_{emf} for sufficiently small sweep rates β, i.e., $V_{\mathrm{hold}} = V_{\mathrm{emf}}$. Figure 6.7 (b) captures this trend by reproducing the linear increase of both V_{th} and V_{hold} with V_{emf}, as extracted from the I–V sweeps presented in Figure 6.7 (a).

Based on sweep rates of $\beta = 625\,\mathrm{V/s}$, 62.5 V/s, 6.25 V/s, 0.625 V/s, 0.0625 V/s, and 0.00625 V/s, the simulation results in Figure 6.8 (a) demonstrate that increasing β shifts V_{th} to the right while V_{hold} moves slightly to the left within an I–V sweep [59]. Figure 6.8 (b) further analyzes these sweeps and reveals the following: As the sweep rate is raised by several orders of magnitude, V_{th} exhibits a linear increase. In contrast, V_{hold} remains constant at the value of V_{emf} until the sweep rate increases by orders of magnitude, exceeding the relaxation dynamics of the device. Now, V_{hold} starts to decrease slightly towards 0 V. Additionally, faster sweep rates leading to larger values of V_{th} is consistent with the device's switching dynamics, where rapid SET processes occur predominantly at higher voltages.

The ionic current illustrated in Figure 6.9 represents the contribution of ions to the overall current, obtained from an I–V sweep simulation with $V_{\mathrm{emf}} = 0.13\,\mathrm{V}$ and a sweep rate of $\beta = 62.5\,\mathrm{mV/s}$. Prior to any switching or relaxation events, this ionic current serves as the driving factor: At 0 V, a relatively large negative ionic current of approximately $-5\,\mathrm{pA}$ can be observed. As the device approaches the dynamic equilibrium at V_{emf}, the ionic current decreases towards zero, before becoming positive for $V_p > V_{\mathrm{emf}}$ and subsequently increasing with positive polarity. At V_{th}, where the ionic current reaches

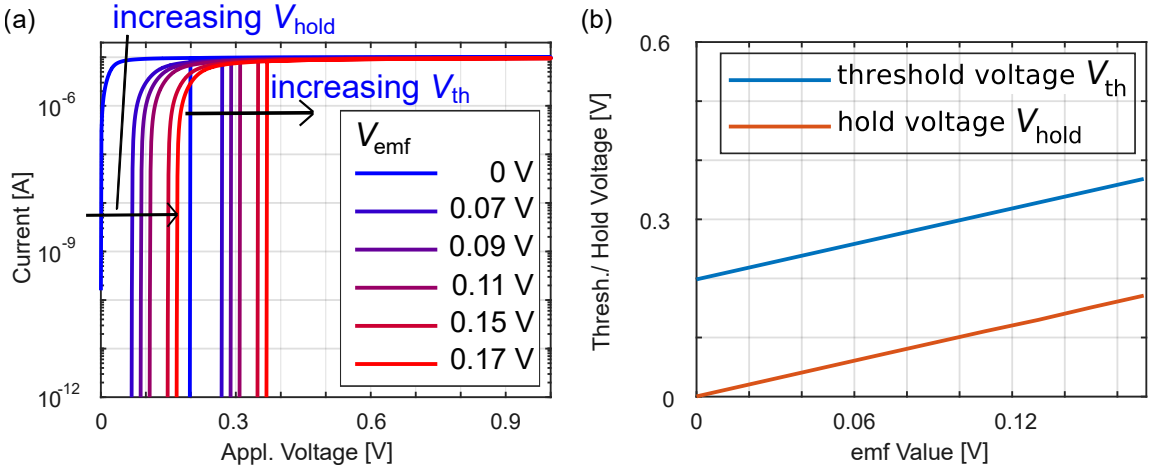

Figure 6.7: (a) Influence of the electromotive force V_{emf} on the I-V sweeps of the device. When compared to the reference case with $V_{\mathrm{emf}} = 0$ V, both the threshold voltage V_{th} and the hold voltage V_{hold} are shifted toward higher values by approximately the amount of V_{emf}. The sweeps are performed with a rate of $\beta = 62.5$ mV/s. (b) Threshold voltages V_{th} and hold voltages V_{hold} extracted from the I–V sweeps shown in (a). An increase in V_{emf} systematically raises both V_{th} and V_{hold}. For low sweep rates, as exemplified here by $\beta = 62.5$ mV/s, V_{hold} essentially coincides with the value of V_{emf}, reflecting the dominant influence of the emf under slow biasing conditions. Adapted under the terms of CC-BY 4.0 license [46].

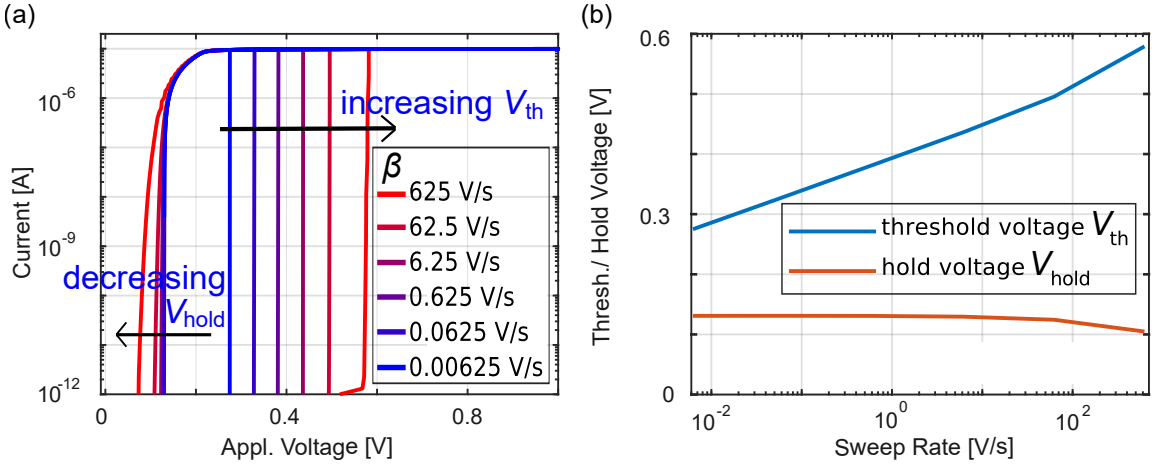

Figure 6.8: (a) Influence of the sweep rate β on the I-V sweeps of the device. The simulations demonstrate that with increasing β, the voltage separation between the threshold voltage V_{th} and the hold voltage V_{hold} widens: while V_{th} systematically increases, V_{hold} shifts downward and tends to approach values close to 0 V. (b) Threshold voltages V_{th} and hold voltages V_{hold} extracted from the I–V sweeps in (a). A higher sweep rate β results in a pronounced increase of V_{th}, whereas V_{hold} exhibits a slight reduction. In contrast to the behavior described in Figure 6.7, for large β the hold voltage no longer coincides with the electromotive force V_{emf}, underscoring the dependence of the relaxation dynamics on the applied sweep dynamics. Adapted under the terms of CC-BY 4.0 license [46].

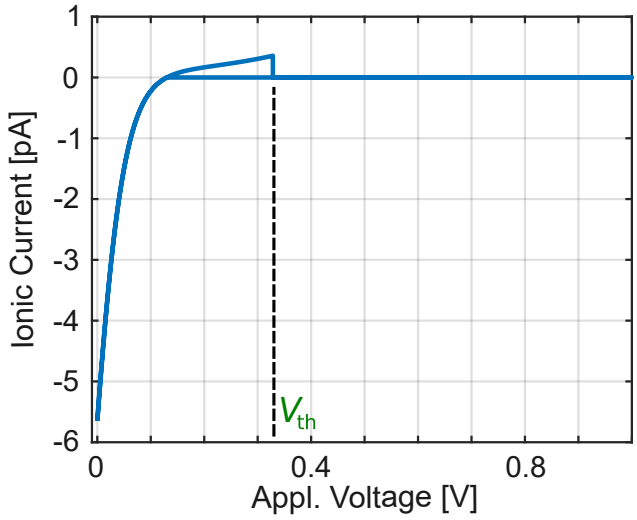

Figure 6.9: Ionic current contribution during a I-V sweep for a configuration with a series resistance of $R_{\text{series}} = 10$ kΩ. For programming voltages $V_{\text{p}} < V_{\text{emf}} = 0.13$ V, the ionic current has negative values, which corresponds to the dissolution of the conductive filament. At the point $V_{\text{p}} = V_{\text{emf}}$, the ionic contributions from growth and dissolution processes exactly compensate each other, resulting in a net ionic current of zero. For voltages $V_{\text{p}} > V_{\text{emf}}$, a positive ionic current is observed prior to threshold switching, indicating the growth of the metallic filament. After the switching event at the threshold voltage V_{th}, the device enters the LRS, where the ionic current rapidly decreases as a consequence of the voltage divider effect between the series resistor and the v-ECM device. Adapted under the terms of CC-BY 4.0 license [46].

about 0.3 pA, it abruptly drops back to zero, thereby marking the switching transition to the LRS. When a sufficiently large series resistance is present, here $R_{\text{series}} = 10\,\text{k}\Omega$, a sharp decrease in V_{dm} occurs. At this point, the device enters a highly conductive state, such that a significant portion of the applied voltage no longer drops across the device itself. As a consequence, the ionic current rapidly falls to nearly zero immediately after the switching event. During the subsequent backward sweep from 1 V to 0 V, the current remains at this suppressed level until the ionic contribution becomes more strongly negative once V_{emf} is crossed again. This triggers the dissolution of the filament and initiates the device's relaxation process.

Summary of simulation study

In summary, the investigations reveal that both the switching kinetics and the relaxation kinetics of the JART v-ECM model exhibit a pronounced nonlinearity. Specifically, the switching and relaxation times decrease significantly as the applied voltage deviates further from the electromotive force value V_{emf}. During a read process within the range

$0 < V_{\mathrm{read}} < V_{\mathrm{emf}}$, the choice of the explicit V_{read} value strongly influences the relaxation behavior. Depending on this choice, relaxation time can vary by several orders of magnitude.

For I–V sweeps, an increase in the emf value V_{emf} results in a higher threshold voltage V_{th} as well as an elevated hold voltage V_{hold}. Conversely, increasing the sweep rate causes V_{th} to rise, while V_{hold} shows a slight reduction. The ionic current contribution I_{ion} to the overall cell current I_{cell} underscores the crucial role of ionic processes within the JART v-ECM framework. For device voltages V_{dm} below V_{emf}, the ionic current is negative, thereby promoting filament dissolution. In contrast, for V_{dm} values exceeding V_{emf}, the ionic current becomes positive and drives filament growth. Finally, the condition $V_{\mathrm{dm}} = V_{\mathrm{emf}}$ reflects the ionic dynamic equilibrium established with I_{ion}.

6.3 Comparison with other Volatile ECM Models in Literature

A broad spectrum of theoretical descriptions for volatile switching in ECM devices has been proposed in the literature. Approaches range from rather generic, behaviour-oriented formulations [166–168], through deterministic, partly physics-based models [169–171], to fully physics-based frameworks that account for phenomena, such as coupled drift, diffusion and thermophoretic effects [172–174]. Additional works include surface/interfacial-energy minimization in combination with surface diffusion [135, 136, 175–179], models based on direct and Fowler–Nordheim tunnelling [180], and descriptions of metallic atom-cluster motion in tilted electric potentials [154, 181, 182]. These physical models operate on different scales: from atomistic treatments [124, 136, 154, 176–178, 181–183] to KMC simulations [136], finite-element formulations [175, 178], and other numerical schemes [177]. The present model places particular emphasis on benchmarking against compact models intended for higher-level circuit simulation [135, 166–174, 176, 179, 180]. Despite this variety, most of the available models still lack the maturity and robustness needed to consistently reproduce the full experimental footprint - covering I–V sweeps, switching (SET) kinetics, and relaxation behaviour.

6.3.1 Comparison with v-ECM Compact Models

Model consistency under different programming and subsequent read conditions is typically ensured only by invoking several external assumptions. In practice, empirical mod-

els [166–171] often fit I–V curves or other static features, but do not capture the device dynamics. The same limitation generally applies to compact models that incorporate drift, diffusion and thermophoresis [172–174]; while these might reproduce certain aspects of relaxation, this has not been demonstrated convincingly, and their suitability for switching dynamics remains unclear. Crucially, most models fail to represent the distinct rate-limiting processes that shape the switching kinetics. Frameworks based on interfacial-energy minimization together with surface diffusion [135, 136, 175–180] usually neglect these process-specific limitations. Moreover, many approaches treat switching and relaxation with different processes or pre-assigned voltage ranges, i.e., in an asynchronous fashion, which leads to internal inconsistency between the two descriptions.

To evaluate how far the present model advances the state of the art, a systematic comparison with published v-ECM models is carried out. The assessment considers both static and dynamic capabilities by checking whether models can reproduce the full set of experimentally observed features. Of primary importance is the ability to capture dynamic behavior, namely the switching kinetics and the relaxation kinetics. If a study has not reported a direct measurement of the switching kinetics, an alternative version of it is sufficient: the device is first programmed by a voltage sweep and allowed to relax, after which a second programming sweep is applied. From the dependence of the second-switching voltage on the waiting time between the end of the first sweep and the start of the second, an effective switching-kinetics curve can be inferred.

A further and strongest criterion is the faithful reproduction of coupled dynamics - switching into the correct resistance state followed by the appropriate relaxation time - over a *wide* range of initially applied programming stimuli. By contrast, reproducing only static I–V sweeps and/or a single case of pulsed switching with one subsequent relaxation event constitutes the weakest criterion. Table 6.3 compiles these criteria and orders them by importance; the leftmost column lists the most decisive criterion, while the rightmost column lists the least informative one for modeling a volatile device.

The presented JART v-ECM model meets the strongest criteria: it correctly predicts the resistance state after switching and the ensuing relaxation time for a broad range of programming-pulse amplitudes. In addition, it reproduces the switching kinetics; since this has been explicitly demonstrated, the aforementioned alternative experiment for switching kinetics is not repeated here. The model can also simulate relaxation kinetics; however, its experimental reproduction is not shown due to missing measurement data. The static characteristics - I–V sweeps and a single pulsed switching followed by a relax-

Table 6.3: Comparison of various v-ECM models regarding static and dynamic device modeling characteristics and capabilities of modeling them; ✓ marks a characteristic that is fully shown and verified by a measurement data fit in the cited work, (✓) describes a characteristic that has been shown but with certain limitations/restrictions, ○ marks characteristics that have not been shown in the corresponding work, × describes a characteristic that cannot be simulated and fitted to actual measurement data by the corresponding work.

Classification of modeling	Volatile ECM model	Switching to correct programmed state followed by correct relaxation time over big $\Delta V_{\text{applied}}$	Switching kinetics	Switching kinetics for a preprogram. and prerelaxated device	Relax. kinetics (e. g. for read process)	*I-V* sweep	One pulsed switching + cons. relaxation event
Empirical/ behavioral/ mathematical model	[166]	×	×	×	×	✓	×
	[167]	×	×	×	○	✓	○
	[168]	×	×	×	×	✓	×
	[169]	×	×	×	×	✓	✓
	[170]	×	(✓)	×	(✓)	✓	(✓)
	[171]	(✓)	(✓)	×	×	✓	✓
Interfacial energy minimization & surface diffusion	[175]	○	(✓)	○	○	○	○
	[176]	(✓)	×	(✓)	○	✓	✓
	[136]	(✓)	×	(✓)	○	✓	×
	[135]	(✓)	×	(✓)	○	✓	✓
	[177]	×	(✓)	×	(✓)	○	○
	[178]	×	×	×	✓	×	×
	[179]	×	(✓)	×	(✓)	○	✓
	[180]	×	×	×	○	✓	×
Drift, diffusion & thermophoresis	[172]	×	×	×	○	✓	○
	[173]	○	○	○	○	✓	✓
	[174]	×	×	×	○	✓	×
Electromotive force (emf)	THIS WORK	✓	✓	○	(✓)	✓	✓

ation event - are easily captured. A key distinguishing feature is that *all* measurements are described consistently by *one* model for both switching and relaxation, using a *single* parameter set.

By comparison, most empirical or semi-mathematical models in the literature - often loosely inspired by physics - are usually presented only alongside their validated volatile I–V sweeps, without additional dynamical evidence for accuracy [166–168]. One study [170] proposes a model that reproduces the I–V sweep, the device's switching kinetics, and its relaxation kinetics, but employs different parameter fits for each of the three simulations; hence, the description is not consistent. A separate mathematical model [169] correctly simulates one isolated switching event with a subsequent relaxation event and also the device's I–V sweep, yet neither a full switching kinetics curve nor relaxation kinetics data are provided. Another work [171] offers an empirical model that reproduces the device's switching kinetics and the correct relaxation time after programming; however, both the relaxation simulation and the switching kinetics analysis are restricted to a narrow voltage window ($\Delta V = 0.4$ V), so that different inherent rate-limiting processes cannot be accessed. Moreover, no study of how the relaxation time varies with sub-emf read voltages ($V < V_{\mathrm{emf}}$) is reported, i. e. the relaxation kinetics is not shown.

A separate set of publications models the volatility of ECM devices by introducing surface diffusion and interfacial/surface-energy minimization as the driving mechanisms for filament dissolution and relaxation. One of these works [136] reproduces a volatile I–V sweep as well as the alternate switching kinetics over a wide range of waiting times, yet the agreement between experiment and simulation is inaccurate for certain voltage intervals; similar limitations apply to related models [135, 176]. Although these approaches can match the relaxation time after programming, they typically assume a *different* initial filament radius for each programming condition, which renders the modeling inconsistent because an additional assumption about the filament thickness is required to obtain the correct subsequent relaxation time. Another study [178] reproduces relaxation kinetics for different current-compliance values but again varies the initial filament radius between cases, thereby underscoring the same inconsistency. An ion-diffusion model motivated by interfacial-energy minimization [180] reproduces only the I–V sweep; another work [175] simulates switching kinetics over a relatively small voltage range without fitting to experimental data. Models following the same theoretical line [177, 179] can reproduce both switching and relaxation kinetics, but only by assuming an initial filament radius; moreover, additional radius assumptions are introduced when the current-compliance setting is changed.

Other physics-based models [172–174] describe relaxation as an interplay of drift, diffusion, and thermophoresis. These succeed mainly in reproducing I–V sweeps, but not the complete set of dynamical phenomena.

It should be stressed that most physics-based models in the literature - especially those grounded in surface diffusion and interfacial/surface-energy minimization - invoke *different* physical mechanisms for switching and for relaxation [135, 176–179]. In contrast, the present work attributes both switching and relaxation consistently to the same processes: electron transfer–based ionic redox reactions together with ion migration.

Overall, the JART v-ECM model establishes a new benchmark. Beyond accurately fitting experimental I–V sweeps and switching kinetics data with a single, unchanged parameter set, it also reproduces - in a consistent manner - the device's relaxation times after programming with a wide span of pulse amplitudes, without changing initial assumptions across programming conditions. (A possible filament-widening effect that may accompany very strong switching is not included in the present model.)

6.4 Summary

This chapter introduces a physics-based compact model for volatile electrochemical metallization memory devices. The model reliably reproduces and predicts the dynamic SET switching and the subsequent relaxation of v-ECM cells, matching experimentally observed switching kinetics and I–V characteristics, including the measured device/cycle variabilities. A key element of the formulation is the explicit inclusion of the electromotive force as a term that opposes the intrinsic ionic processes - nucleation, charge transfer, and ion migration - that govern ECM operation. The emf term also accounts for filament dissolution and hence for device relaxation once the applied bias falls below the hold voltage, enabling faithful simulation of volatile switching behavior.

Parametric studies of relaxation kinetics highlight the role of the read bias: in the sub-emf regime, larger read voltages lead to longer relaxation times. Consistent with prior reports [23, 68], the model captures the characteristic switching kinetics of ECM cells, where the switching time decreases by orders of magnitude as the applied voltage increases. The simulations further show that introducing the emf translates the threshold and hold voltages in an I–V sweep by approximately the emf value. Increasing the voltage sweep rate by orders of magnitude shifts the threshold to higher voltages, whereas at very fast sweep rates the hold voltage tends toward zero. Analysis of the ionic current

confirms that the emf counterbalances the ionic driving forces, establishing a shifted dynamic equilibrium at the emf level.

A head-to-head comparison with existing v-ECM models demonstrates that the proposed approach sets a new benchmark: with a single model and one parameter set it consistently reproduces dynamic behavior, switching and relaxation features, and full I–V sweeps. Its formulation remedies limitations of prior models by accurately and consistently covering a broad range of dynamic characteristics. As a result, the model is well suited to advance both theoretical investigations and practical studies on the implementation of v-ECM devices in large-scale circuit contexts.

The model is ready for direct use in circuit simulators, enabling circuit design for real applications. It can represent selector elements for CIM operations in ANNs and SNNs, serve as a component in hardware neuron circuits such as leaky integrate-and-fire cells that require accurate transient prediction, and support hardware-security use cases. In the upcoming Chapter 7, the v-ECM model is used in a simulated application case in which it serves as select device in the junctions of a passive 1S1R crossbar array. Whether the inherent variability/stochasticity of v-ECM devices is treated as a design challenge to be mitigated or as a feature to be exploited, the variability-aware framework presented here provides a consistent and reliable basis. It also deepens the understanding of the underlying device physics by offering a unified and internally consistent description in which both switching and relaxation are captured within a single robust theory. Despite the successful modeling, the emf as physical origin for v-ECM is a subject of debate, as measured emf potentials remain small and indicate the need for further research.

7 Passive Crossbar Array Simulations of Read and VMM Operations

Crossbar arrays of nanometer scale consisting of nano-electronic ReRAM devices provide the path towards neuromorphic computing and neural network computation within hardware. The fundamental and relevant concepts for the following studies are introduced comprehensively in section 2.6.

To meet density and efficiency requirements for hardware-based CIM operations, such as *multiply–accumulate* (MAC) operations between inputs and learned weights, for neural networks, highly scalable crossbar arrays with cell areas on the order of $4F^2$ have been intensely investigated, as they promise ultra-dense, energy-efficient memory stacks [30, 31]. A first commercial use of such ultra-dense crossbar arrays has been realised by the development of 3D XPoint technology developed jointly by Intel and Micron [184, 185]. A central prerequisite for scaling passive crossbar arrays is the availability of a device that suppresses parasitic (sneak-path) currents as crossbar junction select device to avoid false read/write or VMM operations due to leakage currents. A common solution is to employ a volatile threshold selector in series with a memristive memory element, forming a 1S1R configuration. Beyond the memory-and-selector pair, the arrays also comprise the finite resistances of the interconnecting wires (e.g., word/bit lines), which further influence array behavior and performance [87, 88].

Through special read and write schemes, an accidental programming of neighboring devices is avoided. The same aim is followed, when select devices are utilized for reliable VMM crossbar operations. All devices that show and fulfil the threshold switching and selecting feature, as presented in section 2.6.1, can be considered as the selector devices within a combined 1S1R device.

A static crossbar array model considering line resistance and only one bistable nonlinear device has been presented in [87]. It investigates simple read and write operations. In a further work [88], three novel read-out techniques with linear, selectorless crossbar arrays have been presented. A more recent work [186] investigates an analytical circuit

model for worst-case MAC operations on a 1S1R array. The deviation of the cell bias voltage from the desired value is calculated.

In this work, the performance of a NbO_2-based threshold switch model from literature, presented in 3.2.3, as selector devices within 1S1R crossbar arrays is exemplarily compared with the newly developed JART v-ECM model, presented in section 4.1.2. A focus of this comparison lies on reading of single ReRAM crossbar devices and on performing VMM operations on these 1S1R crossbar arrays. The corresponding ReRAM device is represented by the VCM model, presented in section 3.2.2. A further focus lies on the inclusion of wire resistances and their impact on the 1S1R crossbar array size for reliable reading and computing. Parts of this chapter have been published in [24].

7.1 Simulated Characteristics of a Single 1S1R Crossbar Device

In the following, two distinct 1S1R crossbar junction devices are built up and their transient electric behavior is investigated according to section 2.6.1. The focus lies on their behavior as a single 1S1R device, before integrating them into a large-scale crossbar array.

In order to fulfil the requirements of a 1S1R device, presented in section 2.6.1, the model parameter values introduced in the corresponding references are modified for the goal of this work. By the modification it is ensured that the requirements according to Figure 2.10 are fulfilled, i. e., $V_{\mathrm{hold}} < V_{\mathrm{th}} < V_{\mathrm{SET}}$, and $R_{\mathrm{ON}} < R_{\mathrm{LRS}} < R_{\mathrm{HRS}} < R_{\mathrm{OFF}}$. Here, V_{hold}, V_{th}, R_{ON}, and R_{OFF} belong to the corresponding selector device, whereas V_{SET}, R_{LRS}, and R_{HRS} belong to the ReRAM device - a VCM device in both cases. The parameter value modification is performed for both 1S1R device models, which are presented in the following.

The state variable in the VCM ReRAM device model, which determines the resistance state, is defined as the oxygen vacancy (defect) concentration N_{disc} within the disc region, located in the oxide near the active electrode. $N_{\mathrm{init}} = N_{\mathrm{disc,min}} = 0.02 \cdot 10^{26}$ m^{-3} defines the HRS, whereas the LRS is defined by $N_{\mathrm{init}} = N_{\mathrm{disc,max}} = 1 \cdot 10^{26}$ m^{-3}. This is the only VCM parameter which is actively changed - between these two values - as an initial condition.

7.1.1 The 1S1R Device consisting of a Threshold Switch

The threshold switch model from section 3.2.3 is combined in series with the VCM cell from section 3.2.2 model to make up a 1S1R device. Both models are not self-derived and are taken separately from literature [94–96]. The modified parameter values of the VCM device model and the threshold switch model are presented in Table 7.1 and 7.2, respectively. The selector switches from the OFF state to the ON state once a defined threshold voltage is reached. When the applied voltage subsequently drops below a specific hold voltage, the device reverts to the OFF state. This switching behavior occurs for both voltage polarities. For the nonvolatile VCM device, opposite polarities for SET and RESET are required. Simulated *I-V* sweeps of both devices with a sweep rate of $\beta = 4$ V/ms are compared in Figure 7.1.

Symbol	Value	Symbol	Value
l_{cell}	3 nm	A^*	$6.01 \cdot 10^5$ A/(m^{2}K^2)
l_{disc}	1 nm	$e\phi_{\mathrm{Bn0}}$	0.3 eV
r_{fil}	30 nm	$e\phi_{\mathrm{n}}$	0.1 eV
z_{Vo}	2	μ_{n}	$1 \cdot 10^{-5}$ m^2/(Vs)
a	0.4 nm	N_{plug}	$2 \cdot 10^{27}$ m^{-3}
ν_0	$3 \cdot 10^{11}$ Hz	$N_{\mathrm{disc,max}}$	$1 \cdot 10^{26}$ m^{-3}
ΔW_A	0.9 eV	$N_{\mathrm{disc,min}}$	$2 \cdot 10^{24}$ m^{-3}
ε	$17 \cdot \varepsilon_0$	R_{series}	1200 Ω
$e\phi_{\mathrm{B}}$	$5.5 \cdot \varepsilon_0$	$R_{\mathrm{th,eff}}$	$1 \cdot 10^5$ K/W
T_0	293 K		

Table 7.1: Used model parameter values for the nonvolatile VCM model.

Parameter	Value	Parameter	Value
R_0	340 Ω	R_{ser}	330 Ω
Γ_{th}	$1 \cdot 10^{-7}$ W K^{-1}	E_{a}	0.215 eV
ε_{r}	45	l_{ox}	$8 \cdot 10^{-8}$ m
C_{th}	$2.5 \cdot 10^{-13}$ J K^{-1}		

Table 7.2: Used model parameter values for the threshold switch model.

Parameter choice for designing the 1S1R device. An explanation for the chosen modified parameter values compared to the values given in the references and their effect is given in the following for both the select device and the VCM device: For both

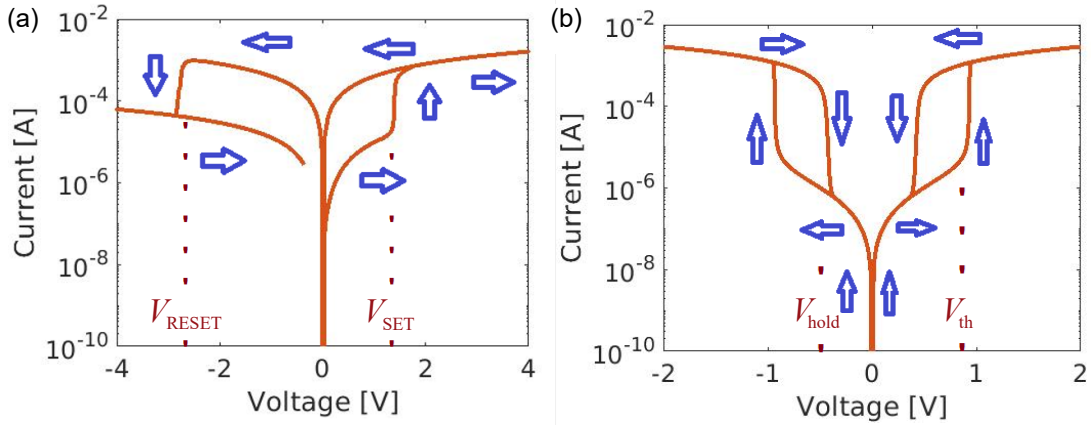

Figure 7.1: Simulated I-V sweeps of a (a) VCM cell and a (b) threshold switch carried out with a sweep rate of $\beta = 4$ V/ms. The used model parameter values are given in Table 7.1 and 7.2. Reproduced with permission from [24], © 2022 IEEE.

devices, an increase in the thermal conductance Γ_{th} raises the absolute SET and threshold voltages in the I-V characteristics. (Γ_{th} is the reciprocal value of the effective thermal resistance $R_{\mathrm{th,eff}}$.) In particular, for the select device, a higher thermal capacitance C_{th} causes a broader hysteresis in the $I-V$ response: the threshold appears at larger absolute voltages and the ON-state current increases slightly. At the same time, the absolute hold voltage is reduced and the OFF-state currents become smaller. Modifying one or both of the internal series resistances R_{series} in the models alters the overall cell current. A suitable tuning of both Γ_{th} (thermal resistance $R_{\mathrm{th,eff}}$) and C_{th} makes it possible to satisfy the condition $V_{\mathrm{th}} < V_{\mathrm{SET}}$. By adjusting the combination of R_{series} and C_{th}, the resistance states of the device can be ordered as $R_{\mathrm{ON}} < R_{\mathrm{LRS}} < R_{\mathrm{HRS}} < R_{\mathrm{OFF}}$. The leakage current and the overall current level can thus be influenced through combined adjustment of R_{series} and C_{th}. Further critical parameters for shaping the I–V characteristics of the ReRAM cell are the initial (minimum) oxygen vacancy concentration N_{init} ($N_{\mathrm{disc,min}}$), the maximum oxygen vacancy concentration $N_{\mathrm{disc,max}}$, the nominal Schottky barrier $e\Phi_{\mathrm{Bn0}}$, the activation energy for ion hopping ΔW_{A}, and the disc length l_{disc}.

Transient pulse characteristics. Figure 7.2 presents the transient electrical response of the 1S1R cell (initially in the HRS) when rectangular voltage pulses of 1.5 V and 2.05 V are applied, including the corresponding voltage drop across the selector. The rise time of the pulse is set to 100 ps and the hold time to 200 µs. At 1.5 V, a distinct change in the selector's voltage drop becomes visible once it switches into the ON state (cf. Figure 7.2 (a)). In this case, the applied bias exceeds V_{th}, leading to a sharp increase of the device current into the µA range. However, the voltage across the VCM cell after

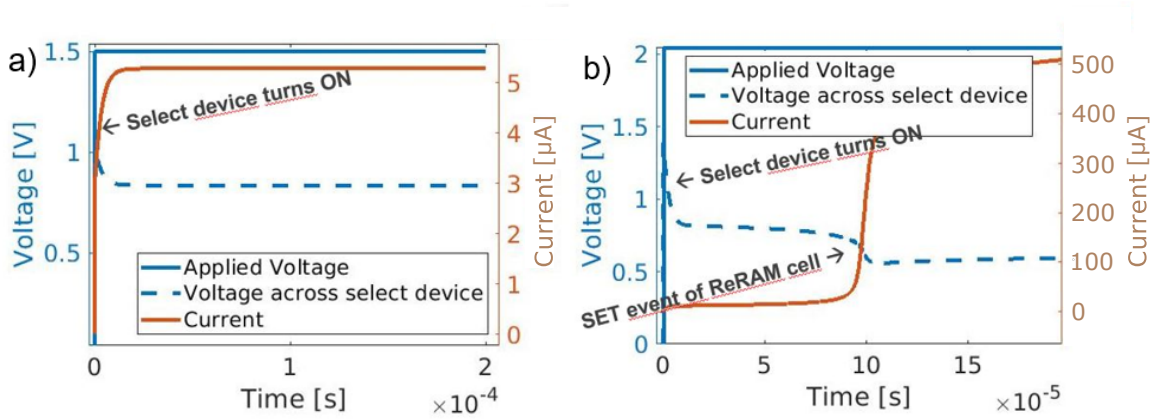

Figure 7.2: Simulated pulse characteristics of a 1S1R cell made up of a VCM cell and a threshold switch. (a) shows the case for an applied voltage of 1.5 V: Only the the threshold switch device turns on. (b) shows the case for an applied voltage of 2.05 V: First threshold switch turns on followed by the SET of the VCM cell. A NDR region becomes observable. The used model parameter values are given in Table 7.1 and 7.2. Reproduced with permission from [24], © 2022 IEEE.

the selector has switched into the ON state does not exceed V_{SET}, indicating that the device remains in the read regime. When a 2.05 V pulse is applied, a rapid voltage drop across the selector drives it into the ON state (cf. Figure 7.2 (b)), accompanied by a slight but noticeable current increase after several microseconds. Since the VCM cell now receives sufficient bias ($> V_{\mathrm{SET}}$), a SET transition occurs after approximately 100 µs, which reflects the expected switching kinetics of ReRAM cells [47, 153]. At the end of the pulse, the current reaches several hundred µA, consistent with the VCM device being in the LRS.

An additional effect becomes evident: after the SET event, the voltage drop across the selector decreases even further, once the VCM cell has switched into its LRS state [96, 187, 188]. This phenomenon is linked to the NDR region of the selector's I-V characteristic in series with a resistor. As the voltage across the selector decreases initially - while the VCM device is in its HRS -, the current continues to rise, clearly revealing the selector's NDR behavior. While the VCM device remains in the HRS, the selector does not fully switch ON. When a 2.05 V bias is applied and the ReRAM undergoes a SET transition, the selector can fully switch ON, and a second NDR region emerges, corresponding to an additional voltage drop across the selector.

In general, when the threshold switch is connected in series to another device, an increase in the current through the selector results in a reduced voltage drop across it. Consequently, the selector allows higher current only when its own resistance decreases.

Once the ReRAM device switches to the LRS, the selector's resistance drops even further than that of the memory element, giving rise to the NDR behavior. It highlights that accurate representation of this effect requires the use of a physics-based or mathematical model that properly accounts for the full dynamical behavior of both devices. A model of threshold switches' NDR effect has been presented in the literature [187, 188]. However, it has not been developed based on physics.

7.1.2 The 1S1R Device consisting of a Volatile ECM Cell

The v-ECM model from section 4.1.2 is combined with the same VCM device model as in the case of the previous 1S1R cell. This combination provides the framework for the second investigated 1S1R cell. Also, the VCM model parameter values stay the same, thus presented in Table 7.1. The modified parameter values of the v-ECM model are presented in Table 7.3. While for the nonvolatile VCM cell opposite polarities for SET and RESET are required, the v-ECM model features switching from and to both states for the positive polarity. Accordingly, the comparison of both simulated I-V characteristics with a sweep rate of $\beta = 4$ V/ms confirms this behavior. The simulated I-V sweep of the v-ECM cell is presented in Figure 7.3.

Table 7.3: Used model parameter values for the v-ECM cell.

Symbol	Value	Symbol	Value
M_{me}	$1.79 \cdot 10^{-22}\,\mathrm{g}$	r_{ac}	$10\,\mathrm{nm}$
z	1	r_{fil}	$1\,\mathrm{nm}$
$\rho_{\mathrm{m,me}}$	$10.49\,\mathrm{g\,cm^{-3}}$	r_{is}	$1\,\mathrm{nm}$
m_{r}	0.84	L	$3\,\mathrm{nm}$
ΔW_0	0.2 eV	ρ_{fil}	$1.7 \cdot 10^{-8}\,\Omega\mathrm{m}$
α_{et}	0.3	R_{series}	$1100\,\Omega$
$k_{0,\mathrm{et}}$	$5 \cdot 10^{3}\,\mathrm{s^{-1}}$	T	$298\,\mathrm{K}$
c	$3 \cdot 10^{28}\,\mathrm{m^{-3}}$	$t_{0,\mathrm{nuc}}$	$2 \cdot 10^{-7}\,\mathrm{s}$
ΔG_{et}	0.35 eV	ΔG_{nuc}	$0.84\,\mathrm{eV}$
a	$0.4\,\mathrm{nm}$	N_{c}	1
f	$1 \cdot 10^{13}\,\mathrm{Hz}$	α_{nuc}	0.25
ΔG_{hop}	$0.15\,\mathrm{eV}$	V_{emf}	$0.13\,\mathrm{V}$

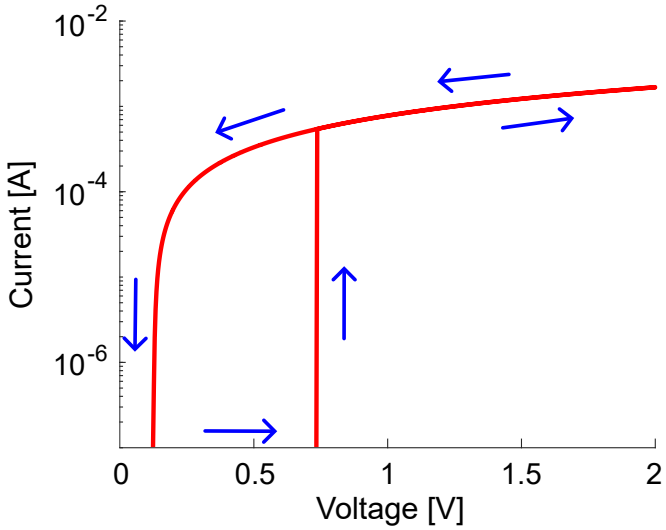

Figure 7.3: Simulated I-V sweeps of a volatile ECM cell carried out with a sweep rate of $\beta = 4$ V/ms. The used model parameter values are given in Table 7.3.

Parameter choice for designing the 1S1R device. Some v-ECM model parameters have been especially modified to fulfil the requirements of a 1S1R device: in order to allow for the lowest resistance when the v-ECM device is in its ON state, ΔW_0 has been reduced to 0.2 eV and $R_{\text{series}} = 1100\ \Omega$. The choice of the parameter values c, ΔG_{et}, ΔG_{hop}, a contribute to a fast switching, providing $V_{\text{hold}} < V_{\text{th}} < V_{\text{SET}}$. A similar device design can be achieved by adapting other parameter values. A feature inherent to ECM cells is especially exploited for more reliable read, write and VMM operations: As the HRS/OFF state of ECM cells is dominated by the high-resistive ionic conduction and electronic conduction is usually highly suppressed, the v-ECM select device provides a relatively high OFF state if it is designed accordingly. Therefore, when applying a v-ECM device as select device it implicates that R_{OFF} has the highest value compared to the other three relevant resistance values.

Transient pulse characteristics. Figure 7.4 (a) and (b) show the applied rectangular voltage pulse of 0.78 V and 1.45 V, respectively, and the corresponding current responses as well as the voltage drops across the v-ECM selector device. With 5.05 µA and 191 µA at $t_{\text{read}} = 200$ µs the current response is similar as in the case of the threshold switch 1S1R device, indicating that the resistance values for the investigated applied volatges are in similar ranges for both 1S1R devices. Figure 7.4 (a) shows the situation in which the select device jumps into its ON state from the OFF state, while the VCM cell remains in its initial HRS. Figure 7.4 (b), however, illustrates the case for which both

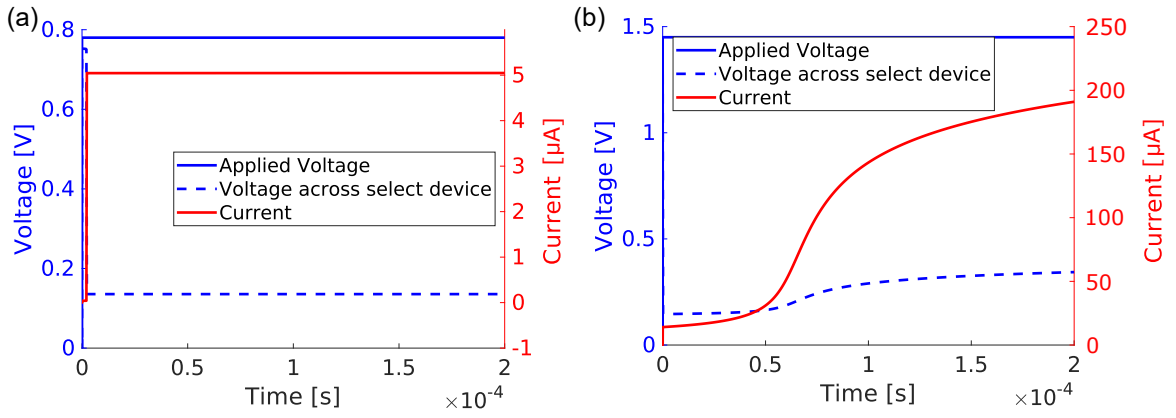

Figure 7.4: Simulated pulse characteristics of a 1S1R cell made up of a VCM cell and a volatile ECM cell. (a) shows the case for an applied voltage of 0.78 V: Only the the v-ECM device turns on. (b) shows the case for an applied voltage of 1.45 V: First the v-ECM cell turns on followed by the SET of the VCM cell. A NDR region is not observable, as the voltage across the select device does not drop further but increases again after the SET event. The used model parameter values are given in Table 7.1 and 7.3.

the select v-ECM device as well as the VCM device change their resistance state from high-resistive to low-resistive. Thus, the VCM is selected and programmed from the HRS to the LRS for the applied 1.45 V. Contrary to the threshold switch, the v-ECM cell does not exhibit a significant NDR: The current only increases with decreasing voltage drop across the select device, when the select device (being in series to the VCM cell) jumps into the high-conducting ON state. However, when the VCM cell undergoes a SET process, the voltage drop across the select device increases again, which implicates that - contrary to a NDR behavior - the voltage drops across the considered device needs to increase whenever a device in series succeeds in reducing its own resistance.

A special case interesting in terms of application realization is observed for the simulation when a 0.675 V rectangular pulse is applied to the 1S1R device and its electric behavior is read out after $t_{\mathrm{read}} = 200$ µs. If the VCM device is initially in its LRS, sufficient voltage drops across the select v-ECM device. This voltage drop succeeds in initiating a resistance change of the select device from the OFF state to the ON state. Thus, the VCM cell in its LRS is successfully selected and a current of 150 µA is calculated after 200 µs. However, if the VCM cell is initially in its HRS, no sufficient voltage can drop across the v-ECM select device to initiate its resistance change. Instead, the v-ECM selector remains in its OFF state, although the major part of the total applied voltage still drops across it. Due to the smaller voltage drop across the selector it needs more time than 200 µs to change its resistance state from OFF to ON, according to

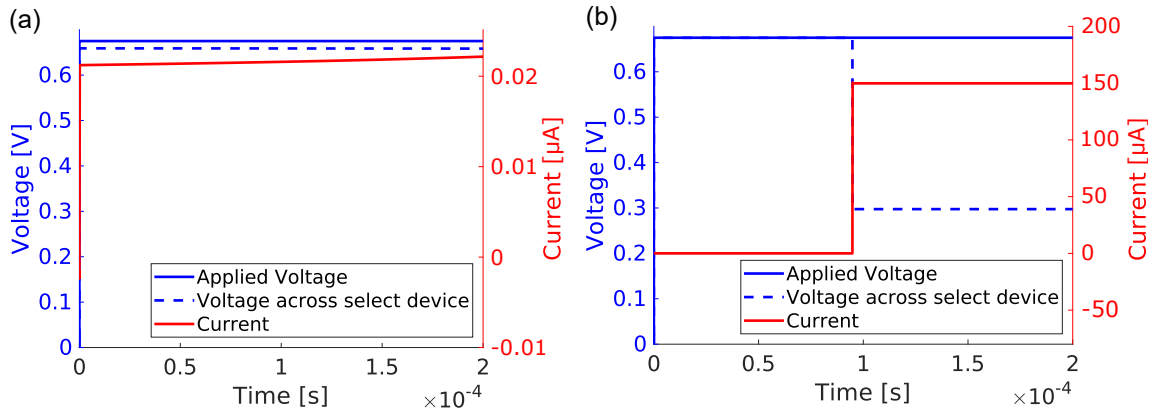

Figure 7.5: The special case of simulated pulse characteristics of a 1S1R cell made up of a VCM cell and a volatile ECM cell. (a) shows the case for an applied voltage of 0.675 V and the VCM in its HRS: Due to non-sufficient voltage drop across the v-ECM cell the whole 1S1R cell stays unselected, as neither the select device switches to the ON state nor the VCM device is read out. (b) shows the case for an applied voltage of also 0.675 V but the VCM in its LRS: Due to a sufficient voltage drop across the select device the 1S1R is selected. A high current distinction is ensured for a non-selected VCM cell in its HRS and a selected VCM cell in its LRS. The used model parameter values are given in Table 7.1 and 7.3.

the switching kinetics of a v-ECM device. The large resistance window spans over four orders of magnitude: The current calculated after 200 µs is only 22.2 nA and is therefore distinctly smaller than the current measured for the VCM cell in its LRS. The same consideration for the threshold switch-based 1S1R device gives only a distinction of two orders of magnitude in current when comparing read of a LRS and HRS. Thus, the switching kinetics, the high OFF state of v-ECM devices and the voltage divider effect are exploited for the 1S1R crossbar device based on a v-ECM cell in order to make crossbar array operations more reliable, as shown in the upcoming sections.

7.2 Read Scheme for 1S1R Crossbar Devices

In the following, for both previously introduced 1S1R devices, the read operation of one single 1S1R device in a 3x3 - crossbar array is investigated and the results are used for the assessment of bigger array's corresponding behavior. An additional focus lies on the inclusion of wire resistances and their effect on a read scheme. They are placed on both terminal ends of the respective 1S1R crossbar junctions. As illustrated in Figure 2.9 and 2.11 and 7.6, a 3x3- crossbar array consists of 9 1S1R cells in the junctions, and 18 wire resistances. The $V/2$ scheme is applied to this crossbar: The 1S1R cell in the

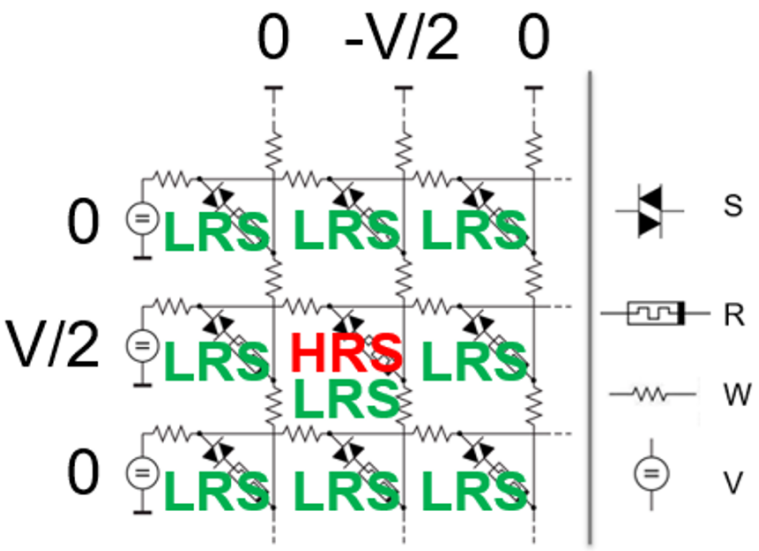

Figure 7.6: For evaluating the worst case for reading a 3×3 - crossbar array, the V/2 - scheme is applied to a selected cell in the middle in its HRS and LRS. Both cases are compared to each other.

middle is selected, while the four cells that share the same bit line (BL) or word line (WL) are half-selected, the remaining four cells are unselected and unbiased devices. For investigating the read of a selected VCM cell in its LRS, all VCM cells on the crossbar are in their LRS. The investigation of reading a selected VCM cell in its HRS is performed with the same configuration with the only difference that the selected VCM cell is in its HRS.

Read scheme without select devices. The first investigation is performed with a 1R crossbar array, i. e., no select device in series to the VCM cell is present. The VCM cell is in its HRS. A rectangular voltage pulse of 0.6 V is applied to the selected device in its HRS in order to read its resistance state. The corresponding current is measured after $t_{\mathrm{read}} = 50$ µs.

As also summarized as case a) in Table 7.4, no current is detected for the non-selected LRS devices, while each of the four half-selected LRS cells carries 118.6 µA and the selected HRS cell carries 4.5 µA. Consequently, the total current on the selected BL reaches 241.7 µA. This outcome demonstrates that reading the selected cell cannot be achieved successfully in the absence of a select device.

Table 7.4: Read scheme scenarios. The current through distinct crossbar cells is given.

$V_{\text{read}} = 0.6$ V for a) $V_{\text{read}} = 1$ V for b) - e) $V_{\text{read}} = 0.675$ V for f) - i)	LRS, nonsel.	LRS, half-sel.	HRS, selected	LRS, selected
a) no wire res, only ReRAM	0 A	118.6 µA	4.51 µA	-
b) no wire res, TS-based 1S1R	0 A	1.01 µA	1.84 µA	-
c) no wire res, TS-based 1S1R	0 A	1.01 µA	-	197.1 µA
d) 1 kΩ wire res, TS-based 1S1R	-1.25 nA/ -2.53 nA	0.978 µA/ 0.992 µA	1.79 µA	-
e) 1 kΩ wire res, TS-based 1S1R	-0.99 nA/ -1.55 nA	0.612 µA/ 0.791 µA	-	60.83 µA
f) no wire res, v-ECM-based 1S1R	-2.390 nA	1.047 nA	22.16 nA	-
g) no wire res, v-ECM-based 1S1R	-2.390 nA	1.047 nA	-	149.9 µA
h) 1 kΩ wire res, v-ECM-based 1S1R	-2.390 nA	1.047 nA	22.13 nA	-
i) 1 kΩ wire res, v-ECM-based 1S1R	-2.390 nA	487.5 pA/ 215.1 pA	-	71.06 µA

7.2.1 Read Scheme in a Threshold Switch-based 1S1R Crossbar Array

First, a threshold switch is integrated into each crossbar junction. It gives the threshold switch-based 1S1R device, as introduced in section 7.1.1.

Introducing a threshold switch select device significantly enhances the read-out operation. The read-out is performed with $V_{\text{read}} = 1$ V after $t_{\text{read}} = 50$ µs. This improvement is confirmed by the cases b) and c) in Table 7.4. In case b), the same configuration as in a) is considered, with the only modification being the integration of a threshold switch connected to each ReRAM cell. The half-selected cells in the LRS exhibit currents of 1.01 µA each, while the HRS-selected cell in the middle shows a current of 1.84 µA (case b)). In case c), all 1S1R cells are in the LRS. Again, the half-selected LRS cells register 1.01 µA each, but the centrally selected LRS cell produces a comparatively large current of 197.1 µA.

Despite the leakage current from the half-selected LRS cells (1.01 µA each), the resistance state of the middle 1S1R cell can still be determined reliably for crossbar arrays up to a maximum size of 194×194. This upper limit is estimated by equating the sum of the $(x-1)$ half-selected LRS currents on the BL and the full-selected HRS cell current and

by comparing it with the current of a fully selected LRS cell. The resulting relationship, 1.84 µA + $(x-1) \cdot 1.01$ µA = 197.1 µA, gives $x = 194$. The adverse influence of leakage current on read-out reliability can be mitigated by employing an ADC with two distinct current ranges (LRS vs. HRS) for state detection.

For cases d) and e), the programmed device resistance states resemble those of b) and c), respectively, but here additional wire resistances (1 kΩ each) are incorporated into the crossbar structure, before and after each cell. The wire resistance value is chosen relatively large, as it contributes to the investigation of an extreme case. This leads to a clear separation of the measured current levels. The four half-selected LRS cells no longer yield a uniform current but instead two distinct levels due to extra voltage drops across the wire resistances. Furthermore, a minor reverse current is observed through non-selected cells for the same reason. These reverse currents remain negligible for the read-out process.

A similar approximation to the one used before indicates that, with these current levels, a feasible crossbar array size is limited to 60×60. The calculation is based on 1.79 µA + $(x-1) \cdot 0.992$ µA = 60.83 µA, which resolves to $x = 60$. These results are derived from Table 7.4, cases d) and e). It should be emphasized, however, that this estimate extrapolates read currents from a 3×3 array without accounting for compulsory additional wire resistances introduced as arrays scale up. Consequently, the practically achievable array size is expected to be even smaller.

7.2.2 Read Scheme in a Volatile ECM-based 1S1R Crossbar Array

Integrating a v-ECM device into each crossbar junction instead of a threshold switch next to the VCM ReRAM cell gives the other 1S1R device, as introduced in section 7.1.2. As it is chosen to perform the read-out with the applied voltage $V_{\text{read}} = 0.675$ V for which the select devices stays off for a HRS VCM device, and switches to the ON state for a LRS VCM device, a beneficial situation is exploited for the read: As the OFF state of the v-ECM device is highly high-resistive, a benefit arises from the distinction of four orders of magnitude between selected LRS and unselected HRS. Its implications on the read process are investigated and discussed in the following via simulations. The read is performed after $t_{\text{read}} = 200$ µs. Cases f) and g) from Table 7.4 represent the same configurations as in b) and c), respectively. The only difference is the choice of the select device and the applied rectangular pulse's value. The half-selected cells in the LRS exhibit currents of 1.047 nA each, while the HRS-selected cell in the middle shows a current of 22.16 nA (case f)). In case g), all 1S1R cells are in the LRS state. Again,

the half-selected LRS cells register 1.047 nA each, but the centrally selected LRS cell produces a comparatively large current of 149.9 µA.

By a similar calculation as in the section before, the largest feasible crossbar array size for which a reliable read-out stays possible can be determined. Solving the equation 22.16 nA + $(x-1) \cdot 1.047$ nA = 149.9 µA gives $x = 143170$, and thus a largest crossbar array size of 143170×143170. Compared to the largest feasible array size of 194×194 for a threshold switch-based 1S1R crossbar array, these are three orders of magnitude more BLs and WLs, respectively. The largest feasible threshold switch-based 1S1R crossbar array consists of 37636 1S1R devices, whereas the largest feasible v-ECM-based one consists of approximately 20.5 billion 1S1R devices. The six orders of magnitude difference in the number of crossbar array devices implicates the huge potential of v-ECM based select devices, when they are accordingly engineered. A striking behavior in the simulation results is as follows: As a voltage drop of 0 V across v-ECM select devices does not describe the ionic dynamic equilibrium any more (but a voltage drop of V_{emf} does), according to the emf theory a small negative ionic current of -2.390 nA is calculated by the simulation for nonselected LRS cells. This is valid for any simulation, disregarding the used wire resistances or the resistance state of the selected 1S1R cell within the array.

For cases h) and i), the programmed device resistance states resemble those of b) and c), respectively, or f) and g), respectively, but also here additional wire resistances (1 kΩ each) are incorporated into the crossbar structure, before and after each cell.

A similar calculation for determining the largest feasible array size indicates that, with these current levels, such an array size is limited to 67851×67851. The calculation is based on 22.13 nA + $(x-1) \cdot 1.047$ nA = 71.06 µA, which resolves to $x = 67851$. These results are derived from Table 7.4, cases h) and i). It should be emphasized, however, that also this estimate extrapolates read currents from a 3×3 array without accounting for compulsory additional wire resistances introduced as arrays scale up. Consequently, the practically achievable array size is expected to be even smaller. Nevertheless, the comparison of both 1S1R crossbar arrays with wire resistances of 1 kΩ again displays the potential of v-ECM devices as select devices: The number of WLs and BLs for the v-ECM-based 1S1R crossbar array is three oders of magnitude larger and the number of 1S1R devices is six order of magnitudes larger (3600 vs. 4.6 billion).

In 1S1R crossbar arrays, read operations are typically more strongly constrained by array parasitics than write operations. While reading only small voltages and currents are applied, so the selected-cell signal becomes comparable to leakage through sneak

paths formed by half-selected and unselected cells, and the effective read margin rapidly degrades with increasing array size [189–191]. In this low-voltage regime, the finite nonlinearity of the selector and the accumulation of sneak path conductances limit the suppression of parasitic currents, while voltage drops along resistive word and bit lines further reduce the voltage delivered to the selected cell so that the sense margin is dominated by voltage drops across wire resistances and sneak-path resistance rather than by the intrinsic HRS/LRS window [189, 190]. In addition, read biases must be constrained to avoid read disturb, since repeated application of small voltages can gradually perturb the resistive state of memristive cells [189, 192]. By contrast, write operations use larger voltages and currents and are mainly limited by half-selected cells that experience a fraction of the write voltage (e.g., $V/2$) and can suffer write disturb and long-term reliability degradation [193, 194]. Consequently, write scheme optimization focuses on selector requirements and half-selected cell stress (write margin, disturb, power), whereas the fundamental array-size limitation due to sneak paths, small sensing currents and voltage drops induced by wire resistances is far more critical for read schemes in large 1S1R crossbar arrays [189, 190].

7.3 Vector-Matrix Multiplication on 1S1R Crossbar Arrays

In this section, a 3×3 1S1R crossbar array is first analyzed to illustrate basic Vector-Matrix Multiplication behavior for individual cells when wire resistances are taken into account. Subsequently, larger crossbar arrays of up to 128×128 are considered to determine the maximum permissible wire resistance that still ensures reliable VMM operation for a particular array size, for both a threshold switch-based and volatile ECM-based 1S1R crossbar array. Figure 2.12 depicts a standard binary VMM operation on a 3×3 crossbar array. The input voltage vector (1,0,1) is applied, where 1 corresponds to 1 V (for the TS-based 1S1R device)/0.675 V (for the v-ECM-based 1S1R device) and 0 to 0 V. The VCM ReRAM devices are either in the LRS state (logical 1) or in the HRS state (logical 0) with $R_{\mathrm{ON}} < R_{\mathrm{LRS}} < R_{\mathrm{HRS}}$. The i-th input voltage entry is multiplied with each of the ReRAM resistance values in the i-th crossbar row/WL for a specific column/BL of the array. All multiplication results along one BL are summed up to yield the corresponding BL current. This process is repeated for all columns/BLs, with the same input voltage vector applied across each BL. The resulting BL currents together form the output current vector. This procedure is identical for larger arrays of any size.

When wire resistances are included in the crossbar array, voltage drops occur across these resistances, causing every cell in the array to experience a unique additional resistance along the current path through its WL and BL. As a result, the current levels of individual cells differ, even though the intrinsic state and the applied voltage remain identical. Cells located farthest from the WL voltage source and the BL read-out node experience the largest cumulative resistance along their path. Conversely, cells positioned closest to the WL voltage source and BL read-out node are affected minimally by wire resistances. Consequently, the non-uniform voltage distribution across the array influences the resulting current levels, potentially impacting the reliability of VMM operations as array size increases.

Three investigations involving simulation of limiting cases are performed for both 1S1R crossbar arrays:

1. HRS leakage current without consideration of wire resistances as first limiting case
2. Suppression of current on nth BL with n LRS devices due to highest amount of wire resistances as second limiting case
3. Suppression of current with 1 LRS device on nth BL due to highest amount of wire resistances compared to leakage current of n HRS devices on first BL as third limiting case

The limiting case out of the three which occurs for the least large array size is determined as the dominating limiting case. However, the first limiting case is rather a first step to assessing the approximate array size for relatively small wire resistances. It should be noted that an estimation of a largest feasible array size for a specific wire resistance value also highly depends on the tuning and choice of the 1S1R model parameter values and on a proper definition of binary resistance states (here: N_{init}) and resulting current levels that are read out after t_{read}.

General description of the first limiting case. To assess the approximate size of the largest feasible crossbar array a simple comparison is performed: The read current of one 1S1R device in its LRS $I(1\text{ LRS})$ is compared to the accumulated read current of n 1S1R devices all occupying the HRS. Therefore, the number n that fulfils

$$I(1\text{ LRS}) > n \cdot I(1\text{ HRS})$$

needs to be determined. Following this limiting case, the largest feasible array size is $n \times n$.

General description of the second limiting case. For worst-case analysis, the focus is further placed on comparing the BL current of the farthest BL with n LRS cells (lowest current level is on the nth BL) with that of the nearest BL with $n-1$ LRS cells (highest current level is on the 1st BL). This is done by biasing all WLs in the array with 1, while all cells are in the LRS, and measuring the current in the nth BL (Figure 7.7 (a) for a 3×3 array). This is then compared to the current in the 1st BL of another array configuration, where only the last n^{th} WL is left unbiased, while all other WLs are biased. Except of the 1S1R devices on the first BL and on the last WL all other 1S1R devices are occupying the HRS (Figure 7.7 (b) for a 3×3 array). For reliable operation, the current in the 1st BL of the latter array (marked in Figure 7.7 (b)) must be smaller than that in the nth BL of the fully-LRS array (marked in Figure 7.7 (a)). However, a slightly modified condition should hold for a $n \times n$ crossbar array:

$$I_{n\text{thBL}}(n \text{ LRS}) \geq I_{1\text{stBL}}(n-1 \text{ LRS}) + I_{1\text{stBL}}(n-1 \text{ LRS})/(2(n-1)) = I_{\text{limit}}.$$

Here, n LRS and $n-1$ LRS represent the number of cells in LRS on the corresponding BLs. I_{limit} approximately corresponds to

$$I_{\text{limit}} \approx (n-1) \cdot I(1 \text{ LRS}).$$

I_{limit} is chosen such that its exact value is equal to or slightly greater than $n-1$ times the current of one 1S1R LRS cell. In larger arrays, $I_{1\text{stBL}}(n-1 \text{ LRS})$ as alternative limiting current is reduced due to voltage drops. Consequently, $I_{n\text{thBL}}(n \text{ LRS})$ can become so small that its value comes too close to this alternative current limit's value. Thus, a guaranteed distinction between these two can become difficult. To ensure a sensing margin that gives a reliable distinction, $I_{1\text{stBL}}(n-1 \text{ LRS})/(2(n-1))$ is added to $I_{1\text{stBL}}(n-1 \text{ LRS})$. This new current limit I_{limit} serves as the upper bound that must not exceed $I_{n\text{thBL}}(n \text{ LRS})$ to enable reliable VMM operation on 1S1R crossbar arrays for the second limiting case. By introducing this refined I_{limit}, a robust distinction between the BL current values can be maintained, enabling reliable system-level operation.

General description of the third limiting case. The other worst-case analysis focuses on comparing the highly reduced current of one LRS device on the farthest nth BL due to affection by a large value of accumulated wire resistances ($I_{n\text{th,BL}}(1 \text{ LRS})$) with the leakage HRS current of n HRS devices on the nearest first BL ($I_{1\text{st,BL}}(n \text{ HRS})$). Also, this analysis is illustrated exemplarily for a 3 ×3 - crossbar array in Figure 7.8. It shows

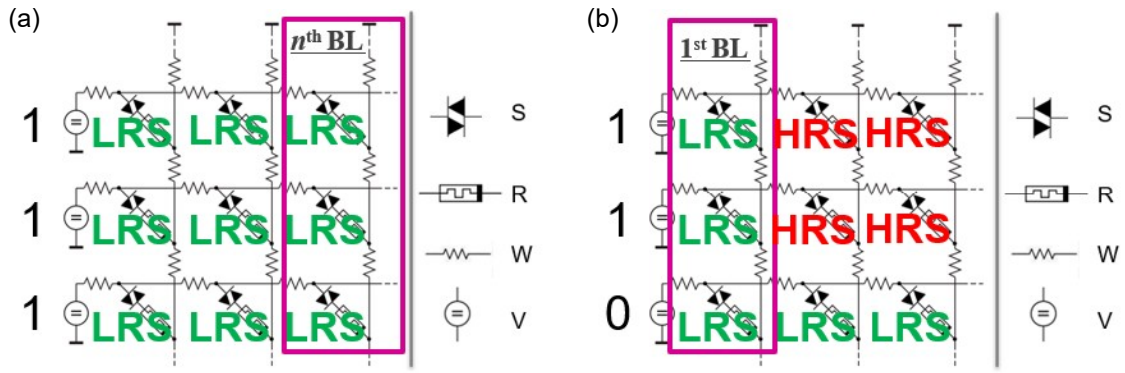

Figure 7.7: For evaluating the second limiting case for VMM with wire resistances, the necessary investigation is exemplarily depicted for a 3×3 - crossbar array. Case (a) that determines the smallest possible current on a BL for n LRS on a $n \times n$ - crossbar array is compared with (b) that determines the largest possible current on a BL for $n-1$ LRS on the same sized crossbar array. Reproduced with permission from [24], © 2022 IEEE.

that the first BL's current of a crossbar array with entirely HRS devices is biased at each WL with 1 and compared to the nth BL current of an array of which only the last WL is biased with 1 and of which all devices are in the LRS apart from n-1 devices of the last nth BL on the WLs 1 to n-1. Consequently, reliable operation is only ensured when the condition

$$I_{n\text{thBL}}(1 \text{ LRS}) > I_{1\text{stBL}}(n \text{ HRS})$$

is fulfilled for a $n \times n$ 1S1R crossbar array.

The circuit simulation results of these three limiting case analysis for both 1S1R crossbar arrays provide the maximum admissible wire resistance for reliable VMM operation as a function of array size, summarized exemplarily for the second limiting case in Table 7.5 and 7.6 for a threshold switch-based and a v-ECM-based 1S1R crossbar array, respectively. These results demonstrate that as the array size increases, the tolerance for wire resistance decreases correspondingly. The results for both 1S1R crossbar arrays are further enlightened in the following.

7.3.1 Vector-Matrix Multiplication on a Threshold Switch-based 1S1R Crossbar Array

In this section, explicit simulation results regarding the three limiting cases for a VMM on threshold switch-based 1S1R crossbar array affected by wire resistances is discussed.

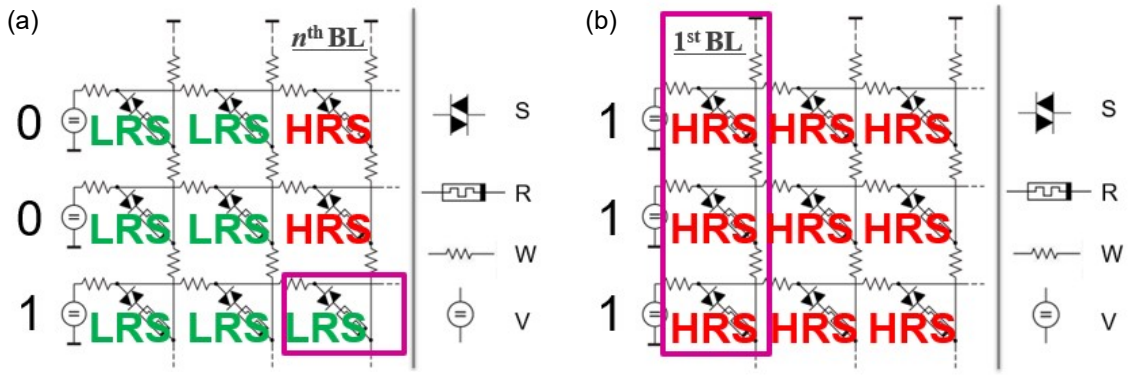

Figure 7.8: For evaluating the third limiting case for VMM with wire resistances, the necessary investigation is exemplarily depicted for a 3×3 - crossbar array. Case (a) that determines the smallest possible current on a BL for 1 LRS on a $n \times n$ - crossbar array is compared with (b) that determines the largest possible current on a BL for n HRS on the same sized crossbar array.

This analysis allows for an estimation of the largest feasible array size for a specific wire resistance value.

Results regarding the first limiting case. The condition $I(1\text{ LRS}) > n \cdot I(1\text{ HRS})$ with $I(1\text{ LRS}) = 197.1\ \mu\text{A}$ and $I(1\text{ HRS}) = 1.84\ \mu\text{A}$ leads to $n < 108$. Therefore, the largest feasible array size for this threshold switch-based 1S1R crossbar array configuration determined by undesired HRS leakage current is $n \times n$ with $n = 107$.

Results regarding the second limiting case. An extensive simulation investigation involving different combinations of wire resistances and crossbar array sizes have been performed regarding the second limiting case for VMM on threshold switch-based 1S1R crossbar arrays. The results including $I_{\text{1stBL}}(n-1\text{ LRS})$, $I_{n\text{thBL}}(n\text{ LRS})$, and I_{limit} after $t_{\text{read}} = 50\ \mu\text{s}$ are presented for each combination in Table 7.5 and their feasibility as reliable crossbar array configuration for VMM is assessed. It is important to recognize that, for larger arrays, the currents predicted by this illustrative simulation would reach unrealistically high values that would exceed the physical limits of the interconnects. Consequently, the presented results are intended solely as a conceptual demonstration. A markedly less conductive LRS of the VCM devices would yield results that are more feasible from an implementation perspective.

The relationship between feasible largest array size and wire resistance value is illustrated in Figure 7.9 as blue dotted line. As the number of rows and columns in the array is doubled, the wire resistance value must be reduced simultaneously, typically by a

Table 7.5: VMM analysis of the second limiting case for threshold switch-based 1S1R crossbar arrays

Array size, wire res value	Current levels			VMM possible?
	$I_{\text{1stBL}}(n-1$ LRS)	$I_{n\text{thBL}}(n$ LRS)	I_{limit}	
a) 8×8, 10 Ω	1.27 mA	1.25 mA	–	No
b) 8×8, 5 Ω	1.32 mA	1.40 mA	$<$ 1.42 mA	No
c) 8×8, 4 Ω	1.33 mA	1.43 mA	$=$ 1.43 mA	Yes
d) 16×16, 1 Ω	2.86 mA	2.88 mA	$<$ 2.95 mA	No
e) 16×16, 0.5 Ω	2.91 mA	3.01 mA	$>$ 3.00 mA	Yes
f) 32×32, 0.1 Ω	5.98 mA	6.10 mA	$>$ 6.07 mA	Yes
g) 64×64, 0.05 Ω	12.03 mA	11.84 mA	–	No
h) 64×64, 0.01 Ω	12.30 mA	12.45 mA	$>$ 12.40 mA	Yes

factor ranging from one-half to nearly an order of magnitude. This observation provides a clear estimate of the correlation between array size and wire resistance, indicating that larger arrays inherently demand lower wire resistance values to maintain stable operation. In essence, the scaling behavior establishes a predictable relationship: as the array grows, the permissible wire resistance shrinks accordingly. For $n < 107$, the second limiting case is the strongest limiting case, and determines the largest feasible crossbar array size. This is approved below with the analysis of the third limiting case and the comparison with it. For wire resistances between 4 Ω and 10 mΩ feasible $n \times n$-crossbar array sizes are between n= 8 and 64.

Realistic reference values are reported in [195]. For a Cu BL with a $90 \times 90\,\text{nm}^2$ cross section and 128 devices connected to the line, the total BL resistance is calculated to be 72 Ω, corresponding to approximately 0.56 Ω per segment. In contrast, for a Cu BL with a $5 \times 5\,\text{nm}^2$ cross section and the same number of connected devices, the total resistance increases to 4080 Ω, equivalent to roughly 31.88 Ω per segment. This comparison demonstrates that the resistance values allowed by the results in the simulations are substantially smaller than those expected from physically realistic interconnect dimensions. However, this statement holds for a BL comprising 128 devices.

Results regarding the third limiting case. Also, the third limiting case is accessed by simulation of different array size and wire resistance combinations. The array size that fulfils the condition $I_{n\text{th,BL}}(1\text{ LRS})) > I_{\text{1st,BL}}(n\text{ HRS}))$ for different wire resistance values is also illustrated in Figure 7.9 as red dotted line. The feasible wire resistance

Table 7.6: VMM analysis of the second limiting case for volatile ECM-based 1S1R crossbar arrays

Array size, wire res value	Current levels			VMM possible?
	$I_{\text{1stBL}}(n-1$ LRS)	$I_{n\text{thBL}}(n$ LRS)	I_{limit}	
a) 8×8, 7 Ω	1.008 mA	1.070 mA	$<$ 1.080 mA	No
b) 8×8, 6 Ω	1.013 mA	1.087 mA	$>$ 1.085 mA	Yes
c) 16×16, 0.9 Ω	2.201 mA	2.270 mA	$<$ 2.274 mA	No
d) 16×16, 0.8 Ω	2.206 mA	2.283 mA	$>$ 2.280 mA	Yes
e) 32×32, 0.4 Ω	4.340 mA	4.392 mA	$<$ 4.410 mA	No
f) 32×32, 0.3 Ω	4.377 mA	4.485 mA	$>$ 4.448 mA	Yes
g) 64×64, 0.08 Ω	8.887 mA	8.956 mA	$<$ 8.958 mA	No
h) 64×64, 0.07 Ω	8.917 mA	9.029 mA	$>$ 8.988 mA	Yes

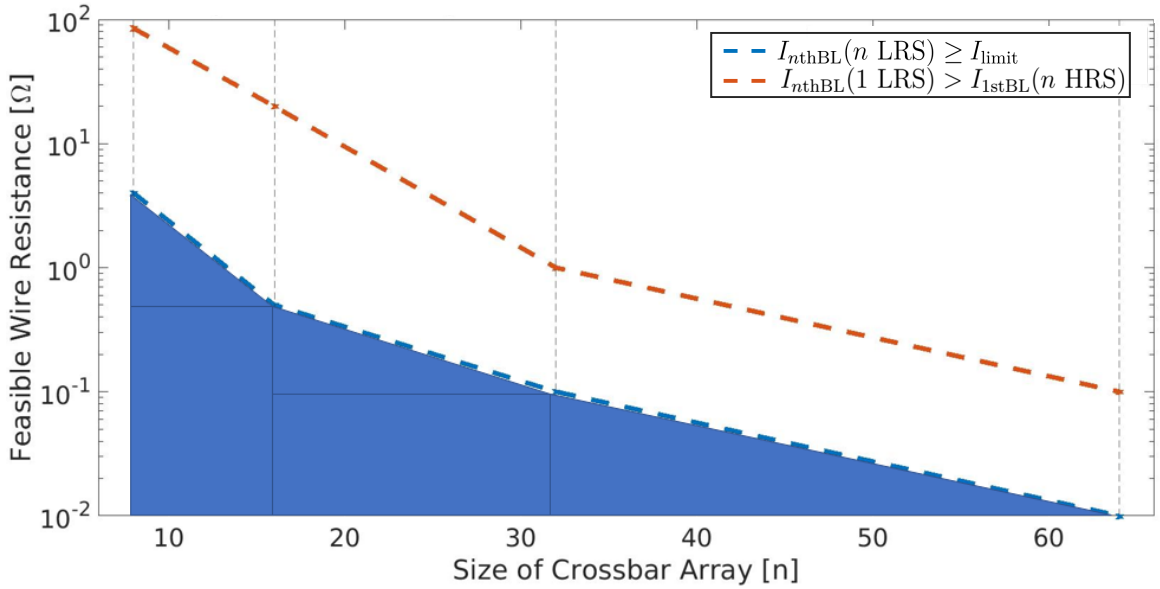

Figure 7.9: The second and third limiting case obtained by simulation for the 1S1R crossbar array based on the threshold switch as select device is illustrated: The largest feasible wire resistance is plotted against the crossbar array size $n \times n$. Here, the second limiting case is the dominating one, as it determines the largest feasible wire resistance: The blue area represents the allowed combinations. The first limiting case does not dominate, as it allows for an array size of 107×107.

shrinks in a very similar qualitative manner as for the second limiting case for increasing array size. Both the second and third limiting cases can be considered up to an array size of 107 × 107- array size, as determined by the first limiting case. For $n < 107$, the third limiting case is not the strongest limiting case, but the second limiting case is and determines the largest feasible crossbar array size. For wire resistances between 100 Ω and 100 mΩ, the third limiting case would permit $n \times n$ crossbar arrays with n between 8 and 64, if it were the dominant constraint. Physically realistic wire resistance values have been discussed above.

7.3.2 Vector-Matrix Multiplication on a Volatile ECM-based 1S1R Crossbar Array

Similar to the section before, simulation results regarding the three limiting cases for a VMM on volatile ECM-based 1S1R crossbar arrays affected by wire resistances are evaluated.

Results regarding the first limiting case. The condition $I(1\text{ LRS}) > n \cdot I(1\text{ HRS})$ with $I(1\text{ LRS}) = 149.8$ µA and $I(1\text{ HRS}) = 22.16$ nA leads to $n < 6760$. Therefore, the largest feasible array size for this v-ECM-based 1S1R crossbar array configuration determined by undesired HRS leakage current is $n \times n$ with $n = 6759$.

Results regarding the second limiting case. Also, for the v-ECM-based 1S1R crossbar array, an extensive simulation investigation involving different combinations of wire resistances and crossbar array sizes have been performed regarding the second limiting case for VMM. The results including $I_{1\text{stBL}}(n-1\text{ LRS})$, $I_{n\text{thBL}}(n\text{ LRS})$, and I_{limit} after $t_{\text{read}} = 200$ µs are presented for each combination in Table 7.6 and their feasibility as reliable crossbar array configuration for VMM is assessed. The relationship between feasible largest array size and wire resistance value for this case is illustrated in Figure 7.10 as blue dotted line.

As the number of rows and columns in the array is doubled, the wire resistance value must be reduced simultaneously, typically by a factor ranging from one-half to nearly an order of magnitude. Although the values differ, the observed trend is equal to the threshold switch-based 1S1R array case. Thus, similarly the same essence is derived: as the array grows, the permissible wire resistance shrinks accordingly. Comparing the second limiting case for both 1S1R devices results in a more beneficial behavior for the latter investigated v-ECM-based 1S1R crossbar array: Considering them, slightly

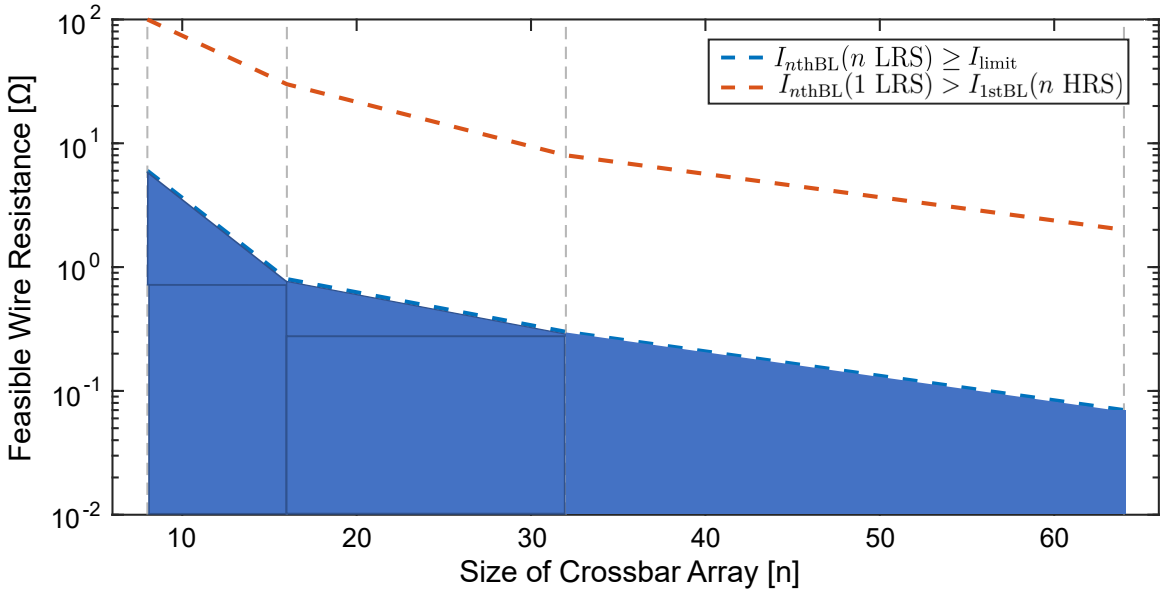

Figure 7.10: The second and third limiting case obtained by simulation for the 1S1R crossbar array based on the volatile ECM cell as select device is illustrated: The largest feasible wire resistance is plotted against the crossbar array size $n \times n$. Here, the second limiting case is the dominating one, as it determines the largest feasible wire resistance: The blue area represents the allowed combinations. The first limiting case does not dominate, as it allows for an array size of 6579×6579.

larger to approximately half order of magnitude larger wire resistance values are still acceptable for any considered array size. For $n < 6759$, the second limiting case is the strongest limiting case, and determines the largest feasible crossbar array size. This is approved below with the analysis of the third limiting case and the comparison with it. For wire resistances between 6 Ω and 70 mΩ feasible $n \times n$-crossbar array sizes are between $n = 8$ and 64. Physically realistic wire resistance values have been discussed above.

Results regarding the third limiting case. The third limiting case for v-ECM-based 1S1R crossbar arrays is also accessed by simulation of different array size and wire resistance combinations. The array size that fulfils the condition $I_{n\text{th,BL}}(1 \text{ LRS})) > I_{1\text{st,BL}}(n \text{ HRS}))$ for different wire resistance values is also illustrated in Figure 7.10 as red dotted line. Also here, the feasible wire resistance shrinks for increasing array size. Both the second and third limiting case can be considered up to an array size of 6759×6759-array size, as determined by the first limiting case (compared to TS-based arrays: 107×107). However, for $n < 6759$, the second limiting case is the stronger limiting case, and determines the largest feasible crossbar array size. For wire resistances between 100 Ω

and 2 Ω the third limiting case would allow for $n \times n$-crossbar array sizes between n= 8 and 64, if it were the dominating limitation. Physically realistic wire resistance values have been discussed above.

Evaluating the full VMM analysis (all three limiting cases) of both 1S1R crossbar array types with considered wire resistances leads to the following insight: The v-ECM-based 8×8 1S1R array simulation allows for wire resistance values up to 6 Ω, whereas the same threshold switch-based configuration allows for wire resistances only up to 4 Ω. For 64×64 - crossbar arrays, the v-ECM-based case allows for wire resistances up to 70 mΩ, whereas the threshold switch-based case allows for wire resistances only up to 10 mΩ. Given that wire resistances are considered, the v-ECM-based 1S1R crossbar array shows a slightly more beneficial VMM operation; if wire resistances are negligible, the potential of v-ECM-based 1S1R crossbar array VMM becomes even more clear: As no sufficient voltage drops across the select device, when the VCM is in its HRS, the select device stays unselected and blocks an access to the VCM device, leading to currents in the nA regime. However, when the VCM is in its LRS, sufficient voltage drops across the select device so that the VCM gets selected and currents up to several 100 µA are calculated. For the realization of this beneficial behavior, it is crucial to choose an appropriate V_{read} as logical 1 (ensuring an ideal voltage divider effect) and an appropriate t_{read} (the switching kinetics of v-ECM cells determines the moment of switching and is considered together with an interplay of different voltage drops across the select device depending on the VCM resistance state in series). This huge difference in current observed here for $V_{\mathrm{read}} = 0.675$ V and $t_{\mathrm{read}} = 200$ µs sheds light on the huge potential of v-ECM devices as select devices in 1S1R crossbar arrays. The investigated cases result in feasible array sizes of 6759 × 6759 for a v-ECM-based 1S1R crossbar array, whereas for threshold switch-based 1S1R crossbar arrays the largest feasible array size is 107 × 107. However, an appropriate engineering stays crucial according to the requirements of a select device within a 1S1R crossbar array device, presented in section 2.6.1. Also, a lower LRS conductance than that assumed in this simulation study must be ensured in order to prevent line damage.

7.4 Summary

A select device connected in series with a memory cell can significantly enhance the reliability of both read and VMM operations in a 1S1R crossbar arrangement. Wire

resistances constitute a major limitation to the achievable array size for reliable VMM execution. This limitation originates from the combined effects of array dimensions, line resistances, device resistance states, and the resulting current levels.

A noteworthy observation for threshold switch-based 1S1R cells is that, when the selector device is switched to the ON state and/or the memory element in the 1S1R configuration is SET to the LRS, the selector exhibits negative differential resistance in its electrical characteristics. This behavior manifests as a reduced voltage drop across the selector while the current flowing through it continues to increase. Under these atypical voltage divider conditions, the resistance of the selector decreases more strongly than the resistance of the memory element. As a result, once the memory cell switches and the selector is already in its ON state, the voltage distribution between the two devices changes in favor of the memory cell. A volatile ECM-based 1S1R cell, however, does not exhibit a NDR behavior: The voltage across the select device increases again once the ReRAM cell is SET to the LRS.

Nevertheless, for a certain applied voltage a special beneficial case is obtained: When the ReRAM cell is in its LRS, the v-ECM select device turns on and a large current of several 100 µA flows through the device. When the memory element, however, is in its HRS, too little voltage drops across the select device so that the 1S1R cell stays unselected due to the limiting effect of its switching kinetics. Owing to high OFF-states of the v-ECM, this 1S1R cell exhibits only a few nA current. This is a distinction of four orders in magnitude in current and can be exploited for opposing the disturbances of current limitation on the farthest away BL caused by wire resistances while performing read- and VMM-operations on 1S1R crossbar arrays. The beneficial effect for read schemes is very high. For the threshold switch-based 1S1R cell, this distinction in current is only in the range of two orders of magnitude. Thus, feasible array sizes for a read scheme are smaller.

However, comparing the smallest current on the farthest away BL for n cells and 1 cell in their LRS with the largest current on the nearest first BL for $n-1$ and no cells, respectively, in their HRS provide further limiting cases for VMM operations. For both the threshold switch-based and the v-ECM-based 1S1R crossbar array, the comparison of n LRS cells on the nth BL with $n-1$ LRS cells on the first BL proves to be the dominating limiting worst case. However, the latter 1S1R crossbar array allows for slightly larger wires resistance values for a certain array size.

8 Conclusions and Outlook

This thesis presents a comprehensive investigation of electrochemical metallization memory (ECM) devices and their compact modeling, with a particular focus on variability, volatile switching dynamics, and the functionality of 1S1R crossbar arrays. The work introduces and advances several physics-based models that consistently reproduce experimentally observed phenomena and provide a reliable foundation for circuit-level studies and practical applications. In the following, the most important findings are summarized and, subsequently, an outlook of this work is presented.

8.1 Summary and Conclusions

First, the JART ECM compact model has been extended to explicitly include device-to-device and cycle-to-cycle variability. By embedding features of realistic measurement conditions and accounting for the stochastic nature of ECM devices, the variability-aware formulation achieves a convincing match with experimental data, even under conditions affected by limited resolution, noise, and intrinsic randomness. The model emulates staircase input ramps, averages current responses, incorporates stepwise parameter variations, and introduces stochastic contributions into the governing differential equation. Using one consistent parameter set, the model captures variability in both SET kinetics and I–V characteristics while reflecting the constraints of the measurement setup and device-inherent fluctuations. Furthermore, the model has been applied successfully to two-dimensional material-based ECM devices, explaining the confined filament growth along van-der-Waals gaps together with reduced variability through it and confirming the crucial role of moisture in enabling resistive switching. However, the switching mechanism in layered 2D materials remains largely unresolved. Since intrinsic ion migration through the 2D layers is highly unlikely, ionic transport is expected to occur either laterally within the interlayer regions or vertically along grain boundaries. A parameter study highlights three different rate-limiting ionic processes that, depending on the stimulus strength, govern the switching speed of ECM devices. This

detailed analysis provides deeper insight into the underlying physics and offers practical guidelines for model fitting.

Second, a dedicated physics-based model for volatile ECM (v-ECM) devices has been developed. This formulation incorporates the electromotive force (emf) as a counteracting term to the intrinsic ionic processes of nucleation, charge transfer, and ion migration. The emf contribution explains device relaxation through filament dissolution once the applied bias falls below the hold voltage, thereby enabling accurate simulation of volatile switching effects. Parametric studies demonstrate that higher read voltages in the sub-emf regime yield longer relaxation times, while increasing the sweep rate shifts threshold voltages to higher values and reduces hold voltages toward zero. Comparisons with established v-ECM models show that the proposed approach sets a new benchmark: with a single parameter set it reproduces dynamic features, switching kinetics, relaxation behavior, and I–V sweeps with high consistency. The model, thus, remedies limitations of previous approaches and is ready for direct integration into circuit simulators. Its applicability extends from selector devices in CIM operations within ANNs, to components in hardware neuron circuits and to hardware security concepts. Importantly, the framework provides a unified and internally consistent description of switching and relaxation, offering both theoretical insights and practical value. Although the model reproduces the experimental behavior well, the emf concept remains exploratory due to possible small discrepancies between predicted and experimentally observed emf values.

Third, the operation of 1S1R crossbar arrays has been analyzed with a focus on the role of select devices. In threshold switch-based 1S1R cells, the selector exhibits NDR once turned ON in combination with a SET of a memory device, which modifies the voltage distribution between the two elements. In contrast, v-ECM-based selectors within 1S1R cells do not display NDR; instead, their voltage drop increases once the memory cell is in LRS. Under specific applied voltage, a beneficial behavior is observed through simulation: in the LRS of the ReRAM cell, the v-ECM selector enables large ON currents, whereas in the HRS the selector remains effectively unselected, leading to an ON/OFF current ratio of four orders of magnitude. This high contrast strongly enhances read and VMM schemes and mitigates limitations caused by line resistances in large crossbar arrays better than in the case of threshold switch-based 1S1R crossbar arrays. Thus, v-ECM-based 1S1R cells allow for larger feasible wire resistances for a given array size and therefore promise improved scalability.

In summary, this work establishes a set of variability-aware and physics-based compact models for ECM and v-ECM devices, and demonstrates their predictive capabilities

in circuit-relevant configurations. By unifying device-level physics with system-level applications, the thesis contributes both fundamental insights and practical tools for the reliable design of ReRAM-based neuromorphic and logic architectures.

8.2 Outlook

Building on the results of this thesis, several research directions can be targeted that may deepen the understanding of ECM devices and broaden the scope of their applications in circuit and system design. The following aspects appear particularly promising.

Fundamental Device Physics and Modeling

A first line of investigation concerns the physical origin of volatility in ECM devices. One possible explanation lies in the instability of the nucleus formed during the nucleation process. After each switching cycle - particularly following a strong RESET - this nucleus may vanish, requiring its re-formation in subsequent cycles. This mechanism could also account for the experimentally observed increase of the SET voltage after extended waiting times between cycles. Parameter studies with the developed models are well suited to test and verify such hypotheses.

In addition, the inclusion of lateral filament growth into the modeling framework represents another opportunity. Its implementation would allow to evaluate the impact of lateral growth processes in both volatile and nonvolatile regimes. Comparing the consequences of such an extension in the volatile ECM model versus the nonvolatile counterpart would shed light on the relative importance of geometry effects and their influence on device dynamics. This model should also reproduce the accurate relaxation time with varying pulse lengths, as the filament's lateral strength is expected to rise with the applied pulse's duration. It should be investigated until which pulse amplitude and pulse length the device rather tends to stay in its volatile fashion than to transition into a nonvlatile fashion.

Another aspect of interest is the effect of parasitic capacitances on voltage-dependent programming and on the subsequent relaxation process. A systematic analysis could reveal to what extent capacitive charging and discharging alter both the switching kinetics and the relaxation time constants of ECM devices.

Moreover, in the present work the electron transfer process is chosen sufficiently fast such that it does not act as a limiting factor during SET. Because nucleation does not occur during relaxation, electron transfer effectively becomes the rate-limiting process

for relaxation, which simplifies the fitting procedure. A natural question arises whether a parameter regime exists in which the electron transfer process limits both SET and relaxation within different effective voltage polarities and ranges. Extending the compact model to explore this scenario could provide valuable insights and enhance the predictive flexibility of the formulation.

Future work should also focus on the experimental validation of the emf approach and on investigations to clarify the exact ion transport pathways in devices based on 2D materials.

Finally, an outlook at the device-to-circuit interface involves the question whether a neuromorphic circuit can be realized in which a v-ECM device constitutes part of the artificial neuron. Demonstrating that the functionality of spiking neurons can be achieved with the developed v-ECM model, and validating this either by simulation or experimental fitting, would constitute an important step toward application.

1S1R Crossbar Arrays and Circuit-Level Perspectives

Further research should also target the dynamics of 1S1R crossbar arrays with different selector-device compositions. A detailed comparison of their transient behavior and operational stability would highlight the benefits and drawbacks of volatile ECM versus threshold switch selectors. In particular, the role of relaxation times in the v-ECM model must be carefully assessed: Do such time constants introduce operational delays in read and VMM tasks?

In this context, it would be insightful to explore whether the NDR characteristic of threshold switches can be exploited beneficially for VMM operations, or whether instead the positive differential resistance (PDR) of v-ECM selectors provides superior performance. Moreover, the possibility of utilizing the intrinsic relaxation dynamics of v-ECM devices in spiking neural networks deserves attention, as such time constants might serve as a natural basis for implementing temporal neuronal behavior.

At the periphery level, the integration of crossbar arrays with ADC/DAC blocks and additional circuit units should be simulated in detail to understand the impact of conversion and interfacing on array performance. Special emphasis should be placed on strategies to mitigate wire resistance effects, which remain a crucial bottleneck for large-scale crossbar arrays. Possible countermeasures include selective biasing of word lines or bit lines, partial activation schemes, or other circuit-level techniques. Potential specific strategies to mitigate these constraints include, for example, (1) restricting the degree of parallelism by activating only portions of the WLs at a given time, and/or (2)

performing measurements on selected BLs while biasing the remaining ones at specific voltages. Such approaches should be taken into account for future investigations. The true magnitude of wire resistances in fabricated arrays is given for Cu BLs in [195]. It varies from a total BL wire resistance value (128 BL) of 72 Ω for a $90 \cdot 90$ nm^2 Cu BL cross section to 4080 Ω for a $5 \cdot 5$ nm^2 cross section. Hence, it is important to consider these specific cases and engineer the wires and crossbar cells accordingly. Also, the mitigation strategies mentioned above either need to be tested and applied or tested and further modified. As the overall line resistance increases with decreasing wire cross section due to scattering, when the wire's cross section gets smaller than the electron mean free path [196], the following consideration is appropriate: According to the largest feasible wire resistance values, the crossbar lines' resistances of different array sizes need to be additionally inspected for different smallest possible line cross sections.

Furthermore, while this thesis concentrates on read schemes and read-based VMM operations, future work should extend the scope to write schemes. Simulations of write-VMM tasks will allow conclusions analogous to those drawn here for read-VMM, such as the determination of maximum feasible array sizes for given wire resistance values. A study of programming schemes for single 1S1R devices in crossbar arrays, as well as of multi-level and analog VMM operation, would be a further valuable direction for future work.

Extended Applications

Finally, the models developed in this thesis open the door to further explorations of application-oriented scenarios. They provide a solid basis for promising use within several possible applications. Also, the 1S1R crossbar array analysis presented in this thesis via simulations gives solid access to and strongly paves the way for designing further extended applications. In this regard, evaluating the v-ECM model's behavior under current control could provide valuable insights for potential applications. Potential directions include the design and simulation of artificial neural networks, logic circuits, true random number generators, and stochastic neuron implementations. Furthermore, simulating a leaky-integrate-and-fire neuron using the v-ECM model represents an interesting direction for future work. By combining variability-aware compact models with circuit- and system-level simulations, both fundamental understanding and practical feasibility of such concepts can be advanced. This would contribute not only to the scientific exploration of nanoionic devices but also to their eventual deployment in emerging computational technologies.

Bibliography

[1] X. Zou, S. Xu, X. Chen, L. Yan, and Y. Han, "Breaking the von Neumann bottleneck: architecture-level processing-in-memory technology", *Science China Information Sciences*, vol. 64, no. Article 160404, p. 160 404, 2021, ISSN: 1674-733X. DOI: 10.1007/s11432-020-3227-1

[2] K. Asifuzzaman, N. R. Miniskar, A. R. Young, F. Liu, and J. S. Vetter, "A survey on processing-in-memory techniques: Advances and challenges", *Memories - Materials, Devices, Circuits and Systems*, vol. 4, p. 100 022, 2023, ISSN: 2773-0646. DOI: 10.1016/j.memori.2022.100022

[3] S. S. Gill, H. Wu, P. Patros, C. Ottaviani, P. Arora, V. C. Pujol, D. Haunschild, A. K. Parlikad, O. Cetinkaya, H. Lutfiyya, V. Stankovski, R. Li, Y. Ding, J. Qadir, A. Abraham, S. K. Ghosh, H. H. Song, R. Sakellariou, O. Rana, J. J. Rodrigues, S. S. Kanhere, S. Dustdar, S. Uhlig, K. Ramamohanarao, and R. Buyya, "Modern computing: Vision and challenges", *Telematics and Informatics Reports*, vol. 13, p. 100 116, 2024, ISSN: 2772-5030. DOI: 10.1016/j.teler.2024.100116

[4] A. de Vries, "The growing energy footprint of artificial intelligence", *Joule*, vol. 7, no. 10, pp. 2191–2194, 2023, ISSN: 2542-4351. DOI: 10.1016/j.joule.2023.09.004

[5] L. Deng, D. Wang, Z. Zhang, P. Tang, G. Li, and J. Pei, "Energy consumption analysis for various memristive networks under different learning strategies", *Physics Letters A*, vol. 380, no. 7, pp. 903–909, 2016, ISSN: 0375-9601. DOI: 10.1016/j.physleta.2015.12.024

[6] R. Dittmann, S. Menzel, and R. Waser, "Nanoionic memristive phenomena in metal oxides: the valence change mechanism", *Advances in Physics*, vol. 70, no. 2, pp. 155–349, 2021. DOI: 10.1080/00018732.2022.2084006

[7] G. W. Burr, R. M. Shelby, A. Sebastian, S. Kim, S. Kim, S. Sidler, K. Virwani, M. Ishii, P. Narayanan, A. Fumarola, L. L. Sanches, I. Boybat, M. L. Gallo, K. Moon, J. Woo, H. Hwang, and Y. Leblebici, "Neuromorphic computing using non-volatile memory", *Advances in Physics: X*, vol. 2, no. 1, pp. 89–124, 2017. DOI: 10.1080/23746149.2016.1259585

[8] F. Zahoor, T. Z. A. Zulkifli, and F. A. Khanday, "Resistive Random Access Memory (RRAM): an Overview of Materials, Switching Mechanism, Performance, Multilevel Cell (mlc) Storage, Modeling, and Applications", *Nanoscale Research Letters*, vol. 15, no. 90, 2020. DOI: 10.1186/s11671-020-03299-9

[9] D. Ielmini, "Resistive switching memories based on metal oxides: mechanisms, reliability and scaling", *Semiconductor Science and Technology*, vol. 31, no. 6, p. 063 002, May 2016. DOI: 10.1088/0268-1242/31/6/063002

[10] M. A. Lebdeh, U. Reinsalu†, H. A. D. Nguyen, S. Wong, and S. Hamdioui, "Memristive Device Based Circuits for Computation-in-Memory Architectures", in *2019 IEEE International Symposium on Circuits and Systems (ISCAS)*, 2019, pp. 1–5. DOI: 10.1109/ISCAS.2019.8702542

[11] R. Waser, R. Dittmann, G. Staikov, and K. Szot, "Redox-Based Resistive Switching Memories – Nanoionic Mechanisms, Prospects, and Challenges", *Advanced Materials*, vol. 21, no. 25-26, pp. 2632–2663, 2009. DOI: 10.1002/adma.200900375

[12] W.-H. Chen, W.-J. Lin, L.-Y. Lai, S. Li, C.-H. Hsu, H.-T. Lin, H.-Y. Lee, J.-W. Su, Y. Xie, S.-S. Sheu, and M.-F. Chang, "A 16Mb dual-mode ReRAM macro with sub-14ns computing-in-memory and memory functions enabled by self-write termination scheme", in *2017 IEEE International Electron Devices Meeting (IEDM)*, 2017, pp. 28.2.1–28.2.4. DOI: 10.1109/IEDM.2017.8268468

[13] Y. Wang, C. Zhang, R. Nadipalli, H. Yu, and R. Weerasekera, "Design exploration of 3D stacked non-volatile memory by conductive bridge based crossbar", in *2011 IEEE International 3D Systems Integration Conference (3DIC), 2011 IEEE International*, 2012, pp. 1–6. DOI: 10.1109/3DIC.2012.6263047

[14] M.-J. Lee, C. B. Lee, D. Lee, S. R. Lee, M. Chang, J. H. Hur, Y.-B. Kim, C.-J. Kim, D. H. Seo, S. Seo, U.-I. Chung, I.-K. Yoo, and K. Kim, "A fast, high-endurance and scalable non-volatile memory device made from asymmetric Ta_2O_{5-x}/TaO_{2-x} bilayer structures", *Nature Materials*, vol. 10, pp. 625–630, 2011. DOI: 10.1038/nmat3070

[15] K. Terabe, T. Hasegawa, T. Nakayama, and M. Aono, "Quantized Conductance Atomic Switch", *Nature*, vol. 433, pp. 47–50, 2005. DOI: 10.1038/nature03190

[16] K. Szot, W. Speier, G. Bihlmayer, and R. Waser, "Switching the electrical resistance of individual dislocations in single-crystalline $SrTiO_3$", *Nature Materials*, vol. 5, pp. 312–320, 2006. DOI: 10.1038/nmat1614

[17] A. C. Torrezan, J. P. Strachan, G. Medeiros-Ribeiro, and R. S. Williams, "Sub-nanosecond switching of a tantalum oxide memristor", *Nanotechnology*, vol. 22, no. 48, p. 485 203, Nov. 2011. DOI: 10.1088/0957-4484/22/48/485203

[18] R. Midya, Z. Wang, J. Zhang, S. E. Savel'ev, C. Li, M. Rao, M. H. Jang, S. Joshi, H. Jiang, P. Lin, K. Norris, N. Ge, Q. Wu, M. Barnell, Z. Li, H. L. Xin, R. S. Williams, Q. Xia, and J. J. Yang, "Anatomy of Ag/Hafnia-Based Selectors with 10^{10} Nonlinearity", *Advanced Materials*, vol. 29, no. 12, p. 1 604 457, 2017. DOI: 10.1002/adma.201604457

[19] R. D. Nikam, K. G. Rajput, and H. Hwang, "Single-Atom Quantum-Point Contact Switch Using Atomically Thin Hexagonal Boron Nitride", *Small*, vol. 17, no. 7, p. 2 006 760, 2021. DOI: 10.1002/smll.202006760

[20] T. Kim, S. Hu, J. Kim, J. Y. Kwak, J. Park, S. Lee, I. Kim, J.-K. Park, and Y. Jeong, "Spiking Neural Network (SNN) With Memristor Synapses Having Nonlinear Weight Update", *Frontiers in Computational Neuroscience*, vol. 15, 2021. DOI: 10.3389/fncom.2021.646125

[21] S. H. Jo, T. Chang, I. Ebong, B. B. Bhadviya, P. Mazumder, and W. Lu, "Nanoscale Memristor Device as Synapse in Neuromorphic Systems", *Nano Letters*, vol. 10, no. 4, pp. 1297–1301, 2010, PMID: 20192230. DOI: 10.1021/nl904092h

[22] H. Abbas, J. Li, and D. S. Ang, "Conductive Bridge Random Access Memory (CBRAM): Challenges and Opportunities for Memory and Neuromorphic Computing Applications", *Micromachines*, vol. 13, no. 5, 2022, ISSN: 2072-666X. DOI: 10.3390/mi13050725

[23] S. A. Chekol, S. Menzel, R. W. Ahmad, R. Waser, and S. Hoffmann-Eifert, "Effect of the Threshold Kinetics on the Filament Relaxation Behavior of Ag-Based Diffusive Memristors", *Advanced Functional Materials*, vol. 32, no. 15, p. 2 111 242, 2022. DOI: 10.1002/adfm.202111242

[24] R. W. Ahmad, D. Wouters, C. Bengel, R. Waser, and S. Menzel, "Analysis of VMM Operations on 1S1R Crossbar Arrays and the Influence of Wire Resistances", in *2022 IEEE International Symposium on Circuits and Systems (ISCAS)*, 2022, pp. 91–95. DOI: 10.1109/ISCAS48785.2022.9937570

[25] I. Boybat, C. Giovinazzo, E. Shahrabi, I. Krawczuk, I. Giannopoulos, C. Piveteau, M. Le Gallo, C. Ricciardi, A. Sebastian, E. Eleftheriou, and Y. Leblebici, "Multi-ReRAM Synapses for Artificial Neural Network Training", in *2019 IEEE International Symposium on Circuits and Systems (ISCAS)*, 2019, pp. 1–5. DOI: 10.1109/ISCAS.2019.8702714

[26] P. Chi, S. Li, C. Xu, T. Zhang, J. Zhao, Y. Liu, Y. Wang, and Y. Xie, "PRIME: A Novel Processing-in-Memory Architecture for Neural Network Computation in ReRAM-Based Main Memory", in *2016 ACM/IEEE 43rd Annual International Symposium on Computer Architecture (ISCA)*, 2016, pp. 27–39. DOI: 10.1109/ISCA.2016.13

[27] Y. Long, T. Na, and S. Mukhopadhyay, "ReRAM-Based Processing-in-Memory Architecture for Recurrent Neural Network Acceleration", *IEEE Transactions on Very Large Scale Integration (VLSI) Systems*, vol. 26, no. 12, pp. 2781–2794, 2018. DOI: 10.1109/TVLSI.2018.2819190

[28] A. Amirsoleimani, F. Alibart, V. Yon, J. Xu, M. R. Pazhouhandeh, S. Ecoffey, Y. Beilliard, R. Genov, and D. Drouin, "In-Memory Vector-Matrix Multiplication in Monolithic Complementary Metal–Oxide–Semiconductor-Memristor Integrated Circuits: Design Choices, Challenges, and Perspectives", *Advanced Intelligent Systems*, vol. 2, no. 11, p. 2 000 115, 2020. DOI: 10.1002/aisy.202000115

[29] G. W. Burr, R. S. Shenoy, K. Virwani, P. Narayanan, A. Padilla, B. Kurdi, and H. Hwang, "Access devices for 3D crosspoint memorya)", *Journal of Vacuum Science & Technology B*, vol. 32, no. 4, p. 040 802, Jul. 2014, ISSN: 2166-2746. DOI: 10.1116/1.4889999

[30] J.-J. Huang, Y.-M. Tseng, W.-C. Luo, C.-W. Hsu, and T.-H. Hou, "One selector-one resistor (1S1R) crossbar array for high-density flexible memory applications", in *2011 International Electron Devices Meeting*, 2011, pp. 31.7.1–31.7.4. DOI: 10.1109/IEDM.2011.6131653

[31] J.-J. Huang, Y.-M. Tseng, C.-W. Hsu, and T.-H. Hou, "Bipolar Nonlinear Ni/TiO_2/Ni Selector for 1S1R Crossbar Array Applications", *IEEE Electron Device Letters*, vol. 32, no. 10, pp. 1427–1429, 2011. DOI: 10.1109/LED.2011.2161601

[32] J. Kim, J. H. Choi, S. Kim, C. Choi, and S. Kim, "Transition of short-term to long-term memory of Cu/TaOx/CNT conductive bridge random access memory for neuromorphic engineering", *Carbon*, vol. 215, p. 118 438, 2023, ISSN: 0008-6223. DOI: 10.1016/j.carbon.2023.118438

[33] C. Schindler, G. Staikov, and R. Waser, "Electrode kinetics of Cu–SiO2-based resistive switching cells: Overcoming the voltage-time dilemma of electrochemical metallization memories", *Applied Physics Letters*, vol. 94, no. 7, p. 072 109, Feb. 2009, ISSN: 0003-6951. DOI: 10.1063/1.3077310

[34] R. W. Ahmad, R. Waser, F. Maudet, O. Toprak, C. Dubourdieu, and S. Menzel, "Variability-aware modeling of electrochemical metallization memory cells", *Neuromorphic Computing and Engineering*, vol. 4, no. 3, p. 034 007, Aug. 2024. DOI: 10.1088/2634-4386/ad57e7

[35] D. Jana, S. Roy, R. Panja, M. Dutta, S. Z. Rahaman, R. Mahapatra, and S. Maikap, "Conductive-bridging random access memory: challenges and opportunity for 3D architecture", *Nanoscale Research Letters*, vol. 10, p. 188, 2015. DOI: 10.1186/s11671-015-0880-9

[36] L. Goux and I. Valov, "Electrochemical processes and device improvement in conductive bridge RAM cells", *physica status solidi (a)*, vol. 213, no. 2, pp. 274–288, 2016. DOI: 10.1002/pssa.201532813

[37] S. Guitarra, P. Mahato, D. Deleruyelle, L. Raymond, and L. Trojman, "Stochastic based compact model to predict highly variable electrical characteristics of organic CBRAM devices", *Solid-State Electronics*, vol. 185, p. 108 055, 2021, ISSN: 0038-1101. DOI: 10.1016/j.sse.2021.108055

[38] F. Maudet, A. Hammud, M. Wollgarten, V. Deshpande, and C. Dubourdieu, "Insights on the variability of Cu filament formation in the SiO2 electrolyte of quantized-conductance conductive bridge random access memory devices", *Nanotechnology*, vol. 34, no. 24, p. 245 203, Mar. 2023. DOI: 10.1088/1361-6528/acbcd7

[39] W. Yi, K. K. Tsang, S. K. Lam, X. Bai, J. A. Crowell, and E. A. Flores, "Biological plausibility and stochasticity in scalable VO_2 active memristor neurons", *Nature Communications*, vol. 9, p. 4661, 2018. DOI: 10.1038/s41467-018-07052-w

[40] H. Chen and J. Ravichandran, "Phase-Change Materials for Volatile Threshold Resistive Switching and Neuronal Device Applications", *Advanced Science*, vol. 12, no. 42, e03209, 2025. DOI: 10.1002/advs.202503209

[41] T. Tuma, A. Pantazi, M. L. Gallo, A. Sebastian, and E. Eleftheriou, "Stochastic phase-change neurons", *Nature Nanotechnology*, vol. 11, pp. 693–699, 2016. DOI: 10.1038/nnano.2016.70

[42] W. Choi, O. Kwon, J. Lee, S. Oh, S. Heo, S. Ban, Y. Seo, D. Kim, and H. Hwang, "Volatile threshold switching devices for hardware security primitives: Exploiting intrinsic variability as an entropy source", *Applied Physics Reviews*, vol. 11, no. 2, p. 021 323, May 2024, ISSN: 1931-9401. DOI: 10.1063/5.0183292

[43] I. Valov, E. Linn, S. Tappertzhofen, S. Schmelzer, J. v. d. Hurk, F. Lentz, and R. Waser, "Nanobatteries in redox-based resistive switches require extension of memristor theory", *Nature Communications*, vol. 4, no. 1771, 2013. DOI: 10.1038/ncomms2784

[44] S. Bhatti, R. Sbiaa, A. Hirohata, H. Ohno, S. Fukami, and S. Piramanayagam, "Spintronics based random access memory: a review", *Materials Today*, vol. 20, no. 9, pp. 530–548, 2017, ISSN: 1369-7021. DOI: 10.1016/j.mattod.2017.07.007

[45] G. S. Syed, M. Le Gallo, and A. Sebastian, "Phase-Change Memory for In-Memory Computing", *Chemical Reviews*, vol. 125, no. 11, pp. 5163–5194, 2025, PMID: 40403708. DOI: 10.1021/acs.chemrev.4c00670

[46] R. W. Ahmad, S. A. Chekol, J. Rasbach, S. Hoffmann-Eifert, and S. Menzel, "Compact Modeling of Volatile-Switching Electrochemical Metallization Memory Cells by Means of the Electromotive Force", *Advanced Intelligent Systems*, vol. n/a, no. n/a, e202501018, DOI: 10.1002/aisy.202501018

[47] S. Menzel, S. Tappertzhofen, R. Waser, and I. Valov, "Switching kinetics of electrochemical metallization memory cells", *Phys. Chem. Chem. Phys.*, vol. 15, pp. 6945–6952, 18 2013. DOI: 10.1039/C3CP50738F

[48] M. Haemori, T. Nagata, and T. Chikyow, "Impact of Cu Electrode on Switching Behavior in a Cu/HfO2/Pt Structure and Resultant Cu Ion Diffusion", *Applied Physics Express*, vol. 2, no. 6, p. 061 401, May 2009. DOI: 10.1143/APEX.2.061401

[49] L. Völkel, R. W. Ahmad, A. Bestaeva, D. Braun, S. Cruces, J. Lee, S. Pasko, S. Krotkus, M. Heuken, S. Menzel, and M. C. Lemme, "Influence of humidity on the resistive switching of hexagonal boron nitride-based memristors", *npj 2D Materials and Applications*, vol. 9, no. 41, May 2025, ISSN: 2397-7132. DOI: 10.1038/s41699-025-00566-0

[50] J. Lee, R. W. Ahmad, S. Cruces, D. Braun, L. Völkel, K. Ran, V. M. Andreadis, J. Mayer, S. Menzel, A. Daus, and M. C. Lemme, "Threshold switching in vertically aligned MoS_2/SiO_x heterostructures based on silver ion migration", *npj 2D Materials and Applications*, vol. 9, no. 86, 2025. DOI: 10.1038/s41699-025-00614-9

[51] T. Tsuruoka, T. Hasegawa, I. Valov, R. Waser, and M. Aono, "Rate-limiting processes in the fast SET operation of a gapless-type Cu-Ta2O5 atomic switch", *AIP Advances*, vol. 3, no. 3, p. 032 114, Mar. 2013, ISSN: 2158-3226. DOI: 10.1063/1.4795140

[52] M. Arita, Y. Ohno, and Y. Takahashi, "Switching of Cu/MoOx/TiN CBRAM at MoOx/TiN interface", *physica status solidi (a)*, vol. 213, no. 2, pp. 306–310, 2016. DOI: 10.1002/pssa.201532414

[53] C. Schindler, K. Szot, S. Karthäuser, and R. Waser, "Controlled local filament growth and dissolution in Ag–Ge–Se", *physica status solidi (RRL) – Rapid Research Letters*, vol. 2, no. 3, pp. 129–131, 2008. DOI: 10.1002/pssr.200802054

[54] S. Fu, J.-H. Park, H. Gao, T. Zhang, X. Ji, T. Fu, L. Sun, J. Kong, and J. Yao, "Two-Terminal MoS2 Memristor and the Homogeneous Integration with a MoS2 Transistor for Neural Networks", *Nano Letters*, vol. 23, no. 13, pp. 5869–5876, 2023, PMID: 37338212. DOI: 10.1021/acs.nanolett.2c05007

[55] L. Liu, Y. Wang, W. Chen, S. Ren, J. Guo, X. Kang, and X. Zhao, "Robust resistive switching in MoS2-based memristor with Ti top electrode", *Applied Surface Science*, vol. 605, p. 154 698, 2022, ISSN: 0169-4332. DOI: 10.1016/j.apsusc.2022.154698

[56] S. Tappertzhofen, I. Valov, T. Tsuruoka, T. Hasegawa, R. Waser, and M. Aono, "Generic Relevance of Counter Charges for Cation-Based Nanoscale Resistive Switching Memories", *ACS Nano*, vol. 7, no. 7, pp. 6396–6402, 2013, PMID: 23786236. DOI: 10.1021/nn4026614

[57] I. Valov and T. Tsuruoka, "Effects of moisture and redox reactions in VCM and ECM resistive switching memories", *Journal of Physics D: Applied Physics*, vol. 51, no. 41, p. 413 001, Aug. 2018. DOI: 10.1088/1361-6463/aad581

[58] S. Tappertzhofen, R. Waser, and I. Valov, "Impact of the Counter-Electrode Material on Redox Processes in Resistive Switching Memories", *ChemElectroChem*, vol. 1, no. 8, pp. 1287–1292, 2014. DOI: 10.1002/celc.201402106

[59] E. Covi, W. Wang, Y.-H. Lin, M. Farronato, E. Ambrosi, and D. Ielmini, "Switching Dynamics of Ag-Based Filamentary Volatile Resistive Switching Devices—Part I: Experimental Characterization", *IEEE Transactions on Electron Devices*, vol. 68, no. 9, pp. 4335–4341, 2021. DOI: 10.1109/TED.2021.3076029

[60] I. Valov, R. Waser, J. R. Jameson, and M. N. Kozicki, "Electrochemical metallization memories—fundamentals, applications, prospects", *Nanotechnology*, vol. 22, no. 25, p. 254 003, May 2011. DOI: 10.1088/0957-4484/22/25/254003

[61] S. Menzel, "Modeling and simulation of resistive switching devices; 1. Aufl.", Zsfassung in dt. und engl. Sprache; Zugl.: Aachen, Techn. Hochsch., Diss., 2012, Ph.D. dissertation, München, 2013, VIII, 146 S. : Ill., graph. Darst. ISBN: 978-3-8439-0964-8.

[62] N. F. Mott and R. W. Gurney, *Electronic Processes in Ionic Crystals*. 1948.

[63] R. Waser, S. Menzel, and R. Bruchhaus, "Chapter 30", in *Nanoelectronics and Information Technology*, R. Waser, Ed., 3rd ed., Wiley-VCH, 2012.

[64] E. J. Dickinson and A. J. Wain, "The Butler-Volmer equation in electrochemical theory: Origins, value, and practical application", *Journal of Electroanalytical Chemistry*, vol. 872, p. 114 145, 2020, Dr. Richard Compton 65th birthday Special issue, ISSN: 1572-6657. DOI: 10.1016/j.jelechem.2020.114145

[65] J. A. V. Butler, "Studies in heterogeneous equilibria. Part I. Conditions at the boundary surface of crystalline solids and liquids and the application of statistical mechanics", *Trans. Faraday Soc.*, vol. 19, pp. 659–665, March 1924. DOI: 10.1039/TF9241900659

[66] J. G. Simmons, "Generalized Formula for the Electric Tunnel Effect between Similar Electrodes Separated by a Thin Insulating Film", *Journal of Applied Physics*, vol. 34, no. 6, pp. 1793–1803, Jun. 1963, ISSN: 0021-8979. DOI: 10.1063/1.1702682

[67] J. G. Simmons, "Electric Tunnel Effect between Dissimilar Electrodes Separated by a Thin Insulating Film", *Journal of Applied Physics*, vol. 34, no. 9, pp. 2581–2590, Sep. 1963, ISSN: 0021-8979. DOI: 10.1063/1.1729774

[68] S. A. Chekol, S. Menzel, R. Waser, and S. Hoffmann-Eifert, "Strategies to Control the Relaxation Kinetics of Ag-Based Diffusive Memristors and Implications for Device Operation", *Advanced Electronic Materials*, vol. 8, no. 11, p. 2 200 549, 2022. DOI: 10.1002/aelm.202200549

[69] S. Tappertzhofen, S. Menzel, I. Valov, and R. Waser, "Redox processes in silicon dioxide thin films using copper microelectrodes", *Applied Physics Letters*, vol. 99, no. 20, p. 203 103, Nov. 2011, ISSN: 0003-6951. DOI: 10.1063/1.3662013

[70] K. S. Novoselov, A. K. Geim, S. V. Morozov, D. Jiang, Y. Zhang, S. V. Dubonos, I. V. Grigorieva, and A. A. Firsov, "Electric Field Effect in Atomically Thin Carbon Films", *Science*, vol. 306, no. 5696, pp. 666–669, 2004. DOI: 10.1126/science.1102896

[71] S. Z. Butler, S. M. Hollen, L. Cao, Y. Cui, J. A. Gupta, H. R. Gutiérrez, T. F. Heinz, S. S. Hong, J. Huang, A. F. Ismach, E. Johnston-Halperin, M. Kuno, V. V. Plashnitsa, R. D. Robinson, R. S. Ruoff, S. Salahuddin, J. Shan, L. Shi, M. G. Spencer, M. Terrones, W. Windl, and J. E. Goldberger, "Progress, Challenges, and Opportunities in Two-Dimensional Materials Beyond Graphene", *ACS Nano*, vol. 7, no. 4, pp. 2898–2926, 2013, PMID: 23464873. DOI: 10.1021/nn400280c

[72] L. Tang, J. Tan, H. Nong, B. Liu, and H.-M. Cheng, "Chemical Vapor Deposition Growth of Two-Dimensional Compound Materials: Controllability, Material Quality, and Growth Mechanism", *Accounts of Materials Research*, vol. 2, no. 1, pp. 36–47, 2021. DOI: 10.1021/accountsmr.0c00063

[73] Q. H. Wang, K. Kalantar-Zadeh, A. Kis, J. N. Coleman, and M. S. Strano, "Electronics and optoelectronics of two-dimensional transition metal dichalcogenides", *Nature Nanotechnology*, vol. 7, pp. 699–712, 2012. DOI: 10.1038/nnano.2012.193

[74] C. R. Dean, A. F. Young, I. Meric, C. Lee, L. Wang, S. Sorgenfrei, K. Watanabe, T. Taniguchi, P. Kim, K. L. Shepard, and J. Hone, "Boron nitride substrates for high-quality graphene electronics", *Nature Nanotechnology*, vol. 5, no. 10, pp. 722–726, 2010. DOI: 10.1038/nnano.2010.172

[75] L. Britnell, R. V. Gorbachev, R. Jalil, B. D. Belle, F. Schedin, A. Mishchenko, T. Georgiou, M. I. Katsnelson, L. Eaves, S. V. Morozov, N. M. R. Peres, J. Leist, A. K. Geim, K. S. Novoselov, and L. A. Ponomarenko, "Field-Effect Tunneling Transistor Based on Vertical Graphene Heterostructures", *Science*, vol. 335, no. 6071, pp. 947–950, 2012. DOI: 10.1126/science.1218461

[76] V. K. Sangwan and M. C. Hersam, "Electronic Transport in Two-Dimensional Materials", *Annual Review of Physical Chemistry*, vol. 69, no. Volume 69, 2018, pp. 299–325, 2018, ISSN: 1545-1593. DOI: 10.1146/annurev-physchem-050317-021353

[77] J. Lee, S. Cruces, D. Braun, L. Völkel, K. Ran, J. Mayer, A. Daus, and M. C. Lemme, "Enhanced Threshold Switching Devices Based on Conductive Filaments in SiOx Through Vertically Aligned MoS2 Layers", in *2025 9th IEEE Electron Devices Technology & Manufacturing Conference (EDTM)*, 2025, pp. 1–3. DOI: 10.1109/EDTM61175.2025.11041161

[78] J. Lee, R. W. Ahmad, S. Cruces, D. Braun, L. Völkel, K. Ran, J. Mayer, S. Menzel, A. Daus, and M. C. Lemme, "Reduced Variability in Threshold Switches Using Heterostructures of SiOx and Vertically Aligned MoS2", *Advanced Electronic Materials*, DOI: 10.1002/aelm.202500800

[79] K. Watanabe, T. Taniguchi, and H. Kanda, "Direct-bandgap properties and evidence for ultraviolet lasing of hexagonal boron nitride single crystal", *Nature Materials*, vol. 3, pp. 404–409, 2004. DOI: 10.1038/nmat1134

[80] J. Yu, J. Li, W. Zhang, and H. Chang, "Synthesis of high quality two-dimensional materials via chemical vapor deposition", *Chem. Sci.*, vol. 6, pp. 6705–6716, 12 2015. DOI: 10.1039/C5SC01941A

[81] P.-Y. Chen and S. Yu, "Compact Modeling of RRAM Devices and Its Applications in 1T1R and 1S1R Array Design", *IEEE Transactions on Electron Devices*, vol. 62, no. 12, pp. 4022–4028, 2015. DOI: 10.1109/TED.2015.2492421

[82] S. Cortese, M. Trapatseli, A. Khiat, and T. Prodromakis, "A TiO2-based volatile threshold switching selector device with 10^7 non linearity and sub 100 pA Off current", in *2016 International Symposium on VLSI Technology, Systems and Application (VLSI-TSA)*, 2016, pp. 1–2. DOI: 10.1109/VLSI-TSA.2016.7480484

[83] L. Zhang, S. Cosemans, D. J. Wouters, G. Groeseneken, M. Jurczak, and B. Govoreanu, "Selector design considerations and requirements for 1 SIR RRAM crossbar array", in *2014 IEEE 6th International Memory Workshop (IMW)*, 2014, pp. 1–4. DOI: 10.1109/IMW.2014.6849358

[84] Z. Jiang, P. Huang, L. Zhao, S. Kvatinsky, S. Yu, X. Liu, J. Kang, Y. Nishi, and H. .-. P. Wong, "Performance Prediction of Large-Scale 1S1R Resistive Memory Array Using Machine Learning", in *2015 IEEE International Memory Workshop (IMW)*, 2015, pp. 1–4. DOI: 10.1109/IMW.2015.7150302

[85] J. Woo, X. Peng, and S. Yu, "Design Considerations of Selector Device in Cross-Point RRAM Array for Neuromorphic Computing", in *2018 IEEE International Symposium on Circuits and Systems (ISCAS)*, 2018, pp. 1–4. DOI: 10.1109/ISCAS.2018.8351735

[86] B. Attarimashalkoubeh and Y. Leblebici, "Novel 3D architecture of 1S1R", in *2019 IEEE/ACM International Symposium on Nanoscale Architectures (NANOARCH)*, 2019, pp. 1–2. DOI: 10.1109/NANOARCH47378.2019.181278

[87] A. Chen, "A Comprehensive Crossbar Array Model With Solutions for Line Resistance and Nonlinear Device Characteristics", *IEEE Transactions on Electron Devices*, vol. 60, no. 4, pp. 1318–1326, 2013. DOI: 10.1109/TED.2013.2246791

[88] A. Serb, W. Redman-White, C. Papavassiliou, and T. Prodromakis, "Practical Determination of Individual Element Resistive States in Selectorless RRAM Arrays", *IEEE Transactions on Circuits and Systems I: Regular Papers*, vol. 63, no. 6, pp. 827–835, 2016. DOI: 10.1109/TCSI.2015.2476296

[89] N. Kopperberg, S. Wiefels, S. Liberda, R. Waser, and S. Menzel, "A Consistent Model for Short-Term Instability and Long-Term Retention in Filamentary Oxide-Based Memristive Devices", *ACS Applied Materials & Interfaces*, vol. 13, no. 48, pp. 58 066–58 075, 2021, PMID: 34808060. DOI: 10.1021/acsami.1c14667

[90] N. Kopperberg, S. Wiefels, K. Hofmann, J. Otterstedt, D. J. Wouters, R. Waser, and S. Menzel, "Endurance of 2 Mbit Based BEOL Integrated ReRAM", *IEEE Access*, vol. 10, pp. 122 696–122 705, 2022. DOI: 10.1109/ACCESS.2022.3223657

[91] P. Stasner, N. Kopperberg, K. Schnieders, T. Hennen, S. Wiefels, S. Menzel, R. Waser, and D. J. Wouters, "Reliability effects of lateral filament confinement by nano-scaling the oxide in memristive devices", *Nanoscale Horiz.*, vol. 9, pp. 764–774, 5 2024. DOI: 10.1039/D3NH00520H

[92] N. Kopperberg, D. Genua Noguera, and S. Menzel, "3D kinetic Monte Carlo-based investigation of the influence of dopants on the reliability of VCM ReRAM", *Journal of Applied Physics*, vol. 137, no. 17, p. 175 105, May 2025, ISSN: 0021-8979. DOI: 10.1063/5.0262843

[93] S. Menzel and C. Bengel, *JART ECM v1*, version V1, 2025. DOI: 10.26165/JUELICH-DATA/4F3ITW

[94] A. Hardtdegen, C. La Torre, F. Cüppers, S. Menzel, R. Waser, and S. Hoffmann-Eifert, "Improved Switching Stability and the Effect of an Internal Series Resistor in HfO2/TiOx Bilayer ReRAM Cells", *IEEE Transactions on Electron Devices*, vol. 65, no. 8, pp. 3229–3236, 2018. DOI: 10.1109/TED.2018.2849872

[95] C. Bengel, A. Siemon, F. Cüppers, S. Hoffmann-Eifert, A. Hardtdegen, M. von Witzleben, L. Hellmich, R. Waser, and S. Menzel, "Variability-Aware Modeling of Filamentary Oxide-Based Bipolar Resistive Switching Cells Using SPICE Level Compact Models", *IEEE Transactions on Circuits and Systems I: Regular Papers*, vol. 67, no. 12, pp. 4618–4630, 2020. DOI: 10.1109/TCSI.2020.3018502

[96] S. Slesazeck, H. Mähne, H. Wylezich, A. Wachowiak, J. Radhakrishnan, A. Ascoli, R. Tetzlaff, and T. Mikolajick, "Physical model of threshold switching in NbO2 based memristors", *RSC Adv.*, vol. 5, pp. 102 318–102 322, 124 2015. DOI: 10.1039/C5RA19300A

[97] G. S. Rose, N. McDonald, L.-K. Yan, B. Wysocki, and K. Xu, "Foundations of memristor based PUF architectures", in *2013 IEEE/ACM International Symposium on Nanoscale Architectures (NANOARCH)*, 2013, pp. 52–57. DOI: 10.1109/NanoArch.2013.6623044

[98] K. S. Woo, J. Kim, J. Han, W. Kim, Y. H. Jang, and C. S. Hwang, "Probabilistic computing using Cu_0.1Te_0.9/HfO_2/Pt diffusive memristors", *Nature Communications*, vol. 13, p. 5762, 2022. DOI: 10.1038/s41467-022-33455-x

[99] K. S. Woo, J. Han, S.-I. Yi, L. Thomas, H. Park, S. Kumar, and C. S. Hwang, "Tunable stochastic memristors for energy-efficient encryption and computing", *Nature Communications*, vol. 15, p. 3245, 2024. DOI: 10.1038/s41467-024-47488-x

[100] R. W. Ahmad and S. Menzel, *JART ECM v1 var*, version V1, 2025. DOI: 10.26165/JUELICH-DATA/WHSSZA

[101] F. Spitzer, *Principles of Random Walk*. Springer, 2001. DOI: 10.1007/978-1-4757-4229-9

[102] R. W. Ahmad and S. Menzel, *JART v-ECM v1*, version V1, 2025. DOI: 10.26165/JUELICH-DATA/NDUPBU

[103] M. Dutta, S. Brivio, and S. Spiga, "Unraveling the Roles of Switching and Relaxation Times in Volatile Electrochemical Memristors to Mimic Neuromorphic Dynamical Features", *Advanced Electronic Materials*, vol. 10, no. 12, p. 2 400 221, 2024. DOI: 10.1002/aelm.202400221

[104] S. Tappertzhofen, E. Linn, U. Böttger, R. Waser, and I. Valov, "Nanobattery Effect in RRAMs—Implications on Device Stability and Endurance", *IEEE Electron Device Letters*, vol. 35, no. 2, pp. 208–210, 2014. DOI: 10.1109/LED.2013.2292113

[105] R. W. Ahmad and S. Menzel, *JART v-ECM v1 var*, version V1, 2025. DOI: 10.26165/JUELICH-DATA/RMT350

[106] H. Yeon, P. Lin, C. Choi, S. H. Tan, Y. Park, D. Lee, J. Lee, F. Xu, B. Gao, H. Wu, H. Qian, Y. Nie, S. Kim, and J. Kim, "Alloying conducting channels for reliable neuromorphic computing", *Nature Nanotechnology*, vol. 15, pp. 574–579, 2020. DOI: 10.1038/s41565-020-0694-5

[107] R. Cao, S. Liu, Q. Liu, X. Zhao, W. Wang, X. Zhang, F. Wu, Q. Wu, Y. Wang, H. Lv, S. Long, and M. Liu, "Improvement of Device Reliability by Introducing a BEOL-Compatible TiN Barrier Layer in CBRAM", *IEEE Electron Device Letters*, vol. 38, no. 10, pp. 1371–1374, 2017. DOI: 10.1109/LED.2017.2746738

[108] M. Barci, G. Molas, C. Cagli, E. Vianello, M. Bernard, A. Roule, A. Toffoli, J. Cluzel, B. De Salvo, and L. Perniola, "Bilayer Metal-Oxide Conductive Bridge Memory Technology for Improved Window Margin and Reliability", *IEEE Journal of the Electron Devices Society*, vol. 4, no. 5, pp. 314–320, 2016. DOI: 10.1109/JEDS.2016.2567219

[109] E. Vianello, C. Cagli, G. Molas, E. Souchier, P. Blaise, C. Carabasse, G. Rodriguez, V. Jousseaume, B. De Salvo, F. Longnos, F. Dahmani, P. Verrier, D. Bretegnier, and J. Liebault, "On the impact of Ag doping on performance and reliability of GeS2-based Conductive Bridge Memories", in *2012 Proceedings of the European Solid-State Device Research Conference (ESSDERC)*, 2012, pp. 278–281. DOI: 10.1109/ESSDERC.2012.6343387

[110] E. Vianello, G. Molas, F. Longnos, P. Blaise, E. Souchier, C. Cagli, G. Palma, J. Guy, M. Bernard, M. Reyboz, G. Rodriguez, A. Roule, C. Carabasse, V. Delaye, V. Jousseaume, S. Maitrejean, G. Reimbold, B. De Salvo, F. Dahmani, P. Verrier, D. Bretegnier, and J. Liebault, "Sb-doped GeS2 as performance and reliability booster in Conductive Bridge RAM", in *2012 International Electron Devices Meeting*, 2012, pp. 31.5.1–31.5.4. DOI: 10.1109/IEDM.2012.6479145

[111] S. Hosseinzadeh, M. Klemm, G. Fischer, and D. Fey, *it - Information Technology*, vol. 65, no. 1-2, pp. 52–64, 2023. DOI: 10.1515/itit-2023-0022

[112] S. Hosseinzadeh, A. Parvaresh, and D. Fey, "Optimization of OLAP In-Memory Database Management Systems with Processing-In-Memory Architecture", in *Architecture of Computing Systems*, G. Goumas, S. Tomforde, J. Brehm, S. Wildermann, and T. Pionteck, Eds., Cham: Springer Nature Switzerland, 2023, pp. 264–278, ISBN: 978-3-031-42785-5. DOI: 10.1007/978-3-031-42785-5_18

[113] Y. Huang, Y. Gu, S. Mohan, A. Dolocan, N. D. Ignacio, S. Kutagulla, K. Matthews, A. Londoño-Calderon, Y.-F. Chang, Y.-C. Chen, J. H. Warner, M. T. Pettes, J. C. Lee, and D. Akinwande, "Reliability Improvement and Effective Switching Layer Model of Thin-Film MoS2 Memristors", *Advanced Functional Materials*, vol. 34, no. 15, p. 2 214 250, 2024. DOI: 10.1002/adfm.202214250

[114] G. Pacchioni, "Improving memristors' reliability", *Nature Reviews Materials*, vol. 7, p. 594, 2022. DOI: 10.1038/s41578-022-00470-9

[115] Y.-R. Jeon, Y. Abbas, A. S. Sokolov, S. Kim, B. Ku, and C. Choi, "Study of in Situ Silver Migration in Amorphous Boron Nitride CBRAM Device", *ACS Applied Materials & Interfaces*, vol. 11, no. 26, pp. 23 329–23 336, 2019, PMID: 31252457. DOI: 10.1021/acsami.9b05384

[116] A. Ali, H. Abbas, M. Hussain, S. H. A. Jaffrey, S. Hussain, C. Choi, and J. Jung, "Thickness-dependent monochalcogenide GeSe-based CBRAM for memory and artificial electronic synapses", *Nano Research*, vol. 15, pp. 2263–2277, 2022. DOI: 10.1007/s12274-021-3793-1

[117] Y.-J. Choi, S. Bang, T.-H. Kim, D. K. Lee, K. Hong, S. Kim, and B.-G. Park, "Effect of Ag source layer thickness on the switching mechanism of TiN/Ag/SiNx/TiN conductive bridging random access memory observed at sub-μA current", *Semiconductor Science and Technology*, vol. 36, no. 5, p. 055 014, Apr. 2021. DOI: 10.1088/1361-6641/abdbc2

[118] B. Cheng, A. Emboras, Y. Salamin, F. Ducry, P. Ma, Y. Fedoryshyn, S. Andermatt, M. Luisier, and J. Leuthold, "Ultra compact electrochemical metallization cells offering reproducible atomic scale memristive switching", *Communications Physics*, vol. 2, no. 28, 2019. DOI: 10.1038/s42005-019-0125-9

[119] A. Belmonte, L. Goux, J. Woo, U. Celano, A. Redolfi, S. Clima, and G. S. Kar, "Enhancement of CBRAM performance by controlled formation of a hourglass-shaped filament", in *2017 17th Non-Volatile Memory Technology Symposium (NVMTS)*, 2017, pp. 1–5. DOI: 10.1109/NVMTS.2017.8171281

[120] T. Gong, Q. Luo, X. Xu, P. Yuan, H. Ma, C. Chen, Q. Liu, S. Long, H. Lv, and M. Liu, "Uniformity and Retention Improvement of TaOx-Based Conductive Bridge Random Access Memory by CuSiN Interfacial Layer Engineering", *IEEE Electron Device Letters*, vol. 38, no. 9, pp. 1232–1235, 2017. DOI: 10.1109/LED.2017.2734907

[121] A. Ali, Y. Abbas, H. Abbas, Y.-R. Jeon, S. Hussain, B. A. Naqvi, C. Choi, and J. Jung, "Dependence of InGaZnO and SnO2 thin film stacking sequence for the resistive switching characteristics of conductive bridge memory devices", *Applied Surface Science*, vol. 525, p. 146 390, 2020, ISSN: 0169-4332. DOI: 10.1016/j.apsusc.2020.146390

[122] F. Ducry, K. Portner, S. Andermatt, and M. Luisier, "Investigation of the Electrode Materials in Conductive Bridging RAM from First-Principle", in *2018 International Conference on Simulation of Semiconductor Processes and Devices (SISPAD)*, 2018, pp. 107–110. DOI: 10.1109/SISPAD.2018.8551694

[123] U. Celano, L. Mirabelli, L. Goux, K. Opsomer, W. Devulder, F. Crupi, C. Detavernier, M. Jurczak, and W. Vandervorst, "Tuning the switching behavior of conductive-bridge resistive memory by the modulation of the cation-supplier alloys", *Microelectronic Engineering*, vol. 167, pp. 47–51, 2017, Materials for Advanced Metallization 2016 (MAM 2016), ISSN: 0167-9317. DOI: 10.1016/j.mee.2016.10.018

[124] N. Shukla, R. K. Ghosh, B. Grisafe, and S. Datta, "Fundamental mechanism behind volatile and non-volatile switching in metallic conducting bridge RAM", in *2017 IEEE International Electron Devices Meeting (IEDM)*, 2017, pp. 4.3.1–4.3.4. DOI: 10.1109/IEDM.2017.8268325

[125] J. Yu, X. Xu, T. Gong, Q. Luo, D. Dong, P. Yuan, L. Tai, J. Yin, X. Zhu, X. Wu, H. Lv, and M. Liu, "Suppression of Filament Overgrowth in Conductive Bridge Random Access Memory by Ta2O5/TaOx Bi-Layer Structure", *Nanoscale Research Letters*, vol. 14, p. 111, 2019. DOI: 10.1186/s11671-019-2942-x

[126] F. Longnos, E. Vianello, C. Cagli, G. Molas, E. Souchier, P. Blaise, C. Carabasse, G. Rodriguez, V. Jousseaume, B. De Salvo, F. Dahmani, P. Verrier, D. Bretegnier, and J. Liebault, "On the impact of Ag doping on performance and reliability of GeS2-based conductive bridge memories", *Solid-State Electronics*, vol. 84, pp. 155–159, 2013, Selected Papers from the ESSDERC 2012 Conference, ISSN: 0038-1101. DOI: 10.1016/j.sse.2013.02.013

[127] H. Abbas, A. Ali, J. Jung, Q. Hu, M. R. Park, H. H. Lee, T.-S. Yoon, and C. J. Kang, "Reversible transition of volatile to non-volatile resistive switching and compliance current-dependent multistate switching in IGZO/MnO RRAM devices", *Applied Physics Letters*, vol. 114, no. 9, p. 093 503, Mar. 2019, ISSN: 0003-6951. DOI: 10.1063/1.5082901

[128] S. Lim, C. Sung, H. Kim, T. Kim, J. Song, J.-J. Kim, and H. Hwang, "Improved Synapse Device With MLC and Conductance Linearity Using Quantized Conduction for Neuromorphic Systems", *IEEE Electron Device Letters*, vol. 39, no. 2, pp. 312–315, 2018. DOI: 10.1109/LED.2018.2789425

[129] F. G. Aga, J. Woo, J. Song, J. Park, S. Lim, C. Sung, and H. Hwang, "Controllable quantized conductance for multilevel data storage applications using conductive bridge random access memory", *Nanotechnology*, vol. 28, no. 11, p. 115 707, Feb. 2017. DOI: 10.1088/1361-6528/aa5baf

[130] J. R. Jameson, N. Gilbert, F. Koushan, J. Saenz, J. Wang, S. Hollmer, M. Kozicki, and N. Derhacobian, "Quantized Conductance in $Ag/GeS_2/W$ Conductive-Bridge Memory Cells", *IEEE Electron Device Letters*, vol. 33, no. 2, pp. 257–259, 2012. DOI: 10.1109/LED.2011.2177803

[131] L. Völkel, D. Braun, M. Belete, S. Kataria, T. Wahlbrink, K. Ran, K. Kistermann, J. Mayer, S. Menzel, A. Daus, and M. C. Lemme, "Resistive Switching and Current Conduction Mechanisms in Hexagonal Boron Nitride Threshold Memristors with Nickel Electrodes", *Advanced Functional Materials*, vol. 34, no. 15, p. 2 300 428, 2024. DOI: 10.1002/adfm.202300428

[132] R. Sasikumar, A. Ajoy, and R. Padmanabhan, "Modeling of Electrochemical Metallization-Based Two-Dimensional Material Memristors for Neuromorphic Applications", *IEEE Transactions on Nanotechnology*, vol. 20, pp. 912–921, 2021. DOI: 10.1109/TNANO.2021.3133356

[133] M. Buttberg, I. Valov, and S. Menzel, "Simulating the filament morphology in electrochemical metallization cells", *Neuromorphic Computing and Engineering*, vol. 3, no. 2, p. 024 010, Jun. 2023. DOI: 10.1088/2634-4386/acdbe5

[134] X. Guan, S. Yu, and H.-S. P. Wong, "A SPICE Compact Model of Metal Oxide Resistive Switching Memory With Variations", *IEEE Electron Device Letters*, vol. 33, no. 10, pp. 1405–1407, 2012. DOI: 10.1109/LED.2012.2210856

[135] W. Wang, M. Laudato, E. Ambrosi, A. Bricalli, E. Covi, Y.-H. Lin, and D. Ielmini, "Volatile Resistive Switching Memory Based on Ag Ion Drift/Diffusion—Part II: Compact Modeling", *IEEE Transactions on Electron Devices*, vol. 66, no. 9, pp. 3802–3808, 2019. DOI: 10.1109/TED.2019.2928888

[136] W. Wang, M. Laudato, E. Ambrosi, A. Bricalli, E. Covi, Y.-H. Lin, and D. Ielmini, "Volatile Resistive Switching Memory Based on Ag Ion Drift/Diffusion Part I: Numerical Modeling", *IEEE Transactions on Electron Devices*, vol. 66, no. 9, pp. 3795–3801, 2019. DOI: 10.1109/TED.2019.2928890

[137] Y. D. Zhao, P. Huang, Z. H. Guo, Z. Y. Lun, B. Gao, X. Y. Liu, and J. F. Kang, "Atomic Monte-Carlo simulation for CBRAM with various filament geometries", in *2016 International Conference on Simulation of Semiconductor Processes and Devices (SISPAD)*, 2016, pp. 153–156. DOI: 10.1109/SISPAD.2016.7605170

[138] F. Ducry, "Ab initio Quantum Transport in Conductive Bridging Random Access Memory", Ph.D. dissertation, 2021. DOI: 10.3929/ethz-b-000474598

[139] Y. Zhao, P. Huang, Z. Zhou, C. Liu, S. Qin, L. Liu, X. Liu, H.-S. P. Wong, and J. Kang, "A Physics-Based Compact Model for CBRAM Retention Behaviors Based on Atom Transport Dynamics and Percolation Theory", *IEEE Electron Device Letters*, vol. 40, no. 4, pp. 647–650, 2019. DOI: 10.1109/LED.2019.2901754

[140] S. Choi, S. Ambrogio, S. Balatti, F. Nardi, and D. Ielmini, "Resistance Drift Model for Conductive-Bridge (CB) RAM by Filament Surface Relaxation", in *2012 4th IEEE International Memory Workshop*, 2012, pp. 1–4. DOI: 10.1109/IMW.2012.6213666

[141] S. Menzel and R. Waser, "Analytical analysis of the generic SET and RESET characteristics of electrochemical metallization memory cells", *Nanoscale*, vol. 5, pp. 11 003–11 010, 22 2013. DOI: 10.1039/C3NR03387B

[142] S. Menzel and R. Waser, "On the SET/RESET current asymmetry in electrochemical metallization memory cells", *physica status solidi (RRL) – Rapid Research Letters*, vol. 8, no. 6, pp. 540–544, 2014. DOI: 10.1002/pssr.201308310

[143] J. B. Roldán, E. Miranda, D. Maldonado, A. N. Mikhaylov, N. V. Agudov, A. A. Dubkov, M. N. Koryazhkina, M. B. González, M. A. Villena, S. Poblador, M. Saludes-Tapia, R. Picos, F. Jiménez-Molinos, S. G. Stavrinides, E. Salvador, F. J. Alonso, F. Campabadal, B. Spagnolo, M. Lanza, and L. O. Chua, "Variability in Resistive Memories", *Advanced Intelligent Systems*, vol. 5, no. 6, p. 2 200 338, 2023. DOI: 10.1002/aisy.202200338

[144] Y. Liu, K. Yang, X. Wang, H. Tian, and T.-L. Ren, "Lower Power, Better Uniformity, and Stability CBRAM Enabled by Graphene Nanohole Interface Engineering", *IEEE Transactions on Electron Devices*, vol. 67, no. 3, pp. 984–988, 2020. DOI: 10.1109/TED.2020.2968731

[145] X. Zhao, S. Liu, J. Niu, L. Liao, Q. Liu, X. Xiao, H. Lv, S. Long, W. Banerjee, W. Li, S. Si, and M. Liu, "Confining Cation Injection to Enhance CBRAM Performance by Nanopore Graphene Layer", *Small*, vol. 13, no. 35, p. 1 603 948, 2017. DOI: 10.1002/smll.201603948

[146] R. D. Nikam and H. Hwang, "Atomic Threshold Switch Based on All-2D Material Heterostructures with Excellent Control Over Filament Growth and Volatility", *Advanced Functional Materials*, vol. 32, no. 29, p. 2 201 749, 2022. DOI: 10.1002/adfm.202201749

[147] K. Ranganathan, M. Fiegenbaum-Raz, and A. Ismach, "Large-Scale and Robust Multifunctional Vertically Aligned MoS2 Photo-Memristors", *Advanced Functional Materials*, vol. 30, no. 51, p. 2 005 718, 2020. DOI: 10.1002/adfm.202005718

[148] T. Lehenkari, S.-D. Huang, K. Kordas, and H.-P. Komsa, "First-principles study of Ag, Au, Cu, and Li defects in MoS_2 and their application to memristors", *Phys. Rev. Mater.*, vol. 9, p. 014 001, 1 Jan. 2025. DOI: 10.1103/PhysRevMaterials.9.014001

[149] C. Stern, S. Grinvald, M. Kirshner, O. Sinai, M. Oksman, H. Alon, O. E. Meiron, M. Bar-Sadan, L. Houben, and D. Naveh, "Growth Mechanisms and Electronic Properties of Vertically Aligned MoS_2", *Scientific Reports*, vol. 8, p. 16 480, 2018. DOI: 10.1038/s41598-018-34222-z

[150] A. Bondi, "van der Waals Volumes and Radii", *The Journal of Physical Chemistry*, vol. 68, no. 3, pp. 441–451, 1964. DOI: 10.1021/j100785a001

[151] J. van den Hurk, S. Menzel, R. Waser, and I. Valov, "Processes and Limitations during Filament Formation and Dissolution in GeSx-based ReRAM Memory Cells", *The Journal of Physical Chemistry C*, vol. 119, no. 32, pp. 18 678–18 685, 2015. DOI: 10.1021/acs.jpcc.5b03622

[152] F. Longnos, E. Vianello, G. Molas, G. Palma, E. Souchier, C. Carabasse, M. Bernard, B. De Salvo, D. Bretegnier, and J. Liebault, "On disturb immunity and P/E kinetics of Sb-doped GeS2/Ag conductive bridge memories", in *2013 5th IEEE International Memory Workshop*, 2013, pp. 96–99. DOI: 10.1109/IMW.2013.6582107

[153] S. Menzel, U. Böttger, M. Wimmer, and M. Salinga, "Physics of the Switching Kinetics in Resistive Memories", *Advanced Functional Materials*, vol. 25, no. 40, pp. 6306–6325, 2015. DOI: 10.1002/adfm.201500825

[154] H. Jiang, D. Belkin, S. E. Savel'ev, S. Lin, Z. Wang, Y. Li, S. Joshi, R. Midya, C. Li, M. Rao, M. Barnell, Q. Wu, J. J. Yang, and Q. Xia, "A Novel True Random Number Generator Based on a Stochastic Diffusive Memristor", *Nature Communications*, vol. 8, no. 882, Oct. 2017. DOI: 10.1038/s41467-017-00869-x

[155] Q. Hua, H. Wu, B. Gao, M. Zhao, Y. Li, X. Li, X. Hou, M.-F. (Marvin) Chang, P. Zhou, and H. Qian, "A Threshold Switching Selector Based on Highly Ordered Ag Nanodots for X-Point Memory Applications", *Advanced Science*, vol. 6, no. 10, p. 1 900 024, 2019. DOI: 10.1002/advs.201900024

[156] S. Menzel, "Comprehensive modeling of electrochemical metallization memory cells", *Journal of Computational Electronics*, vol. 16, pp. 1017–1037, 2017. DOI: 10.1007/s10825-017-1051-2

[157] J. Aeschlimann, F. Ducry, C. Weilenmann, J. Leuthold, A. Emboras, and M. Luisier, "Multiscale Modeling of Metal-Oxide-Metal Conductive Bridging Random-Access Memory Cells: From Ab Initio to Finite-Element Calculations", *Phys. Rev. Appl.*, vol. 19, p. 024 058, 2 Feb. 2023. DOI: 10.1103/PhysRevApplied.19.024058

[158] S. Yu and H.-S. P. Wong, "Compact Modeling of Conducting-Bridge Random-Access Memory (CBRAM)", *IEEE Transactions on Electron Devices*, vol. 58, no. 5, pp. 1352–1360, 2011. DOI: 10.1109/TED.2011.2116120

[159] Y.-R. Jeon, D. Akinwande, and C. Choi, "Volatile threshold switching and synaptic properties controlled by Ag diffusion using Schottky defects", *Nanoscale Horiz.*, vol. 9, pp. 853–862, 5 2024. DOI: 10.1039/D3NH00571B

[160] E. Passerini, M. Lewerenz, M. Csontos, N. Jimenez Olalla, K. Keller, J. Aeschlimann, F. Xie, A. Emboras, X. Zhang, M. Fischer, Y. Fedoryshyn, M. Luisier, T. Schimmel, U. Koch, and J. Leuthold, "Controlling Volatility and Nonvolatility of Memristive Devices by Sn Alloying", *ACS Applied Electronic Materials*, vol. 5, no. 12, pp. 6842–6849, 2023. DOI: 10.1021/acsaelm.3c01275

[161] X. Lei, X. Zhu, H. Wang, Y. Dai, H. Zhang, C. Zhai, S. Wang, J. Yan, and W. Zhao, "Nonvolatile and volatile resistive switching characteristics in MoS2 thin film for RRAM application", *Journal of Alloys and Compounds*, vol. 969, p. 172 443, 2023, ISSN: 0925-8388. DOI: 10.1016/j.jallcom.2023.172443

[162] T. Liu, "Nonvolatile and Volatile Resistive Switching — Characterization, Modeling, Memristive Subcircuits", Ph.D. dissertation, Department of Electrical, Computer Engineering, Virginia Polytechnic Institute, and State University, Blacksburg, VA, USA, 2013.

[163] K. S. Woo, H. Park, N. Ghenzi, A. A. Talin, T. Jeong, J.-H. Choi, S. Oh, Y. H. Jang, J. Han, R. S. Williams, S. Kumar, and C. S. Hwang, "Memristors with Tunable Volatility for Reconfigurable Neuromorphic Computing", *ACS Nano*, vol. 18, no. 26, pp. 17 007–17 017, 2024, PMID: 38952324. DOI: 10.1021/acsnano.4c03238

[164] Z. Wang, M. Rao, R. Midya, S. Joshi, H. Jiang, P. Lin, W. Song, S. Asapu, Y. Zhuo, C. Li, H. Wu, Q. Xia, and J. J. Yang, "Threshold Switching of Ag or Cu in Dielectrics: Materials, Mechanism, and Applications", *Advanced Functional Materials*, vol. 28, no. 6, p. 1 704 862, 2018. DOI: 10.1002/adfm.201704862

[165] T. Moon, K. Soh, J. S. Kim, J. E. Kim, S. Y. Chun, K. Cho, J. J. Yang, and J. H. Yoon, "Leveraging volatile memristors in neuromorphic computing: from materials to system implementation", *Mater. Horiz.*, vol. 11, pp. 4840–4866, 20 2024. DOI: 10.1039/D4MH00675E

[166] P. Liu, L. Song, K.-P. Pun, and G. Hu, "Threshold Switching Memristor Modeling for Spiking Neuron Design", *IEEE Electron Device Letters*, vol. 45, no. 9, pp. 1649–1652, 2024. DOI: 10.1109/LED.2024.3424586

[167] A. Bou, C. Gonzales, P. P. Boix, Y. Vaynzof, A. Guerrero, and J. Bisquert, "Kinetics of Volatile and Nonvolatile Halide Perovskite Devices: The Conductance-Activated Quasi-Linear Memristor (CALM) Model", *The Journal of Physical Chemistry Letters*, vol. 16, no. 1, pp. 69–76, 2025, PMID: 39699063. DOI: 10.1021/acs.jpclett.4c03132

[168] T. Patni, R. Daniels, and S. Kvatinsky, "V-VTEAM: A Compact Behavioral Model for Volatile Memristors", in *2024 IEEE International Flexible Electronics Technology Conference (IFETC)*, 2024, pp. 1–4. DOI: 10.1109/IFETC61155.2024.10771870

[169] T. Wang, R. Zhao, Y. Xu, Y. Zhuo, R. S. Williams, and J. J. Yang, "A Faithful and Compact Diffusive Memristor Model", *IEEE Transactions on Circuits and Systems for Artificial Intelligence*, vol. 1, no. 2, pp. 141–148, 2024. DOI: 10.1109/TCASAI.2024.3484370

[170] A. Nabil, T. N. Kumar, and H. A. F. Almurib, "A generic volatile memristor model", *Physica Scripta*, vol. 99, no. 12, p. 125 031, Nov. 2024. DOI: 10.1088/1402-4896/ad92e8

[171] Y. Zhuo, R. Midya, W. Song, Z. Wang, S. Asapu, M. Rao, P. Lin, H. Jiang, Q. Xia, R. S. Williams, and J. J. Yang, "A Dynamical Compact Model of Diffusive and Drift Memristors for Neuromorphic Computing", *Advanced Electronic Materials*, vol. 8, no. 8, p. 2 100 696, 2022. DOI: 10.1002/aelm.202100696

[172] C. Tsioustas, P. Bousoulas, G. Kleitsiotis, S. D. Mantas, and D. Tsoukalas, "Impact of inert electrode on the volatility and non-volatility switching behavior of SiO2-based conductive bridge random access memory devices", *Applied Physics Letters*, vol. 125, no. 2, p. 023 508, Jul. 2024, ISSN: 0003-6951. DOI: 10.1063/5.0209676

[173] C. Tsioustas, P. Bousoulas, J. Hadfield, T. P. Chatzinikolaou, I.-A. Fyrigos, V. Ntinas, M.-A. Tsompanas, G. C. Sirakoulis, and D. Tsoukalas, "Simulation of Low Power Self-Selective Memristive Neural Networks for in situ Digital and Analogue Artificial Neural Network Applications", *IEEE Transactions on Nanotechnology*, vol. 21, pp. 505–513, 2022. DOI: 10.1109/TNANO.2022.3205698

[174] Y. Zhao, C. Fang, X. Zhang, X. Xu, T. Gong, Q. Luo, C. Chen, Q. Liu, H. Lv, Q. Li, F. Zhang, L. Li, and M. Liu, "A Compact Model for Drift and Diffusion Memristor Applied in Neuron Circuits Design", *IEEE Transactions on Electron Devices*, vol. 65, no. 10, pp. 4290–4296, 2018. DOI: 10.1109/TED.2018.2865225

[175] F. Vaccaro, A. G. Mauri, S. Perotto, S. Brivio, and S. Spiga, "Modeling and simulation of electrochemical and surface diffusion effects in filamentary cation-based resistive memory devices", *Applied Mathematical Modelling*, vol. 134, pp. 591–610, 2024, ISSN: 0307-904X. DOI: 10.1016/j.apm.2024.06.021

[176] W. Wang, A. Bricalli, M. Laudato, E. Ambrosi, E. Covi, and D. Ielmini, "Physics-based modeling of volatile resistive switching memory (RRAM) for crosspoint selector and neuromorphic computing", in *2018 IEEE International Electron Devices Meeting (IEDM)*, 2018, pp. 40.3.1–40.3.4. DOI: 10.1109/IEDM.2018.8614556

[177] W. Wang, E. Covi, Y.-H. Lin, E. Ambrosi, A. Milozzi, C. Sbandati, M. Farronato, and D. Ielmini, "Switching Dynamics of Ag-Based Filamentary Volatile Resistive Switching Devices—Part II: Mechanism and Modeling", *IEEE Transactions on Electron Devices*, vol. 68, no. 9, pp. 4342–4349, 2021. DOI: 10.1109/TED.2021.3095033

[178] W. Wang, M. Wang, E. Ambrosi, A. Bricalli, M. Laudato, Z. Sun, X. Chen, and D. Ielmini, "Surface Diffusion-Limited Lifetime of Silver and Copper Nanofilaments in Resistive Switching Devices", *Nature Communications*, vol. 10, no. 81, 2019. DOI: 10.1038/s41467-018-07979-0

[179] W. Wang, E. Covi, Y.-H. Lin, E. Ambrosi, and D. Ielmini, "Modeling of switching speed and retention time in volatile resistive switching memory by ionic drift and diffusion", in *2019 IEEE International Electron Devices Meeting (IEDM)*, 2019, pp. 32.3.1–32.3.4. DOI: 10.1109/IEDM19573.2019.8993625

[180] Y. Dai, J. Zou, Z. Feng, X. Li, X. Wang, G. Hu, Y. Zhu, and Z. Wu, "Modeling of a diffusive memristor based on the DT-FNT mechanism transition", *Semiconductor Science and Technology*, vol. 37, no. 9, p. 095 001, Jul. 2022. DOI: 10.1088/1361-6641/ac78ff

[181] Z. Wang, S. Joshi, S. E. Savel'ev, H. Jiang, R. Midya, P. Lin, M. Hu, N. Ge, J. P. Strachan, Z. Li, Q. Wu, M. Barnell, G.-L. Li, H. L. Xin, R. S. Williams, Q. Xia, and J. J. Yang, "Memristors with diffusive dynamics as synaptic emulators for neuromorphic computing", *Nature Materials*, vol. 16, pp. 101–108, Jan. 2017, ISSN: 1476-4660. DOI: 10.1038/nmat4756

[182] A. Akther, Y. Ushakov, A. G. Balanov, and S. E. Savel'ev, "Deterministic modeling of the diffusive memristor", *Chaos: An Interdisciplinary Journal of Nonlinear Science*, vol. 31, no. 7, p. 073 111, Jul. 2021, ISSN: 1054-1500. DOI: 10.1063/5.0056239

[183] S. J. Yang, L. Liang, Y. Lee, Y. Gu, J. Fatheema, S. Kutagulla, D. Kim, M. Kim, S. Kim, and D. Akinwande, "Volatile and Nonvolatile Resistive Switching Coexistence in Conductive Point Hexagonal Boron Nitride Monolayer", *ACS Nano*, vol. 18, no. 4, pp. 3313–3322, 2024, PMID: 38226861. DOI: 10.1021/acsnano.3c10068

[184] J. Liu and S. Chen, "Initial experience with 3D XPoint main memory", *Distributed and Parallel Databases*, vol. 38, pp. 865–880, 2020. DOI: 10.1007/s10619-019-07277-8

[185] D. Waddington, C. Dickey, L. Xu, T. Janssen, J. Tran, and D. Kshitij, "Evaluating Intel 3D-Xpoint NVDIMM Persistent Memory in the Context of a Key-Value Store", in *2020 IEEE International Symposium on Performance Analysis of Systems and Software (ISPASS)*, 2020, pp. 202–211. DOI: 10.1109/ISPASS48437.2020.00035

[186] J. Kim, H. C. Woo, T. Jeong, J.-H. Choi, and C. S. Hwang, "In-Depth Analysis of One Selector–One Resistor Crossbar Array for Its Writing and Reading Operations for Hardware Neural Network with Finite Wire Resistance", *Advanced Intelligent Systems*, vol. 4, no. 4, p. 2 100 174, 2022. DOI: 10.1002/aisy.202100174

[187] A. Ascoli, S. Slesazeck, H. Mähne, R. Tetzlaff, and T. Mikolajick, "Nonlinear Dynamics of a Locally-Active Memristor", *IEEE Transactions on Circuits and Systems I: Regular Papers*, vol. 62, no. 4, pp. 1165–1174, 2015. DOI: 10.1109/TCSI.2015.2413152

[188] A. Ascoli, A. S. Demirkol, R. Tetzlaff, S. Slesazeck, T. Mikolajick, and L. O. Chua, "On Local Activity and Edge of Chaos in a NaMLab Memristor", *Frontiers in Neuroscience*, vol. Volume 15 - 2021, 2021, ISSN: 1662-453X. DOI: 10.3389/fnins.2021.651452

[189] C.-L. Lo, T.-H. Hou, M.-C. Chen, and J.-J. Huang, "Dependence of Read Margin on Pull-Up Schemes in High-Density One Selector–One Resistor Crossbar Array", *IEEE Transactions on Electron Devices*, vol. 60, no. 1, pp. 420–426, 2013. DOI: 10.1109/TED.2012.2225147

[190] S. Kim, H.-D. Kim, and S.-J. Choi, "Numerical study of read scheme in one-selector one-resistor crossbar array", *Solid-State Electronics*, vol. 114, pp. 80–86, 2015, ISSN: 0038-1101. DOI: 10.1016/j.sse.2015.08.001

[191] Y. Cassuto, S. Kvatinsky, and E. Yaakobi, "Sneak-path constraints in memristor crossbar arrays", in *2013 IEEE International Symposium on Information Theory*, 2013, pp. 156–160. DOI: 10.1109/ISIT.2013.6620207

[192] Y. Ho, G. M. Huang, and P. Li, "Nonvolatile memristor memory: device characteristics and design implications", in *Proceedings of the 2009 International Conference on Computer-Aided Design*, ser. ICCAD '09, San Jose, California: Association for Computing Machinery, 2009, pp. 485–490, ISBN: 9781605588001. DOI: 10.1145/1687399.1687491

[193] S. Kim, J. Zhou, and W. D. Lu, "Crossbar RRAM Arrays: Selector Device Requirements During Write Operation", *IEEE Transactions on Electron Devices*, vol. 61, no. 8, pp. 2820–2826, 2014. DOI: 10.1109/TED.2014.2327514

[194] H. Li, H.-Y. Chen, Z. Chen, B. Chen, R. Liu, G. Qiu, P. Huang, F. Zhang, Z. Jiang, B. Gao, L. Liu, X. Liu, S. Yu, H.-S. P. Wong, and J. Kang, "Write disturb analyses on half-selected cells of cross-point RRAM arrays", in *2014 IEEE International Reliability Physics Symposium*, 2014, MY.3.1–MY.3.4. DOI: 10.1109/IRPS.2014.6861158

[195] V. V. Zhirnov, R. K. Cavin, S. Menzel, E. Linn, S. Schmelzer, D. Bräuhaus, C. Schindler, and R. Waser, "Memory Devices: Energy–Space–Time Tradeoffs", *Proceedings of the IEEE*, vol. 98, no. 12, pp. 2185–2200, 2010. DOI: 10.1109/JPROC.2010.2064271

[196] E. Sondheimer, "The mean free path of electrons in metals", *Advances in Physics*, vol. 1, no. 1, pp. 1–42, 1952. DOI: 10.1080/00018735200101151

List of Figures

2.1 Conceptual illustration of ECM cells' I-V sweep . . . 8
2.2 Exemplary SET kinetics characteristics of an ECM cell . . . 9
2.3 Illustrated ionic processes of a nonvolatile ECM cell for different stages of an I-V sweep . . . 13
2.4 Illustration of the ion hopping energy profile between hopping sites . . . 17
2.5 Illustration of the electron transfer processes' energy profile . . . 19
2.6 Energetic profile illustration of electronic transport across metal-insulator-metal interfaces . . . 22
2.7 Illustrations of the electromotive force's origins . . . 26
2.8 Illustration of a Ag/SiO_x/$VAMoS_2$/Au ECM stack as an example for 2D materials in the insulating layer . . . 28
2.9 Exemplary illustration of a 3×3 - crossbar array . . . 30
2.10 Simplified diagram of requirements for a 1S1R device design . . . 32
2.11 Schematic illustration of the $V/2$ - scheme for a 1S1R crossbar aray . . . 34
2.12 Exemplary representation of the VMM on a 3×3 1S1R crossbar array . . . 35

3.1 Illustration of the nonvolatile ECM model's equivalent circuit diagram . . . 40

4.1 Schematic illustration of a v-ECM device's different dynamical regimes . . . 53
4.2 Illustration of the volatile ECM model's equivalent circuit diagram . . . 54

5.1 Schematic representation and cross-sectional TEM image of the Cu/SiO_2/W device stack . . . 63
5.2 Illustration of SET delay times via current-time characteristics . . . 65
5.3 Experimentally obtained and simulated device-to-device variability of SET kinetics . . . 65
5.4 Experimentally obtained and simulated cycle-to-cycle variability of I-V sweeps 68
5.5 Illustration of simulated I-V sweeps depicting the impact of four individual model modifications . . . 69
5.6 Illustration of the applied volatge pulse to the SiO_x/$VAMoS_2$ and SiO_x-only devices . . . 71
5.7 Measured and simulated current response variabilities of SiO_x/$VAMoS_2$ and SiO_x-only devices . . . 72
5.8 Illustration of the proposed filament growth within the SiO_x/$VAMoS_2$ and SiO_x-only device . . . 75
5.9 Experimental and simulated SET kinetics data for the h-BN device . . . 78
5.10 Parameter study of the SET kinetics d2d variability focusing on the nucleation parameters . . . 82
5.11 Parameter study of the SET kinetics d2d variability focusing on the parallel-shifting electron transfer parameters . . . 84

5.12 Parameter study of the SET kinetics d2d variability focusing on the slope-changing electron transfer parameters . . . 86
5.13 Illustration of the electron transfer coefficient's fastest-switching edge case . . . 87
5.14 Parameter study of the SET kinetics d2d variability focusing on the parallel-shifting parameters of the mixed-control regime . . . 89
5.15 Parameter study of c2c variability in the I–V characteristics with focus on nucleation parameters . . . 94
5.16 Parameter study of c2c variability in the I–V characteristics with focus on parallel-shifting electron transfer-related parameters . . . 95
5.17 Parameter study of c2c variability in the I–V characteristics with focus on slope-changing electron transfer-related parameters . . . 96
5.18 Parameter study of c2c variability in the I–V characteristics with focus on parallel-shifting mixed control-regime parameters . . . 99
5.19 Parameter study of c2c variability in the I–V characteristics with focus on purely ion hopping parameters . . . 102
5.20 Study on accessing different ionic rate-limiting regimes by exclusively varying the I–V sweep rate . . . 105
5.21 Flow chart on the variability-aware fitting procedure for ECM cells . . . 110

6.1 Conceptual illustration of a v-ECM device's I-V sweep and the Ag/HfO_2/Pt v-ECM device stack . . . 116
6.2 Experimentally obtained and simulated c2c I-V sweeps of the v-ECM device . 116
6.3 Illustration of the experimental and simulated d2d SET kinetics data . . . 119
6.4 Illustration of the v-ECM device's transient voltage input and obtained current response . . . 120
6.5 Experimental and simulated d2d relaxation times as a function of the applied programming voltage . . . 121
6.6 Illustration of a v-ECM device's simulated relaxation and threshold switching kinetics . . . 123
6.7 Influence of the electromotive force on the I-V sweeps of a v-ECM device . . . 125
6.8 Influence of the sweep rate on the I-V sweeps of a v-ECM device . . . 125
6.9 Ionic current contribution during a v-ECM device's I-V sweep . . . 126

7.1 Simulated I-V sweeps of a VCM cell and a threshold switch . . . 136
7.2 Simulated pulse characteristics of a 1S1R cell made up of a VCM cell and a threshold switch . . . 137
7.3 Simulated I-V sweeps of a volatile ECM cell . . . 139
7.4 Simulated pulse characteristics of a 1S1R cell made up of a VCM cell and a volatile ECM cell . . . 140
7.5 Special case of simulated pulse characteristics of a 1S1R cell made up of a VCM cell and a volatile ECM cell . . . 141
7.6 Simulated V/2 - scheme for reading a 3×3 - crossbar array . . . 142
7.7 Illustration of the second limiting case for VMM with wire resistances . . . 149
7.8 Illustration of the third limiting case for VMM with wire resistances . . . 150
7.9 Simulated limiting cases for a 1S1R crossbar array based on a threshold switch 152
7.10 Simulated limiting cases for a 1S1R crossbar array based on a volatile ECM cell 154

List of Tables

3.1 Comparison of physics-based, mathematical, empirical, and behavioral compact models . . . 38

5.1 Deterministic mean model parameters of a nonvolatile $Cu/SiO_2/W$ ECM device for measurement fit . . . 64
5.2 Variability model parameters for measurement fit to a nonvolatile $Cu/SiO_2/W$ ECM device . . . 66
5.3 Model parameters and values for measurement fits to $SiO_x/VAMoS_2$- and SiO_x-only- based ECM devices . . . 74
5.4 Model parameters and values for the h-BN ECM device model . . . 77
5.5 Deterministic mean model parameters for SET kinetics parameter and variability study. . . . 80
5.6 Variability model parameters (Gaussian distribution) for SET kinetics parameter and variability study. . . . 81
5.7 ECM model parameter study overview: Influence of model parameters on characteristic switching properties for pulse and sweep operation . . . 92
5.8 Mean model parameters for study of sweep rate β . . . 103

6.1 Deterministic mean model parameters of a volatile $Ag/HfO_2/Pt$ ECM device for measurement fitting . . . 117
6.2 Variability model parameters for measurement fit of a $Ag/HfO_2/Pt$ ECM device 118
6.3 Comparison of various v-ECM models regarding static and dynamic device modeling . . . 129

7.1 Used model parameter values for the nonvolatile VCM model. . . . 135
7.2 Used model parameter values for the threshold switch model. . . . 135
7.3 Used model parameter values for the v-ECM cell. . . . 138
7.4 Read scheme scenarios: current through distinct crossbar cells . . . 143
7.5 VMM analysis of the second limiting case for threshold switch-based 1S1R crossbar arrays . . . 151
7.6 VMM analysis of the second limiting case for volatile ECM-based 1S1R crossbar arrays . . . 152

List of Abbreviations

1S1R	one-selector-one-resistor	167
1T1R	one-transistor-one-resistor	4
2D	two-dimensional	24
ADC	Analog-Digital Converter	4
AI	Artificial Intelligence	5
ALD	atomic layer deposition	1
ANN	Artificial Neural Network	11
BL	bit line	76
c2c	cycle-to-cycle	32
CBRAM	conductive-bridge random access memory	1
CIM	computation-in-memory	9
CPU	Central Processing Unit	2
CV	cyclic voltammetry	5
CVD	chemical vapor deposition	1
d2d	device-to-device	27
DC	Direct Current	1
dm	diffusive memristor	37
ECD	equivalent circuit diagram	3
ECM	electrochemical metallization memory	257
EDA	Electronic Design Automation	2
emf	electromotive force	159
FEM	finite element method	1
GUI	Graphical User Interface	2
h-BN	hexagonal boron nitride	9
HRS	high-resistive state	93
I	insulating layer	4
IDE	Interactive Design Environment	2

I-V	current-voltage	142
J-V	current density-voltage	1
JART	Jülich Aachen Resistive Switching Tool	43
KMC	Kinetic Monte Carlo	4
LRS	low-resistive state	127
M	metal	22
MAC	multiply-accumulate	4
MIEC	mixed ionic electronic conducting	1
MIM	metal/insulator/metal	4
MoS_2	molybdenum disulfide	5
MRAM	magnetoresistive random access memory	1
NDR	negative differential resistance	17
ODE	ordinary differential equation	7
Ox-RAM	oxide-based random access memory	1
PCM	phase change memory	1
PDR	positive differential resistance	1
PF	Poole-Frenkel	3
PUF	Physical Unclonable Function	1
ReRAM	redox-based resistive switching random access memory	106
RRAM	resistive random access memory	3
SNN	Spiking Neural Network	5
TCM	thermochemical memory	3
TRNG	True Random Number Generator	8
TS	threshold switching	12
$VAMoS_2$	vertically aligned molybdenum disulfide	38
VCM	valence-change mechanism	73
vdW	van-der-Waals	6
v-ECM	volatile threshold-switching ECM	142
VMM	vector-matrix multiplication	63
WL	word line	15

Supervised Students

Project Thesis within Master Study

Yaohui Liu, "Mathematical model development of a Ti/HfO_2/GaO_x/W memristive device", Materials Science M. Sc., December 2023

List of Publications

Articles in Peer-Reviewed Journals

R. W. Ahmad, S. A. Chekol, J. Rasbach, S. Hoffmann-Eifert, and S. Menzel, "Compact Modeling of Volatile-Switching Electrochemical Metallization Memory Cells by Means of the Electromotive Force", *Advanced Intelligent Systems*, 2025, DOI: 10.1002/aisy.202501018.

R. W. Ahmad, R. Waser, F. Maudet, O. Toprak, C. Dubourdieu, and S. Menzel, "Variability-Aware Modeling of Electrochemical Metallization Memory Cells", *Neuromorphic Computing and Engineering*, vol. 4, no. 3, pp. 034007, 2024, DOI: 10.1088/2634-4386/ad57e7.

J. Lee, **R. W. Ahmad**, S. Cruces, D. Braun, L. Völkel, K. Ran, J. Mayer, S. Menzel, A. Daus and M. C. Lemme, "Reduced Variability in Threshold Switches Using Heterostructures of SiO_x and Vertically Aligned MoS_2", *Advanced Electronic Materials*, 2026, DOI: 10.1002/aelm.202500800.

S. Menzel, B. Kersting, **R. W. Ahmad**, A. Sebastian, and G. S. Syed, "A Device-Level Compact Model for Mushroom-Type Phase Change Memory", *Advanced Electronic Materials*, vol. 12, no. 1, 2026, DOI: 10.1002/aelm.202500496.

Y. Fa, M. Buttberg, K. Ran, **R. W. Ahmad**, D. Braun, L. Völkel, J. Lee, S. Cruces, B. Macco, B. Canto, H. Lerch, T. Wahlbrink, H. Kalisch, M. Heuken, A. Vescan, J. Mayer, Z. Wang, I. Valov, S. Menzel, and M. C. Lemme, "Intermediate Resistive State in Wafer-Scale Vertical MoS_2 Memristors Through Lateral Silver Filament Growth for Artificial Synapse Applications", *Advanced Functional Materials*, 2025, DOI: 10.1002/adfm.202526682.

J. Lee, **R. W. Ahmad**, S. Cruces, D. Braun, L. Völkel, K. Ran, V. M. Andreadis, J. Mayer, S. Menzel, A. Daus, and M. C. Lemme, "Threshold Switching in Vertically Aligned MoS_2/SiO_x Heterostructures Based on Silver Ion Migration", *npj 2D Materials and Applications*, vol. 9, no. 1, pp. 86., 2025, DOI: 10.1038/s41699-025-00614-9.

S. Son, A. Bende, D. Schön, **R. W. Ahmad**, D. Nielinger, V. Rana, and S. Menzel, "A Comprehensive Compact Model for Multilevel Switching in TaO_x-Based Memristive 1T-1R Cells", *IEEE Access*, vol. 13, pp. 127280-127291, 2025, DOI: 10.1109/ACCESS.2025.3590140.

L. Völkel, **R. W. Ahmad**, A. Bestaeva, D. Braun, S. Cruces, J. Lee, S. Pasko, S. Krotkus, M. Heuken, S. Menzel, and M. C. Lemme, "Influence of Humidity on the Resistive Switching of Hexagonal Boron Nitride-Based Memristors", *npj 2D Materials and Applications*, vol. 9, no. 1, pp. 41, 2025, DOI: 10.1038/s41699-025-00566-0.

S. A. Chekol, S. Menzel, **R. W. Ahmad**, R. Waser, and S. Hoffmann-Eifert, "Effect of the Threshold Kinetics on the Filament Relaxation Behavior of Ag-Based Diffusive Memristors", *Advanced Functional Materials*, vol. 32, no. 15, pp. 2111242, 2022, DOI: 10.1002/adfm.202111242.

Articles in Conference Proceedings

R. W. Ahmad, D. Wouters, C. Bengel, R. Waser, and S. Menzel, "Analysis of VMM Operations on 1S1R Crossbar Arrays and the Influence of Wire Resistances", *2022 IEEE International Symposium on Circuits and Systems (ISCAS)*, 28 May - 1 June 2022, Austin, TX, USA, 2022, DOI: 10.1109/ISCAS48785.2022.9937570.

M. Galicia, S. Menzel, F. Merchant, M. Müller, H.-Y. Chen, Q.-T. Zhao, F. Cüppers, A. R. Jalil, Q. Shu, P. Schüffelgen, G. Mussler, C. Funck, C. Lanius, S. Wiefels, M. von Witzleben, C. Bengel, N. Kopperberg, T. Ziegler, **R. W. Ahmad**, A. Krüger, L. Pöhls, R. Dittmann, S. Hoffmann-Eifert, V. Rana, D. Grützmacher, M. Wuttig, D. Wouters, A. Vescan, T. Gemmeke, J. Knoch, M. Lemme, R. Leupers, and R. Waser, "NEUROTEC: Neuro-Inspired Artificial Intelligence Technologies for the Electronics of the Future", *2022 Design, Automation & Test in Europe Conference & Exhibition (DATE)*, 14–23 March 2022, Antwerp, Belgium, DOI: 10.23919/DATE54114.2022.9774755.

Conference Talks

R. W. Ahmad, R. Waser, F. Maudet, O. Toprak, C. Dubourdieu, and S. Menzel, "Variability-Aware Modeling of Electrochemical Metallization Memory Cells", *6th International Conference on Memristive Materials, Devices & Systems (MEMRISYS 2023)*, 6–10 November 2023, Torino, Italy.

R. W. Ahmad, D. Wouters, C. Bengel, R. Waser, and S. Menzel, "Analysis of VMM Operations on 1S1R Crossbar Arrays and the Influence of Wire Resistances", *2022 IEEE International Symposium on Circuits and Systems (ISCAS)*, 28 May - 1 June 2022, Austin, TX, USA.

Conference Posters

R. W. Ahmad, R. Waser, F. Maudet, O. Toprak, C. Dubourdieu, and S. Menzel, "Variability-Aware Compact Modeling and Model Parameter Study of Electrochemical Metallization Memory Cells", *International Conference on Neuromorphic Computing and Engineering (ICNCE)*, 3–6 June 2024, Aachen, Germany.

S. Son, A. Bende, **R. W. Ahmad**, V. Rana and S. Menzel, "Compact modeling of multilevel TaOx based 1T1R cells by an improved thermal model", *International Conference on Neuromorphic Computing and Engineering (ICNCE)*, 3–6 June 2024, Aachen, Germany.